

ML 3/7/80  
Indian J. pure appl. Phys., Vol. 18 No. 9 pp. 639-732

September 1980

CODEN : IJOPAU ISSN: 0019-5596

18 (9) 639-732 (1980)

649

3.10.80

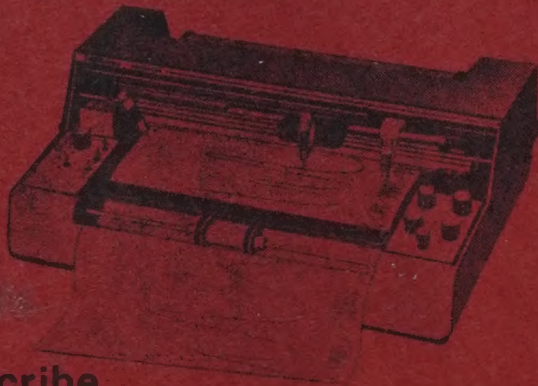
# INDIAN JOURNAL OF PURE & APPLIED PHYSICS



Published by  
PUBLICATIONS & INFORMATION DIRECTORATE, CSIR, NEW DELHI  
in association with  
THE INDIAN NATIONAL SCIENCE ACADEMY, NEW DELHI



# a quantum leap in recorder technology now available to the discriminating research scientist a range of reliable 'state of the art' recording instruments



## **DigiScribe**

Strip Chart Recorders One to Four Pens,  
0.5 mV full scale and up, 0.5 sec response



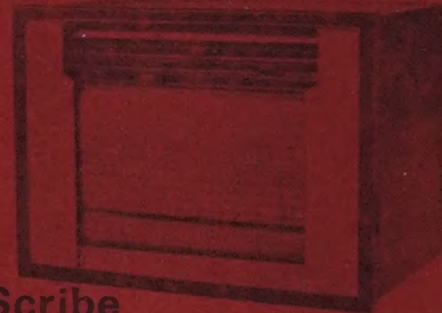
## **DigiGraphic**

XY/t Recorders with plug-in modules to give  
wide ranges of sensitivity, time base facility  
and log recording.



## **HiScribe Oscillographic**

Oscillographic Recorders DC to 80 Hz, One  
to eight channels, Heat or ink writing. Plug in  
modules to give wide range of sensitivities



## **MultiScribe**

One to Three Pen and 6, 12 and 24 point  
Recorders. Rack mounting with alarm  
contacts, cold junction compensation, and  
other features.

## **APPLICATIONS IN THE FIELDS OF**

- METEOROLOGY • MATERIAL SCIENCES
- LIFE SCIENCES • PHYSICAL SCIENCES
- CHEMICAL AND ELECTROCHEMICAL SCIENCES
- BIOLOGICAL SCIENCES • PHYSIOLOGICAL AND  
BEHAVIOURAL SCIENCES • COMPUTER SCIENCES
- ENVIRONMENTAL AND POLLUTION STUDIES
- ENERGY STUDIES • PHARMACOLOGY
- MECHANICAL/ELECTRICAL ENGINEERING
- METALLURGY/METALLURGICAL ENGINEERING
- AERODYNAMICS/AERONAUTICAL ENGINEERING
- BIO-MEDICAL ENGINEERING
- QUALITY CONTROL APPLICATIONS

MANUFACTURED BY:

**DIGITAL ELECTRONICS LIMITED**

A Company in collaboration with

**houston  
instrument**

DIVN OF **BAUSCH & LOMB** 

Office & Factory:

Digilog House, 74/II, C, Cross Road, Marol Industrial Area, MIDC,  
Andheri (East), Bombay-400 093. Phone: 577676, Gram: 'DIGILOG'



# Indian Journal of Pure & Applied Physics

VOLUME 18

No. 9

SEPTEMBER 1980

## EDITORIAL BOARD

Dr B A Dasannacharya  
Bhabha Atomic Research Centre  
Bombay

Prof. B M Deb  
Indian Institute of Technology  
Bombay

Prof. P Krishna  
Banaras Hindu University  
Varanasi

Prof. Krishnaji  
Allahabad University  
Allahabad

Prof. K V Ramanathan  
Tata Institute of Fundamental Research  
Bombay

Dr S Chandrasekhar  
Indian National Science Academy  
New Delhi/Raman Research  
Institute Bangalore

Prof. A K Saha  
Saha Institute of Nuclear Physics  
Calcutta

Prof. N C Sil  
Indian Association for  
Cultivation of Science  
Calcutta

Prof. R Srinivasan  
Indian Institute of Science  
Bangalore

Prof. K Venkata Ramiah  
Osmania University  
Hyderabad

Dr K L Chopra  
Indian National Science Academy  
New Delhi/Indian Institute of  
Technology New Delhi

Shri Y R Chadha, *Ex-officio* Secretary & Chief Editor

---

## EDITORIAL STAFF

### *Editors*

D S Sastry & K S Rangarajan

### *Assistant Editors*

G N Sarma, J B Dhawan & Tarun Banerjee

---

Published by the Publications & Information Directorate, CSIR, Hillside Road, New Delhi 110 012

Chief Editor : Y R Chadha

The Indian Journal of Pure & Applied Physics is issued monthly. The Directorate assumes no responsibility for the statements and opinions advanced by contributors. The editorial staff in its work of examining papers received for publication is assisted, in an honorary capacity, by a large number of distinguished scientists, working in various parts of India.

Communications regarding contributions for publication in the journal should be addressed to the Editor, Indian Journal of Pure & Applied Physics, Publications & Information Directorate, Hillside Road, New Delhi 110 012.

Correspondence regarding subscriptions and advertisements should be addressed to the Sales & Distribution Officer, Publications & Information Directorate, New Delhi 110 012.

### Annual Subscription

Rs. 100.00 £ 16.50 \$ 42.00

### Single Copy

Rs. 10.00 £ 1.80 \$ 4.50

50% Discount is admissible to research workers and students and 25 % discount to non-research individuals, on annual subscription. Payments in respect of subscriptions and advertisements may be sent by cheque, bank draft, money order or postal order marked payable *only* to Publications & Information Directorate, New Delhi 110 012. Claims for missing numbers of the journal will be allowed only if received within 3 months of the date of issue of the journal plus the time normally required for postal delivery of the journal and the claim.



# CSIR SCIENTIFIC PERIODICALS

## JOURNAL OF SCIENTIFIC & INDUSTRIAL RESEARCH (monthly)

With a fine record of over 35 years' service to the scientific community, this Journal has grown into India's leading general science periodical. Intended to fulfil the responsibility of helping the research workers to keep themselves abreast of current developments in various fields of science and technology, the Journal carries editorial features highlighting important scientific events in India and abroad; articles on science policy and management of science; review articles on topics of current research interest; technical reports on international and national conferences; reviews of scientific and technical publications; and notes on major advances in various fields.

Annual subscription	Rs 60.00	£ 10.00	\$ 25.00
Single copy	6.00	1.00	2.50

## INDIAN JOURNAL OF CHEMISTRY (monthly)

This Journal which is running the 18th year of its publication, Consists of the following two sections.

**Section A:** This section is devoted to papers in Inorganic, Physical, Theoretical and Analytical Chemistry.

Annual subscription	Rs 70.00	£ 12.00	\$ 30.00
Single copy	7.00	1.20	3.00

**Section B:** This section is devoted to papers in Organic Chemistry including Medicinal Chemistry.

Annual subscription	Rs 70.00	£ 12.00	\$ 30.00
Single copy	7.00	1.20	3.00

## INDIAN JOURNAL OF PURE & APPLIED PHYSICS (monthly)

This Journal, which is running the 18th year of its publication, is devoted to original research communications (full papers and short communications) in all conventional branches of physics (except radio and space physics).

Annual subscription	Rs 100.00	£ 16.50	\$ 42.00
Single copy	10.00	1.80	4.50

## INDIAN JOURNAL OF RADIO & SPACE PHYSICS (bimonthly)

This Journal serves as a medium for the publication of original research work (full papers and communications) in various areas of radio and space physics.

Annual subscription	Rs 60.00	£ 10.00	\$ 25.00
Single copy	12.00	2.00	5.00

## INDIAN JOURNAL OF TECHNOLOGY (INCLUDING ENGINEERING) (monthly)

This Journal publishes papers reporting results of original research of applied nature pertaining to unit operations, heat and mass transfer, products, processes, instruments, and appliances, etc. The Journal is of special interest to research workers in the departments of applied sciences in

universities, institutes of higher technology, commodity research laboratories, industrial cooperative research institutes, and industrial research laboratories.

Annual subscription	Rs 60.00	£ 10.00	\$ 25.00
Single copy	6.00	1.00	2.50

## INDIAN JOURNAL OF EXPERIMENTAL BIOLOGY (monthly)

This Journal, devoted to the publication of research communications in the fields of experimental botany, zoology, microbiology, pharmacology, endocrinology, nutrition, etc. is the only one in India with such a wide coverage and scope.

Annual subscription	Rs 120.00	£ 20.00	\$ 50.00
Single copy	12.00	2.00	5.00

## INDIAN JOURNAL OF BIOCHEMISTRY & BIOPHYSICS (bimonthly)

This Journal, published in association with the Society of Biological Chemists (India), Bangalore, is the only research Journal in India devoted exclusively to original research communications in biochemistry and biophysics.

Annual subscription	Rs 40.00	£ 7.00	\$ 17.00
Single copy	8.00	1.40	3.50

## INDIAN JOURNAL OF MARINE SCIENCES (quarterly)

Commencing publication from June 1972, this Journal is devoted to research communications (full papers and short communications) pertaining to various facets of marine research, viz. biological, physical, geological and chemical oceanography.

Annual subscription	Rs 40.00	£ 7.00	\$ 17.00
Single copy	12.00	2.00	5.00

## RESEARCH & INDUSTRY (quarterly)

Intended to serve as a link between science and industry, this Journal is addressed primarily to technologists, engineers, executives and others in industry and trade. It publishes informative original articles containing practical details of processes and products developed in India, which show promise of ready utilization, and technical digests on new processes, products, instruments and testing methods which are of interest to industry. Developments in Indian industry are regularly reported.

Annual subscription	Rs 24.00	£ 4.00	\$ 10.00
Single copy	7.25	1.30	3.50

## INDIAN JOURNAL OF TEXTILE RESEARCH (quarterly)

Commencing publication from March 1976, this Journal is devoted to the publication of papers reporting results of fundamental and applied researches in the field of textiles.

Annual subscription	Rs 36.00	£ 6.00	\$ 15.00
Single copy	12.00	2.00	5.00

Please contact

THE SALES & DISTRIBUTION OFFICER  
PUBLICATIONS & INFORMATION DIRECTORATE, CSIR  
HILLSIDE ROAD, NEW DELHI 110 012



# Indian Journal of Pure & Applied Physics

VOLUME 18

No. 9

SEPTEMBER 1980

## CONTENTS

### Solid State Physics

- Magnetic Properties of Si-Doped YIG Single Crystals ... 639

R K PANDEY

- Creation & Elimination of Dislocations in Float Zone  
Silicon Crystals ... 642

R K BAGAI, W N BORLE, M BAL & O P NANGIA

- Phonon-Roton Excitation in Superfluid  $^4\text{He}$  ... 649

M KUMAR & C M KACHHAVA

- I-V* Model for Photolysis Using Si as Catalyst ... 654

V P SUNDAR SINGH & P P WARNEKAR

- Study of Solid-Liquid Interface of Bismuth-Antimony  
Alloy Single Crystals ... 658

V P BHATT, G R PANDYA & A R VYAS

- Temperature Dependence of Effective Mass of  
Electrons & Holes & Intrinsic Concentration in Silicon ... 662

R K JAIN

### Chemical Physics

- Resonance Energies of Non-Alternant Hydrocarbons ... 665

M M TIWARI, R K UPADHYAY & A K SRIVASTAVA

### Dielectrics & Microwaves

- Effect of Ion Diffusion from Double Layer Capacitors on rf  
Conduction in Polar Liquids ... 669

R GHOSH & IRA CHAUDHURY

### Plasma Physics

- Reflection & Transmission of Ion Acoustic Soliton at a  
Plasma Interface ... 673

S R SHARMA & R S TIWARI

### Nuclear Physics

- Dipole Pomeron & Neutron-Proton Elastic Scattering  
between 70 & 400 GeV/c ... 678

MOHAMMAD SALEEM & FAZAL-E-ALEEM



# CONTENTS

## Electronics

- Investigations on the Second Harmonic Generation at  
Breakdown in *p-n* Junctions ... .. 682

ANIL K GOVIL, SHARWAN KUMAR & R PARSHAD

- Electrical Characteristics of 50 kV Resistance Potential  
Divider ... .. 687

S BEG

## Acoustics

- Formant Structure of Bengali Vowels & Some Possible  
Uses of a Tracking Loop Formant Extraction System ... .. 692

S K CHAKRABARTI

## COMMUNICATIONS

- Preliminary X-ray Study of Pyrene Picrate ... .. 702

S D PURKAYASTHA & A N TALUKDAR

- Temperature Dependence of <sup>35</sup>Cl NQR in Some  
Chloronitrotoluenes ... .. 702

J UCHIL, D L R SETTY, A INDUMATHY  
& J RAMAKRISHNA

- Centres Associated with 480 K Thermal Glow Peak  
in KBr:Ti ... .. 704

R V JOSHI & R T CHAUDHARI

## NOTES

- Resistivity of Thin Bismuth Films ... .. 706

A R VAMDATT

- Photodielectric Effect in SrS : Mn : Zr Phosphors ... .. 707

KU N RODAY, KU N CHAKRAVORTY, M S SISODIA  
& P C KAMARA

- Thermoelectric Effect in Fe-Ni Films ... .. 709

M A ANGADI & A M KARGUPPIKAR

- Lattice Energies of Some Metal Complexes ... .. 711

LAMBODAR THAKUR



# CONTENTS

## NOTES (contd)

On the Symmetry Group of Non-rigid Molecule $\text{BF}_2\text{CH}_3$	...	...	...	713
T S G KRISHNA MURTY, L S R K PRASAD & M KONDALA RAO				
Intramolecular Force Fields & Mean Amplitudes of Vibration of Group IV Tetrabromides	...	...	...	715
R K GOEL, S K GUPTA & M L AGARWAL				
Molecular Constants of Some Octahedral Hexahalo & Hexaoxy Ions	...	...	...	718
R K GOEL & S K GUPTA				
Molecular Constants & Vibrational Amplitudes of Some Tetrahedral Systems	...	...	...	722
NITISH K SANYAL, R K GOEL & S D SHARMA				
Sparking Potentials in Longitudinal Magnetic Fields	...	...	...	725
A NATARAJAN & V SELVARAJAN				
Plasmon Excitation in Solids during X-ray Scattering	...	...	...	727
K S SRIVASTAVA				
Lifetimes of Single-Particle States Near $^{48}\text{Ca}$	...	...	...	728
C M BHAT & N G PUTTASWAMY				
Second Moment of Solid Hippuric Acid by Wide-line NMR	...	...	...	731
N R JAGANNATHAN, S GANAPATHY & R SRINIVASAN				







## Magnetic Properties of Si-Doped YIG Single Crystals

R K PANDEY

Department of Electrical Engineering, Texas A & M University, College Station, TX 77843

Received 14 May 1979; revised received 22 February 1980

Temperature dependence of low field magnetization ( $\sigma$ ) and paramagnetic susceptibility ( $\chi$ ) of Si-doped yttrium-iron-garnet [YIG(Si)], single crystals between room temperature and about 750 °C are discussed. It is found that the temperature coefficient of  $\sigma$ ,  $d\sigma/dT$ , is positive for the magnetic fields smaller than a critical field,  $H_K$ ; negative for the fields larger than  $H_K$ ; and zero when the field subjected to the samples equals  $H_K$ . The temperature coefficient of magnetization exhibits crystalline anisotropy. Silicon-doping reduces the susceptibility, asymptotic Curie point,  $\chi_0$  and  $C$  of pure YIG.

### 1. Introduction

Silicon-doped yttrium iron garnet [YIG(Si)], single crystal is a well known photomagnetic material first reported by Teale and Temple.<sup>1</sup> Though a substantial amount of work has been done in studying the photomagnetic effect in YIG(Si), not much information is available in the literature regarding its high temperature magnetic properties. The purpose of this paper is to report about the temperature dependence of unsaturated magnetization ( $\sigma$ ), and paramagnetic susceptibility ( $\chi$ ), between room temperature and 750 °C.

Thermal behaviour of low field magnetization ( $\sigma$ ) is particularly interesting. Such a study was originally done by Pandey<sup>2</sup> in YIG(Si) single crystals. It was reported that the temperature coefficient of low field magnetization,  $d\sigma/dT$ , is positive when the magnetic field applied to the sample,  $H_{app1}$ , is less than its saturated demagnetizing field,  $H_{d,s}$ ; whereas it is negative for  $H_{app1} > H_{d,s}$ . Further, it was found that Si-doping reduces the saturation magnetization, lattice constant and Curie point of pure YIG. Since  $d\sigma/dT$  changes its sign from positive to negative there must be a value of  $H_{app1}$  for which  $\sigma$  should become temperature independent. The experimental determination of this field should aid in understanding the mechanism of the physical phenomenon involved. Therefore, investigations were undertaken to study in greater detail the temperature dependence of  $\sigma$  at various field strengths. The experimental procedures and their results are presented in the subsequent sections.

### 2. Experimental Details

Single crystals of YIG and YIG(Si) were grown by slightly modifying the methods described by

Pandey<sup>2</sup> and Nielson.<sup>3</sup> Instead of permitting the crystals to grow by spontaneous nucleation, a small crystal seed was introduced in the charge by suspending it by means of a thin platinum wire through a small hole in the centre of the platinum crucible cover. The other end of the wire was fixed mechanically to the outer surface of the cover adjusting its length so that the seed could submerge just below the molten surface of the charge. After the growth was accomplished, crystals were recovered from the PbO/PbF<sub>2</sub> flux by draining it at about 1000 °C through a platinum sieve placed on an empty crucible. After cooling to room temperature, the crystals were cleaned by boiling them in a solution of 25% HNO<sub>3</sub> and 25% acetic acid. Fairly large shiny crystals with well grown faces were obtained; a few of them were as large as 2 cm × 1 cm × 0.5 cm. The method mentioned here for recovery of the crystals from flux is fast and superior to the standard method of chemical etching which is very time consuming.

Small spherical samples weighing roughly 120-150mg were made by the method described by Pandey.<sup>2</sup> In order to reduce the strain and also to homogenize the crystals, the samples were annealed for several hours at 1000 °C. Various magnetic parameters of YIG(Si) crystals were measured using a vibrating sample magnetometer. Magnetically inert boron nitride sample holders were utilized to hold the samples at the saddle point of the pick-up coils. Temperature of the sample was monitored by attaching a calibrated thin chromel/alumel thermocouple to the sample holder. All measurements were done by filling the sample zone with pure Ar gas to obtain a uniform thermal distribution. The nominal value of Si-doping in YIG samples is 0.2/mole. The doping level was determined by using



the method of wet chemical analysis which showed that it is about 0.19/mole.

### 3. Results and Discussion

Temperature dependence of unsaturated moment ( $\sigma$ ) when samples are subjected to low fields, is shown in Fig. 1 for the fields varying from 23.1 to 350 Oe. When fields are low, a sharp transition is obtained at the Curie point. The Curie points for YIG(Si) and YIG have been accurately determined by using the method of low field magnetization as suggested earlier.<sup>2</sup> The values obtained are  $537 \pm 2$  K for YIG(Si) and  $557 \pm 2$  K for unsubstituted YIG. The Curie point,  $T_c$ , for unsubstituted YIG is reported to be 560 K by Bertaut and Pauthenet<sup>4</sup> and 545 K by Gilleo and Geller.<sup>5</sup> The later value seems to be a bit low and it is possible that the sample contained some non-ferromagnetic impurities. Our measured value for  $T_c$  of YIG is in good agreement with the value reported in Ref. 4. The lower value of  $T_c$  in the case of YIG(Si) is obvious because of the presence of  $\text{Si}^{4+}$  ions in the crystal. In the charge for crystal growth, the value of  $\text{Si}^{4+}$  was 0.2 per 5  $\text{Fe}^{3+}$  ions, i.e. a dilution of  $\text{Fe}^{3+}$  ions by 4%. Comparing the values of the Curie points of the two materials, we find that the Curie point of YIG(Si) is 4% lower than that of YIG. This is in good agreement with the result obtained by the wet chemical analysis for the doping level. An accurate determination of the Curie point of substituted magnetic

materials can be used as a tool to determine the doping levels  $x$  non-destructively. The determination that  $x = 0.19/\text{mole}$  for our sample is also in good agreement with the results of Geller *et al.*<sup>6</sup> when an analysis is done using data for magnetic moment dependence of the lattice constant for varying Si-doping of YIG. The lattice parameter for the composition of our sample, according to Pandey,<sup>2</sup> is  $12.364 \text{ \AA}$ .

Further, we observe that the slope,  $d\sigma/dT$ , is positive for fields up to 300 Oe and it is negative when the field is 325 Oe or more. Thermal behaviour of  $\sigma$  was explained by Pandey<sup>2</sup> on the basis of the saturated demagnetizing field,  $H_{d,s}$ , of YIG(Si). The effective field,  $H_{\text{eff}}$ , experienced by a magnetic sample is given by:

$$H_{\text{eff}} = H_{\text{appl}} - H_d \quad \dots (1)$$

and

$$H_d = N d \sigma \quad \dots (2)$$

where  $H_{\text{appl}}$ ,  $N$  and  $d$  are the externally applied field, demagnetizing factor and density of the sample, respectively. As  $\sigma \approx \sigma_s$ ,  $H_d$  of the sample approaches its saturated value  $H_{d,s}$ . It was believed that  $d\sigma/dT$  is positive for  $H_{\text{appl}} < H_{d,s}$  and it is negative for  $H_{\text{appl}} > H_{d,s}$ . For the YIG(Si) crystal, where  $\text{Si} \approx 0.2/\text{mole}$ ,  $H_{d,s} \approx 490$  Oe at room temperature. But from Fig. 1, we observe that  $d\sigma/dT$  is already negative for  $H_{\text{appl}} (\approx 325 \text{ Oe})$  which is substantially smaller than 490 Oe.

Unsaturated samples have a small effective field which is of the order of the coercivity,  $H_c$ . As  $H_c$  approaches zero,  $H_{\text{eff}} \approx 0$ , i.e.  $H_d = N d \sigma \approx H_{\text{appl}}$ . This would mean that  $\sigma \propto H_{\text{appl}}$ . The results presented in Fig. 1 are in good agreement with this argument. For a thorough understanding of the nature of  $d\sigma/dT$  as a function of  $H_{\text{appl}}$  a detailed study of the domain structure of this material is warranted. It is also quite likely that the behaviour of  $d\sigma/dT$  as a function of magnetic field is closely related to the thermal expansion of the material.

In a series of experiments, it was also observed that the absolute value of  $\sigma$  is different for different crystallographic directions. In Fig. 2 the results of  $d\sigma/dT$  versus  $H$  for the [111] and [110] axes have been shown; here I and II correspond to the [110] and [111] crystallographic directions, respectively. For YIG(Si) the magnetic easy axis is [111], whereas [100] is the hard axis and [110] the intermediate magnetic axis. We find from Fig. 2 that  $d\sigma/dT$  becomes zero at a certain critical field,  $H_K$ . Both  $d\sigma/dT$  and  $H_K$  show dependence on the crystallographic directions. For YIG(Si) single crystals, the value of  $H_K$  is 320 Oe in [111] directions, whereas it is 318 Oe in [110]

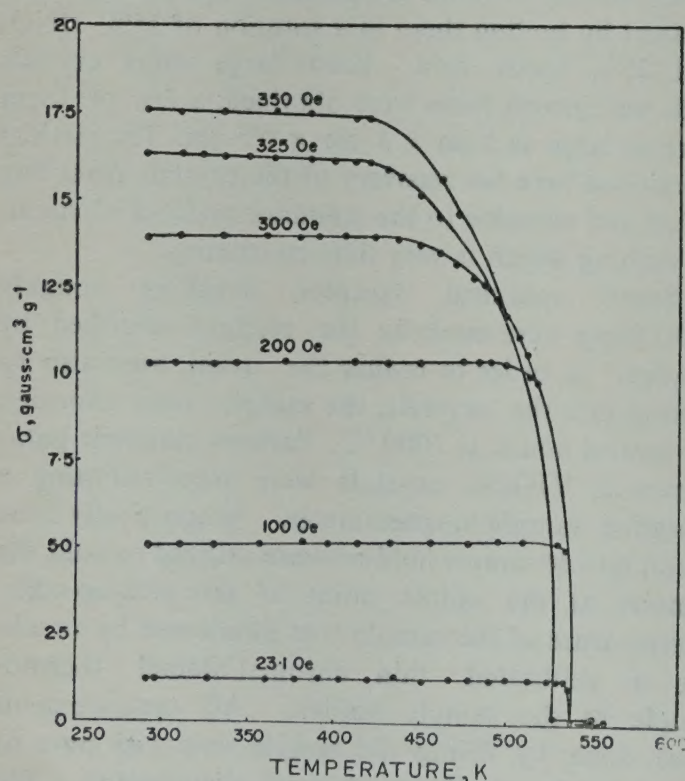
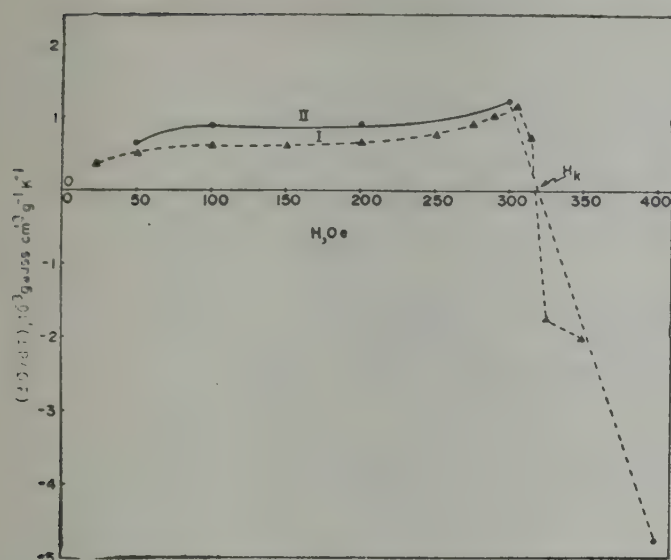


Fig. 1—Low field magnetization of YIG(Si) versus temperature




 Fig. 2— $d\sigma/dT$  versus  $H$  of YIG(Si)

{I, [110] Direction; II, [111] direction} direction. The existence of  $H_K$  could have some interesting technological applications since below the Curie point, the unsaturated magnetization,  $\sigma$ , becomes practically temperature independent when the sample is biased by a field equal to  $H_K$ .

The paramagnetic susceptibility ( $\chi$ ) as a function of temperature is shown in Fig. 3 for both YIG(Si) and YIG single crystals between 275 and 750 °C. The behaviour of  $\chi^{-1}$  versus  $T$  for YIG and YIG(Si) is typical of ferrimagnetic materials in the paramagnetic state. It is given by the relation:

$$\frac{1}{\chi} = \frac{T}{C} + \frac{1}{\chi_0} - \frac{\rho}{T - T_c} \quad \dots(3)$$

where  $C$ ,  $\chi_0$ , and  $\rho$  are constants.

The term  $\left(\frac{T}{C} + \frac{1}{\chi_0}\right)$  represents the asymptotic line to which the  $\chi^{-1}$  versus  $T$  plot should approach at high temperature where the term  $\rho/(T - T_c)$  becomes zero. The extrapolation of the asymptotic line would intersect the abscissa at the so-called asymptotic Curie point given by :

$$T_a = \frac{C}{\chi_0} \quad \dots(4)$$

The intersection of this asymptotic line with the ordinate of the  $\chi^{-1}$  versus  $T$  curve at  $T = 0$  K

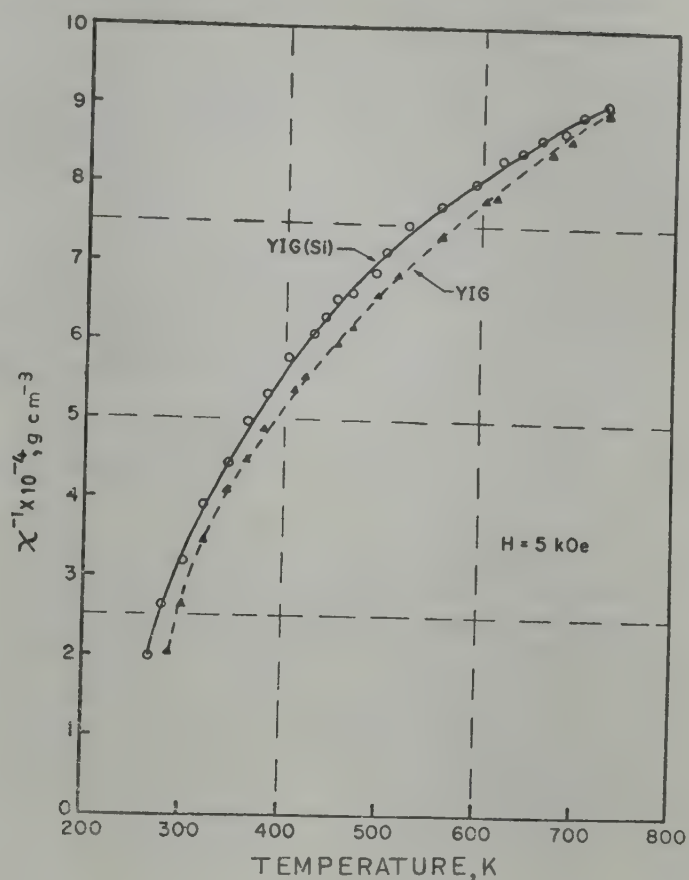


Fig. 3—Temperature dependence of paramagnetic susceptibility of YIG(Si) and YIG

gives the value of  $1/\chi_0$ . From  $\chi^{-1}$  versus  $T$  plots, the value of  $\chi_0$  and  $T_a$  have been obtained. They are  $\chi_0 = 1.25 \times 10^{-4} \text{ cm}^3 \cdot \text{g}^{-1}$  and  $T_a = -103$  K for YIG; and  $\chi_0 = 0.9 \times 10^{-4} \text{ cm}^3 \cdot \text{g}^{-1}$  and  $T_a = -139$  K for YIG(Si). Silicon doping lowers the asymptotic Curie point as well as  $\chi_0$  and  $C$  of pure YIG. The value of  $C$  for YIG(Si) single crystals is about 3% lower than that of pure YIG.

#### References

1. Teale R W & Temple D W, *Phys. Rev. Lett.*, 19 (1967), 904.
2. Pandey R K, *J. appl. Phys.*, 45 (1974), 3216.
3. Nielsen J W, *J. appl. Phys.*, 31 (1960), 515.
4. Bertaut F & Pauthenet R, *Proc. IEEE B. Suppl.*, 104 (1957), 261.
5. Gillo M A & Geller S, *Phys. Rev.*, 110 (1958), 73.
6. Geller S, Williams H J, Sherwood R C & Espinosa G P, *J. Phys. Chem. Solids*, 23 (1962), 1525.



## Creation & Elimination of Dislocations in Float Zone Silicon Crystals

R K BAGAI, W N BORLE, M BAL & O P NANGIA

Solid State Physics Laboratory, Lucknow Road, Delhi 110 007

Received 26 May 1979; revised received 7 April 1980

The growth of float zone silicon crystal has been classified and analyzed in three stages, viz. (i) stage of seeding, (ii) stage of necking and (iii) stage of bulk growth. The creation and elimination of dislocations and their dependence on the growth speed at the various stages of growth are discussed. It is observed that during necking, the dislocations cannot be removed simply by propagation along  $\{111\}$  planes but sufficient number of vacancies are required for their complete removal by climb process. The sudden appearance of dislocations after the dislocation-free neck, has been found to be due to the condensation of point defects and not because of thermal stresses. It is further observed that depending upon the diameter of the growing crystal, there is a critical speed at which a crystal grows free of dislocations during the bulk growth.

### 1. Introduction

Dislocations in silicon crystals are known to have a harmful effect on the device performance and hence must be controlled during the growth. A method for the growth of dislocation-free (df) silicon crystal was first developed by Dash<sup>1,2</sup> for CZ (Czochralski technique) and pedestal grown crystals. It was later modified both for CZ as well as float zone (FZ) methods by others.<sup>3-5</sup> df FZ silicon crystals are increasingly in demand in the electronics industry mainly because of their better purity than CZ crystals. The growth of df FZ silicon crystals is difficult as compared to CZ because of various practical difficulties. Though commercially dfFZ silicon crystals are available, the exact experimental details are not given in the literature and is still a proprietary item of some of the international firms. The details are not known about the mechanism of dislocation-creation, elimination and their dependence on various growth parameters while growing the crystals by FZ method. Contradictory statements exist in the open literature regarding the creation of new dislocations in the growing crystal. Shroder and Wolf<sup>6</sup> predicted that thermal stress is the source of new dislocations whereas, the calculations made by Geil *et al.*<sup>7</sup> have shown that the thermal stress is not sufficient for the formation of new dislocations in FZ silicon crystals. Another mechanism, viz. the generation of dislocations due to the condensation of point defects has also been suggested by De Kock *et al.*<sup>8</sup>

The purpose of the present study is to understand clearly the creation, multiplication and elimination of dislocations during various stages of growth. Such studies are essential for the development of a technique for the growth of df FZ silicon crystal.

### 2. Experimental Details

An inside work-coil type float zoner manufactured by Kokusai Electric Co, Japan (model F294C) has been used for the growth of crystals. All the crystals are grown in vacuum. Seeds ( $5 \times 5$  mm) oriented along  $\langle 111 \rangle$  and  $\langle 100 \rangle$  directions are used. Polycrystalline rods are tapered at the bottom to reduce the difference in the dimension of seed and poly rod. In some cases highly doped (phosphorus) rods or seeds are also employed. After forming a stable zone, dislocation-free necks (Dash region) are formed by two different processes. In the first process, necks are formed by stretching the molten zone downward by lowering the seed, while the rf coil slowly moves upward. Thin and long neck of uniform diameter could be formed in one stretch and at high speed. For df necks, a growth speed of more than 12 mm/min is required.

In the second process, necks are formed by stretching the molten zone upward by raising the charge rod upward. Here also the coil moves upward. In this case, the necks cannot be formed



in one stretch and the high growth speeds of the above order cannot be achieved. However, df necks could be formed even at the growth speed of nearly 1.5 mm/min.

After the df necks, the growth conditions are to be suitably controlled for the continuation of df growth of bulk crystals.

This technique is different from that used by De Kock *et al.*<sup>8</sup> where a pedestal technique for growing the crystals is used in which the feed rod of sufficiently bigger diameter is kept below and the seed is attached to the upper shaft. The top portion of the feed rod is melted by the rf coil and from this molten silicon which is supported by the feed rod, the crystal is pulled just as in the case of CZ method.

Preferential etching and photomicrographic techniques have been used for the evaluation of the crystals.

### 3. Results and Discussion

The process of crystal growth can be visualized in the form of the following 3 stages, (i) the stage of seeding, (ii) the stage of necking and (iii) the stage of bulk growth.

#### 3.1 Stage of Seeding

The stage is fairly well understood<sup>3,9,10</sup> hence is discussed briefly here. At the time of seeding, the dislocations present in the seed and which emerge at the solid-liquid interface will propagate into the growing crystal because a dislocation can only terminate at another dislocation or at the external crystal surface. The different possible processes by which dislocations from the seed can propagate into the growing crystal have already been discussed.<sup>10</sup> Even if a df seed is used, dislocations will be created in it by the thermal shock resulting from dipping the seed into the melt and the use of df seed is not purposeful. Thus the dislocations propagating from the seed into the growing crystals are to be eliminated which is done during the stage of necking.

#### 3.2. Stage of Forming Thin Neck Component

Various experiments were conducted forming thin necks under various conditions of growth and the dislocation density was measured at different distances from the seed end. Curves have been plotted showing the average dislocation etch pit density against distance from the seed end (Figs. 1 and 2). It can be seen from Figs. 1 and 2 that in the case of undoped crystals grown along  $\langle 111 \rangle$

direction, the minimum distance at which the neck becomes almost free of dislocations is always more than 17 mm, irrespective of whether the neck is formed by pulling the zone upward or downward.

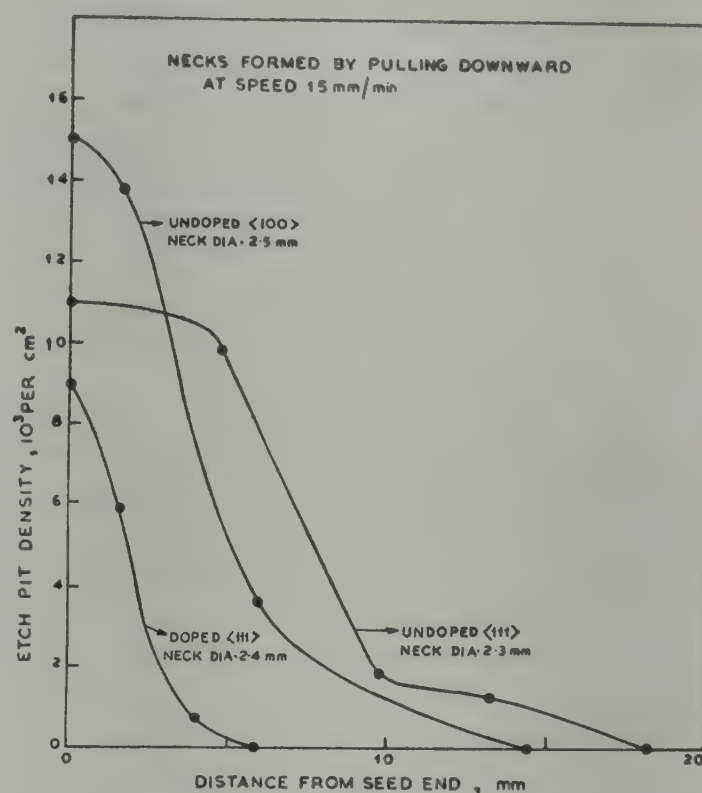


Fig. 1—Variation of dislocation density with increasing distance from the seed end (For the necks formed by pulling downward)

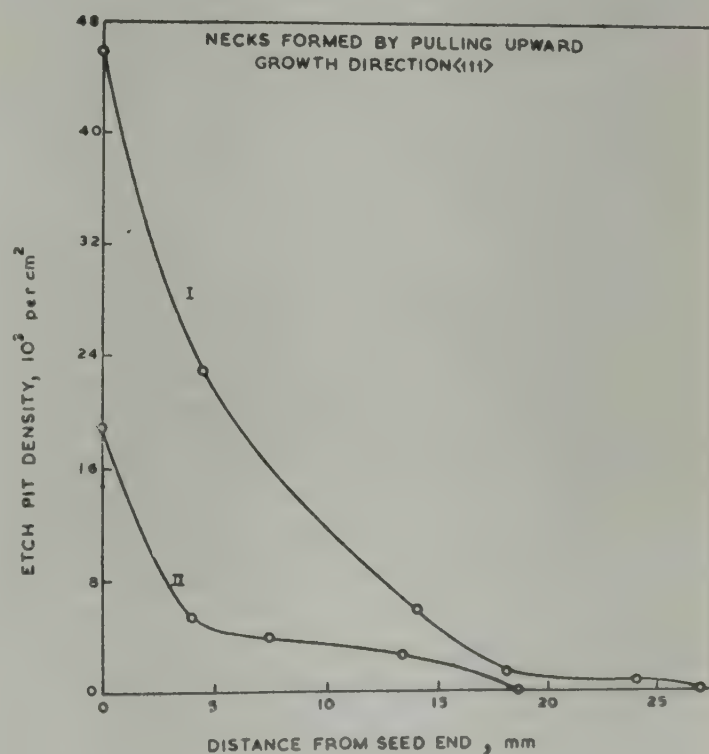


Fig. 2—Variation of dislocation density with increasing distance from the seed end (For the necks formed by pulling upward) Growth speeds : I, 2.5 mm/min, II, 3.0 mm/min]



It is known that the major mechanisms of elimination of dislocations are climb mechanism<sup>10,11</sup> and by propagation along  $\{111\}$  planes.<sup>5,12</sup> If the dislocations were to be eliminated only by the simple propagation along  $\{111\}$  planes then all the dislocations should disappear up to the maximum distance  $L$ , given by  $L = D \tan \theta$ , where  $D$  is the maximum diameter of growing crystal;  $\theta$  is the angle between the growth front ( $111$ ) plane and other slanting  $\{111\}$  planes. During the necking, the maximum diameter (5 mm) is that of seed and the value of  $\theta$  is  $70^\circ$ . Thus all the dislocations should disappear upto a distance of 13.5 mm. If both the mechanisms are operative then the dislocations obviously should disappear even earlier to this. However, it has been found that dislocations are not removed completely though they are reduced significantly near about this distance. This indicates that new dislocations are also being added simultaneously. This can happen either by creation of new ones or by multiplication of the existing ones during the growth of thin neck. The creation of new dislocations is ruled out as the thermal stresses are negligible during the necking and so presumably the dislocations are added by multiplication only.

Since, new dislocations are being continuously added up during the growth, the necks will never become completely free of dislocations by the mechanism of dislocation propagation along  $\{111\}$  planes. Thus the only alternative to remove the dislocations completely from the neck is to enhance the climb process. For this, more number of vacancies must be created and this can be conveniently done by increasing the growth speed. It is found, (for the case when the neck is formed by pulling the zone upward), that df necks can only be formed above certain critical growth speed, e.g. the necks formed at a speed less than 1.5 mm/min do not become df but for similar dimensions, the necks formed above 1.5 mm/min are free of dislocations.

Secondly, the df necks formed at higher growth rate become free of dislocations at lengths shorter than the necks formed at a lower speed of growth. This is illustrated in Fig. 2. The number of vacancies being more at the high speeds than at low speeds, will help in the faster removal of dislocations by climb.

**3.2.1. Growth along  $\langle 111 \rangle$  and  $\langle 100 \rangle$  directions**—Under similar experimental conditions, the distance from the seed end at which dislocations disappear in the neck is less in the case of  $\langle 100 \rangle$  as compared to growth along  $\langle 111 \rangle$  (Fig. 1). This

is due to the fact that during growth along  $\langle 100 \rangle$  direction, four  $\{111\}$  glide planes are available as compared to only three  $\{111\}$  glide planes during growth along  $\langle 111 \rangle$  direction. Further the angle  $\theta$  between the growing plane and the  $\{111\}$  glide planes will be less in case of growth along  $\langle 111 \rangle$  direction. Hence elimination of dislocations is faster in this case.

**3.2.2. Use of highly doped rods**—It is observed that for  $n$ -type (phosphorus doped) crystals, dislocation elimination is quite fast and the distance at which they disappear is much shorter than in the case of undoped rods for similar growth conditions (Fig. 1). The comparison has been made for the necks formed by stretching the melt downward at a fast speed around 15 mm/min. Sometimes it has been found that the distance at which dislocations disappear is even shorter than that given by the equation  $L = D \tan \theta$ . This difference is due to the effect of using highly doped ( $n$ -type) rod to provide extra number of vacancies<sup>11,13</sup> enabling dislocation elimination (by climb process) faster.

### 3.3. Stage of Bulk Growth

It is found that the maintenance of df growth after the neck is very critical and dislocations are suddenly introduced during the growth process.

To find suitable conditions for the growth of df crystals after the neck, a number of experiments were conducted. Results of some of the experiments is given in Table 1. The following important observations are evident from Table 1.

I. The spontaneous formation of dislocations after the neck, mainly depends on the speed of growth as indicated below:

- (i) If the growth speed is kept extremely low, i.e. less than 0.5 mm/min, the df region extends slightly above the neck and then again the dislocations are introduced.
- (ii) If the speed of the growth lies between 0.5 and 1.5 mm/min, then the dislocations appear immediately after the neck.
- (iii) If the speed of growth is increased and made higher than 2.0 mm/min then the df region is extended to much higher lengths in the shoulder region and even to some portion of the constant diameter of the crystal.
- (iv) For a particular diameter of the growing crystal, there is a critical speed at which the crystal can grow free of dislocations to sufficiently long length.



Table 1—Experimental Data on the Growth of FZ Silicon Crystals

Seed orientation	Seed rotation (RPM)	Poly rod diameter (mm)	Coil diameter (mm)	Speed during bulk growth (mm/min)	Distance above neck where dislocations are introduced (mm)	Diameter where dislocations are introduced (mm)	Diameter of bulk crystal (mm)	Total length of crystal above df neck (cm)
$\langle 111 \rangle$	15	12.5 (Undoped)	15	0.35	4.0	6.0	12.5	4.0
$\langle 111 \rangle$	12	14.0 (Phosphorus doped)	13	1.2	Immediately after neck	2.8	11.5	4.0
$\langle 111 \rangle$	12	—do—	13	0.9-1.2	—do—	2.9	11.0	2.5
$\langle 111 \rangle$	18	13.5 (undoped)	15	1.0	—do—	2.9	12.0	8.0
$\langle 111 \rangle$	10	12.5	15	Initially varied for shorter length from 1.5 to 3.0 and then maintained at 3.0	10.0	9.5	13.5	4.5
$\langle 100 \rangle$	18	13.0	17	Increased to 3.0 comparatively faster and then maintained it	22.0	12.0	13.0	5.5
$\langle 111 \rangle$	30	10.0	15	2.5	d.f.	—	10.0	5.5
$\langle 100 \rangle$	30	10.0	15	2.5 and then slowly reduced to 2.3	d.f.	—	10.0	11.5
$\langle 100 \rangle$	30	14.5	20	2.5 and then slowly reduced to 2.1	d.f.	—	14.0	10.0
$\langle 100 \rangle$	30	15.0	20	Varied from 2.5 to 5.0	16.0	10.0	15.0	6.5
$\langle 100 \rangle$	18	13.0	17	Immediately increased to 5.0	Just above neck	3.0	13.0	4.0

(v) If the growth speed is made much higher than this critical speed, then also the dislocations are spontaneously introduced.

II. During the growth along  $\langle 111 \rangle$  direction, the cross-section of the crystal is of pill-box type immediately after the neck but becomes cylindrical after the shoulder region.

Further, (111) //  $(\bar{1}\bar{1}\bar{1})$  twinning has also been observed a few times, near the shoulder region or slightly above it.

The possible causes for the sudden formation of dislocations after df neck are discussed below.

It has hitherto been considered that the main causes of the dislocation introduction and multiplication are excessive stresses due to the radial temperature gradients present in the growing crystal and gross growth disturbances such as melt vibrations and drastic power fluctuations.

The temperature distribution during the growth depends on rf coil design, crystal dimension and gas

convection, etc. with the result it is very difficult to calculate the stress present in the growing crystal. However, some rough estimates and calculations on the thermal stress present during the growth of FZ silicon, were made by Schroder and Wolf.<sup>6</sup> These estimates (based on Tiller<sup>14</sup> equation) have shown that the stress is sufficient for the creation of new dislocations. Therefore, they had explained the sudden appearance of dislocation lines (while preparing df silicon crystals with increasing diameter) to be due to the excessive thermal stresses.

Geil *et al.*<sup>7</sup> have contradicted the findings of Schroder and Wolf<sup>6</sup> by denouncing the use of Tiller equation for estimating the stress in FZ method. The value of the stress calculated by Geil *et al.* is smaller by a factor of 4.5 and hence is not sufficient for the formation of new dislocations in FZ silicon crystal. It is observed that in crystals grown along  $\langle 111 \rangle$  direction, the cross-section of the crystal near the shoulder region is of pill-box type and frequently (111) //  $(\bar{1}\bar{1}\bar{1})$  twinning is also observed.



From this it can be implied that the crystallization front is flat<sup>15,16</sup> which further suggests that the thermal stress is low across the growth front.

In view of the above and the earlier findings by Dash<sup>10</sup> that once the df growth starts, it is very difficult to introduce new dislocations by thermal shock, the thermal stress present in the growing crystal cannot be a source for creating new dislocations.

Dislocation generation mechanism due to the condensation of point defects was recently suggested by De Kock *et al.*<sup>8</sup> The predominant cause for the loss of df growth of FZ crystals, particularly of large diameter (25 mm) was shown to be due to the emission of dislocation arrays from the vacancy clusters. It is thus likely that the mechanism of vacancy condensation may be operative.

The formation of dislocation loops by the condensation of vacancies in the case of quenched metals is well known<sup>17,18</sup> but this received very little attention in the case of silicon single crystal growth. However, the recent studies on the microdefects<sup>8,19-22</sup> in df FZ silicon crystals show that this mechanism should be reconsidered. It is known that such crystals are supersaturated with vacancies while they are being grown and that the typical striated patterns (swirls) are due to the clustering of these vacancies. These clusters have been found to be the dislocation loops by transmission electron microscopy (TEM) observations.<sup>23,24</sup> According to the earlier studies and the analysis, it was surmised that the swirl defects consist of vacancy clusters<sup>8,19-22</sup> but as per the recent findings the swirls are considered to be formed by the agglomeration of silicon self-interstitials,<sup>25-27</sup> and at high temperature, self-interstitials are found to be the dominating point defects rather than vacancies.

Two types of swirl defects (*A* and *B* clusters) have been identified in df FZ silicon crystals. *A*-clusters are found to be the dislocation loops which are mainly located in (111) plane and are elongated along  $\langle 110 \rangle$  directions. It has also been found<sup>8</sup> that when *A*-clusters are allowed to increase to a critical size (around 100  $\mu\text{m}$ ) they can start generating dislocations. The size of the loops can increase when the crystal pulling rate and consequently the cooling rate is reduced.

All the crystals under investigation are grown in vacuum using the normal FZ method, while on the other hand De Kock *et al.* had used the pedestal arrangements with argon gas atmosphere. It has been observed that the dislocations start generating after the growth of df neck component whereas De Kock *et al.* observed the spontaneous formation

of dislocations on increasing the diameter (more than 25 mm) of the growing crystal.<sup>8</sup> In the pedestal method, the crystal is pulled up from the molten zone whereas in FZ method, crystal is drawn downwards from the zone. Other parameters such as the coil design, coupling between the coil and the molten zone, etc. are also different in the two cases.

The dependence of the onset of dislocations on the growth speed and other results of various experiments (Table I) are discussed below.

**3.3.1 When the growth speed is extremely low, i.e. less than 0.5 mm/min**—Once the df neck is formed, the onset of new dislocations in the further growth depends on the velocity of growth of the crystal. For example, as seen from Table I, if the growth speed is kept approximately 0.35 mm/min, the df region after the neck extends only slightly before new dislocations are suddenly introduced. The growth speed could not be kept lower than this because of the limitation of our FZ equipment.

At such a low cooling rate (or growth speed), it is expected that the concentration of point defects (vacancies/interstitials) will decrease because they get time for diffusion to the crystal surface and also to anneal out to some extent. If the number of remaining point defects is below the critical value necessary for the formation of clusters, then the dislocation generation cannot take place. It has been reported<sup>28</sup> that at a cooling rate value below 5° C/min, the formation of clusters can be suppressed. (This was the case for 23 mm diameter crystal and grown in argon atmosphere by pedestal pulling technique). To attain such low cooling rates, a growth speed as low as 0.2 mm/min was used. In the present study, the growth speed could not be kept to such a low value. However, it seems to be low enough to keep the concentration of point defects below the critical value required for the cluster formation for some length of the growth and as the growth proceeds further, concentration of point defects may increase slowly to a critical level at some stage and lead to the spontaneous creation of dislocations.

Thus under such circumstances df region could be extended only to limited extent.

**3.3.2 When the growth speed is greater than 0.5 mm/min but less than 1.5 mm/min**—For growth speeds within the range of 0.5 to 1.5 mm/min, it is observed that dislocations appear immediately after the neck. As expected, with the increase in growth speed the concentration of point defects will increase and also the diffusion of point defects to the surface will be reduced and hence the overall concentration



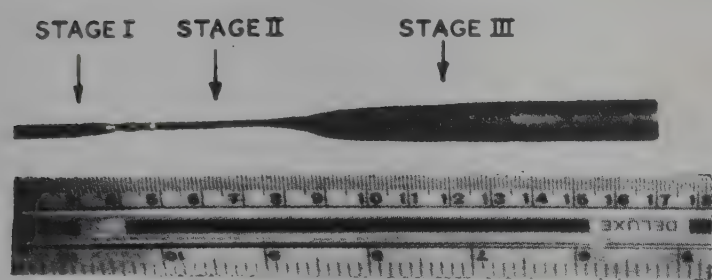


Fig. 3—Photograph of a typical FZ silicon crystal grown free of dislocations

of point defects in the growing crystal will further increase leading to cluster formation. These clusters interact with others at high temperature and increase in size. On reaching the suitable critical size<sup>8</sup> (around 100  $\mu\text{m}$ ), they can start generating dislocations. Thus the dislocations are generated immediately after the neck. If the growth speed is increased beyond 1.5 mm/min, then the formation of dislocations is suppressed (see Table 1). This implies that at such growth speeds the point defect clusters do not get sufficient time to interact with each other and hence increase in size to generate dislocations. It can be seen from Table 1 that by making the speed more than 1.5 mm/min and also increasing the diameter of the growing crystal slowly, df region could be extended above the neck portion. It has been observed that to grow a crystal of a particular diameter, e.g. 14 mm, if the growing speed is kept in the beginning around 2.5 mm/min and then decreased slowly to 2.0 mm/min as the growth proceeds, df crystals could continue to grow for longer lengths. The critical speed for the growth of df crystal depends on the diameter of the growing crystal. A typical crystal grown free of dislocations is shown in the Fig. 3.

**3.3.3 When the growth speed is higher than 3 mm/min—**For still higher growth speeds, i.e. higher than those discussed above, dislocations are again introduced fast. From Table 1, it can be seen that at higher speeds, e.g. 3 mm/min and above, higher the speed of growth, earlier the onset of dislocations (keeping all other parameters including the diameter of the crystals almost similar). The formation of dislocations at higher speeds above the critical speed is most probably due to the high temperature gradient across the diameter of the growing crystals. It is expected that at higher growth speeds, the cooling rate of the crystals is also high and hence the temperature gradient will also be high resulting into a curved solid-liquid interface.

The present results regarding the higher speeds of growth, i.e. more than 3 mm/min are apparently in contradiction to that of De Kock *et al.*<sup>8</sup> It is found

that at that high speed of growth, dislocations are introduced immediately whereas De Kock *et al.* have recommended such high growth speeds to suppress the formation of the vacancy clusters and hence avoid the formation of dislocations. This may largely be due to different experimental conditions in the two cases as has already been pointed out earlier.

## Conclusions

The present investigations lead to the conclusions that for the growth of FZ silicon crystals, dislocations from thin neck component cannot be completely removed simply by propagation along {111} planes but sufficient number of vacancies are necessary to make the neck completely free of dislocations. Secondly after the growth of df neck (Dash region) the maintenance of df state during the bulk growth depends critically on the growth speed. The sudden creation of dislocations during the bulk growth is due to the condensation of point defects upto a certain limit of growth speed while beyond that range, the creation of dislocations is due to thermal stresses.

## Acknowledgements

The authors are grateful to Prof S C Jain, Director, Solid State Physics Laboratory, Delhi, for his kind permission to publish this paper and for his constant encouragement during this study. They also thank Dr G C Trigunayat and Dr A V R Warriar for useful discussions.

## References

1. Dash W C, *J. appl. Phys.*, **29** (1958), 736.
2. Dash W C, *J. appl. Phys.*, **30** (1959), 459.
3. Ziegler G, *Z. Naturf.*, **16a** (1961), 219.
4. Keller W & Ziegler G, *DBPI*, 128, 413; filed November 25, 1960, patented Nov. 1962.
5. Borle W N, Tata S & Varma S K, *J. crystal Growth*, **8** (1971), 223.
6. Schroder W & Wolf E, *Kryst. Tech.*, **9** (1974), 275.
7. Geil W, Lebek A & Schmugge K, *Kryst. Tech.*, **9** (1974), K 109.
8. De Kock A J R, Roksnoer P J & Boonen P G T, *J. crystal Growth*, **30** (1975), 279.
9. Lindergaard Anderson A, *Studies on the growth mechanism and imperfections in silicon crystals grown by FZ method*, Ph D thesis, Tech. Univ. Denmark, 1967.
10. Dash W C, *Growth and perfection of crystals* (John Wiley, New York) 1958, 361.
11. Milvidiskii M G, Stolyarov O G & Berkova A V, *Soviet Phys. Solid St.*, **6** (1965), 2606.
12. Akiyama K & Yamaguchi J, *Proc. of the conference on ultrapurification of semiconductor materials*, Massachusetts, April 1961, p 522.
13. Bagai R K, Bal M, Nangia O P & Borle W N, *Indian J. pure appl. Phys.*, **25** (1977), 726.



14. Tiller W A, *The art and science of growing crystals*, 1963.
15. Borle W N, Bagai R K & Seth G L, *Indian J. pure appl. Phys.*, **14** (1976), 394.
16. Borle W N, *Studies on silicon crystal growth*, Ph D thesis, Nagpur University, Nagpur, 1973.
17. Hirsch P B & Silcox J, *Growth and perfection of crystals* (John Wiley, New York) 1958.
18. *Lattice defects in quenched metals* edited by R M J Cotterill *et al.* (Academic Press, New York) 1965.
19. Plaskett T S, *Trans. Am. Inst. Mech. Engng.*, New York, **233** (1965), 809.
20. Chikawa J, Asaeda Y & Fujimoto I, *J. appl. Phys.*, **41** (1970), 1922.
21. Bernewitz L I & Mayer K R, *Phys. Status Solidi (a)*, **16** (1973), 579.
22. De Kock A J R, *Phillips Res. Rep., Suppl. No. 1* (1973).
23. Bernewitz L I, Kolbesen B O, Mayer K R & Shuh G E, *Appl. phys. Lett.*, **25** (1974), 277.
24. Foll H & Kolbesen B O, *Appl. Phys.*, **8** (1975), 319.
25. Foll H, Kolbesen B O & Frank W, *Phys. Status Solidi (a)*, **29** (1975), 83.
26. Seeger A, Foll H & Frank W, *Inst. Phys. Conf. Ser.*, **31** (1977), 12.
27. Foll H, Gosele U & Kolbesen B O, *J. crystal Growth*, **40** (1977), 90.
28. Roksnoer P J, Bartels W J & Bulle C W T, *J. crystal Growth*, **35** (1976), 245.



## Phonon-Roton Excitation in Superfluid $^4\text{He}$

M KUMAR\* & C M KACHHAVA

Physics Department, University of Rajasthan, Jaipur 302 004

Received 11 June 1979; revised received 9 August 1979

A power series expansion formula is proposed for a thorough investigation of excitation energy spectrum of superfluid  $^4\text{He}$  at 1.1 K. The expansion coefficients are rigorously determined by making use of certain stringent conditions. These lead to the spectrum which reproduces the experimental data exceedingly well in the whole range of wave-vectors except near the truncation limit where an extra roton valley springs up. The spectrum so obtained yields very satisfactory results for the parameters of the Landau spectrum as also for the critical velocity. Finally, an attempt is made to critically examine the nature and importance of the quadratic and cubic terms of the energy dispersion formula.

### 1. Introduction

The study of the properties of liquid  $^4\text{He}$  continues to be a fascinating area of condensed matter research because of its immense practical importance as a refrigerant in the rapidly growing industry surrounding the various applications of superconductivity. On the other hand, superfluid  $^4\text{He}$  has been drawing the attention of theorists because this liquid is one of the model many-body systems.

Owing to its weak excitation from the ground state at relatively low temperatures, the liquid  $^4\text{He}$  system is amenable to theoretical attack. The pioneering theoretical investigations of excitation spectrum of this liquid below the transition temperature have been carried out by various workers.<sup>1-6</sup> However, these first principle approaches could succeed only in the qualitative reproduction of the excited spectrum. A very convenient approach based upon an entirely different kind of formulation consisting of the use of the series type expansion of energy in terms of wavevector has become available in recent years and has been thoroughly summarized by Maris.<sup>7</sup> The best theoretical results obtained on the basis of the power series expansion formula are due to Brooks and Donnelly,<sup>8</sup> who employ seven terms in the expansion ignoring the quadratic term in momenta. Since our present interest dwells on the energy expansion theory it would be convenient and fruitful to summarize the status of this formulation as applied to superfluid  $^4\text{He}$  in what follows.

- (1) No thorough satisfactory calculation on the power series expansion exists. For example, the theoretical results are available only upto the roton

valley. Even the results of the excitation spectrum based on the work of Brooks and Donnelly<sup>8</sup> beyond roton minimum yield large deviations from the experimental data. Moreover, there is no systematic representation of the results in the numerical or graphical form.

- (2) There exists, in the literature, a controversy regarding the presence of the quadratic term in the power series.
- (3) It was generally believed that the cubic term in the expansion
 
$$E(p) = cp(1 - \gamma p^2 - \delta p^4 \dots) \quad \dots(1)$$
 is positive, but Maris and Massey<sup>9</sup> suggested that it may in fact be negative as well.

The motivation of the present study originated with the realization that the expansion theory holds much brighter prospects than its hitherto recorded achievements. This has been attempted to be proved by exploring the entire range of excitation spectrum on the basis of properly determined parameters of the series formula. Such an approach is expected to provide reliable answers to the questions, raised above, specially in offering predictions regarding the role of the quadratic and cubic terms.

### 2. Theory

Although there is no *a priori* theoretical basis for power expansion, yet there is some physical justification for it. For example, the linear term gives the sound velocity whereas the quadratic term represents kinetic energy at least qualitatively. Kemoklidze and Pitaevskii<sup>10</sup> as well as Feenberg<sup>11</sup> have shown that because of the long-range van der Waals potential between helium atoms there is a term in  $E$  proportional to  $k^4$ . There has been considerable

\* On leave from Physics Department, Meerut College, Meerut 250 001



discussion about which powers of  $k$  should actually be present in the expansion. However, it is an established fact that the low order polynomial cannot describe the spectrum over an extended range of momentum. Thus one must either choose a more complicated form for the dispersion curve, or alternatively use different polynomial expressions for different ranges of momenta. We adopt the former approach in suggesting

$$E(k) = \sum_{i=1}^9 a_i \cdot k^i, \quad \dots(2)$$

where this form recognizes the fact that the dispersion curve passes through the origin. The case in which  $a_2 = 0$  is considered through the series

$$E(k) = a_1 k + \sum_{i=3}^{18} a_i k^i \quad \dots(3)$$

The number of coefficients  $a_i$  appearing in Eqs. (2) and (3) has been conserved for the purpose of maintaining consistency for the sake of comparison. The parameters of both these equations have been adjusted to achieve an over-all best reproduction of the experimental dispersion curve in such a way that the following conditions inherent to the experimental spectrum are also fulfilled:  $E' = 0$  both at the phonon maxima and at the roton minima;  $E' = \hbar c$  as  $k \rightarrow 0$ , and also at  $k = 2.27 \text{ \AA}^{-1}$ ; and  $E'' = 0$  at  $k = 2.4 \text{ \AA}^{-1}$ . Here the number of primes over  $E$  refers to the order of differentiation with respect to  $k$ .

The coefficients relevant to the two equations are cited in Table 1, which on critical examination shows that the various coefficients, with the exception of  $a_1$  and  $a_2$ , assume opposite signs for the Eqs. (2) and (3).

### 3. Results

#### 3.1 General Spectrum

The theoretical results of the excitation spectrum on the basis of Eqs. (2) and (3) are reported in Table 2 along with experimental data and percentage error. The data are also graphically represented in Fig. 1. An inspection of the graph shows that the two approaches yield identical results in the roton valley. However, there are large differences in the phonon-part as well as near the truncation of the spectrum. In the region of the large disagreement, the curve according to Eq. (3) lies near the experimental graph, while the results of Eq. (2) are far away. In the latter case, the deviations are as large as 82 and 20% respectively in the phonon-region and

Table 1—Values of Coefficients ( $a_n$ ) Expressed in  $\text{K \AA}$

Coefficient $a_n$	In Eq. (2)	In Eq. (3)
$a_1$	18.1547	18.1547
$a_2$	180.2549	—
$a_3$	−699.528175	67.0307541
$a_4$	1115.95593	−271.877473
$a_5$	−963.108856	435.514938
$a_6$	479.659561	−379.758522
$a_7$	−137.254127	192.971622
$a_8$	20.9189854	−56.6743618
$a_9$	−1.31459302	8.8911995
$a_{10}$	—	−0.57586862

at the end of the spectrum. The average absolute percentage deviations are 4.3 and 13.1 for the series with  $a_2 = 0$  and  $a_2 \neq 0$  respectively. Thus, the results obtained from Eq. (3) are excellent and may be considered as the best so far available on the basis of various theories. It is gratifying to observe that the theoretical points lie on both sides (upper and lower) of the experimental data. The behaviour of Eq. (2) in the phonon region is as expected, because the dispersion curve is made to satisfy the equation  $E' = \hbar c$  as  $k \rightarrow 0$ , it is impossible for it to simultaneously absorb the quadratic term for the reproduction of measured values of the energy. On the other hand, the roton part of the spectrum is to be typically represented by  $k^2$ -term and hence leads to a perfect agreement. The measured spectrum beyond roton portion becomes flat, which as is obvious cannot be depicted by a quadratic term.

An unusual, but a common feature of both the approaches of the present theoretical dispersion curves is the appearance of an additional roton valley near the end of the spectrum. One may regard the existence of second roton minimum as a mathematical artifact and may not attach much significance to it because of the procedure followed in the present investigation. However, one must keep in mind the suggestion of Harris<sup>12</sup> that the numerical value of the critical velocity is explainable only on the basis of the existence of secondary roton valley.

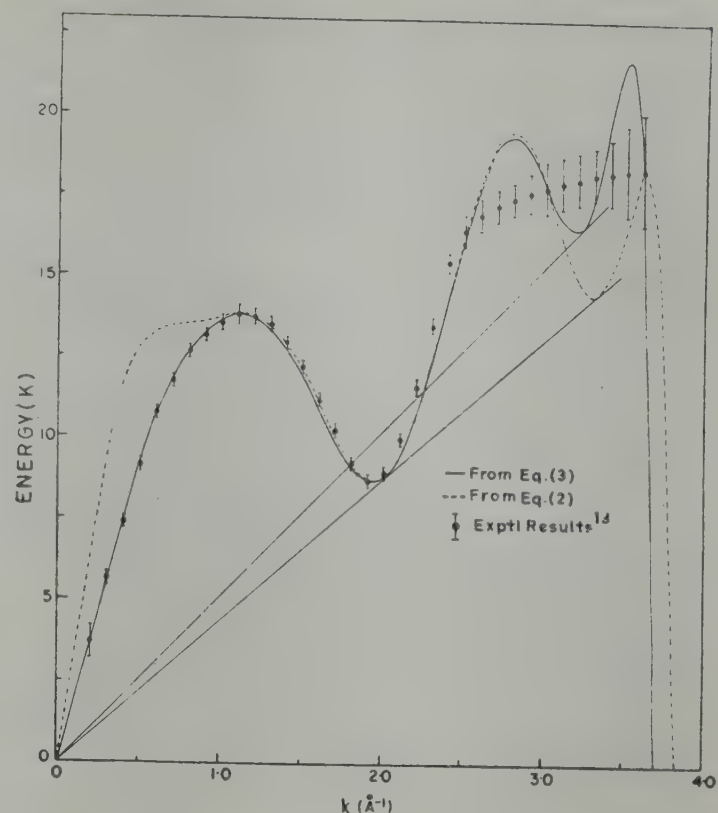
The cut-off for the theoretical excitation spectrum is found to be at  $k = 3.82 \text{ \AA}^{-1}$  and  $3.7 \text{ \AA}^{-1}$  respectively from Eqs. (2) and (3). This is in close agreement with the experimental value of  $3.6 \text{ \AA}^{-1}$  given by Cowley and Woods.<sup>13</sup>



Table 2—Energy of Superfluid  $^4\text{He}$  as a Function of Wave-vector and Expressed in Units of K on the Basis of Eq. (3)

$k (\text{\AA}^{-1})$	$E(k)$		% Error
	Theor.	Exptl.	
0.1	1.86	—	—
0.2	3.85	$3.7 \pm 0.5$	4.05
0.3	5.87	$5.65 \pm 0.20$	3.89
0.4	7.78	$7.4 \pm 0.20$	5.14
0.5	9.44	$9.15 \pm 0.20$	3.17
0.6	10.82	$10.75 \pm 0.20$	0.47
0.7	11.91	$11.75 \pm 0.20$	1.36
0.8	12.73	$12.65 \pm 0.20$	0.63
0.9	13.32	$13.15 \pm 0.20$	1.29
1.0	13.68	$13.55 \pm 0.25$	0.96
1.1	13.80	$13.80 \pm 0.30$	0.00
1.2	13.67	$13.75 \pm 0.25$	-0.58
1.3	13.28	$13.50 \pm 0.25$	-1.63
1.4	12.64	$12.95 \pm 0.20$	-2.39
1.5	11.79	$12.20 \pm 0.20$	-3.36
1.6	10.82	$11.20 \pm 0.20$	-3.39
1.7	9.88	$10.25 \pm 0.20$	-3.61
1.8	9.12	$9.25 \pm 0.20$	-1.41
1.9	8.70	$8.70 \pm 0.20$	0.00
2.0	8.78	$8.95 \pm 0.20$	-1.90
2.1	9.45	$10.00 \pm 0.20$	-5.50
2.2	10.69	$11.65 \pm 0.25$	-8.24
2.3	12.42	$13.55 \pm 0.25$	-8.34
2.4	14.43	$15.50 \pm 0.30$	-6.90
2.5	16.44	$16.45 \pm 0.5$	-0.06
2.6	18.12	$17.0 \pm 0.5$	6.59
2.7	19.18	$17.3 \pm 0.5$	10.87
2.8	19.43	$17.5 \pm 0.5$	11.03
2.9	18.90	$17.7 \pm 0.6$	6.78
3.0	17.85	$17.85 \pm 0.8$	0.00
3.1	16.84	$18.00 \pm 0.8$	-6.44
3.2	16.57	$18.15 \pm 0.8$	-8.71
3.3	17.63	$18.30 \pm 0.8$	-3.66
3.4	19.92	$18.35 \pm 1.0$	8.56
3.5	21.77	$18.40 \pm 1.4$	18.32
3.6	18.45	$18.45 \pm 1.7$	0.00
3.7	0.08	—	—
3.70024	0.0016	—	—

Average absolute percentage deviation = 4.26

Fig. 1—Energy wavenumber dependence of liquid  $^4\text{He}$  at 1.1 K

## 3.2 Phase and Group Velocities

One may obtain the detailed behaviour of excitation spectrum in the small wavenumber region from the phonon phase and phonon group velocity which are respectively given by

$$c(k) = \frac{E(k)}{k}, \text{ and } v(k) = \frac{\partial E(k)}{\partial k}$$

The calculated values of these velocities (hence forth we assume  $a_2 = 0$  unless otherwise stated), are displayed graphically in Fig. 2. The results obtained on the basis of experimental data are plotted in Fig. 3, for ready comparison. We may also observe that the present results are identical to the ones previously found by Maris.<sup>7</sup>

Due to the non-availability of the experimental values in the region of  $k \rightarrow 0$ , the corresponding graph of Fig. 3 is just the result of extrapolation and is, therefore, not exact. However, the abnormal nature (viz. the appearance of maxima) of the velocities is evident. This anomalous behaviour characterizes the phenomenon of superfluidity in  $^4\text{He}$ . It is gratifying to note that our series expansion formula of Eq. (3) also reflects this unusual behaviour. In fact, our calculations show that the maxima of  $v(k)$  and  $c(k)$  are respectively found to lie at  $0.22$  and  $0.32 \text{\AA}^{-1}$ , showing complete agreement with the work of Maris.<sup>7</sup> Also the sound velocity calculated from the slope of the dispersion curve at small  $k$  reproduced the experimental value  $238.69 \text{ msec}^{-1}$ .



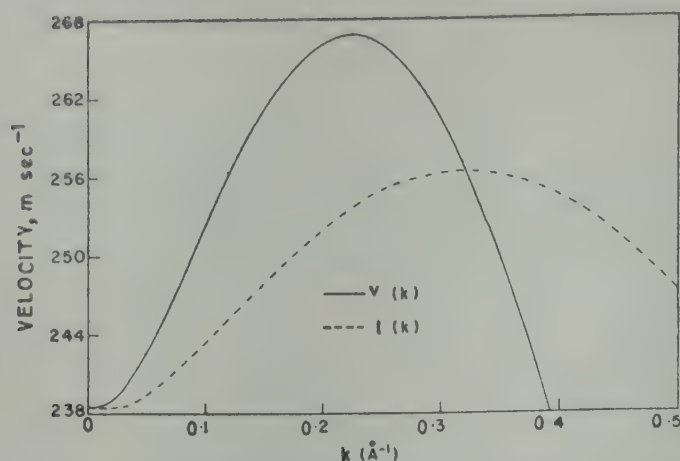


Fig. 2—Small wave-vector dependence of phonon phase and group velocity according to the present work.

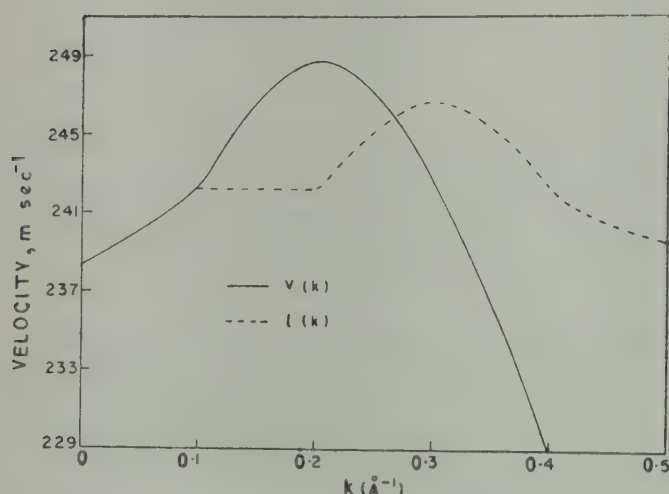


Fig. 3—Small wave-vector dependence of phonon and group velocity according to the experiment

### 3.3 Roton Spectrum and Critical Velocities

The excitation spectrum showing a minimum at  $k = k_0$  and separated by an energy gap  $\Delta$  from the phonon ground state is called the roton spectrum. Experimental observations locate this minimum precisely at  $k_0 = 1.936 \text{ \AA}^{-1}$ . Following Landau, the spectrum for small range of  $k$ -values in the vicinity of energy minimum can be analytically described by the parabolic form

$$E(k) = \Delta + \frac{\hbar^2 (k - k_0)^2}{2\mu}$$

in which the constant  $\mu$  is termed as the effective mass of the roton and is expressed in terms of  $m_{\text{He}}$ , the mass of a helium atom.

We can now provide the description of the roton minima in the mathematical language proposed by Landau. The various parameters are as follows :

$$\Delta = 8.67\text{K}; k_0 = 1.936\text{\AA}^{-1}; \mu/m_{\text{He}} = 0.226$$

These results are certainly superior to the ones obtained by Kumar and Kachhava.<sup>14</sup> Our results show that at  $k = 1.936\text{\AA}^{-1}$  the roton valley is not symmetric about the minima and hence the value of

$\mu$  varies from point to point so that we select an intermediate value of  $\mu$ .

The startling success of the power series formula to trace the first roton minima is obvious from its competence to exactly reproduce the experimental values of  $k_0$  and  $\Delta$ . However, its yielding of a figure of 0.23 against a measured value of 0.15 for the dimensionless parameter  $\mu/m_{\text{He}}$  at first sight might seem discouraging. We may emphasize that this disagreement is not a consequence of the formula but instead originates from the failure of Landau's parabolic equation to faithfully describe the low lying energy dispersion curve of the roton.

It is well-established that the superfluidity is a property of roton spectrum. In particular, the critical velocity  $V_c$  is given just by the slope of the tangent from the origin to the roton spectrum as demonstrated in Fig. 1. The value  $V_c$ , critical velocity for the first minima, is found to be  $57.6 \text{ msec}^{-1}$  and compares exceedingly well with  $58.8 \text{ msec}^{-1}$  as obtained from the spectrum calculated by Brooks and Donnelly.<sup>8</sup> It may be stated that the critical velocities for Eqs. (2) and (3) are the same.

### 4. Conclusion

We observe that in the present work we have successfully exploited the power series expansion formula for predicting the excitation spectrum of liquid  $^4\text{He}$  at 1.1 K in the whole range of excitation spectrum in contrast to Brooks and Donnelly who could predict the spectrum only upto the roton valley. In this sense, this investigation supersedes their findings. This puts us in a position where we are able to answer the basic questions raised in the motivation of the present work. From the present investigation we also conclude that  $a_2 = 0$  yields excellent results except near the termination of the spectrum where also the results may be categorized as satisfactory. On the other hand, the series with non-zero  $a_2$  provides a similar description of the dispersion curve except in the phonon region. This is comprehensible in view of the fact that owing to the linking of the coefficient  $a_1$  with sound velocity, the existence of a quadratic term is expected to modify substantially the otherwise obtained linear portion of the phonon dispersion curve. Even at the cost of deterioration of small wavenumber behaviour of energy spectrum, if we take  $a_1$  as a free variable parameter, the situation does not improve to any considerable extent. Thus we conclude that  $a_2$  must be zero for the small  $k$ -dependence of the dispersion relation. For Eq. (3) value of  $a_3$  is positive confirming the positive dispersion as proposed by Maris and Massey<sup>9</sup> and the value of  $\gamma$  [Eq. (1)] given by  $a_3/c = 33.205 \times 10^{37} \text{ cm}^{-3} \text{ g}^{-2} \text{ sec}^2$ , is comparable



with the value given by Brooks and Donnelly<sup>8</sup>. However,  $a_3$  is negative for the series with  $a_2 \neq 0$ , even then the dispersion is abnormal for small  $k$ -values. We, therefore, assert that the exact status of the sign of  $a_3$  is uncertain. It will, indeed, depend upon the number of terms in the power series as also on the fashion in which the interdependent coefficients of the series are determined. Also, the coefficients of the power expansion could be strongly temperature dependent.

Finally, it may be confessed that the various terms of expansion formula have been grouped in a purely empirical way and are not rigorously derived. We attribute the disagreement between experimental and theoretical spectrum to the neglect of terms which may spring up in a reasonable formalism. For example, Gould and Wong<sup>15</sup> showed that by summation of selected diagrams of the self-energy of a weakly interacting Bose gas, the interaction between elementary excitations gives rise to a  $k^4 \ln(1/k)$  contribution to the dispersion term,<sup>16</sup>  $f(k) = [E(k)/\hbar ck] - 1$  of the spectrum of the single-particle Green's function. Thus, the question of the form and magnitude of the dispersion function is still open but further experimental data and their theoretical analysis on the physical basis of the elementary excitation picture are expected to clarify the situation to a reasonable degree.

### Acknowledgement

The authors are thankful to Dr M P Saksena, Head of the department for providing the departmental facilities. One of them (MK) wishes to express his gratitude to the University Grants Commission, for offering him a teacher-fellowship.

### References

1. Landau L D, *J. Phys. (SSSR)*, 5 (1941), 71.
2. Landau L D, *J. Phys. (SSSR)*, 11 (1947), 91.
3. Bogoliubov N N, *J. Phys. (SSSR)*, 11 (1947), 23.
4. Feynman R P, *Phys. Rev.*, 94 (1954), 262.
5. Feynman R P & Cohen M, *Phys. Rev.*, 102 (1956), 1189.
6. Brueckner K A & Sawada K, *Phys. Rev.*, 106 (1957), 1117, 1128.
7. Maris H J, *Rev. mod. Phys.*, 49 (1977), 341.
8. Brooks J S & Donnelly R J, *Physics Lett.*, 46A (1973), 111.
9. Maris H J & Massey W E, *Phys. Rev. Lett.*, 25 (1970), 220.
10. Kemoklidze M P & Pitaevskii L P, *Zh. Eksp. Teor. Fiz.* 59 (1970), 2187; *Soviet Phys. JETP*, 32 (1972), 1183.
11. Feenberg E, *Phys. Rev. Lett.*, 26 (1971), 301.
12. Harris E G, *Introduction to modern theoretical physics*, Vol. 2 (John Wiley, New York), 1975, 770.
13. Cowley R A & Woods A D B, *Can. J. Phys.*, 49 (1971), 177.
14. Kumar M & Kachhava C M, *Physica*, 95B (1978), 203.
15. Gould H & Wong V K, *Phys. Rev. Lett.*, 27 (1971), 301.
16. Reatto L, *Nuovo Cim.*, 5 (1975), 108.



## *I-V* Model for Photolysis Using Si as Catalyst

V P SUNDAR SINGH & P P WARNEKAR

Department of Electrical Engineering, Indian Institute of Technology, Bombay 400 076

Received 28 April 1979; revised received 7 May 1980

A model to explain the current-voltage (*I-V*) characteristics observed during photolysis of water using single crystal silicon electrode has been developed. Using this model, the observed variation of saturation point with intensity of light and the exponential and linear nature of the *I-V* characteristics have been explained whereas other models fail to do so.

### 1. Introduction

Models for current-voltage (*I-V*) characteristics during photolysis have been described by Butler<sup>1</sup> and Ronald M Wilson.<sup>2</sup> According to these models, the photolytic current will saturate beyond a certain voltage and the saturation point is a function of the absorption coefficient, flat band potential and the doping density. Hence, the saturation point is independent of the intensity of light. It is the aim of the present investigation to explain the shift of saturation point with the intensity of light (other parameters being constant) which is specially observed in case of silicon.

### 2. Experimental Details

The *I-V* characteristics of *p*-silicon (10 ohm-cm) in 0.5% HF electrolyte are taken using an electrochemical cell and a static potentiostat. The light source used was a tungsten lamp having a red filter which cuts-off frequencies above  $4.6 \times 10^{14}$  c/s. The intensity was varied by inserting intensity filters in the incident light path. Fig. 1 shows the *I-V* characteristics of silicon in 0.5% HF with various light intensities.

### 3. Results and Discussion

From Fig. 1 it is clear that the saturation point is a function of light intensity. The ratios of saturation currents as measured from Fig. 1 are  $i_1 : i_2 : i_3 = 1 : 3.49 : 13.05$ . The measured intensities of light are  $I_1 : I_2 : I_3 = 1 : 3.3 : 12.87$ . This is in agreement with models of Butler and Wilson.<sup>1,2</sup> However, the linear variation of current with voltage which is observed in all the four curves at least for a certain voltage range and saturation at different voltages for different light intensities cannot be explained by the models of Butler and Wilson. But this can be

explained using the model, developed by us in this paper.

In the present model, it is assumed that the incremental applied voltage falls completely inside the semiconductor. Then, the charge concentration and the band diagram in the depletion layer for silicon under applied bias and with different light intensities are shown in Fig. 2. When light intensity is zero, the charge in the depletion layer is due to ionized impurities (Fig. 2a). When surface is irradiated with light, the electron concentration in the bulk increases. The electrons which reach the surface can either go to  $H_3O^+$  level or to valence band. But the valence band is completely filled up because of depletion region, neglecting the holes generated in the depletion region due to light absorbed there, especially since low frequency light is used. Further, the number of electrons which can go to  $H_3O^+$  level is limited by surface recombination velocity and

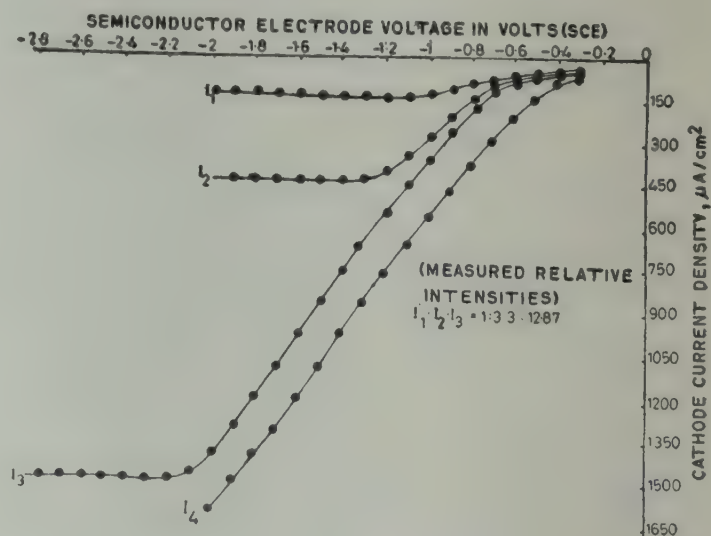


Fig. 1—*I-V* Characteristics for *p*-silicon for different light intensities



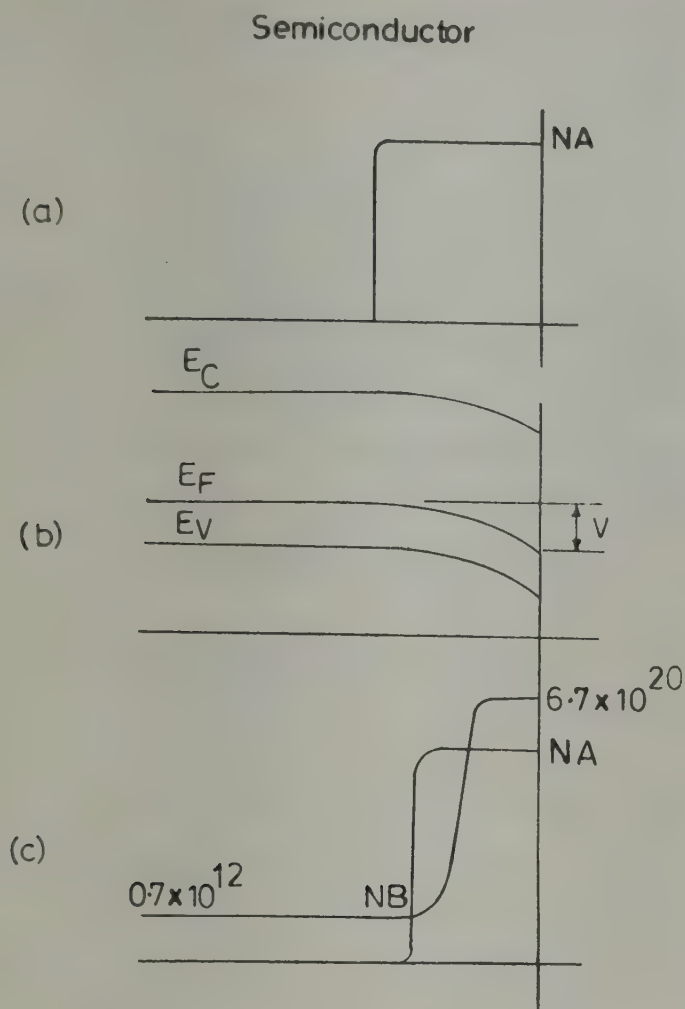


Fig. 2—(a) Concentration of ionized acceptor atoms with illumination; (b) Energy band diagram without illumination; (c) Concentration of ionized acceptor atoms and electrons in the depletion region under applied bias with illumination.

the surface concentration of electrons. Hence, the external current can be represented as

$$i = S N_s q \quad \dots(1)$$

In Eq. (1),  $S$  is surface recombination velocity defined as the number of electrons recombining with  $H_3O^+$  ions in unit time per unit concentration of electrons in the surface;  $N_s$  the concentration of electrons in the surface;  $q$  the elementary electric charge;  $S$  is proportional to the free energy change of electrons in the conduction band, hence

$$S = K_0 (E + A) \quad \dots(2)$$

where,  $E$  is the average free energy gain of electrons from the surface field and  $A$  is free energy gain<sup>3</sup> from light.

From Eq.(1), it is evident that by using Maxwells factor, the surface concentration is finite for a given surface current density, and can be related to the concentration at the end of the depletion region, as

$$N_s = N_B \exp \left[ q \frac{V_{fb} + V}{kT} \right] = N_B R \quad \dots(3)$$

where  $R = \exp q (V_{fb} + V)/kT$

$N_B$  = equilibrium concentration at the end of depletion region

$V_{fb}$  = flat band potential under illumination

$V$  = voltage fall in the depletion region

$\frac{kT}{q} = V_T$ , thermal equivalent voltage.

But, the maximum value of  $N_s$  is determined by the quasi-Fermi level of electrons and not by Eq. (3). In a neutral semiconductor, quasi-Fermi level for electrons under illumination is given by<sup>4</sup>

$$E_{FC} = E_C + \frac{h\nu - E_C}{2} \quad \dots(4)$$

$$\text{For } \lambda = 7500 \text{ \AA}; E_{FC} = 1.37 \text{ eV} \quad \dots(5)$$

The measured value of  $V_{fb}$  for 10 ohm-cm *p*-silicon in 2.5 pH electrolyte under illumination corresponding to  $I_3$  is

$$V_{fb} = 0.20 \text{ V (NHE)} \quad \dots(6)$$

The maximum number of electrons that can exist in the conduction band is given by

$$N_{s\max} = \int_{E_C}^{\infty} N(E) \frac{1}{1 + \exp \left( \frac{E - E_{FC}}{kT} \right)} dE$$

$$= F_{1/2} N_C \quad \dots(7)$$

In Eq. (7),  $F_{1/2}$  is determined from Fermi-Dirac integrals<sup>5</sup>

$$N_C = 2.8 \times 10^{19} / \text{cm}^3$$

For 7500 Å

$$N_{s\max} = 6.7 \times 10^{20} / \text{cm}^3 \quad \dots(8)$$

Thus Eq. (3) can be used only in those cases in which the electron concentration as calculated by it does not exceed that given by Eq. (8). Hence, for large generation of carriers in the bulk, the charge concentration profile in the depletion layer will be as shown by Fig. 2C. Further, when surface concentration is less than  $6.7 \times 10^{20} / \text{cm}^3$ , the expression for external current will be

$$J = S N_B R q \quad \dots(9)$$

$$= K_0 [E + A] N_B R q \quad \dots(10)$$

In Eq. (10)

$$E = \epsilon_s \times I \quad \dots(11)$$



In Eq. (11)

$\epsilon_s$  = surface electric field which is assumed to be constant within distance  $l$ .

$l$  = mean free path for electron in silicon  
= 100 Å [Ref. 6]

$$\epsilon_s = \left[ \frac{2q N_A (V_{fb} + V)}{\epsilon_r \epsilon_0} \right]^{1/2} = C [V_{fb} + V]^{1/2} \quad \dots(12)$$

In Eq. (12)

$$C = \left[ \frac{2q N_A}{\epsilon_r \epsilon_0} \right]^{1/2} \quad \dots(13)$$

where,  $q$  is electronic charge;  $N_A$ , acceptor density;  $\epsilon_r$ , relative permittivity of silicon; and  $\epsilon_0$ , vacuum permittivity

Substituting Eq. (12) in Eq. (10), we have

$$J = K_0 [C(\sqrt{V_{fb} + V}) l + A] N_B R_q \quad \dots(14)$$

Hence Eq. (14) shows that initial  $I$ - $V$  characteristics should be exponential. This equation is valid when

$$N_B R = 6.7 \times 10^{20} \quad \dots(15)$$

This happens for the applied voltage 0.56 (SCE) [ $V_s + 0.24$ ] for  $N_B = 0.7 \times 10^{12}/\text{cm}^3$  (for the curve  $I_3$  in Fig. 1) which is in agreement for the log  $I$  versus  $V$  curve for  $I_3$  as shown in Fig. 3.

When the applied voltage  $V_a$  is increased beyond this, the surface concentration saturates at  $6.7 \times 10^{20}$  and the width of the saturated region increases to counterbalance the increased voltage. The width of this region is determined from Eq. (16).

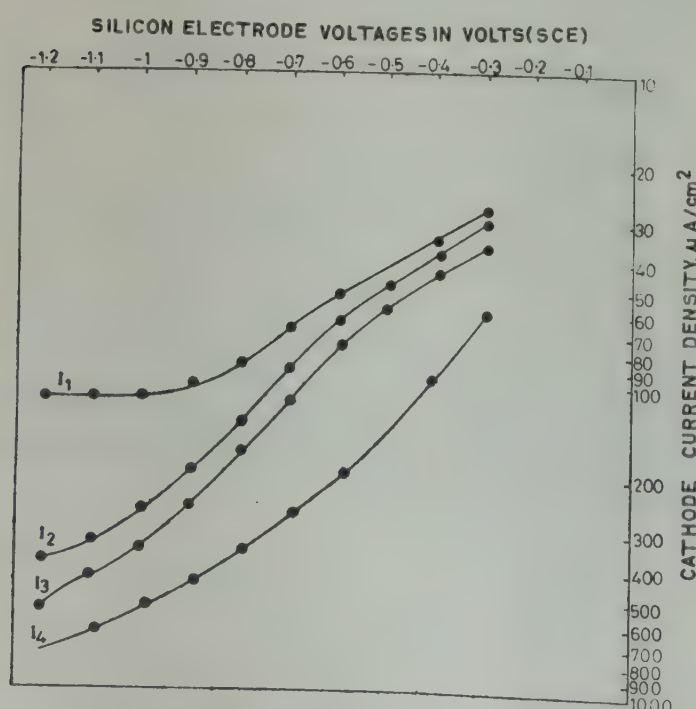


Fig. 3—Log  $I$  versus voltage for  $p$ -silicon for different light intensities

$$W = \left\{ \frac{2\epsilon_0 \epsilon_r [V_a - (V_s + V_{fb} + 0.24)]}{q N_a} \right\}^{1/2} \quad \dots(16)$$

For  $V_a - V_{fb} = 2V$

$$W = \left[ \frac{2 \times 12 \times 8.8 \times 10^{-14} \times 1.44}{1.6 \times 10^{-19} \times 6.7 \times 10^{20}} \right]^{1/2} = 16 \text{ Å}$$

This shows that the electrons can gain the complete energy of the applied voltage since the mean free path of electrons is 100 Å. Hence,

$$S = K_0 [V_a - (V_s + 0.24) - V_{fb} + A] \quad \dots(17)$$

Eq. (17) is valid only for  $V_a > (V_s + 0.24)$ .

In Eq. (17)  $A^3$  ie

$$A = \frac{kT}{q} \ln \left[ 1 + \frac{\Delta n}{n} \right] \quad \dots(18)$$

For curve  $I_3$  in Fig. 1  $\Delta n = 0.7 \times 10^{12}/\text{cm}^3$

$$n = 1.12 \times 10^5/\text{cm}^3; \quad A = 0.025 \times 2.3 \times 7 = 0.4 \text{ eV} \quad \dots(19)$$

$$S = K_0 [V_a - (V_s + 0.24) - V_{fb} + 0.4] \quad \dots(20)$$

At low voltages, the expression for current from Eq. (14) reduces to

$$J = K_0 A N_B R_L \quad \dots(21)$$

since  $C\sqrt{V_{fb} + V} l \ll A$

Since  $K_0$  is dependent on surface conditions, theoretical evaluation is extremely difficult. However,  $K_0$  can be determined from the practically observed exponential characteristics of Fig. 3. Hence

$$\frac{dJ}{dV} = \frac{K_0 A q N_B R}{V_T} \quad \dots(22)$$

Since  $dJ/dV = 200 \times 10^{-6}$  at  $V = 0.2V$ , from Eq. (22),  $K_0$  comes out to be  $11.4 \times 10^{-6.2}$ .

At high applied voltage, substituting Eq. (20) in Eq. (14)

$$J = K_0 [V_a - (V_s + 0.24) - V_{fb} + 0.4] N_{s\max} q \quad (23)$$

Eq. (23) shows a linear relation for  $J$ - $V$  characteristics and the slope is given by

$$\begin{aligned} \frac{dJ}{dV_a} &= K_0 N_{s\max} q \\ &= 11.4 \times 10^{-6.2} \times 6.7 \times 10^{20} \times 1.6 \times 10^{-19} \\ &= 0.81 \times 10^{-3} \frac{A}{V\text{-cm}^2} \quad \dots(24) \end{aligned}$$

The measured value of  $dJ/dV$  from  $I_3$  of Fig. 1 is  $1 \times 10^{-3} \text{ A/V-cm}^2$ . Thus, the agreement is reasonably good considering the inaccuracies involved in the measurement of  $V_{fb}$  and  $N_b$ . The measurement of  $V_{fb}$  has to be very precise because the current variation is exponentially dependent on it.



### Conclusion

The model developed in this paper explains the initial exponential characteristics, the voltage at which the linear characteristic begins and the slope of the linear region. Considering the inaccuracies involved in the measurement of  $V_{fb}$  and  $N_b$ , the agreement between theoretical and practically observed slope for  $J$  versus  $V$  curve is reasonable. Further, this model is valid only in case of narrow bandgap semiconductors having large mean free-path.

### References

1. Butler M A, *J. appl. Phys.*, **48** (1977), 1914.
2. Wilson R M, *J. appl. Phys.*, **48** (1977), 4292.
3. Gerischer H, *J. electrochem. Soc.*, **11** (1966), 1174.
4. Sze S M, *Physics of semiconductor devices* (Wiley Interscience, New York) 1969.
5. Dougall J M & Stoner E C, *Phil. Trans. R. Soc. Lond., Math. & Phys. Sci. Series A*, (1938), 237.
6. Moll J L, *Physics of semiconductors*, (McGraw-Hill, New York) 1964.



## Study of Solid-Liquid Interface of Bismuth-Antimony Alloy Single Crystals

V P BHATT, G R PANDYA & A R VYAS\*

Physics Department, M S University of Baroda, Baroda 390 002

Received 4 July 1979

The systematic study of the solid-liquid interface of single crystals of Bi-Sb alloy containing 1 at.% of Sb is reported. Various substructures such as striations, elongated cells, hexagonal cells, irregular cells and cellular dendrites have been observed on increasing growth velocity. It has been found that the growth proceeds by the addition of {111} planes by a layer mechanism.

### 1. Introduction

Several papers<sup>1-3</sup> have appeared in regard to the preparation of Bi-Sb alloy (up to 15 at.% Sb) by repeated zone melting method. A few workers<sup>3,4</sup> have studied the microsegregation and solidification substructure of the solid-liquid interface of Bi-Sb alloy crystals. Bhatt *et al.*<sup>5</sup> have grown single crystals of Bi-Sb alloys containing 1-20 at.% antimony and have reported features observed on the top free surface and on the cleavage plane of the crystal. As a part of this programme, the features on the solid-liquid interface of the growing crystals are studied and the results are reported in this paper.

Usually there are two methods of studying the directional solidification process in solid solution and alloys. In one method, the concentration of component metals in the alloy is kept fixed and the rate of growth is varied. In the second method, the rate of growth is kept constant and the concentration of one of the component metals is varied. We have adopted the first method and studied the features observed on the solid-liquid interface of Bi-Sb alloys containing 1 at.% of Sb.

### 2. Experimental Details

Single crystals of Bi-Sb alloy containing 1 at.% antimony were grown by zone melting method using different growth rates ranging from 0.2 cm/hr to 1.8 cm/hr. The temperature gradient (65°C/cm) in the furnace was kept constant throughout the work. After achieving desired length of the crystal, (about 4 cm) the solid-liquid interface was obtained by decanting the liquid from the solid during solidification by rapidly tilting the container. The interface

was grounded and polished to remove strained region. The specimens were then examined under Vicker's projection microscope.

### 3. Results and Discussion

Fig. 1 shows the features observed on the solid-liquid interface of the crystal grown at the velocity 0.2 cm/hr. The interface reveals a set of almost parallel vertical lines resembling striations. It has been shown by Bhatt *et al.*<sup>5</sup> that Bi-Sb single crystals grow by the addition of {111} planes in  $\langle 112 \rangle$  directions. Hence it seems that the vertical lines (Fig. 1) are produced due to the intersection of any of the {111} planes with the solid-liquid interface.

Fig. 2 shows features observed when growth velocity was 0.4 cm/hr. Here the effect of constitutional super-cooling is clearly seen. The planar interface now no longer exists but the development of elongated cell is clearly visible. Biloni *et al.*<sup>6</sup> have reported the transition of planar solid-liquid interface to the elongated cells in dilute tin alloys

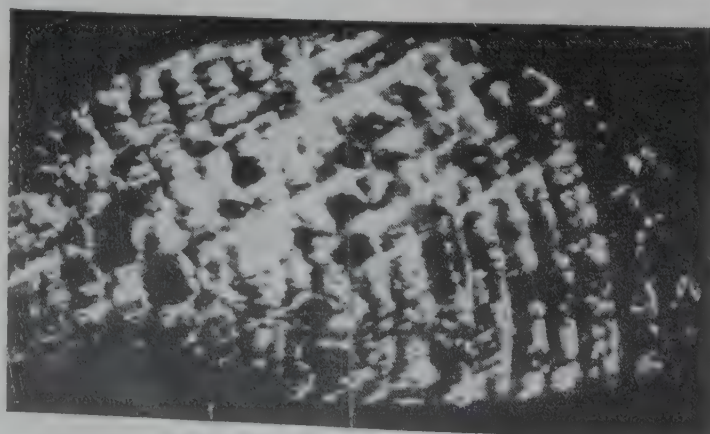


Fig. 1—Set of parallel lines on the solid-liquid interface observed for the growth velocity 0.2 cm/hr ( $\times 10$ )

\*Present address: Alembic Chemical Works Ltd, Baroda.



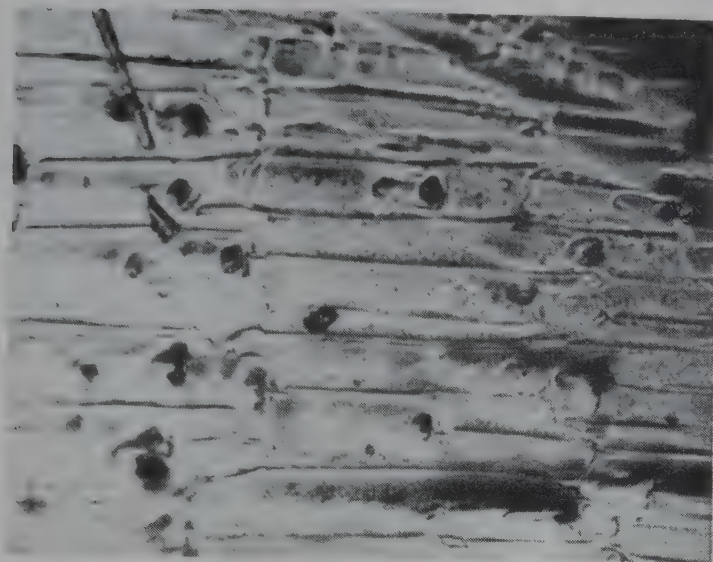


Fig. 2—Elongated cells (growth velocity 0.4 cm/hr) ( $\times 150$ )



Fig. 3—Cellular substructure (growth velocity 0.6 cm/hr) ( $\times 150$ )

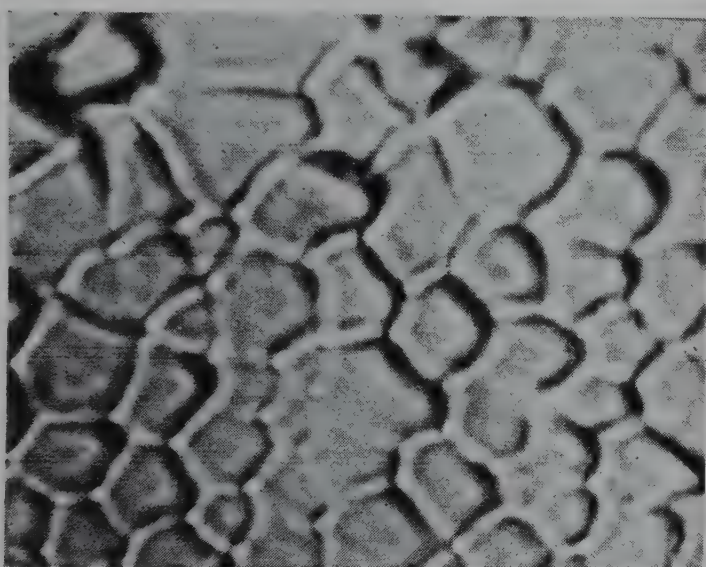


Fig. 4—Cells of different shapes having four-, five- and six-sides (growth velocity 0.7 cm/hr) ( $\times 780$ )

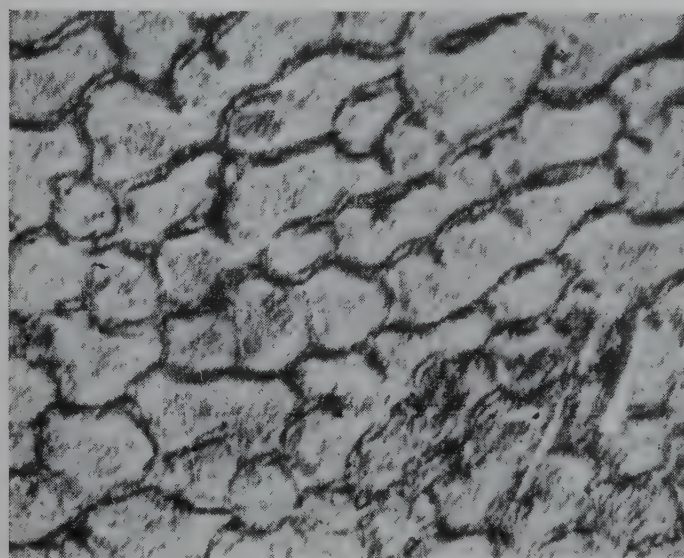


Fig. 5—Cells similar to those in Fig. 4 observed after cutting and polishing the interface ( $\times 780$ )

resulting from the increase in the constitutional supercooling. When the growth velocity was 0.6 cm/hr the cellular substructure was observed on the solid-liquid interface as shown in Fig. 3. The forms of cell are less regular in character. It is worthwhile to mention that the ridges were also observed on the top free surface of this crystal when solid-liquid interface exhibited cellular substructure. It has been shown by Rutter and Chalmers<sup>7</sup> that the origin of the cellular substructure can be accounted for in terms of constitutional supercooling.

When the growth velocity was 0.7 cm/hr, the solid-liquid interface was obtained by suddenly decanting the liquid from the solid by rapidly tilting the container. Fig. 4 shows the cellular substructure observed on the solid-liquid interface. This photograph clearly shows cells of different sizes having four, five and six sides. To establish whether the cellular

structure is a surface or body phenomenon, showing the true nature of the solid-liquid interface, the crystal was cut with a sharp jeweller's saw near the interface. The crystal was lapped on 0, 2/0, 3/0, and 4/0 grade emery papers successively. This was followed by electrolytic polishing using the electrolyte reported by Yim.<sup>1</sup> Fig. 5 shows cells similar to Fig. 4, suggesting that the cell structure is a body phenomenon. The breaking up of the cell structure and the beginning of the development of dendrites is shown in Fig. 6. This was observed on the solid-liquid interface of the crystal grown at the rate of about 0.9 cm/hr. An example of cellular dendrite is shown in Fig. 7. This feature was observed on the solid-liquid interface of the crystals grown at the rate of 1.1 cm/hr and is due to high constitutional supercooling.





Fig. 6—Broken cells (growth velocity 0.9 cm/hr) ( $\times 90$ )

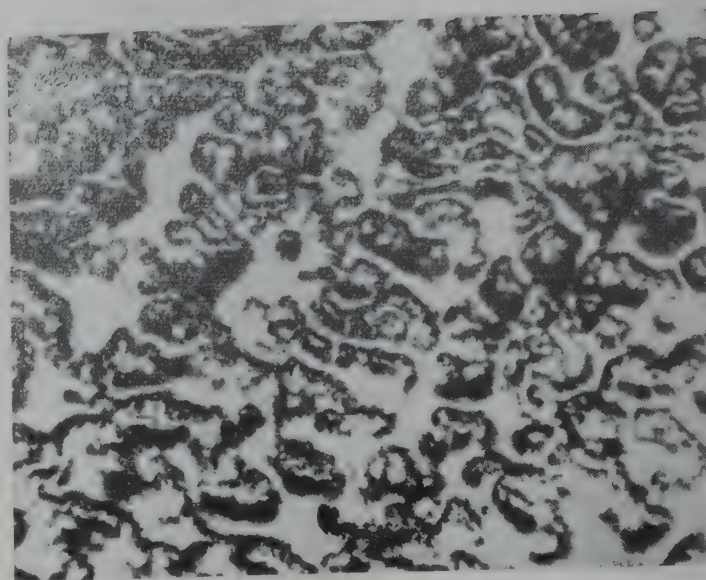


Fig. 7—Cellular dendrites (growth velocity 1.1 cm/hr) ( $\times 90$ )

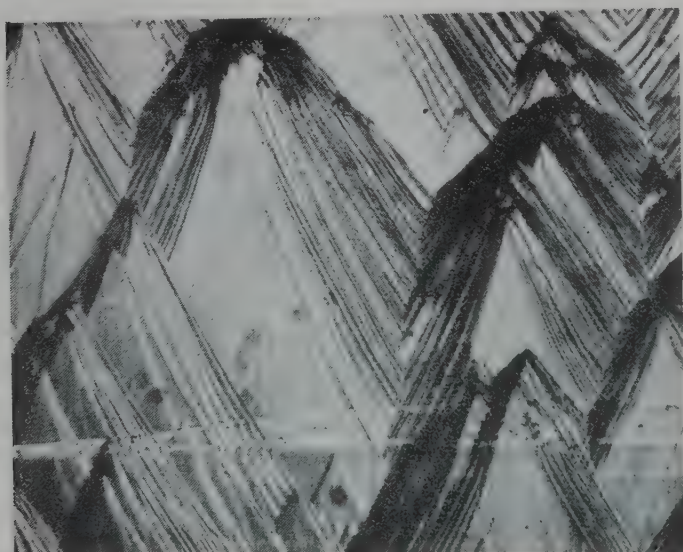


Fig. 8—Mountain-like growth features (growth velocity 0.7 cm/hr) ( $\times 100$ )

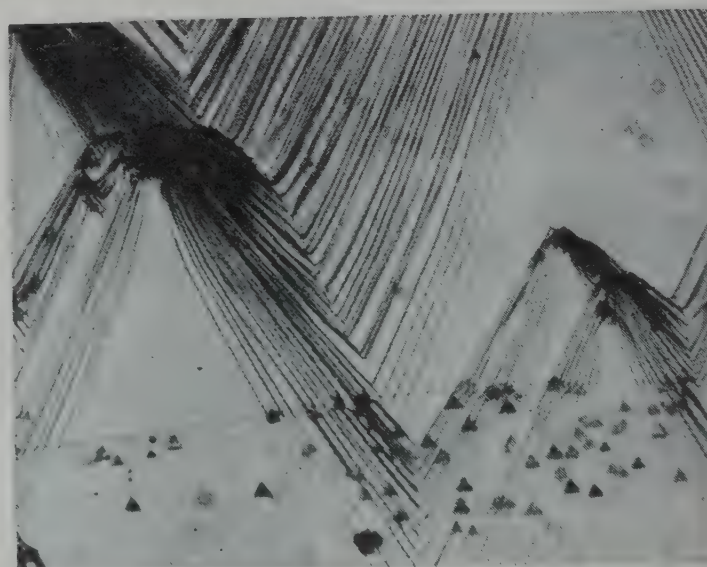


Fig. 9—Details of features of the central area of Fig. 8 at higher magnification ( $\times 300$ )

When the growth rate of the crystal was more than 1.1 cm/hr, the solid-liquid interface exhibited free dendrites. It may be noted that at these velocities, it was impossible to grow homogeneous single crystals, and the percentage yield of single crystal was extremely low. Table 1 shows the discrete stages of substructure changes, as constitutional supercooling increases during growth process.

It is worthwhile to mention that when the grown crystal (growth velocity: 0.7 cm/hr) had attained a length of about 1 cm, the liquid in contact with the solid crystal was decanted exposing the solid-liquid interface. Fig. 8 shows the features observed on the solid-liquid interface. Mountain-like features, triangular in shape, are clearly visible. It seems that the growth has proceeded by addition of the layers of  $\{111\}$  planes. It may be noted that cleavage plane

[which is (111)] in this case was almost parallel to the solid-liquid interface. It seems that the conversion of cellular features (Fig. 4) into mountain-like features (Fig. 8) may be due to the increased constitutional supercooling effects with time.

In order to obtain more details, the photograph of this feature was taken at higher magnification. Fig. 9 shows the details of the features of the central area of Fig. 8 at higher magnification. Small dark flat triangles are clearly visible in the photograph, the edges of which are almost parallel to the main growth edges. Bhatt *et al.*<sup>8</sup> have reported such triangular features on the cleavage plane of antimony crystals. They have shown that these triangles are somewhat analogous to growth trigons in diamond, where the whole body of the crystal is filled with triangular hollow features. It seems that in the present case also the dark small triangular features



Table 1—Discrete Stages of Substructures Observed on Solid-Liquid Interface

Growth velocity cm/hr	Description of substructure
0.2	Planar interface intersected by almost vertical lines (striations)
0.4	Elongated cells
0.6	Less regular cells
0.7	Six-, five-, and four-sided cells
0.9	Broken cells, cellular dendrites
1.1	Cellular dendrites

are analogous to the growth trigons reported by Tolansky and Wilcock.<sup>9</sup>

#### 4. Conclusions

1. The discrete substructures observed on the solid-liquid interface change continuously as constitutional supercooling increases.

2. The triangular features (Figs. 8 and 9) observed on the solid-liquid interface are analogous to the growth trigons in diamond and the crystal grows by the layer mechanism by adding {111} planes.

#### Acknowledgement

The authors are thankful to Prof. M M Patel for his keen interest and kind help in the present work.

#### References

1. Yim W M & Dismukes J P, *J. Phys. Chem. Solids*, **27** (Suppl.), (1966), 187.
2. Jain A L, *Phys. Rev.*, **114** (1959), 1578.
3. Brown D M & Heumann F K, *J. appl. Phys.*, **35** (1964), 1947.
4. Leistike O & Andersen A L, *J. appl. Phys.*, **40** (1969), 4659.
5. Bhatt V P, Pandya G R & Rao R D, *J. Cryst. Growth*, **16** (1972), 283.
6. Biloni H, Bolling G F & Cole G S, *Trans. Met. Soc. AIME*, **236** (1966), 930.
7. Rutter J W & Chalmers B, *Can. J. Phys.*, **31** (1953), 15.
8. Bhatt V P, Talati M C & Shah H M, *Indian J. pure appl. Phys.*, **8** (1970), 236.
9. Tolansky S & Wilcock W L, *Nature, Lond*, **157** (1946), 583.



## Temperature Dependence of Effective Mass of Electrons & Holes & Intrinsic Concentration in Silicon

R K JAIN

Solid State Devices Division, Central Electronics Engineering Research Institute, Pilani 333 031

Received 21 January 1980

New empirical relations to describe the temperature dependence of effective masses of the electron and hole density-of-states are reported. These relations are used to compute the temperature dependence of the intrinsic concentration in silicon. Results of the calculations agree with the available experimental information.

### 1. Introduction

An accurate knowledge of intrinsic concentration ( $n_i$ ) and effective masses of electrons ( $m_e^*$ ) and holes ( $m_h^*$ ) is essential for a satisfactory interpretation of various characteristics of any bulk or doped semiconductor device. The temperature dependence of  $n_i$ ,  $m_h^*$  and  $m_e^*$  is also equally important for such studies. In the literature, experimentally determined values of intrinsic concentration ( $n_i$ ) are available.<sup>1-3</sup> Sufficient experimental information on the temperature dependence of the effective mass of electron density-of-states ( $m_e^*$ ) is also available.<sup>4-8</sup> Though considerable experimental information about the temperature dependence of the effective mass ( $m_h^*$ ) of the hole density-of-states is reported in literature,<sup>6,8,9</sup> there are some inconsistencies in the results reported. However, it is well understood that  $n_i$ ,  $m_e^*$  and  $m_h^*$  all increase with temperature.

The purpose of this paper is to report empirical relations for the temperature dependence of  $m_e^*$  and  $m_h^*$  in the range 300-1500 K. It is observed that the relations agree closely with the earlier experimental results. Further, the proposed relations on temperature dependence of  $m_e^*$  and  $m_h^*$  are used for computing the variation of intrinsic concentration with temperature which compares with the previous reported results.

### 2. Temperature Dependence of $m_e^*$

A series of experiments have been made to determine the temperature dependence of  $m_e^*$ .<sup>4-8</sup> Of these the experimental results of Ukhanov and Mal'tsev<sup>4</sup> and Stradling and Zhukov<sup>5</sup> gave sufficient evidence, to support the temperature dependence of the effective

mass of electron density-of-states. Stradling and Zhukov<sup>5</sup> performed cyclotron resonance measurements on ultra-high purity *n*-type silicon over the temperature range 4-206 K. Of the two samples studied by them, one had a resistivity of  $10^3$  ohm-cm at 300 K with a high degree of compensation and the other had a resistivity of  $3 \times 10^3$  ohm-cm at 300 K, but relatively uncompensated. Yet the results were the same for both samples over the entire temperature range. It was found that the transverse effective mass increases with the temperature. Ukhanov and Mal'tsev<sup>4</sup> performed Faraday rotation experiments on *n*-type ( $3.7 \times 10^{17}$  atoms cm<sup>-3</sup>) silicon over the temperature range 300-600 K and observed an increase in the effective mass. In Fig. 1, the combined experimental results of Ref. 4 and 5 are plotted as curve 1.

Recently, Heasell<sup>10</sup> suggested that the temperature dependence of the effective mass of electron density-of-states ( $m_e^*$ ) can be empirically found out by considering the quadratic dependence of the transverse effective mass  $m_t$  on the energy band gap. These results considered better as compared to the assumption of a linear dependence of  $m_t$  (curve 3) on the band gap, are shown as curve 2 in Fig. 1. From Fig. 1 we observe that Heasell's<sup>10</sup> curve is in good agreement with the experimental curve in the range 200-600 K but starts deviating rapidly at higher temperatures (600-1200 K) for which he has calculated the intrinsic concentration. In this paper, we propose a new empirical relation for  $m_e^*$ , which seems to follow the experimental curve of Ukhanov and Mal'tsev, that of Stradling and Zhukov quite closely and is better than other relations suggested earlier.<sup>10-12</sup> The expression is as follows:

$$m_e^*(T) = m_e^*(300\text{ K}) \frac{E_G(300\text{ K})}{E_G(T)} \quad \dots(1)$$



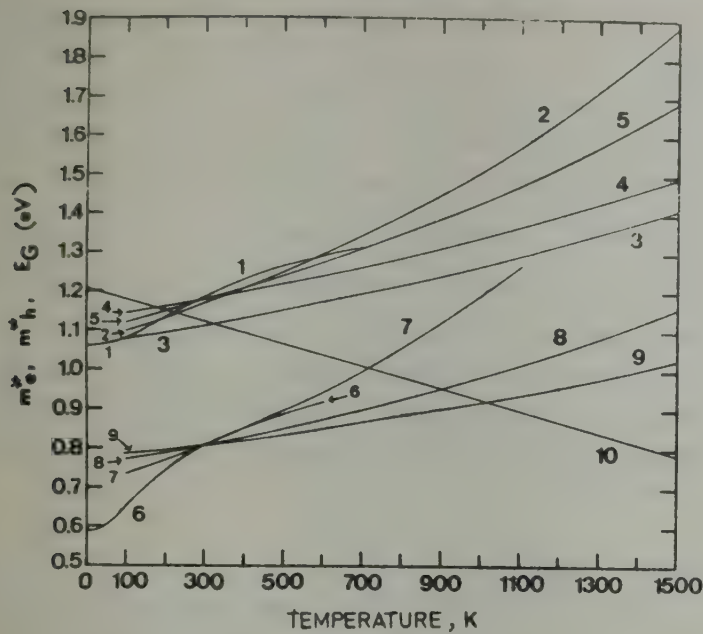


Fig. 1—Plots of temperature dependences of  $m_e^*$ ,  $m_h^*$  and  $E_G$

Curve No.	Parameter	Nature	Ref.
1.	$m_e^*$	Exptl	4,5
2.	$m_e^*$	$m_t \propto E_G^2$	10
3.	$m_e^*$		
4.	$m_e^*$		
5.	$m_e^*$	Semi-empirical	12
6.	$m_h^*$	Eqs. (1) and (2)	Present study
7.	$m_h^*$	Theoretical	11
8.	$m_h^*$	Eq. (3)	Present study
9.	$m_h^*$	Eq. (4)	Present study
10.	$E_G$	Semi-empirical	12
		Eq. (2)	14

Curve 5 of Fig. 1 shows the plot of Eq. (1) in the temperature range 200-1500 K, using  $m_e^*(300 \text{ K}) = 1.18$  after Barber.<sup>11</sup> We have also tried several other empirical possibilities<sup>13</sup> but Eq. (1) seems to be better. In Eq. (1),  $E_G$  is the silicon energy band gap, whose temperature dependence can be reliably estimated by using the results obtained by Macfarlane *et al.*<sup>14</sup> and is usually described mathematically for temperatures equal and above 300 K as:

$$E_G(T) = 1.205 - 2.8 \times 10^{-4} T \quad \dots(2)$$

### 3. Temperature Dependence of $m_h^*$

The experimental information for the temperature dependence of the effective mass  $m_h^*$  of hole density of states is rather very poor as compared to  $m_e^*$ . Conflicting experimental results from different workers<sup>6,8,9</sup> are available. Barber<sup>11</sup> has calculated theoretically values of  $m_h^*$  using Kane's valence band

structure<sup>15</sup> and including the effects of the non-parabolicity of the valence band temperature dispersion. In Fig. 1 we have shown the available theoretical results of Barber<sup>11</sup> exhibiting temperature dependence of  $m_h^*$  in the range 0-600 K (curve 6). Now we suggest a simple empirical temperature dependence of  $m_h^*$  given by:

$$m_h^*(T) = m_h^*(300 \text{ K}) \left\{ \frac{E_G(300 \text{ K})}{E_G(T)} \right\}^2 \quad \dots(3)$$

In Fig. 1 we have plotted (curve 7) Eq. (3) using Eq. (2) and taking  $m_h^*(300 \text{ K}) = 0.81$  after Barber.<sup>11</sup> We observe that in the range 300-600 K, the agreement with the theoretical results of Barber is excellent, but afterwards,  $m_h^*$  increases rapidly and the curve is unreliable at higher temperatures. Hence an alternative empirical relation as follows is given:

$$m_h^*(T) = m_h^*(300 \text{ K}) \frac{E_G(300 \text{ K})}{E_G(T)} \quad \dots(4)$$

Curve 8 of Fig. 1 shows the plot of Eq. (4). This variation of  $m_h^*$  with temperature seems to be more reliable than the empirical approach proposed by Jain and Van Overstraeten<sup>12,13</sup> (curve 9). Anyhow, more experimental research is needed to verify the present empirical approach for the temperature dependence of  $m_e^*$  and  $m_h^*$ , but we try to justify the present relations by calculating the intrinsic concentration, considered in the next section.

### 4. Temperature Dependence of $n_i$

To check the validity of the empirical temperature dependences of  $m_e^*$  and  $m_h^*$  suggested in the previous sections, we use these results for computing temperature variation of the intrinsic carrier concentration  $n_i$  and comparing it with the available reliable results. Many workers<sup>1-3,10-12</sup> have reported the calculation of the intrinsic carrier concentration in silicon using various experimental and theoretical approaches. We computed the intrinsic carrier concentration  $n_i$  as a function of temperature in the same way as described in Ref. 12. At every temperature, first the Fermi level was computed using the charge neutrality condition for a lightly doped silicon crystal and then the electron and hole concentrations were calculated using the following equations:

$$n = \int_{-\infty}^{+\infty} \rho_e(E) \cdot f(E) dE \quad \dots(5)$$

$$p = \int_{-\infty}^{+\infty} \rho_h(E) \cdot \{1 - f(E)\} dE \quad \dots(6)$$



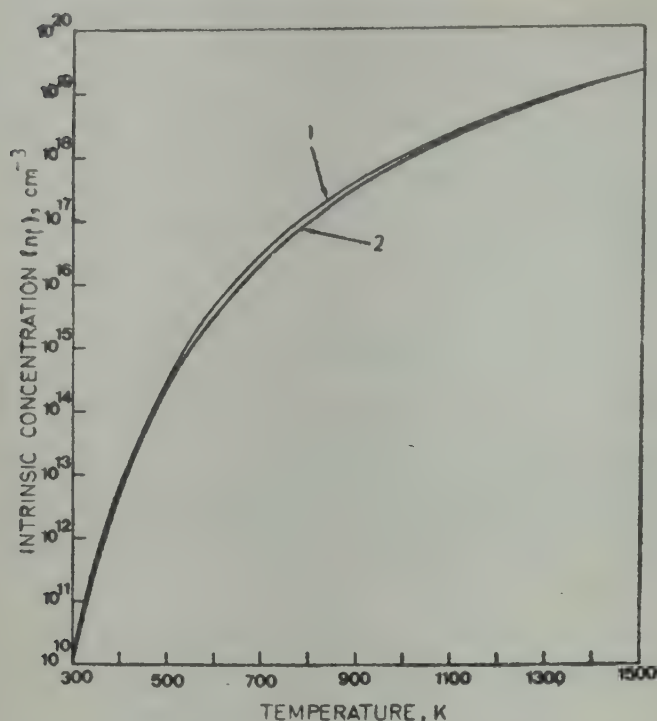


Fig. 2—Temperature dependence of the intrinsic concentration ( $n_i$ ) in a lightly doped silicon (having  $10^{17}$  boron atoms  $\text{cm}^{-3}$  and  $2 \times 10^{17}$  phosphorus atoms  $\text{cm}^{-3}$ ) [Curve 1: Data from Morin and Maita<sup>1</sup>, curve 2: present study]

where  $n$  and  $p$  are respectively the electron and hole concentrations,  $f(E)$  is the Fermi-Dirac distribution function,  $\rho_e$  and  $\rho_h$  are respectively the total electron and hole density of states. More details of the calculation are found in Refs. 12 and 16. Finally  $n_i$  is calculated by using the standard relation,

$$n_i = (np)^{1/2} \quad \dots (7)$$

In Fig. 2, we have plotted the computed (on IBM 370/155) temperature dependence of the intrinsic concentration in the range 300-1500 K using the empirical temperature dependence of  $m_e^*$  and  $m_h^*$  suggested by us in Eqs. (1) and (4) respectively. For comparison, in Fig. 2 we have also plotted the well-known results of Morin and Maita<sup>1</sup> and the agreement is quite good. This supports the validity of the empirical temperature dependences of  $m_e^*$  and  $m_h^*$  proposed here. Now instead of using Eq. (4),

if we had used Eq. (3), then the  $n_i$  results are slightly better in the lower temperature range but above 1100 K, the deviation from the Morin and Maita's results curve is wide. This shows that temperature dependence of  $m_h^*$  represented by Eq. (3) is not valid at high temperatures. The semi-empirical approach for the temperature dependence of  $m_e^*$  and  $m_h^*$  proposed recently by Jain and van Overstraeten<sup>12</sup> also gave quite satisfactory results. Anyhow, whenever individual calculations are involved the present empirical relations can be expected to give more reliable data.

### Acknowledgement

Most of this work was done at the Department Elektrotechniek, K U L, Heverlee, Belgium. The author thanks Prof. Dr R Van Overstraeten for many stimulating discussions and encouragement.

### References

1. Morin F J & Maita J P, *Phys. Rev.*, **96** (1954), 28.
2. Herlet A, *Z. angew. Phys.*, **9** (1957), 155.
3. Putley E H & Mitchell W H, *Proc. phys. Soc. Lond.*, **72A** (1958), 193.
4. Ukhanov Yu I & Mal'tsev Yu V, *Soviet Phys. Solid St.*, **5** (1964), 2144.
5. Stradling R A & Zhukov V V, *Proc. phys. Soc. Lond.*, **87** (1966), 263.
6. Geist D, *Naturwissenschaften*, **45** (1958), 33.
7. Sonder E & Stevens D K, *Phys. Rev.*, **110** (1958), 1027.
8. Cardona M, Paul W & Brooks H, *Helv. Phys. Acta*, **33** (1960), 110.
9. Keesom P H & Seidel G, *Phys. Rev.*, **113** (1959), 33.
10. Heasell E L, *Solid St. Electron.*, **16** (1973), 651.
11. Barber H D, *Solid St. Electron.*, **10** (1967), 1039.
12. Jain R K & van Overstraeten R J, *IEEE Trans.*, **ED 21** (1974), 155.
13. Jain R K & van Overstraeten R J, FEH internal report, May 1973.
14. Macfarlane G G, Mclean T P, Quarrington J E & Roberts V, *Phys. Rev.*, **III** (1958), 1245.
15. Kane E O, *J. Phys. Chem. Solids*, **1** (1956), 82.
16. van Overstraeten R J, De Man H J & Mertens R P, *IEEE Trans.*, **ED 20** (1973), 290.



## Resonance Energies of Non-Alternant Hydrocarbons

M M TIWARI, R K UPADHYAY & A K SRIVASTAVA

Department of Chemistry, University of Allahabad, Allahabad 211 002

Received 5 November 1979

Mulliken-Parr or empirical resonance energies have been calculated for a number of non-alternant hydrocarbons and it has been shown that the results are qualitatively in excellent agreement with the concept of aromaticity.

### 1. Introduction

If a compound possesses more than one structure, the resonance energy is regarded as a physical measure of the stability of the most stable structure relative to other possible structures. Among the many possible definitions for the term resonance energy, those due to Hückel<sup>1</sup> and Mulliken-Parr<sup>2</sup> are the ones that are most commonly used. The Mulliken-Parr or empirical resonance energy is taken to be the difference between the bond energies of (I) and (II).

$$E_R = E_b(\text{I}) - E_b(\text{II}) \quad \dots (1)$$

where (I) represents an aromatic structure with all bonds equal to 1.40 Å and (II) represents a structure with alternating C—C bond length and C=C bond length respectively. The bond energies may be calculated with the help of following equations:

$$E_b(\text{I}) = N E_c + N_H E_H + E_{\pi b}(\text{I}) \quad \dots (2)$$

and

$$E_b(\text{II}) = N_1 E_1 + N_2 E_2 + N_H E_H \quad \dots (3)$$

In which  $E_{\pi b}(\text{I})$  is the  $\pi$ -bonding energy of (I).  $E_1$  and  $E_2$  are the energies of a C—C bond of length 1.48 Å and C=C bond of length 1.34 Å respectively.  $N_1$ ,  $N_2$ ,  $N_H$ ,  $E_H$  represent respectively the number of single and double bonds and number and energy of carbon-hydrogen bonds.

Now since the values of  $E_1$  and  $E_2$  are very uncertain, we shall use the following scheme instead of using them directly,

$$E_R = N A_0 + (N_1 - N_2) A_1 + E_{\pi b}(\text{I}) \quad \dots (4)$$

where

$$A_0 = E_c - \frac{E_1 + E_2}{2} \quad \dots (5)$$

$$A_1 = \frac{E_2 - E_1}{2} \quad \dots (6)$$

However,  $A_0$  and  $A_1$  are to be treated as empirical parameters.

For calculating resonance energy with the help of Eq. (4), we must first evaluate the  $\pi$ -bonding energy, i.e.  $E_{\pi b}(\text{I})$ .

### 2. Calculation of the $\pi$ -Bond Energy

The total  $\pi$ -bond energy ( $E_{\pi b}$ ) of a molecule is defined as the energy required when isolated carbon atoms, each with a  $\pi$ -electron, combine to form  $\pi$ -bonds. In the SCF-MO theory,<sup>3</sup> this energy is given by,

$$E_{\pi b} = (\text{total molecular orbital energy}) - (\text{total interelectronic repulsion}) + (\text{total core repulsion}) - (\text{total energy of } \pi\text{-electrons in widely separated carbon atoms}) \quad \dots (7)$$

Since the total molecular orbital energy includes twice the total interelectronic repulsion, if the molecule is neutral, the Coulomb repulsion of the cores of the atoms should be more or less balanced by the Coulomb repulsion of the electrons attached to these cores. Since in the ground state, the molecule as well as the atoms in them are supposed to be neutral, the total  $\pi$ -bond energy of a molecule may be given by,

$$E_{\pi b} = (\text{total molecular orbital energy}) - (\text{total energy of } \pi\text{-electrons in widely separated carbon atoms}) \quad \dots (8)$$

However, it may be pointed out that in SCF-MO method, the Hartree-Fock eigen values involve two types of repulsion integrals, Coulomb integrals ( $J_{rs}$ ) and exchange integrals ( $K_{rs}$ ). Now since the core repulsion approximately cancels only the Coulomb integrals and leaves the exchange integrals uncompensated for, the total interelectronic repulsion in the SCF-MO method is not completely balanced by the total core repulsion. On the other hand, the matrix elements  $H_{rr}$  and  $H_{rs}$  used in the present calculation, involve only Coulomb integrals and in no way involve exchange integrals. Therefore, the



total interelectronic repulsion included in the total molecular orbital energy, is approximately completely canceled by the total core repulsion of the atoms. Therefore,

$$E_{\pi b} = \sum_r \sum_s p_{rs} H_{rs} - n\alpha \quad \dots (9)$$

Here we have used the matrix elements of the simplified version of IOC- $\omega$  technique (inclusion of overlap charges in  $\omega$ -technique) described elsewhere.<sup>4,5</sup> Thus, we have used the following matrix elements:

$$H_{rr} = \alpha + \omega [1 - \frac{1}{2} \sum_s (p_{rs} S_{rs} + p_{sr} S_{sr})] \quad \dots (10)$$

$$\text{and } H_{rs} = \beta \quad \dots (11)$$

Combining Eqs. (9), (10) and (11), we get the following expression for the  $\pi$ -bonding energy,

$$E_{\pi b} = - [\omega \sum_r q_r (1 - q_r) - \omega S \sum_r \sum_{s \neq r} q_r p_{rs} + 2\beta \sum_{r < s} \sum p_{rs}] \quad \dots (12)$$

### 3. Values of Various Parameters

Parameters  $\omega$  and  $\beta$  have been empirically adjusted and their values were found to be  $-1.3$  and  $-1.5$  eV, respectively. For  $S$ , we have used its most extensively used value, i.e.  $0.25$ . Parameters  $A_0$  and  $A_1$  appearing in Eq. (4) have been adjusted with reference to the resonance energies of azulene and fulvene as calculated by Dewar and de Llano.<sup>6</sup> Thus we have used  $A_0 = -1.501$  and  $A_1 = +1.142$ .

### 4. Discussion

The immediate advantage of defining the resonance energy with Eq. (1) is that both the magnitude and sign of the resonance energy can serve as a criterion of aromaticity. If an unsaturated molecule has a negative resonance energy when the bond lengths in it are equal, it is clear that in its equilibrium configuration the bond lengths must alternate. Such a molecule will not be aromatic and it will

Table 1—Comparison of Calculated Empirical Resonance Energies ( $E_R$ ) of Some Non-Alternant Hydrocarbons

Compound *	$E_b$	Calculated $E_R$ values in eV					
		Present method	Hückel <sup>12</sup>	Pople <sup>12</sup>	SPO <sup>12</sup>	Dewar <sup>6</sup>	Hess (jr) <sup>9</sup>
Azulene I	15.538	+0.169	+2.058	+1.365	+1.206	+0.169	+0.231
Acenaphthylene II	19.448	+0.718	—	—	—	+1.335	+0.473
Fluoranthene III	26.614	+1.531	—	—	—	+2.141	—
Fulvene IV	9.056	+0.047	+0.894	+0.136	+0.437	+0.047	-0.01
Pentalene V	12.168	-0.199	+1.427	+0.735	+0.773	+0.007	-0.141
Heptalene VI	17.850	-0.521	+2.170	+0.826	+0.851	+0.094	-0.050
Heptafulvene VII	11.668	-0.334	+1.223	+0.154	+0.517	—	-9.02
Pyracylene VIII	22.835	+0.744	—	—	—	—	+0.254
Fulvalene IX	14.408	-0.951	+1.610	+0.694	+0.986	—	-0.33
s-Indacene X	18.869	+1.281	—	—	—	—	+0.11
as-Indacene XI	18.449	+0.861	—	—	—	—	—
Methyl cyclopropene XII	5.632	-0.362	—	—	—	—	—
6-Vinyl-fulvene XIII	11.687	-0.321	—	—	—	—	—
2,3-Benzfulvene XIV	15.123	-0.246	—	—	—	—	—
1,2-Benzfulvene XV	15.688	+0.319	—	—	—	—	—
Dibenzfulvene XVI	22.535	+0.803	—	—	—	—	—
Vinyldibenz fulvene XVII	25.550	+0.816	—	—	—	—	—
Heptafulvalene XVIII	21.056	-0.317	—	—	—	—	—
Sesquiifulvalene XIX	18.460	+0.089	—	—	—	—	—
Fulvadiene XX	18.600	+0.229	—	—	—	—	—
1,2,4,5-Dibenzpentalene XXI	25.950	+0.857	—	—	—	—	—
1,2,5,6-Dibenzpentalene XXII	25.524	+0.431	—	—	—	—	—
Acepleiadylene XXIII	26.474	+1.381	—	—	—	—	—
Di-biphenylene ethylene XXIV	42.889	+2.068	—	—	—	—	—

\* The Roman numerals given by the side of the name of the compound refer to its chemical structure as given in Fig. 1



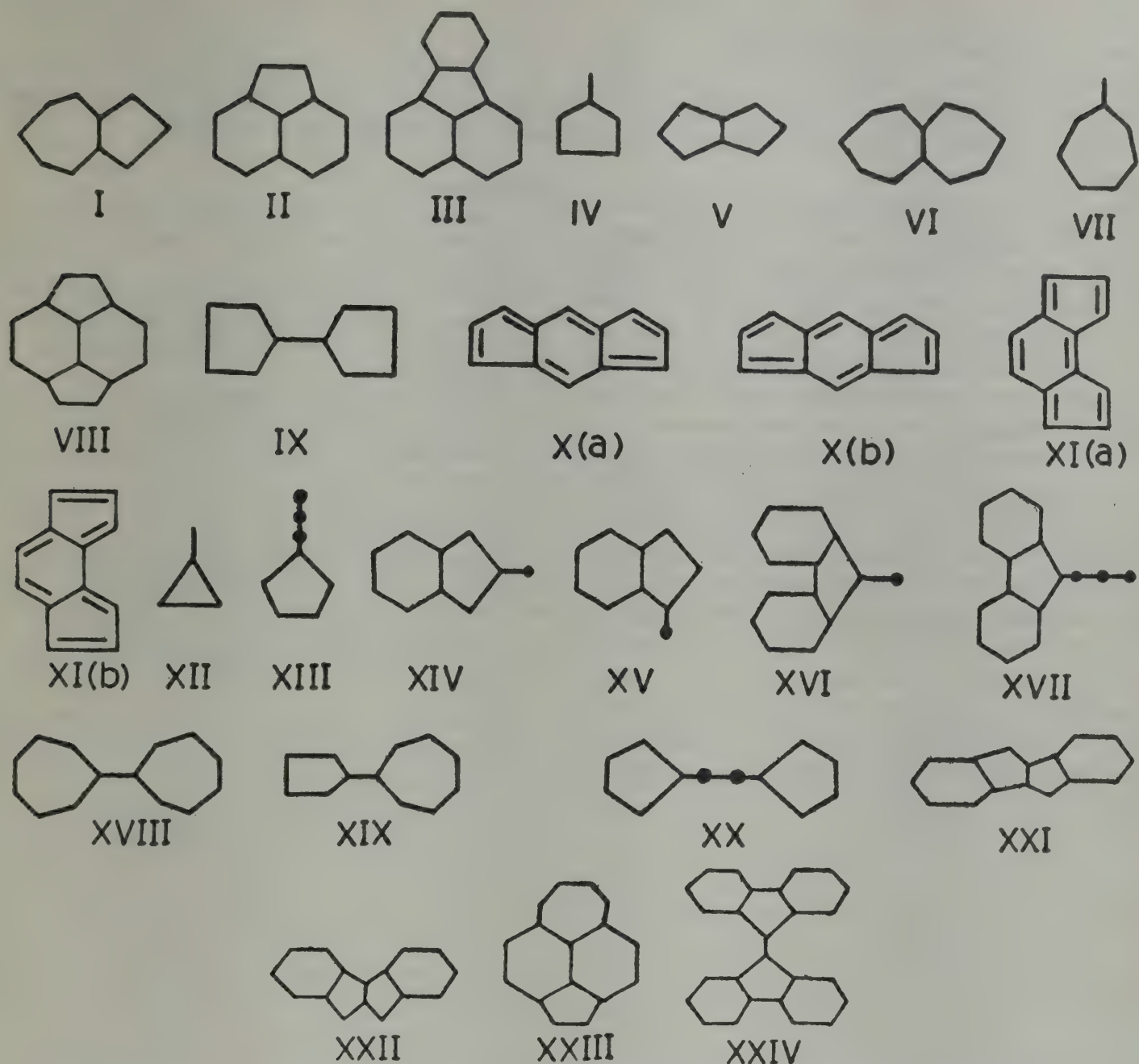


Fig. 1—Structures of molecules studied [The Roman numerals indicate the compound as given in Table 1]

resist attempts to force it into a coplanar geometry. If on the other hand, an unsaturated molecule has a positive resonance energy of reasonable magnitude, it should tend to be coplanar and is likely to favour a structure with equal bond lengths; such a molecule should show aromatic properties.

Among the many non-benzenoid hydrocarbons<sup>7</sup> fulvene (IV), pentalene (V), heptalene (VI), heptafulvene (VII), heptafulvalene (XVIII), etc. have been found directly or indirectly to be non-aromatic and to possess alternating C—C single and C=C double bonds. Also azulene (I), acenaphthylene (II), fluoranthene (III), pyracylene (VIII), acepleiadylene (XIII), etc. have been predicted to be aromatic on the basis of either  $4n + 2$  rule of Hückel or Craig's rule<sup>8</sup> or both.

From a close examination of Table 1 comparing values of  $E_R$  calculated by different procedures, it

can be said that although they assign lower resonance energies to non-benzenoid hydrocarbons than their benzenoid counterparts, all the previous methods employed by Hückel, Pople and also the SPO method, incorrectly predict that the non-benzenoid hydrocarbons should all be aromatic. Only recent calculations by Dewar and de Llano,<sup>6</sup> and by Hess (jr)<sup>9</sup> have been able to predict the differences somewhat correctly.

The success of our method lies in the fact that it assigns negative resonance energies to some known anti-aromatic non-alternants and also successfully assigns positive resonance energies to those non-alternant hydrocarbons which are known to be aromatic. Further, the higher resonance energy of s-indacene (X) (1.281 eV) than that of as-indacene (XI) (0.861 eV) show that s-indacene is more stable than its as-isomer, a result which can be explained



qualitatively in terms of the simplest 'resonance' concepts. s-Indacene has two equivalent most stable contributing structures X(a) and X(b) as does benzene. On the other hand, the two most stable contributing structures XI (a) and XI (b) for as-indacene are not equivalent.

There is in fact, no quantitative experimental measure of 'aromaticity'. There is only a qualitative idea that aromatic compounds should be unusually stable, and that typically they should undergo substitution rather than addition. We observe, that in fact compounds with positive resonance energies are stable and do react by electrophilic substitution. Compounds with negative resonance energy usually have not been synthesized or exist only fleetingly. We can elaborate this point with some specific examples. pentalene and fulvalene should be highly unstable or anti-aromatic due to their large negative resonance energies. In fact, pentalene has never been prepared despite many attempts.<sup>8</sup> Fulvalene has been prepared in dilute solution but all attempts to isolate it have led to a polymer, attesting to its high degree of unstability.<sup>10</sup> Fulvene has been isolated but undergoes polymerization readily.<sup>11</sup> Heptafulvene has also been prepared but it is too reactive to be

isolated.<sup>10</sup> Hence neither fulvene nor heptafulvene is least aromatic in its chemical behaviour.

Therefore, it can be said that our calculated resonance energy values are qualitatively in excellent agreement with the observed facts.

# References

1. Hückel E, *Z. phys. Chem.*, **70** (1931), 204.
2. Mulliken R S & Parr R G, *J. chem. Phys.*, **19** (1951), 1271.
3. Dewar M J S, *The molecular orbital theory of organic chemistry* (McGraw Hill, New York) 1969, 167.
4. Srivastava A K & Krishna B, *Indian J. pure appl. Phys.*, **10** (1972), 481.
5. Srivastava A K & Krishna B, *Indian J. pure appl. Phys.*, **11** (1973), 354, 356.
6. Dewar M J S & de Llano C J. *Am. Chem. Soc.*, **91** (1969), 789.
7. Streitwieser (Jr) A, *Molecular orbital theory for organic chemists*, (John Wiley, New York), 1961.
8. Badger G M, *Aromatic character and aromaticity* (Cambridge University Press, New York), 1969.
9. Hess (Jr) B A & Schaad L J, *J. Am. Chem. Soc.*, **93** (1971), 305, 2413; *J. Org. Chem.*, **36** (1971), 3418.
10. Doering W Von, *Theor. Org. Chem. Pap. Kekula Symp.*, (1958), 59, 35.
11. Thiec J & Wiemann J, *Bull. Soc. Chem.*, (1956), 177.
12. Dewar M J S & Chung A L H, *J. chem. Phys.*, **42** (1965), 756.



## Effect of Ion Diffusion from Double Layer Capacitors on rf Conduction in Polar Liquids

R GHOSH & IRA CHAUDHURY

Department of Physics, North Bengal University, Darjeeling

*Received 4 June 1979; revised received 15 December 1979*

A low dc field from storage batteries has been applied across the pair of electrodes of a dielectric cell containing polar liquids such as acetone, methyl-ethyl ketone, *n*-butyl alcohol and iso-amyl alcohol. Observation of temporal variation of current was continued till a final saturation value was reached, signifying the accumulation of free ions near electrodes and thus creating electrical double layers. After this, the variation of rf conductivity (at 400 kHz) of the liquids with time caused by diffusion of ions from the double layer charge capacitors were observed. From the extrapolation of the curves of rf conductivity versus time, the conductivity due to displacement current only were obtained for different liquids. Using expressions derived from the Debye theory in conjunction with experimental data, the values of dielectric loss, relaxation time, molecular radius, mobility and number density of active and natural ions present in the liquids were calculated. The values agree fairly well with the literature values.

### 1. Introduction

A dielectric liquid should not give any ionic conduction, but due to the dissociation of chemical impurity molecules into ion pairs, an organic dielectric liquid shows an apparent dielectric loss and specially at low rf field, a significant dielectric conduction loss is observed in organic polar liquids. Traces of moisture have a great influence on the value of conduction not only because water itself is a conducting species, but also because it will almost invariably increase the concentration of ions in the medium. In addition to this, the current carrier ions may also be produced by cosmic rays, natural radioactivity, thermal dissociation and also by the  $\pi$ -electrons emitted from the electrode surface. But the magnitude of the ions produced by such background effects is extremely low in comparison to that of the ions created due to dissociation of chemical impurities; the magnitude of the latter is of the order of  $10^{12}$ - $10^{13}$  ions/cc. Adamezewski<sup>1</sup> measured the self-conduction of current of highly purified hexane (conductivity  $10^{-19}$  ohm<sup>-1</sup> cm<sup>-1</sup>) and estimated that about 420 ions/cc are produced due to the influence of cosmic rays. Evidence for the existence of free ions in both polar and non-polar dielectric liquids has been reported by various workers.<sup>2-5</sup> Assuming the existence of ions in polar dielectric liquids, Sen and Ghosh<sup>4</sup> gave a theoretical expression for the rf conductivity which explains the weak electrolytic behaviour of polar dielectric liquids in a low rf field. It has been observed that

by the application of a dc field across the pair of electrodes of a cell containing a polar liquid, the initial current gradually decreases with time to a minimum steady value and the decay of current as assumed by Gemant<sup>6</sup> and Sen and Ghosh<sup>7</sup> is due to the accumulation of free ions near the surface of the electrodes thereby forming a charge condenser close to the electrodes. The present investigation has been undertaken to determine the variation of rf conductivity with the ion density in the liquid and thereby to get further information regarding the properties of polar dielectric liquids.

### 2. Experimental Arrangement

The experimental arrangements made for measuring the rf conductivity at 400 kHz range has been described in detail in one of the authors' previous papers.<sup>8</sup> The only extra arrangement added is a low dc field from a storage battery of 45V applied across the pair of electrodes of the dielectric cell. The cell was made up of pyrex glass tube of diameter 2 cm with a pair of circular brass electrodes of diameter 1.2 cm separated by a distance of 0.89 cm. Before filling the dielectric liquids, the glass cell was first cleaned with chromic acid, then with distilled water and lastly with benzene. The liquids under investigation such as acetone, methyl ethyl ketone, butyl and amyl alcohols were all of AnalaR grade obtained from M/s BDH, London. The viscosities of the liquids were measured using an Ostwald viscometer.



### 3. Results and Discussion

A low dc field from storage batteries was applied across the pair of electrodes of the dielectric cell containing polar dielectric liquid and a temporal variation of current was observed. The final saturated current signifies that all the free ions present in the liquid dielectric have accumulated near the surface of the electrodes, thus forming a pair of charge capacitors. At that particular stage, the dc field was switched off and an rf field of 400 kHz was applied across the electrodes and the temporal variation of resonant current was recorded till the value of resonant current reaches a saturation value. The diffusion of ions from the double layer charge capacitors is responsible for the variation of rf conductivity of the liquid. The maximum absorption current or the maximum rf conductivity  $K'_{\max}$  indicates that almost all the active ions are in diffusion through the liquid. The extremely low value of rf conductivity  $K'_{\min}$  obtained from the extrapolation of the curve rf conductivity  $K'$  against time  $t$  shown in Fig. 1 indicates that under this condition almost all the free active ions present in the liquid have accumulated near the surface of the electrode, thereby making the liquid resistivity extremely high. Under such conditions, the liquid behaves like a perfect dielectric, and therefore, the extrapolated conductivity value  $K'_{\min}$  has been assumed to be due to capacitive or displacement current only. The dielectric loss under such conditions could be expressed as  $\epsilon''_d = 2K'_{\min}/f$  and that of ionic conduction region  $\epsilon''_c = 2K'_{\max}/f$  where  $K'_{\min}$  and  $K'_{\max}$  are the minimum and maximum rf conductivities respectively in esu and  $f$  is the applied frequency. The di-

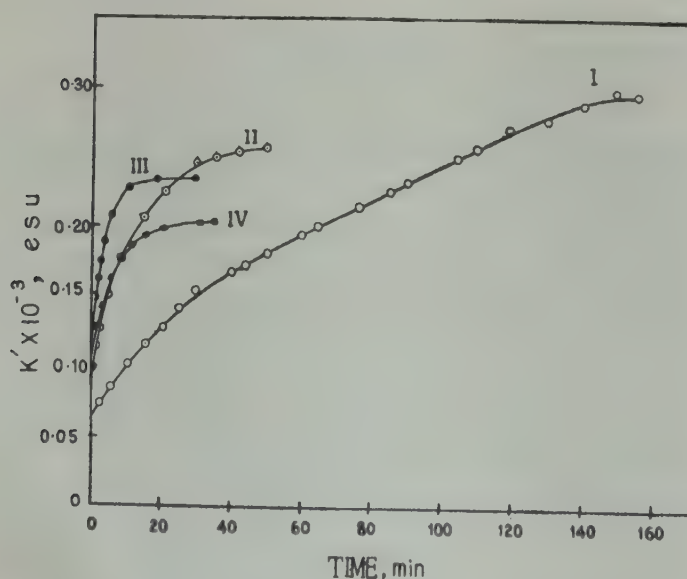


Fig. 1—Variation of rf conductivity  $K'$  at 400 kHz with time  $t$  in different liquids [I, acetone; II, methyl ethyl ketone; III,  $n$ -butyl alcohol and IV, Iso-amyl alcohol]

electric relaxation time  $\tau_1$  of an electrostatically filtered liquid in which the percentage of free ion density present in the liquid is extremely small thereby making the liquid resistivity extremely high ( $>10^9$  ohm) has been calculated from the Debye<sup>9</sup> relation

$$\epsilon''_d = \frac{(\epsilon_0 - \epsilon_\infty) \omega \tau}{1 + \omega^2 \tau^2} \quad \dots(1)$$

where  $\epsilon_0$  is the static dielectric constant and  $\epsilon_\infty$ , the limiting value of  $\epsilon'$  on the high frequency side of the dipole dispersion region, i.e. when orientation polarization effects are negligible and  $\omega = 2\pi f$ . The relaxation times calculated from Eq. (1) are reported in Tables 1 and 2 and the values agree fairly well with the literature values of relaxation time in dilute solution. Further, it has been observed from Table 1 that the values of radius of the molecules ( $a_1$ ) obtained from Debye expression<sup>9</sup>

$$\tau = \frac{4\pi a_1^3 \eta}{kT} \quad \dots(2)$$

are lower in comparison to those calculated from the volume determined according to the kinetic theory. The present experiment shows that the nature of variation of conductivity for a polar dielectric liquid at low rf field at a particular temperature is electrolytic, and therefore, the conductivity may be expressed as

$$K' = Ne \mu \quad \dots(3)$$

Table 1—Values of Dielectric Loss, Relaxation time, Molecular Radius, Number of Free Ions/cc Ionic Mobility and Viscosity of the Liquids (Applied frequency 400 kHz and Temperature 23°C)

Pure liquid	$\epsilon''_d \times 10^4$	$\tau_1 \times 10^{12}$ , sec.	$a_1 \times 10^8$ , cm (Debye)	$\epsilon''_c \times 10^3$	$\tau_2 \times 10^{10}$ , sec	$a \times 10^8$ , cm	$\mu \times 10^4$ , cm <sup>2</sup> V <sup>-1</sup> Sec <sup>-1</sup>	$N \times 10^{13}$ , ion/cc	$N_0 \times 10^{13}$ , ion/cc (from extrapolation)	$\eta \times 10^3$ , cP
Acetone (C <sub>3</sub> H <sub>6</sub> O)	3.37	6.6	1.94	1.5	2.38	3.07	1.03	2.1	2.0	0.32
Methyl ethyl ketone (C <sub>4</sub> H <sub>8</sub> O)	4.3	10.07	2.01	1.3	2.808	3.28	1.00	1.8	4.0	0.4
$n$ -Butyl alcohol (C <sub>4</sub> H <sub>9</sub> OH)	5.5	14.45	1.14	1.10	2.7	3.3	1.01	1.56	10.0	3.2
Iso-amyl alcohol (C <sub>5</sub> H <sub>11</sub> OH)	6.0	15.7	1.20	1.05	8.175	3.5	0.383	3.78	30.0	4.33



Table 2—Values of Relaxation Time in Polar Liquids (Experimental and Literature Values)

Polar liquid	$\tau_1, 10^{-12}$ sec		$\tau_2, 10^{-10}$ sec	
	Exptl. at 23°C	Literature in dilute solution	Exptl. at 23°C	Literature Pure liquid
Acetone	6.6	3.3 at 19°C (Ref. 10)	2.38	2.227 at 31°C (Ref. 12)
Methyl ethyl ketone	10.07	2.16 at 20°C (Ref. 11)	2.808	2.473 at 31°C (Ref. 12)
n-Butyl alcohol	14.45	—	2.7	6.4 at 19°C (Ref. 10)
Iso-amyl alcohol	15.7	—	8.17	10.0 at 19°C (Ref. 10)

where  $N$  is the charge density,  $e$  the electronic charge and  $\mu$  the mobility of the ions. The ion density  $N$  of iso-amyl alcohol has been calculated from the slope of the linear curve of  $K'_c$  versus  $1/\eta$  (Sen and Gosh<sup>4</sup>),  $\eta$  being the viscosity of the liquid, the slope of the curve is given by  $Ne^2/6\pi a$ . The ion densities of acetone, methyl ethyl ketone and  $n$ -butyl alcohol have also been calculated by the above mentioned procedure. The mobility of acetone, methyl ethyl ketone,  $n$ -butyl alcohol and iso-amyl alcohol have been calculated from Eq. (3) and are presented in Table 1.

Eq. (1) does not take into consideration the presence of free ions. Therefore, in the absence of any other expression which takes this aspect into consideration, the relaxation time  $\tau_2$  of a liquid having free ions has been calculated from the following expression developed from the Einstein-Stokes' relation:

$$\frac{D\eta}{T} = \frac{k}{6\pi a} \quad \dots(4)$$

where  $D$  is the diffusion constant,  $\eta$  the viscosity,  $a$  the radius of the molecule,  $k$  the Boltzmann's constant and  $T$  the temperature in K. On analyzing Eq. (4) and considering  $\eta = \tau_2 kT/4\pi a^3$  and  $D = \mu kT/e$  we get

$$\tau_2 = \frac{2a^2 e}{3\mu kT} \quad \dots(5)$$

where  $\tau_2$  is the dielectric relaxation time of the liquid  $e$  the electronic charge and  $\mu$  the mobility of the ions. Eq. (5) is similar to the relation given by Hasted.<sup>13-14</sup> The relaxation times  $\tau_2$  calculated from Eq. (5) are presented in Tables 1 and 2, values of which agree fairly well with the literature values.

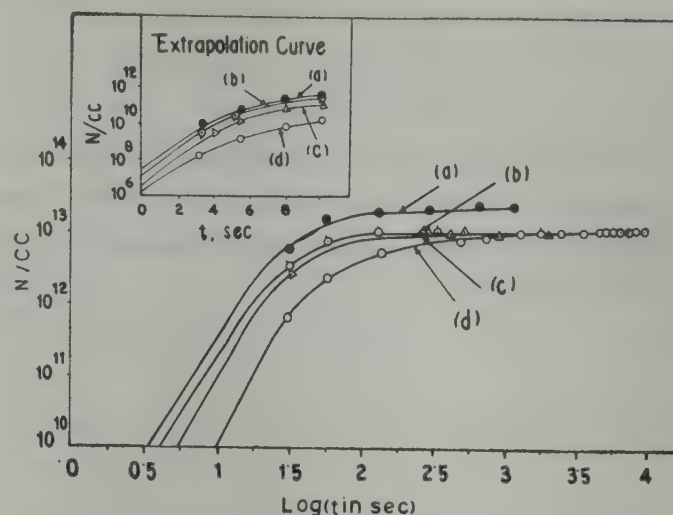


Fig. 2—Variation of number density of ions ( $N/cc$ ) with  $\log t$ . Inset: Extrapolation curve of  $N/cc$  against time  $t$  in sec. [(a) iso-amyl alcohol, (b)  $n$ -butyl alcohol, (c) methyl ethyl ketone and (d) acetone]

The high values of  $\tau_2$  indicate that the rotation of dipole is hindered by the interionic forces and further  $\tau_1$  and  $\tau_2$  clearly show that the relaxation times in polar liquids increases with the number of carbon atoms in the molecule. Moreover from Table 1, it is observed that dielectric loss due to orientation of molecules, i.e.  $\epsilon''_d$  increases with the number of carbon atoms in the molecules whereas the dielectric loss due to ionic conduction ( $\epsilon''_c$ ) decreases with number of carbon atoms. It is further observed from Fig. 2 that the variation of ion density  $N$  with  $\log t$  (in sec) shows that free ions ( $\sim 10^6$  ion/cc) are always present in a liquid. To estimate the presence of natural ions and the degree of imperfection of polar dielectric liquids some experiments are in progress in this laboratory and the results will be reported in subsequent communications.

#### Acknowledgement

The authors are indebted to Prof. S N Sen, the Head of the Department of Physics, for helpful discussions and suggestions during the progress of the work. One of them (IC) is grateful to the University Grants Commission, New Delhi, and the Department of Physics, North Bengal University, for the award of a Teacher Fellowship under the Faculty Improvement Programme.

#### References

1. Adamezewski I, *Ionization conduction and breakdown in dielectric liquids* (Taylor and Francis, London), 1969.
2. Jachym A & Jachym B, *Acta Phys. Polon.*, 31 (1967), 733.
3. Prabhakar Rao P & Govinda Raju G R, *J. Phys.*, D3 (1970), 341.



4. Sen S N & Ghosh R, *J. phys. Soc. Japan*, 36 (1974), 743.
5. Lohneysen H V & Nagerl H, *J. Phys.*, D4 (1971), 1781.
6. Gemant A, *Phys. Rev.*, 58 (1940), 904.
7. Sen S N & Ghosh R, *J. phys. Soc. Japan*, 38 (1975), 1445.
8. Sen S N & Ghosh R, *J. phys. Soc. Japan*, 33 (1972), 838.
9. Debye P, *Polar molecules* (Chemical Catalogue Co., New York), 1929.
10. Bottcher C J F, *Theory of electric polarization* (Elsevier, New York), 1952, 391, 383.
11. Curtis A J, McGreer P L, Rathmann G B & Smyth C P, *J. Am. chem. Soc.*, 74 (1952), 644.
12. Sen S N, *Indian J. Phys.*, 1 (1951), 25.
13. Hasted J B, *Aqueous dielectric* (Chapman Hall, London), 1973, 173.
14. Choudhury I & Ghosh R, *Bull. Chem. Soc. Japan*, 1979, in Press.



## Reflection & Transmission of Ion Acoustic Soliton at a Plasma Interface

S R SHARMA

Department of Physics, University of Rajasthan, Jaipur 302 004

&

R S TIWARI

Muslim Higher Secondary School, Jaipur, Rajasthan

Reflection and transmission properties of an ion acoustic soliton incident on a plane boundary separating two different semi-infinite plasmas are considered. It is found that a soliton is reflected with reduced-amplitude if  $\beta > 1$ , where  $\beta$  is the ratio of ion sound speeds in the first and the second medium. The number of transmitted solitons is one or more according as  $\beta \geq 1$  or  $< 1$ . The energy and momentum conservations are checked, before and after the soliton hits the interface.

### 1. Introduction

In recent years, a great deal of interest has been shown in the study of weakly dispersive nonlinear wave phenomena governed by  $KdV$  equation. This equation arises in a variety of situations, for example, in the study of water waves, anharmonic lattice, nonlinear optics, plasmas, etc. Washimi and Taniuti<sup>1</sup> showed that weakly nonlinear ion acoustic waves are governed by  $KdV$  equation. It has been demonstrated<sup>2</sup> that in the bounded stationary solutions, solitons retain their characteristics even after collisions with other solitons. The existence and properties of ion acoustic solitons in plasmas were experimentally verified by Ikezi *et al.*<sup>3</sup> and Ikezi.<sup>4</sup>

Experimental<sup>5</sup> and theoretical<sup>6,7</sup> studies on the propagation of ion acoustic solitary waves in a weakly inhomogeneous plasma with weak density gradient (with scale size many times the width of the soliton) have shown that the waves are able to retain their stationary structure by readjusting their amplitude and speed to match the slowly changing dispersion. However, little attention has been paid on the reflection and transmission of solitons from plasma interface. Recently, experimental reports of studies using double plasma machines have been made. In these studies, reflection and transmission of ion acoustic solitons from sharp density gradients have been investigated. In these experiments,<sup>8</sup> scale size of the density gradient is smaller than the width of the soliton. However, theories on propagation of ion acoustic solitary waves in sharp density gradients in gaseous plasmas do not exist. Recently some authors<sup>9,10</sup> have considered this problem for lattice solitons. The object of the present paper is (i) to

study the problem of reflection and transmission of an ion acoustic soliton from a plasma interface, and (ii) to examine the conservations of momentum and energy in this process.

### 2. Formulation of Problem

We consider the problem of reflection and transmission of a soliton from the boundary at  $x = 0$ , separating the two plasmas having different densities, ion masses, and electron temperatures. For the sake of equilibrium of the boundary, we assume that equilibrium pressure is same on the two sides. We consider one-dimensional collision-free plasma. The continuity and momentum equations for cold ion species are:

$$\frac{\partial N_j}{\partial t} + \frac{\partial}{\partial x} (N_j u_j) = 0 \quad \dots(1)$$

$$\frac{\partial u_j}{\partial t} + u_j \frac{\partial u_j}{\partial x} = - \frac{e}{M_j} \frac{\partial \phi_j}{\partial x} \quad \dots(2)$$

Making the usual approximation of ignoring the electron inertia, the momentum transport equation for isothermal electrons takes the form

$$\frac{\partial n_j}{\partial x} = - \frac{e}{T_j} n_j \frac{\partial \phi_j}{\partial x} \quad \dots(3)$$

The set of basic equations is completed by the Poisson's equation

$$\frac{\partial^2 \phi_j}{\partial x^2} = - 4\pi e(N_j - n_j) \quad \dots(4)$$

Here  $j = 1$  and  $2$  correspond to the quantity belonging to the plasma on the left and on the right of the interface at  $x = 0$ , respectively.  $N_j$ ,  $u_j$  and  $m_j$  are the density, fluid velocity, and mass of ion



species.  $n_j$  and  $T_j$  are the electron density and temperature of electrons, and  $\phi_j$  is the electric potential. It is convenient to define

$$\xi = \epsilon^{1/2} x, \tau_1 = \epsilon^{1/2} t, \tau_2 = \epsilon^{3/2} t \quad \dots(5)$$

where  $\epsilon$  is a small parameter.

We use the reductive perturbation method,<sup>1</sup> and expand  $N_j, n_j, \phi_j$  and  $u_j$  in powers of  $\epsilon$  as

$$f = \sum_{l=0}^{\infty} \epsilon^l f^{(l)} \quad \dots(6)$$

where  $f^{(0)}, f^{(1)}, f^{(2)}, \dots$  are the equilibrium and higher order quantities.

Using Eqs. (1)-(6), and following the usual procedure, a set of equations belonging to different orders is obtained. Eliminating all other variables except  $u_j^{(1)}$  and  $N_j^{(1)}$ , the first order equations are

$$\frac{\partial u_j^{(1)}}{\partial \tau_1} + \frac{s_j^2}{N_j^{(0)}} \frac{\partial N_j^{(1)}}{\partial \xi} = 0 \quad \dots(7)$$

and

$$\frac{\partial N_j^{(1)}}{\partial \tau_1} + N_j^{(0)} \frac{\partial u_j^{(1)}}{\partial \xi} = 0 \quad \dots(8)$$

where  $s_{1,2} = (T_{1,2}/M_{1,2})^{1/2}$  is the ion sound speed in the left (right) semi-infinite plasma.

We are interested in the case of a soliton incident on the interface from the left resulting in reflected and/or transmitted solitons with or without residual ripples. For this study, it is convenient to introduce the following variables:

$$\left. \begin{aligned} \xi_1 &= \xi - s_1 \tau_1 + \epsilon \theta_1(\xi_1, \xi_2, \tau_2) \\ \xi_2 &= \xi + s_1 \tau_1 + \epsilon \theta_2(\xi_1, \xi_2, \tau_2) \end{aligned} \right\} \quad \dots(9)$$

for  $\xi < 0$

$$\text{and } \eta = \xi - s_2 \tau_1 \quad \text{for } \xi > 0 \quad \dots(10)$$

where  $\theta_1$  and  $\theta_2$  are arbitrary functions of  $\xi_1, \xi_2$  and  $\tau_2$  and have been introduced to take care of any possible phase shifts which may arise due to mutual interaction at the interface. Using Eq. (9), we see that Eqs. (7) and (8) admit linear superposition of function of  $\xi_1$  and  $\xi_2$  for  $\xi < 0$ . Hence we write

$$N_1^{(1)} = N_1^{(0)} [\psi_i(\xi_1, \tau_2) + \psi_r(\xi_2, \tau_2)] \quad \dots(11a)$$

$$u_1^{(1)} = s_1 [\psi_i(\xi_1, \tau_2) - \psi_r(\xi_2, \tau_2)] \quad \dots(11b)$$

For  $\xi > 0$ , we use Eq. (10) in Eqs. (7) and (8). Since there is only the out-going wave in this region, so we write

$$N_2^{(1)} = N_2^{(0)} \psi_t(\eta, \tau_2) \quad \dots(12a)$$

$$u_2^{(1)} = s_2 \psi_t(\eta, \tau_2) \quad \dots(12b)$$

where  $\psi_i(\xi_1, \tau_2)$ ,  $\psi_r(\xi_2, \tau_2)$  and  $\psi_t(\eta, \tau_2)$  represents the incident, reflected, and transmitted waves moving with velocity  $s_1, -s_1$  and  $s_2$ , respectively.

We eliminate  $u_1^{(1)}, \phi_1^{(1)}$  and  $n_1^{(1)}$  from the second order equations and obtain the following equation for region  $\xi < 0$ :

$$\begin{aligned} & \frac{1}{N_1^{(0)}} \left( \frac{\partial^2}{\partial \xi_1 \partial \xi_2} (N_1^{(2)} - \psi_i \psi_r) \right. \\ & + \frac{1}{2} \frac{\partial}{\partial \xi_1} \left( \frac{1}{s_1} \frac{\partial \psi_i}{\partial \tau_2} + \psi_i \frac{\partial \psi_i}{\partial \xi_1} \right. \\ & + \frac{T_1}{8\pi e^2 N_1^{(0)}} \frac{\partial^3 \psi}{\partial \xi_1^3} \left. \right) - \frac{1}{2} \frac{\partial}{\partial \xi_2} \left( \frac{1}{s_1} \frac{\partial \psi_r}{\partial \tau_2} \right. \\ & - \psi_r \frac{\partial \psi_r}{\partial \xi_2} - \frac{T_1}{8\pi e^2 N_1^{(0)}} \frac{\partial^3 \psi_r}{\partial \xi_2^3} \left. \right) \\ & + \frac{\partial}{\partial \xi_1} \left[ \left( \frac{\partial \theta_1}{\partial \xi_2} - \frac{\psi_r}{2} \right) \frac{\partial \psi_i}{\partial \xi_1} \right] \\ & + \frac{\partial}{\partial \xi_2} \left[ \left( \frac{\partial \theta_2}{\partial \xi_1} - \frac{\psi_i}{2} \right) \frac{\partial \psi_r}{\partial \xi_2} \right] = 0 \quad \dots(13) \end{aligned}$$

where we have used  $\xi_1, \xi_2, \tau_2$  instead of  $\xi, \tau_1, \tau_2$  as variables and have also made use of Eq. (11). We further assume that the phase shifts  $\theta_1$  and  $\theta_2$  are determined by

$$\frac{\partial \theta_1}{\partial \xi_2} - \frac{\psi_r}{2} = 0 \quad \dots(14a)$$

and

$$\frac{\partial \theta_2}{\partial \xi_1} - \frac{\psi_i}{2} = 0 \quad \dots(14b)$$

From the condition of non-secularity of the solution of  $N_1^{(2)}$ , we require that

$$\begin{aligned} & \frac{1}{s_1} \frac{\partial \psi_i}{\partial \tau_2} + \psi_i \frac{\partial \psi_i}{\partial \xi_1} \\ & + \frac{T_1}{8\pi e^2 N_1^{(0)}} \frac{\partial^3 \psi_i}{\partial \xi_1^3} = 0 \quad \dots(15a) \end{aligned}$$

and

$$\begin{aligned} & \frac{1}{s_1} \frac{\partial \psi_r}{\partial \tau_2} - \psi_r \frac{\partial \psi_r}{\partial \xi_2} \\ & - \frac{T_1}{8\pi e^2 N_1^{(0)}} \frac{\partial^3 \psi_r}{\partial \xi_2^3} = 0 \quad \dots(15b) \end{aligned}$$

Eqs. (15a) and (15b) represent the *KdV* equations for the incident and the reflected waves. Similarly for  $\xi > 0$  we obtain

$$\begin{aligned} & \frac{1}{N_2^{(0)}} \left( \frac{\partial^2}{\partial \tau_1^2} - s_2^2 \frac{\partial^2}{\partial \xi^2} \right) N_2^{(2)} \\ & = 2 \frac{\partial}{\partial \eta} \left( \frac{1}{s_2} \frac{\partial \psi_t}{\partial \tau_2} + \psi_t \frac{\partial \psi_t}{\partial \eta} \right. \\ & + \frac{T_2}{8\pi e^2 N_2^{(0)}} \frac{\partial^3 \psi_t}{\partial \eta^3} \left. \right) \end{aligned}$$



In order that the  $N^{(2)}$  be bounded, we must have

$$\frac{1}{s_2} \frac{\partial \psi_i}{\partial \tau_2} + \psi_i \frac{\partial \psi_i}{\partial \eta} + \frac{T_2}{8\pi e^2 N^{(0)}} \frac{\partial^3 \psi_i}{\partial \eta^3} = 0 \quad \dots(16)$$

which is the  $KdV$  equation for the transmitted waves.

### 3. Reflection and Transmission of Solitons

The boundary conditions require that the fluid velocity and pressure must be continuous across the interface at  $\xi = 0$ . Thus at  $\xi = 0$

$$\left. \begin{aligned} u^{(1)}_1 &= u^{(1)}_2 \\ P^{(1)}_1 &= P^{(1)}_2 \text{ or } n^{(1)}_1 = n^{(1)}_2 \end{aligned} \right\} \quad \dots(17)$$

where we have assumed the electrons to be isothermal. Using Eqs. (11) and (12), the boundary conditions lead to the following expressions at  $\xi = 0$

$$\psi_r(s_1 \tau_1 + \epsilon \theta_2, \tau_2) = \beta - 1/\beta + 1 \psi_i(-s_1 \tau_1 + \epsilon \theta_1, \tau_2)$$

$$\psi_i(-s_2 \tau_1, \tau_2) 2\beta/\beta + 1 \psi_i(-s_1 \tau_1 + \epsilon \theta_1, \tau_2)$$

where  $\beta = s_1/s_2 = (T_1 M_2/T_2 M_1)^{1/2}$

Neglecting the terms of order  $\epsilon$  in the arguments of  $\psi_i$  and  $\psi_r$ , these boundary conditions can be written in a useful form<sup>10</sup>

$$\psi_r(\xi_2, 0) = (\beta - 1)/(\beta + 1) \psi_i(-\xi_2, 0) \quad \dots(18a)$$

$$\psi_i(\eta, 0) = 2\beta/(\beta + 1) \psi_i(\beta \eta, 0) \quad \dots(18b)$$

Eqs. (18a) and (18b) can be treated as the initial waveforms for the reflected and transmitted waves respectively.

Let us assume that a soliton is incident on the interface from the left with velocity  $s_1(1 + \epsilon\sigma)$ . The incident soliton,  $\psi_i$ , is a function of  $\xi_+ = \epsilon^{1/2} [x - s_1(1 + \epsilon\sigma)t] = \xi_1 - \sigma s_1 \tau_2$ ; so that  $\psi_i(\xi_1, \tau_2) = \psi_i(\xi_+)$ . If we integrate Eq. (15a) with respect to  $\xi_+$  and impose the conditions that  $\psi_i(\xi_+)$  and its derivatives vanish at  $\xi_+ = \pm \infty$ . We get

$$\psi_i(\xi_1, 0) = 3 \sigma \operatorname{sech}^2 \left[ \left( \frac{\sigma}{4v_1} \right)^{1/2} (\xi_1 + \xi_0) \right] \quad \dots(19)$$

where  $v_1 = \frac{T_1}{8\pi N^{(0)} e^2}$ , and  $\xi_0$  is a constant.

Corresponding to incident soliton, the initial waveforms for the reflected and transmitted waves at the interface are given by Eqs. (18a) and (18b), respectively. From these initial values, the number of bounded states or soliton solutions can be determined by using the inverse scattering method.<sup>11</sup> Using this procedure<sup>10</sup> the amplitudes of the reflected and transmitted solitons can be easily determined and are given by the following expressions

$$\frac{A_r}{A_0} = \frac{1}{4} \left\{ \left[ 1 + \frac{8(\beta - 1)}{\beta + 1} \right]^{1/2} - 1 \right\}^2 \text{ for } \beta > 1$$

$$= 0 \quad \text{for } \beta \leq 1 \quad \dots(20)$$

$$\frac{A_{i_n}}{A_0} = \frac{\beta^2}{4} \left\{ \left[ 1 + \frac{16}{\beta(\beta + 1)} (T_1/T_2)^2 \right]^{1/2} - (2n - 1) \right\}^2 \quad (21)$$

provided

$$\left[ 1 + \frac{16}{\beta(\beta + 1)} (T_1/T_2)^2 \right]^{1/2} > (2n - 1) \quad \dots(22)$$

where  $n$  is a positive integer corresponding to the number of solitons which are formed in the transmitted part of the waveform and  $A_0 = \sigma/2v_1$  is the amplitude of the incident soliton.

### 4. Energy and Momentum Conservations

We shall now show that the energy and momentum of the incident soliton are conserved in the interaction giving rise to the reflected and transmitted waves. The basic Eqs. (1) to (4) describe a non-dissipative isothermal system and can be used to obtain

$$\frac{\partial \mathcal{E}}{\partial t} + \frac{\partial \mathcal{L}}{\partial x} = 0 \quad \dots(23)$$

where  $\mathcal{E} = \frac{1}{2} m_j N_j u_j^2 + \frac{1}{8\pi} \left( \frac{\partial \phi_j}{\partial x} \right)^2 + e n_j \phi_j - n_j T_j$  is the energy density and

$$\mathcal{L} = -\frac{1}{2} N_j N_j u_j^2 u_j + e n_j \phi_j u_j$$

is the energy flux vector.

Thus, the integral  $\int \mathcal{E} dx$  is conserved. Hence, within an additive constant, the total energy  $E$  of the system can be written as

$$E = \int_{-\infty}^{+\infty} \left\{ \frac{1}{2} m_j N_j u_j^2 + \frac{1}{8\pi} \left( \frac{\partial \phi_j}{\partial x} \right)^2 + e n_j \phi_j - n_j T_j \right\} dx \quad \dots(24)$$

Using Eqs. (5)-(6) we can expand the dependent variables in terms of  $\epsilon$  and obtain

$$E = \epsilon^{3/2} \int_{-\infty}^{+\infty} \left( \frac{1}{2} m_j N_j^{(0)} u_j^{(1)2} + e n_j^{(1)} \phi_j^{(1)} + e n_j^{(0)} \phi_j^{(2)} T_j \right) d\xi + \text{higher order terms} \quad (25)$$

Initially there is only the incident soliton, hence the initial energy of the system is

$$E_i = \epsilon^{3/2} N_1^{(0)} T_1 \int_{-\infty}^{+\infty} \psi_i^2(\xi, \tau_1) d\xi \quad \dots(26)$$



After the interaction, the energy of the system  $E_f$  is located in the reflected and transmitted waves moving away from the interface, hence

$$\begin{aligned} E_f &= E_r(\tau_2) + E_t(\tau_2) \\ &= \epsilon^{3/2} N_1^{(0)} T_1 \int_{-\infty}^{+\infty} \psi_r^2(\xi, \tau_2) d\xi + \epsilon^{3/2} N_2^{(0)} T_2 \int_{-\infty}^{+\infty} \psi_t^2(\xi, \tau_2) d\xi \\ &= \epsilon^{3/2} \int_{-\infty}^{+\infty} [N_1^{(0)} T_1 \psi_r^2(\xi, 0) + N_2^{(0)} T_2 \psi_t^2(\xi, 0)] d\xi = E_i \quad \dots(27) \end{aligned}$$

where use is made of Eq. (18) and the invariants of  $KdV$  equation

$$\frac{\partial E_r}{\partial \tau_2} = \frac{\partial E_t}{\partial \tau_2} = \frac{\partial E_i}{\partial \tau_2} = 0$$

This shows that the energies of reflected and transmitted waves are equal to the energy of the initial soliton. The momentum of incident soliton is given by

$$P_i = \epsilon^{1/2} \int_{-\infty}^{+\infty} m_1 N_1^{(0)} s_1 \psi_i(\xi, \tau_2) d\xi \quad \dots(28)$$

After the interaction, the reflected and transmitted waves are moving away from the interface. Hence the final momentum of the system is

$$\begin{aligned} P_f(\tau_2) &= -\epsilon^{1/2} m_1 s_1 N_1^{(0)} \int_{-\infty}^{+\infty} \psi_r(\xi, \tau_2) d\xi \\ &\quad + \epsilon^{1/2} m_2 s_2 N_2^{(0)} \int_{-\infty}^{+\infty} \psi_t(\xi, \tau_2) d\xi \\ &= P_i(0) \quad \dots(29) \end{aligned}$$

where use is again made of Eq. (18) and the invariants of  $KdV$  equation

$$\frac{\partial P_r}{\partial \tau_2} = \frac{\partial P_t}{\partial \tau_2} = \frac{\partial P_i}{\partial \tau_2} = 0$$

This shows that momentum of reflected and transmitted waves is equal to the incident soliton.

## 5. Discussion

Eq. (20) gives the ratio of the amplitude of the reflected and the incident soliton. It is seen that soliton is reflected only if  $\beta > 1$ , i.e. when the ion

sound speed in the first medium is greater than that in the second medium. Eqs. (20) to (22) have been derived for arbitrary values of  $\beta = s_1/s_2 = (T_1 M_2 / T_2 M_1)^{1/2}$ . In practice, it is difficult to have a sharp boundary separating plasmas of different electron temperatures. However, it is possible, e.g. using double plasma machines to generate two independent plasmas separated by sharp density gradients. Experiments<sup>8</sup> have also been reported on reflection and transmission of solitons from sharp density gradients. However, we could not compare the results with this experiment because of lack of required data and because of large absorption of the wave at the grid. In general, in the absence of collisions, a plasma has a large thermal conductivity. The heat conduction speed is of the order of electron thermal speed which, in general, is greater than the soliton speed. Hence special mechanism, e.g. use of magnetic field, etc. can be used to achieve an equilibrium with unequal temperatures. In such situations, the basic equations get modified and the present treatment is no longer applicable. However, if the two plasmas have different ion masses but equal electron temperatures and density, values of

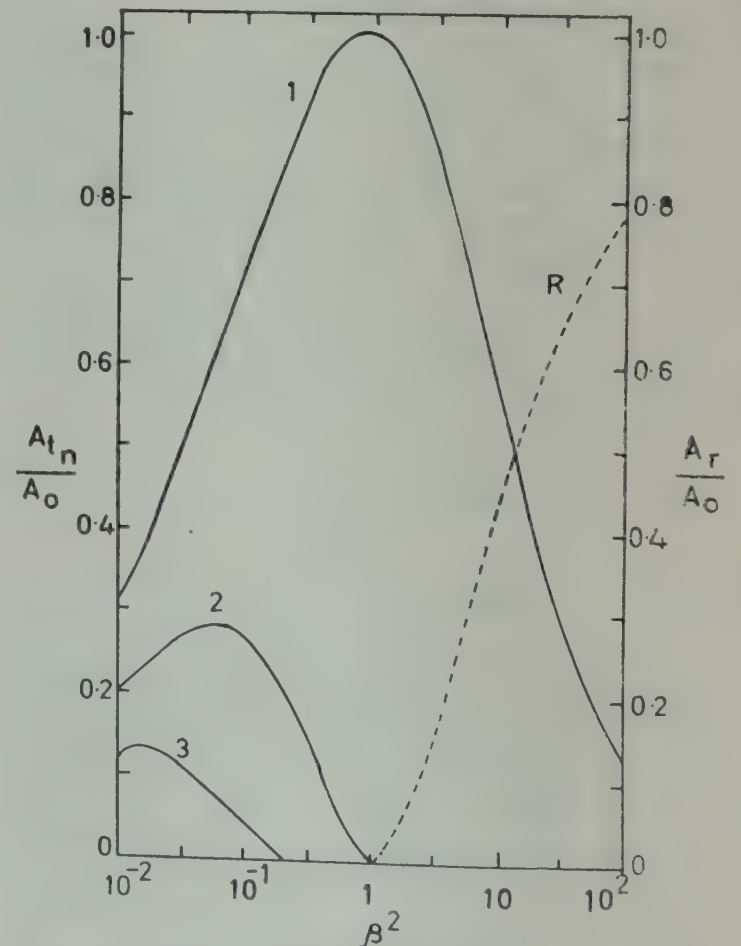


Fig. 1—Variation of the ratio of the amplitude of the reflected ( $A_r$ ) or transmitted ( $A_{tn}$ ) soliton to that of the incident ( $A_0$ ) soliton as a function of  $\beta^2$ . Curve  $R$  is for the reflected soliton and 1, 2, 3 ... refer to the transmitted solitons of decreasing amplitudes



$\beta$  different from unity can be achieved and we expect the present treatment to be applicable. Hence we assumed  $T_1 = T_2$  for the discussion of results. The ratio  $A_r/A_0$  is plotted in Fig. 1 for various values of  $\beta^2$ . The amplitude of the reflected soliton increases as  $\beta$  increases and it becomes equal to the amplitude of incident soliton as  $\beta \rightarrow \infty$ . This corresponds to the case of a reflection from a rigid surface and is also expected from physical considerations.

Eq. (21) gives the ratio of amplitudes of transmitted to incident soliton and Eq. (22) decides the number of solitons which are transmitted. It is noted that the number of transmitted soliton will be only one if  $\beta > 1$ . At  $\beta = 1$ , the incident soliton is simply transmitted. The number of transmitted solitons is more than one, if  $\beta < 1$ . In this case, there is no reflected soliton. The amplitudes of different transmitted solitons is given by Eq. (21) and are shown in Fig. 1. The amplitudes of the  $n$ th soliton arranged in order of decreasing amplitudes goes to zero when

$$\beta = 1/2 \left[ -1 + \{1 + 64/[(2n-1)^2 - 1]\}^{1/2} \right] \dots (30)$$

### Acknowledgement

One of the authors (RST) is thankful to the Secretary and Management Committee of Muslim H S School, Jaipur, for their active interest and encouragement.

### References

1. Washimi H & Taniuti T, *Phys. Rev. Lett.*, 17 (1966), 996.
2. Zabusky N J & Krushal M D, *Phys. Rev. Lett.*, 15 (1965), 240.
3. Ikezi H, Taylor R J & Backer R D, *Phys. Rev. Lett.*, 25 (1970), 11.
4. Ikezi H, *Phys. Fluids*, 16 (1973), 1668.
5. John P I & Saxena P C, *Physics Lett.*, 56A (1976), 386.
6. Nishikawa K & Kaw P K, *Physics Lett.*, 50A (1975), 455.
7. Goswami B N & Sinha M, *Pramana*, 7 (1976), 141.
8. Dahiya R P, John P I & Saxena Y C, *Physics Lett.*, 65A (1978), 323.
9. Yoshida F, Nakayama T & Sakuma T, *J. phys. Soc. Japan*, 40 (1976), 901; Yoshida F & Sakuma T, *J. phys. Soc. Japan*, 42 (1977), 1412.
10. Yajima N, *Progress of theoretical physics*, 58 (1977), 1114.
11. Gardner G S, Green J M, Krushal M D & Muira R M, *Phys. Rev. Lett.*, 19 (1967), 1095.



## Dipole Pomeron & Neutron-Proton Elastic Scattering between 70 & 400 GeV/c

MOHAMMAD SALEEM & FAZAL-E-ALEEM

Department of Physics, Punjab University, Lahore, Pakistan

Received 28 January 1980

The most recent measurements of the differential and total cross-sections of neutron-proton elastic scattering from 70 to 400 GeV/c have been explained by using dipole pomeron model. The predictions are also made regarding the energy dependence of dip and bump structure in angular distribution.

### 1. Introduction

Neutron-proton elastic scattering cross-sections at various momenta have been measured in several experiments. Gibbard *et al.*<sup>1</sup> showed that the np cross-sections were similar to existing pp data over the range of the incident laboratory momentum  $p_L$  from 5 to 30 GeV/c for  $0.2 \lesssim -t \lesssim 12$  (GeV/c)<sup>2</sup>. Engler *et al.*<sup>2</sup> have measured the differential cross-sections for np elastic scattering from  $-t = 0.06$  to 3 (GeV/c)<sup>2</sup> for incident momenta between 10 and 24 GeV/c. Bohmer *et al.*<sup>3</sup> measured  $d\sigma/dt$  for this reaction between 10 and 70 GeV/c and for  $-t$  between 0.1 and 2.8 (GeV/c)<sup>2</sup>. Perl *et al.*<sup>4</sup> measured np elastic scattering cross-sections extending well beyond 90° in the CM system with the incident laboratory momentum ranged from 2 to 7 GeV/c. Stone *et al.*<sup>5</sup> performed a rather comprehensive experiment on np elastic scattering for  $p_L = 4.5$  to 12.5 GeV/c, the data extending from small angles to about 145° in the CM system. Recently, DeHaven *et al.*<sup>6,7</sup> have measured neutron-proton elastic differential cross-section from 70 to 400 GeV/c. The results of their work from 100 to 360 GeV/c and in a range in  $-t$  from 0.15 to 3.6 (GeV/c)<sup>2</sup> are shown in Fig. 1. The continuous neutron spectrum was divided into seven momentum bins: the bin-widths ranging from 35 to 60 GeV/c. The measurements of  $-t$  were also made in bins. The np elastic scattering data of Refs. 6, 7 and 8 show the following characteristics:

(1) The usual diffraction peak shrinks with increasing energy.

(2) There is a gradual evolution of a dip in the differential cross-section near  $-t = 1.4$  (GeV/c)<sup>2</sup> as the incident neutron energy increases.

(3) While the dip is similar to that previously reported in pp elastic scattering,<sup>9-11</sup> the np cross-

sections are generally higher in this region and do not appear to fluctuate as rapidly as a function of energy. The cross-sections then rise to a second maximum and begin to fall in a much slower fashion.

(4) As in pp data, the logarithmic slope is  $2$  (GeV/c)<sup>-2</sup> or 20% of the diffraction slope.

(5) The total cross-section in the measured range rises with energy.

In the present paper, we shall explain the results obtained by DeHaven *et al.*<sup>6-8</sup> by using the dipole pomeron model.

### 2. Calculations and Comparison with Experiment

The relevance of the double pomeron pole to diffraction phenomena has been emphasized by several authors.<sup>12-16</sup> Jenkovszky and Wall<sup>17</sup> have tried to explain pp elastic scattering at high energy for  $0 \lesssim -t < 4$  (GeV/c)<sup>2</sup>. Since we will be following the same technique, we reproduce it with some modification.

Neglecting spin, the scattering amplitude for this reaction can be written as

$$\begin{aligned} T(s, t) &= \frac{d}{d\alpha} \left[ e^{-i\pi\alpha/2} (s/s_0)^\alpha G(\alpha) \right] \\ &= e^{-i\pi\alpha/2} (s/s_0)^\alpha G'(\alpha) \\ &\quad \left[ 1 + \phi(\alpha) \ln s/s_0 - i \frac{\pi}{2} \phi(\alpha) \right] \\ &\quad \sqrt{s} \text{ mb (GeV/c)}^{-1}, \end{aligned} \quad \dots(1)$$

where  $\alpha = \alpha(t)$  is the pomeron trajectory,  $s_0$  is a constant,

$\phi(\alpha) = G(\alpha)/G'(\alpha)$ , and the factor  $1/\sin(\pi\alpha/2)$  has been absorbed in  $G(\alpha)$ . In Ref. 13,  $\sin(\pi\alpha/2)$  has been taken as approximately constant. This is, however, not valid because  $\alpha(t)$  varies from 1 to -1



as  $-t$  goes from zero to  $8(\text{GeV}/c)^2$ . From the structure of Eq. (1), we note that the first term in square brackets gives the contribution from the simple pole,  $G'(\alpha) \sin(\pi\alpha/2)$  being the residue at this pole. The function  $G'(\alpha)$  is assumed to fall exponentially. If we take the pomeron trajectory as linear, viz.  $\alpha(t) = \alpha_0 + \alpha't$ , we may write

$$G'(\alpha) = A e^{b[\alpha(t)-\alpha_0]} = A e^{b\alpha't} \quad \dots(2)$$

where  $A$  and  $b$  are free parameters to be fixed from experiment. The function  $G(\alpha)$  is obtained by integrating the above equation:

$$G(\alpha) = \frac{A}{b} e^{b\alpha't} + \gamma \quad \dots(3)$$

where  $\gamma$  is a constant. From Eqs. (2) and (3), we get

$$\phi(\alpha) G(\alpha)/G'(\alpha) = \frac{1}{b} + \frac{\gamma}{A e^{b\alpha't}} \quad \dots(4)$$

The parameter  $\gamma$  can be determined from the condition

$$\phi[\alpha(t=0)] = \lambda.$$

By using the norm

$$\frac{d\sigma}{dt} = \frac{s_0^2}{s^2} |T(s, t)|^2$$

we get the following relations for the differential and total cross-sections:

$$\frac{d\sigma}{dt} = \left( \frac{s}{s_0} \right)^{2\alpha-2} G'^2(\alpha) \left[ \left\{ 1 + \phi(\alpha) \ln \frac{s}{s_0} \right\}^2 + \frac{\pi^2}{4} \phi^2(\alpha) \right] \text{mb (GeV/c)}^{-2} \quad \dots(5)$$

$$\sigma_T = 4\sqrt{\pi} \sqrt{0.389} \frac{s_0}{s} \text{Im } T(s, t=0) \text{mb} \quad \dots(6)$$

Eqs. (5) and (6) can be written as

$$\begin{aligned} \frac{d\sigma}{dt} &= A^2 \exp \{ [2\alpha'b + \ln(s/s_0)] t \} \\ &\left[ \left\{ 1 + \left( \frac{1}{b} + (\lambda - \frac{1}{b}) e^{-b\alpha't} \right) \ln(s/s_0) \right\}^2 \right. \\ &\quad \left. + \frac{\pi^2}{4} \left\{ \frac{1}{b} + (\lambda - \frac{1}{b}) e^{-b\alpha't} \right\}^2 \right] \quad \dots(7) \end{aligned}$$

$$\sigma_T = -4.42 A (1 + \lambda \ln s/s_0)$$

The position of the dip is given by

$$-t = \frac{1}{\alpha'b} \ln \frac{1 - \lambda b}{1 + b/\ln(s/s_0)}$$

We find that, by taking the pomeron trajectory as  $\alpha(t) = 1 + 0.31 t$ , a very good fit with experiment is obtained by the following choice of parameters:

$$A = -7.14 \sqrt{\text{mb}} (\text{GeV}/c)^{-1}, b = 11.82,$$

$$\lambda = 0.0825, \quad s_0 = 20 \text{ GeV}^2,$$

Fig. 1 shows the differential cross-section  $d\sigma/dt$  plotted against  $-t$  at various momenta. The curves which represent the calculated values of  $d\sigma/dt$  obtained from the model show that the agreement with experiment is very good.

In Fig. 2, the experimental results<sup>6</sup> for  $d\sigma/dt$  at 100, 200 and 360 GeV/c have been compared to the Reggeised absorption model of Kane and Seidl (KS)<sup>18</sup> and to the dipole pomeron model. At the lowest momentum, the KS model and the data agree upto  $-t \approx 0.6 (\text{GeV}/c)^2$ . At 200 GeV/c, the agreement is out to  $-t \approx 0.7 (\text{GeV}/c)^2$  while at the highest momentum, the agreement extends to  $-t \approx 0.9 (\text{GeV}/c)^2$ . Thus, as the incident momentum increases, the agreement between the KS model and the data extends to higher values of  $-t$ . However, this analysis is valid

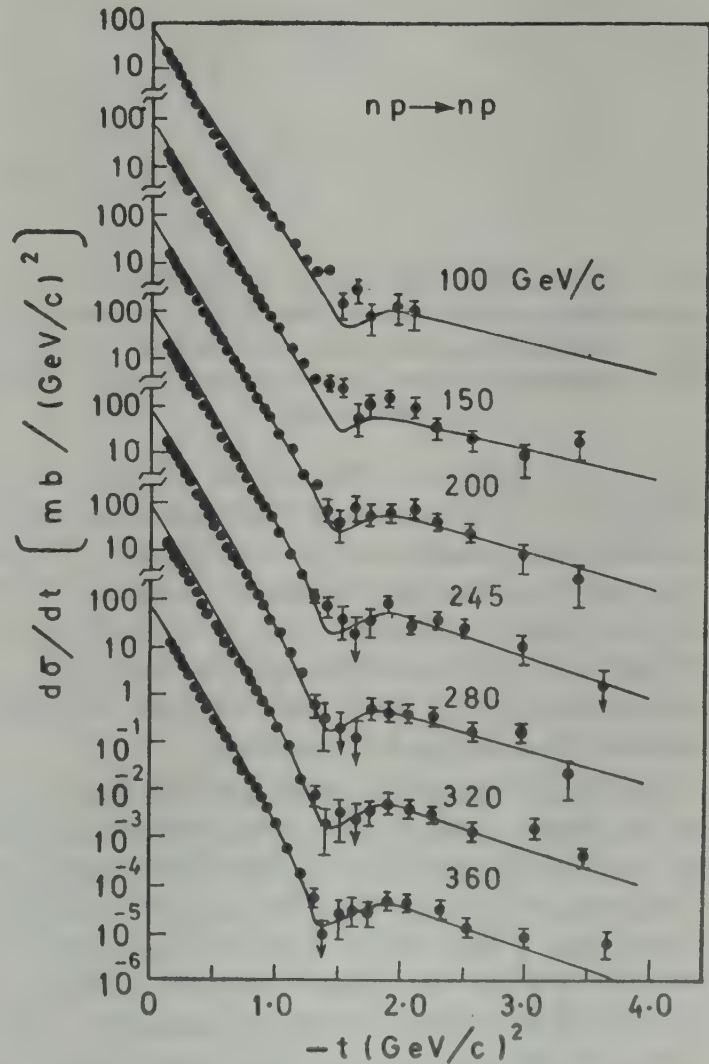


Fig. 1—Comparison of theoretical results (solid curve) with the experimental data for neutron-proton elastic scattering differential cross-sections plotted against  $-t$  for laboratory momenta from 70 to 400 GeV/c. Experimental points have been taken from Ref. 7



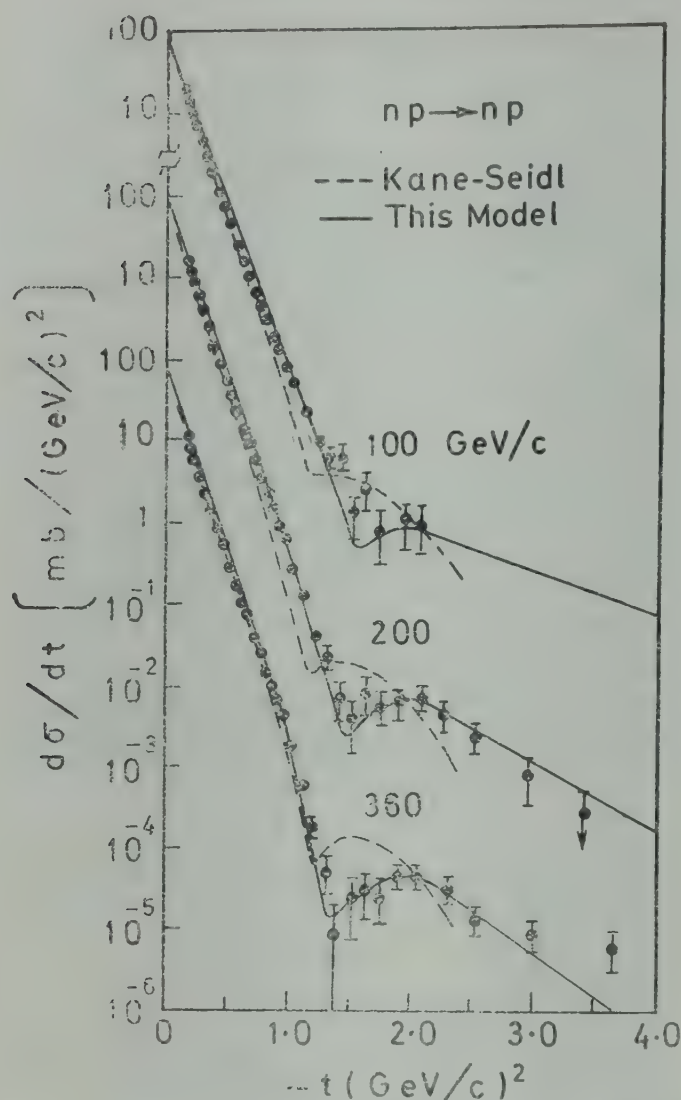


Fig. 2—Comparison of the neutron-proton elastic differential cross-sections at 100,200 and 360 GeV/c as measured in Ref. 7 with the Reggeized absorption model of Kane and Seidl (dashed curves) and with the dipole pomeron model (solid curves)

only in the region to the left of the dip. In the vicinity of the dip there is a complete disagreement between the KS model and the experiment. On the other hand, we find that the dipole pomeron model fits well with experiment for  $-t$  extending upto  $3.6 \text{ (GeV/c)}^2$ . In view of the fact that  $d\sigma/dt$  and  $-t$  measurements have been made in bins, the agreement can be considered as excellent.

The dipole pomeron model predicts that dip as well as bump positions are energy dependent. The dip positions at 100,200 and 360 GeV/c are found to be given by  $-t = 1.51, 1.45$  and  $1.41 \text{ (GeV/c)}^2$  respectively. This shows that the dip moves towards  $t = 0$  as the energy increases. Moreover,  $d\sigma/dt$  at the dip decreases with an increase in energy. Similar results hold good for the bump. The available data are not sufficiently accurate to check this prediction.

The total cross-section results are shown in Table 1. The agreement between the calculated values

Table 1—Comparison of Calculated and Experimental Values of  $\sigma_T$  at Different Momenta

$P_L \text{ (GeV/c)}$	$\sigma_T \text{ (mb)}$ (Exptl.)	$\sigma_T \text{ (mb)}$ (Present study)
100	38.83	37.41
150	39.14	38.46
200	39.45	39.22
245	39.72	39.75
280	39.92	40.09
320	40.13	40.44
360	40.34	40.75

and the experimental results is within the experimental accuracy. It is interesting to note that the Regge pole models cannot explain the rising total cross-section without violating the Froissart bound.<sup>18-21</sup> However, this rise in total cross-section at high energies emerges as a natural consequence of the dipole pomeron model.

We conclude that with only four free parameters  $A, b, d\sigma/dt$  and  $s_0$ , the differential and total cross-sections for momenta between 70 and 400 GeV/c can be explained satisfactorily by using a dipole pomeron model.

#### Acknowledgement

The financial assistance from the Pakistan Science Foundation under contract No. P-PU-Phy (11/1) is gratefully acknowledged.

#### References

- Gibbard B G, Longo M J, Jones L W, O'fallon (Jr), Kreisler M N & Perl M L, *Nucl. Phys.*, **30B** (1971), 77.
- Engler J, Flanger W, Gibbard B, Monning F, Pack K, Runge K & Schopper H, *Nucl. Phys.*, **62B** (1973), 160.
- Bohmer V, Engler J, Flanger W, Keim H, Monning F, Pack K & Schopper H, *Nucl. Phys.*, **91B** (1975), 22.
- Perl M, Cox J, Longo M J & Kreisler M N, *Phys. Rev.*, **D1** (1970), 1857.
- Stone J L, Chanowski J P & Longo M J, *Phys. Rev. Lett.*, **38** (1977), 1317.
- DeHaven (Jr) C E, *Neutron-proton elastic scattering from 70-400 GeV/c* Ph D thesis, University of Michigan, Michigan, 1978.
- DeHaven (Jr) C E, Ayre C A, Gustafson H R, Jones W L, Longo M J, Ramana Murthy P V, Roberts T J & Wholley M R, *Phys. Rev. Lett.*, **41** (1978), 669.
- DeHaven (Jr) C E, *Nucl. Phys.*, **148B** (1979), 1.
- Bohm A, Bozzo M, Ellis R, Foeth H, Ferrero M I, Maderni G, Naroska B, Rubbia C, Sette G, Staude A, Strolin P & De Zorzi G, *Physics Lett.*, **49B** (1974), 491.
- Akerlof C W, Kottaus R, Loweless R L, Meyer D I, Ambats I, Meyer W T, Ward C E W, Earthy D P, Lundy R A, Pruss S N, Vov-Novitch D D & Rust D R, *Phys. Rev.*, **14D** (1976), 2864.



11. Kwak N, Lohramann E, Nagy E, Regler M, Schmidt-Parzefall W, Schubert K R, Winter K, Brandt A, Neibergall F, Sschumacher P E, Aubert J J, Broll G, Coignet G, Favier F, Massonnet L, Vivargent M, Bartl W, Chinger H E, Goltfried & Neuhofer N, *Physics Lett.*, 58B, 233.
12. Burgi A I, *Lett. Nuovo Cim.*, 6 (1973), 577.
13. Jenkovszky L L., *Rising total cross-sections and multi-pole pomeron phenomenology*, Preprint ITP-74-1028, Kieve, 1974.
14. Philips R J N, *A dipole pomeron ansatz*, Rutherford Lab. Preprint R L-74-034, Chilton, 1974.
15. Joshi G C, *Lett. Nuovo Cim.*, 10 (1974), 815.
16. Fujisaki H, *Progr. Theoret. Phys.*, 53 (1975), 1420.
17. Jenkovszky L L & Wall A N, *Czech. J. Phys.*, 26B (1976), 447.
18. Kane G L & Seidl A, *Rev. mod. Phys.*, 48 (1976), 309.
19. Collins P D B, Gault F D & Martin A, *Nucl. Phys.*, 80B (1974), 135.
20. Joynson D W & Martin B A, *Univ. College of London Preprint*, (Nov.), 1977.
21. Kamran M, *Nuovo Cim.*, A51 (1979), 43.



## Investigations on the Second Harmonic Generation at Breakdown in $p$ - $n$ Junctions

ANIL K GOVIL, SHARWAN KUMAR & R PARSHAD

National Physical Laboratory, New Delhi 110 012

Received 24 April 1979; revised received 8 February 1980

Second harmonic generation (SHG) both in the forward and reverse directions, has been studied for varying temperatures in solid state diodes. The diodes studied were of silicon, germanium and gallium arsenide and had breakdowns of both kinds, avalanche and field emission. The second harmonics occurred at the regions of breakdown potential in the reverse direction and at the offset voltage in the forward direction. SHG at breakdown was sharper for diodes having avalanche breakdown compared to the diodes having field emission breakdown. It was observed that the variation of SHG with temperature corresponds with that of temperature variation of the reverse breakdown and offset voltage of the diodes. It was also observed that the SHG occurred in multipeaks (about 50 mV broad), spaced about 0.1 V apart at the breakdown of silicon diodes. In germanium diodes, broad SHG single peaks were observed at about 200 mV in the reverse direction; the SHG extending on the two sides of the peak in both the reverse and forward directions. The SHG seems to be associated with generation of optical phonons and occurrence of microplasmas at  $p$ - $n$  junction

### 1. Introduction

The second harmonic generation in  $p$ - $n$  junctions and in others has been widely used for different applications, e.g. at low temperatures, the generation of second harmonics is linked to generation or absorption of phonons,<sup>1</sup> and at room temperature the generation of second harmonics has been used to investigate impurity profiles in the presence of both shallow and deep level impurities.<sup>2-4</sup> In the present study, a new application of measurement of second harmonics has been made while investigating the breakdown phenomena in diodes. In principle, second harmonics would be produced whenever there is a departure from linearity in the  $V$ - $I$  characteristics of the diode, the intensity of the harmonics increasing with the nonlinearity (or the sharpness of the kink) in the  $V$ - $I$  characteristics. These departures in the linearity (or kinks) can, in principle, be determined from the static  $V$ - $I$  characteristics themselves, but the sensitivity of detection at the kinks becomes much greater if the method of measurement of the generated second harmonics is used. The use of the method of detection of second harmonics for investigating nonlinearities is all the more useful because the method will differentiate the real nonlinearities from any spurious nonlinearities or kinks occurring in the  $V$ - $I$  characteristics when they are graphically drawn from experimental observations. The discontinuities or the kinks in the characteristics as detected by the measurements on second harmonics indicate the presence of new physical processes or

phenomena taking place during the current flow in the diodes. Thus the measurements of the generated second harmonics will contribute to a better understanding of the processes governing current flow in the diodes both in the forward and the reverse directions

### 2. Experimental Details

The circuit used for applying the input voltage of fundamental frequency and detection of the second harmonics, to the diode, is shown in Fig. 1. The circuit has already been used in an earlier investigation<sup>5</sup> and is based on a still earlier circuit described by Jaklevic and Lambe.<sup>6</sup> A sinusoidal voltage of a fundamental frequency  $f_0$  (600 Hz) is applied to the diode by a signal generator, through a rejection notch filter tuned to  $2f_0$ . The output form of the diode is in the form of a distorted sine wave indicating the presence of harmonics. The second harmonic thus generated at the diode is passed on to the output through an isolating transformer and through a rejection notch filter tuned to  $f_0$ . Obviously the first filter prevents the second harmonic in being dissipated in the fundamental frequency generator and the second filter prevents the fundamental frequency from appearing at the output. No attempts were made to detect harmonics higher than the second. Silicon, germanium and gallium arsenide diodes were used and the results on these diodes are reported in what follows:



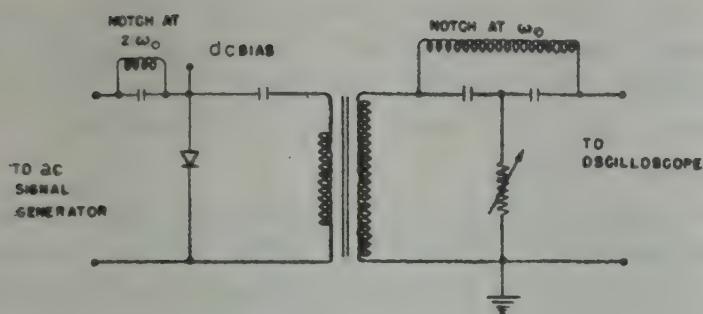


Fig. 1—Circuit used for second harmonic generation

### 2.1 Silicon

For silicon, both the reverse and the forward  $V$ - $I$  characteristics have been examined for second harmonic generation (SHG).

**Reverse characteristics**—The silicon  $p$ - $n$  junctions investigated were a few Zener diodes of different breakdown voltages varying from about 3 to 36 V. Figs. 2 and 3 depict the variation of SHG for diodes of nominal breakdown voltages 6.8 and 9.1 V respectively, as a function of applied reverse voltage at different temperatures.

Comparison of Figs. 2 and 3 shows that the SHG curves as a function of applied voltage are broader for the diode 1Z6.8 than for the diode 1Z9.1. This observation matches with the well known fact that the breakdown voltages are sharper for the avalanche diodes than for the field emission diodes. Of the diodes used 1Z9.1 is almost a pure avalanche diode while 1Z6.8 has the characteristics of both avalanche and field emission breakdowns. In correspondence with the above, it was found that for

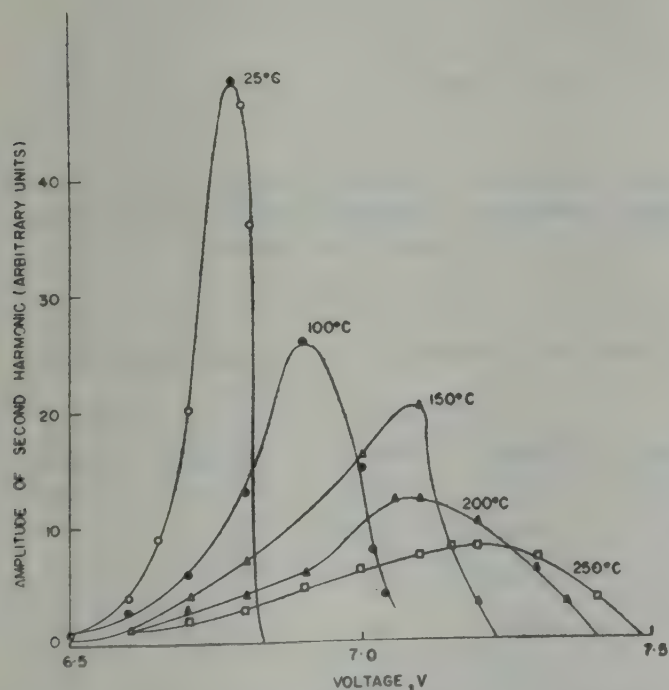


Fig. 2—Amplitude of second harmonic as a function of applied voltage for reverse bias for zener diode 1Z6.8 at different temperatures

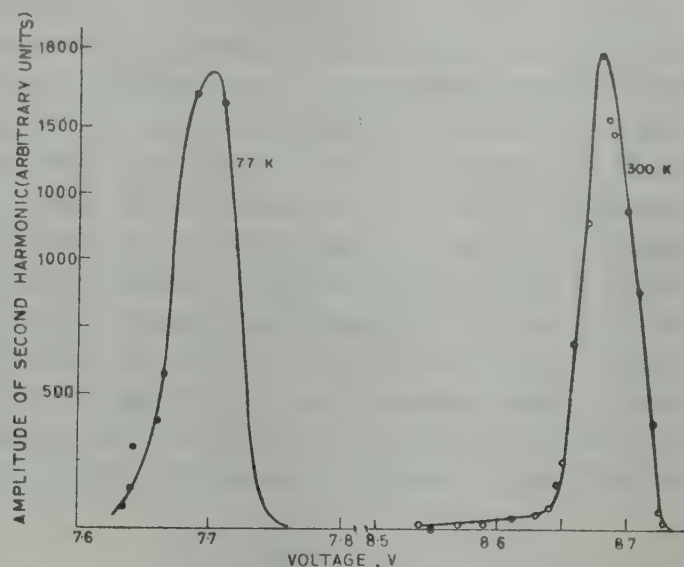


Fig. 3—Amplitude of second harmonic as a function of applied voltage for reverse bias for diode 1Z5.1, at temperatures 77 and 300°K

diodes of lesser breakdown voltages like 1Z3 and 1Z5.1 having a nominal breakdown voltage of 3 and 5.1 V respectively, it was noticed that as the breakdown voltage increased, the SHG became sharper, or in other words, the width of the voltage peak became narrower. It may also be mentioned here that as the breakdown voltage increased, the amplitude of SHG increased.

Regarding the variation of SHG with temperature, both Figs. 2 and 3 show that as the temperature increased, the SHG for diodes 1Z9.1 and 1Z6.8 occurred at a higher voltage. This fact correlates with the phenomenon of increase of breakdown voltage of avalanche diodes with increase of temperature. In contrast, for the diodes giving field emission breakdown (1Z3 and 3Z5.1) the SHG showed peaks which shifted towards lower voltages with increase of temperature. This fact of course corresponds with the decrease of breakdown voltage (of field emission type) with the increase of temperature.

In the above, the ac voltage being applied to the diode (from the signal generator) got varied with the change of dc bias to the diode even if the nominal setting of the output voltage on the signal generator remained unchanged. This was so because the change of dc current in the diode would change its resistance, which in its turn, due to the finite impedance of the signal generator, would result in the change of output voltage (from the generator). For this reason, in Figs. 2 and 3, the relative magnitudes of the voltage peaks at different temperatures do not have fundamental significance.

In another set of experiment, the ac voltage fed to the diode was stabilized, unlike in the cases



mentioned above. The method of stabilization employed was that adopted earlier by Tiemann.<sup>7</sup> Using voltage stabilization, it was noticed that the avalanche diodes of higher breakdown voltages (11 V or higher) exhibited, apart from the main large peak of SHG, other smaller peaks spaced at about 0.1 V from the main peak. It may be mentioned here that for varying voltages smoothly within precisely adjusted small intervals, special voltage supplies had to be used. Also, for measuring small voltage intervals, use of a digital voltmeter had become a necessity. In Table 1 are reported the voltages at which different SHG peaks were

observed for different diodes. About three or four peaks were generally observable for each diode. The magnitude of the peaks decreased fast on traversing away from the main peak which occurred at the lowest voltage.

**Forward bias**—It is well known that silicon diodes give a threshold or offset voltage of about 0.5 to 0.6 V for conduction in the forward direction. In the present study it was observed that the SHG peaks occurred at these voltages. SHG for two different diodes is depicted in Figs. 4 and 5 along with the variation of SHG with temperature. Both Figs. 4 and 5 show that as the temperature increases, the SHG occurs at lower voltages, and the width of the SHG peaks decreases. The change of voltage setting for SHG corresponds with decrease of offset voltage with temperature. At the higher temperatures (100–250°C), the width remains almost constant and of course, less than that at room temperature or liquid air temperature.

It may be mentioned here that the shift of SHG with temperature in the forward direction is much

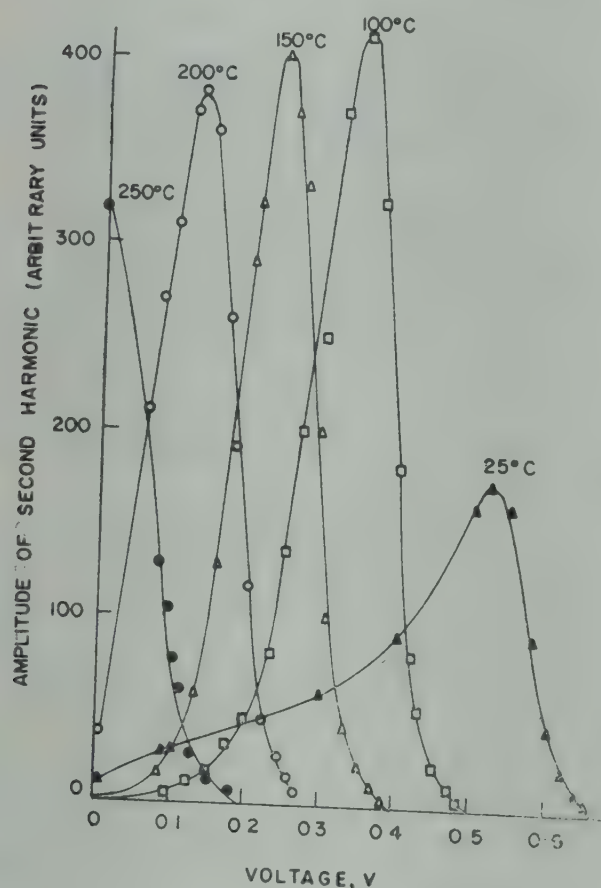


Fig. 4—Amplitude of second harmonic as a function of applied voltage for forward bias for diode 3Z5.1 at different temperatures

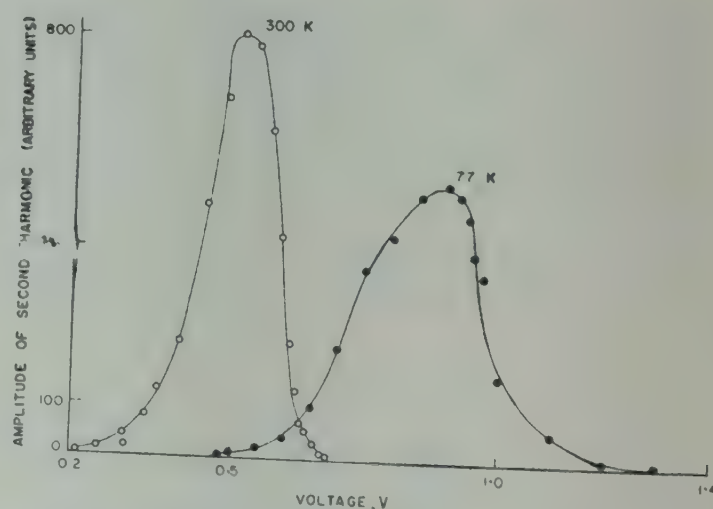


Fig. 5—Amplitude of second harmonic as a function of applied voltage for forward bias for diode 3Z9.1 at temperatures 77 and 300°K

Table 1—Voltage of Occurrence of SHG Peaks and Their Widths in the Breakdown Region of Different Silicon Diodes

Diode	Ist Peak		IInd Peak		IIIrd Peak		IV Peak	
	voltage, V	width, mV	voltage, V	width, mV	voltage, V	width, mV	voltage, V	width, mV
1Z24	24.24	50	24.36	40	24.48	80	—	—
1Z20	18.92	60	18.99	40	19.06	20	—	—
1Z13	12.04	30	12.08	20	12.24	60	12.36	5
1Z11	11.05	90	11.17	70	11.39	50	—	—
1Z9.1	8.40	40	—	—	—	—	—	—
1Z6.8	6.68	90	—	—	—	—	—	—



faster than it is for the reverse direction. This fact has correspondence with the dependence of breakdown and offset voltages on temperature.

## 2.2 Germanium

For investigation of germanium diodes, the base-emitter portions of transistors AF114, AF115, AF116, and Philco 6528 were used. Additionally, diodes DS10 and DR25 (made by Bharat Electronics Limited) were also investigated.

In the germanium transistor AF series (AF114, 115 and 116), the SHG in the reverse direction was sharp and occurred, as expected, at the respective breakdown voltages of the diodes. For AF114, the SHG was at 2.24 V, for AF115 at 1.95 V and for AF116, the SHG occurred at 1.485 V.

In the case of diodes DS10 and DR25, the SHG maximum was observed in the reverse direction near zero volt (200 mV for DR25 and 150 mV for DS10). The SHG was broadly produced round this maximum, on both sides of the current flow, forward and reverse. Fig. 6 represents the behaviour of DS10 at room temperature.

With regard to variation of SHG with temperature in the diodes DS10 and DR25, it was noticed that with increase of temperature the maximum of SHG shifted towards increasing reverse voltages. Thus for 100°C, the maximum of SHG occurred at 0.675 V instead of at 200 to 300 mV at room temperature and had a much decreased amplitude. It may be mentioned here that no SHG was investigated in the regular breakdown region of the diodes DS10 and DR25. For Philco transistor 6528, SHG was found at the reverse breakdown voltage of 8.5 V.

## 2.3 Gallium Arsenide

The observation of SHG only in the forward direction was attempted for gallium arsenide light emitting diodes. The SHG behaviour was similar to that for silicon diodes, the SHG occurring near the offset voltages.

## 3. Results and Discussion

It should be noted that for all types of diodes, the SHG occurs where it is expected, i.e. at the discontinuities of  $V$ - $I$  characteristics caused by breakdown in the reverse direction and offset voltages in the forward direction.

As expected, the temperature variation of SHG corresponds with temperature variation of the breakdown and offset voltages.

Again, the amplitude of SHG increases as the breakdown voltage increases, i.e. as the avalanche

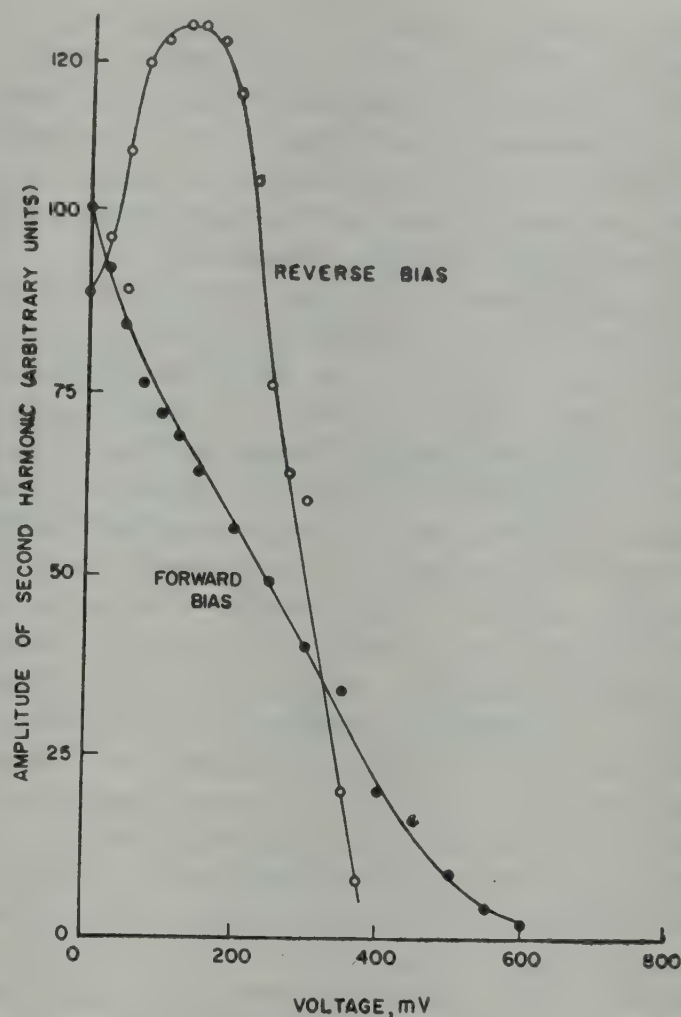


Fig. 6—Amplitude of second harmonic as a function of applied voltage both for forward and reverse bias for germanium diode DS10 at room temperature

character of the breakdown increases. This is in keeping with the fact that the avalanche breakdowns are much sharper than the field emission type of breakdowns.

Though no new information from the above is forthcoming, yet the correlation between SHG generation and the expected discontinuities in the  $V$ - $I$  characteristics indicated the possibility of the application of SHG generation for detecting discontinuities (in the  $V$ - $I$  characteristics), in cases where such discontinuities are not easily detectable by other experimental means. The occurrence of SHG in these cases can then be used to formulate possible physical processes causing the SHG.

An observation which is not easy to deduce from the  $V$ - $I$  characteristics is the occurrence of subsidiary SHG peaks, spaced a few millivolts from the main SHG peak, at the reverse breakdown of silicon diodes exhibiting pure avalanche type breakdowns. The occurrence of subsidiary peaks, seem to be due to the microplasmas generated at discrete points at a  $p$ - $n$  junction near breakdown. The occurrence and theory of these microplasmas is already well documented.<sup>8-12</sup> The occurrence of microplasmas is



already known to be reflected in the generation of noise peaks.<sup>8,13</sup> The present study shows that the SHG can also be advantageously used for the detection of generation of microplasmas. It is interesting to observe that both microplasmas as detected and SHG are found to occur only for those diodes which have pure avalanche type of breakdown.

In germanium diode, the SHG, apart from occurring at reverse breakdown voltages as in the case of silicon diode, also occurs as mentioned above round about 0V, with a maximum in the reverse direction. The SHG seems to be associated with the generation of optical phonons. These optical phonons, due to their enough high energy ( $\approx 100$  mV) in contrast to acoustic phonons, are not generally existent in the lattice by thermal excitation. These phonons would be produced by lattice collisions of electrons accelerated in the depletion layer of *p-n* junctions. In literature, it is well known that generation of optical phonons plays an important part in the reverse breakdown mechanism of diodes.<sup>14-17</sup> The accelerated electrons generate the optical phonons and thus lose energy and hence cause ionization only if cumulatively they gather enough energy between collisions for the inelastic collisions to take place. The present study indicates the generation of phonons in the non-breakdown regions of germanium diodes also. The suggested cause for SHG in terms of generation of optical phonons is supported by the fact that at higher temperatures, the SHG decreases fast. At these temperatures, the optical phonons would be thermally generated in the lattice and hence the accelerated

electrons by collisions with the lattice would both generate and absorb phonons, the integrated effect of optical phonons on SHG being thus decreased.

#### Acknowledgement

The authors thank the Director, for providing the facilities for the study and Shri Vipin Kumar for useful discussions.

#### References

1. Logan R A, *Tunnelling phenomena in solids*, edited by Elias Burstein & S Lundqvist, (Plenum Press, New York) 1969, 149.
2. Meyer N I & Guldbrandsen, *Proc. IEEE*, 51 (1963), 1631.
3. Zohta Y, *Appl. Phys. Lett.*, 17 (1970), 284.
4. Shibli E G, *Solid St. Electron.*, 15 (1972), 137.
5. Govil A K, Sharma R N, Vipin Kumar & Ram-Parshad, *Vijnana Parishad Anusandhan Patrika*, 20 (1977), 267-275.
6. Jaklevic R C & Lambe J, Ref. 1, p. 233.
7. Tiemann J J, *Rev. scient. Instrum.*, 32 (1961), 1093.
8. McKay K G, *Phys. Rev.*, 94 (1954), 877.
9. Chynoweth A G & McKay K G, *Phys. Rev.*, 102 (1956), 369.
10. Rose D J, *Phys. Rev.*, 105 (1957), 413.
11. Tokuyama T, *Japan J. appl. Phys.*, 1 (1962), 324.
12. Chynoweth A G, *Semiconductors and semimetals*, Vol. 4 edited by R K Willardson and Albert C Beer, (Academic Press, New York) 1968, 313.
13. Golovko A G & Shermergor T D, *Soviet. Phys. Semi-cond.*, 8 (1975), 877.
14. Wolf P A, *Phys. Rev.*, 95 (1954), 1415.
15. Baraff G A, *Phys. Rev.*, 128 (1962), 2507.
16. Bartelink D J, Moll J L & Mayer N, *Phys. Rev.*, 130 (1963), 972.
17. Chynoweth A G, Ref. 12, p. 268.



## Electrical Characteristics of 50 kV Resistance Potential Divider

S BEG

Department of Physics, Quaid-i-Azam University, Islamabad, Pakistan

Received 19 July 1979; revised received 22 November 1979

The response of the compensated resistance probe is suitable for power system harmonic and transient voltage analysis. The appropriate mathematical derivations concerning the electrical characteristics of the prototype 50 kV probe are given and the effect of various parameters discussed.

### 1. Introduction

Various aspects of the performance of resistance dividers for high voltage measurements and their representation by complicated equivalent circuits have been studied in detail in a number of papers.<sup>1-3</sup> In this paper is described the response of the compensated resistance probe suitable for power system harmonic and transient voltage analysis.

### 2. Analysis

Fig. 1 shows the electrical representation of a typical resistance divider network. Normally  $C_s$ , the stray capacitance to ground varies with the distance from the earthy end of the probe. In the divider where the outer surface of the tube is held at earth potential,  $C_s$  will be constant and independent of the distance. Fig. 2 shows the representation of such a system.

The theoretical characteristics as shown in Figs. 3-6 are based on equation of the transmission line network.

$$V_s = V_R \cosh \theta L + Z_c I_R \sinh \theta L \quad \dots(1)$$

$$\text{or } V_s = A V_R + B I_R \quad \dots(2)$$

$$\text{where } A = \cosh \theta L \quad \dots(3)$$

$$\text{and } B = Z_c \sinh \theta L \quad \dots(4)$$

$$\text{But } I_R = \frac{V_R}{R_0} \quad \dots(5)$$

Substituting Eqs. (5) into Eq. (2) gives

$$V_R' = \frac{V_s R_0}{A R_0 + B} \quad \dots(6)$$

For an ideal divider (dc conditions)

$$V_R' = \frac{V_s R_0}{R + R_0} \quad \dots(7)$$

Hence

$$\frac{V_R}{V_R'} = \frac{V_s R_0 / R'}{(A R_0 / R' + B / R')} \times \frac{(1 + R_0 / R')}{(V_s R_0 / R')} \dots(8)$$

$$\frac{V_R}{V_R'} = \frac{(1 + R_0 / R')}{(A R_0 / R' + B / R')} \quad \dots(9)$$

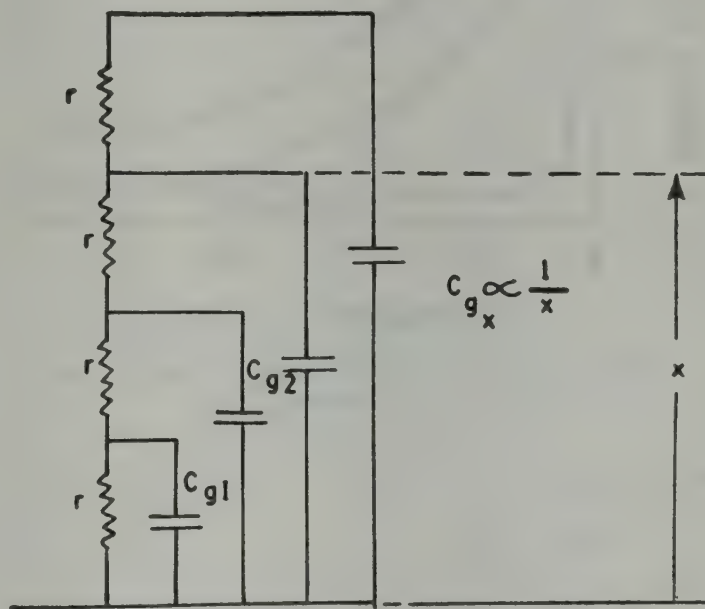


Fig. 1—Electrical circuit of a typical R-C divider probe

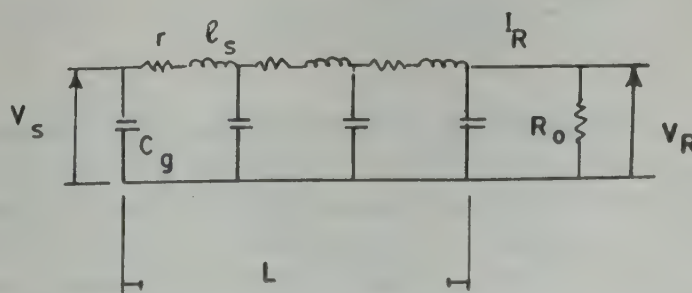


Fig. 2—Electrical circuit showing constant  $C_s$ , the stray capacitance to ground



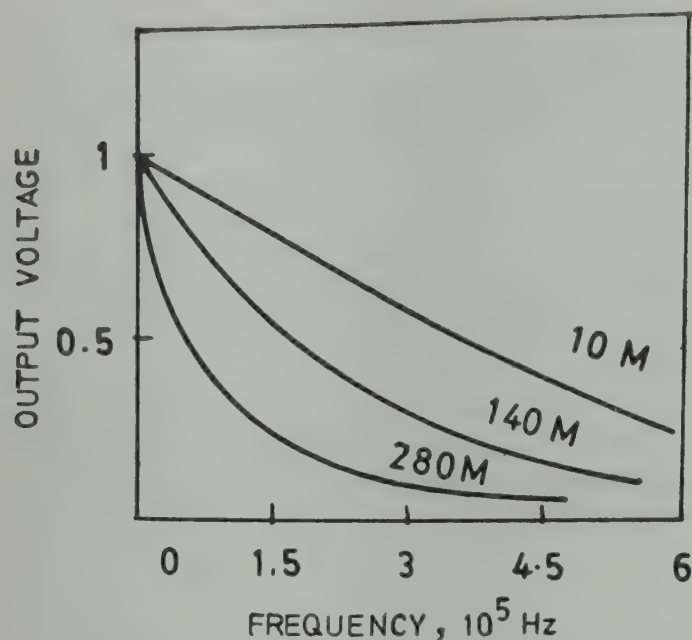


Fig. 3—Frequency response due to change in total resistance of the probe (calculated)

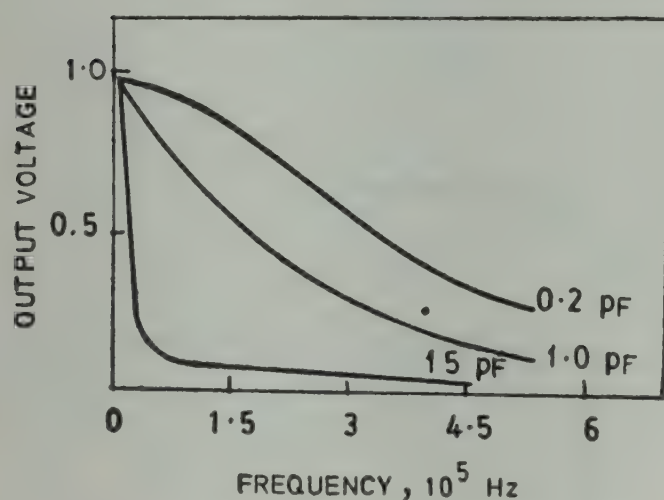


Fig. 4—Frequency response due to change in stray capacitance

But  $R' \gg R_0$

$$\frac{V_R}{V_{R'}} = \frac{R'}{B} \quad \dots(10)$$

Substituting for B from Eq. (4)

$$\frac{V_R}{V_{R'}} = \frac{R'}{\sqrt{Z/Y} \sin h \sqrt{ZY}} \quad \dots(11)$$

The values of the parameters chosen are  $L=45$  cm,  $C_s = 1$  pF and  $1s = 8 \mu$ H. In Figs. 3-5, the total resistance  $R$ , shunt capacitance  $C_s$ , and length  $L$  of the probe are independent variables. It is evident from these figures that the frequency response varies inversely as the magnitude of  $R$ ,  $C_s$  and  $L$ . Fig. 6 is the calculated response due to

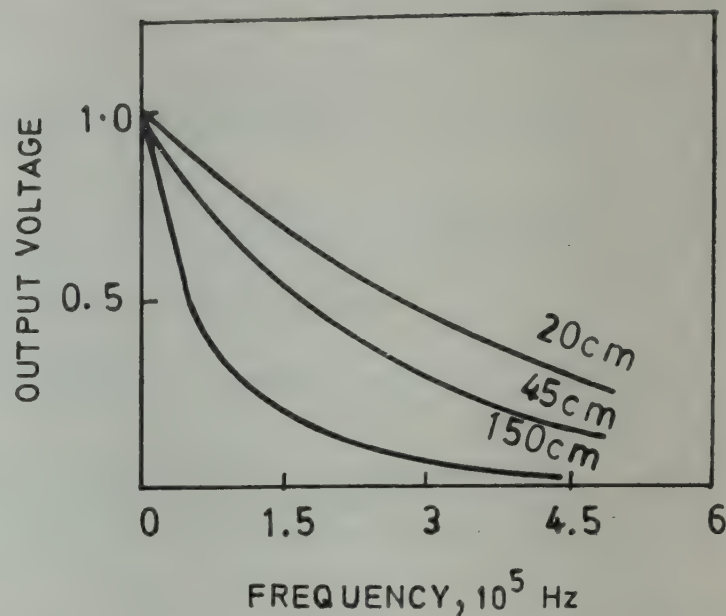


Fig. 5—Frequency response due to change in the total length of the probe (calculated)

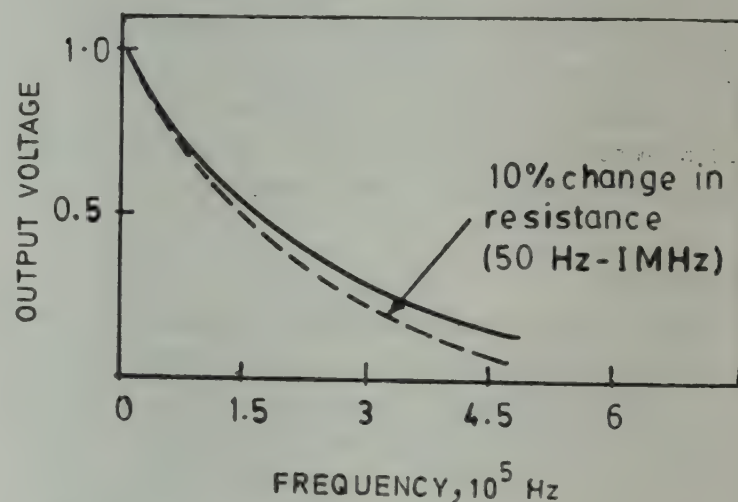


Fig. 6—Frequency response due to change in resistance due to frequency (calculated)

change in frequency-dependent resistance. A 10% change in resistance does not create any significant deviation in frequency response. Comparison of Fig. 4 with Fig. 6 suggests that the main errors in probe response are due to stray capacitance  $C_s$ , to ground. The effect of the length of the probe on skin effect ratio is given by the relation

$$\frac{R_{ac}}{R_{dc}} \propto a \sqrt{\frac{\omega/\mu}{K}} \quad \dots (12)$$

where  $R_{ac}$  is the ac resistance,  $R_{dc}$  the dc resistance,  $\omega$  the angular frequency,  $\mu$  is the permeability,  $K$  is the resistivity and

$$R_{dc} = \frac{KL}{a} \quad \dots (13)$$

The skin effect ratio increases with the length of the probe  $L$ . Hence change in resistance due to frequency may be reduced by limiting the length of the probe.



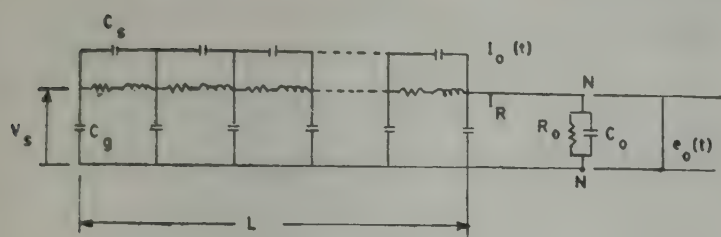


Fig. 7—Equivalent circuit of the probe including  $C_s$  across the resistors

Errors due to stray capacitance  $C_s$  may be minimized by using increased parallel capacitance  $C_s$  across the resistor elements.  $C_s$  may be made large so that charging current to all the capacitance below it can be provided.

The equivalent circuit of the probe including the shunt capacity  $C_s$  across the resistor elements is shown in Fig. 7.

Ignoring  $C_s$  and  $C$ , the linear voltage distribution ( $e$ ) along resistor chain is :

$$e = V_s - \frac{V_s}{L} x \quad \dots(14) \quad \text{or}$$

where distance  $x$  is taken from the top end of the resistor chain. In Fig. 8, for capacitive chain  $C_s$  and  $C_g$  alone,

$$\frac{di}{dx} = -ey \quad \dots(15)$$

$$\text{and} \quad \frac{de}{dx} = -iz \quad \dots(16)$$

where  $y = +j\omega C_s$  and  $z = -j/\omega C_s$

Substituting Eq. (14) into Eq. (15) gives

$$\frac{di}{dx} = \frac{V_s xy}{L} - V_s Y \quad \dots(17)$$

$$i = \int \left( \frac{V_s xy}{L} - V_s y \right) dx \quad (18)$$

$$= \frac{V_s x^2 y}{2L} - V_s y x + C \quad \dots(19)$$

where  $C$  is a constant of integration.

When  $x = L$ ,  $i = I_{e0}$  (current through the bottom end of the capacitor chain).

$$\text{Therefore, } I_{e0} = C - \frac{V_s y L}{2} \quad \dots(20)$$

From Eq. (14)

$$\frac{de}{dx} = -\frac{V_s}{L} \quad \dots(21)$$

Using Eq. (16)

$$\frac{V_s}{L} = iz \quad \dots(22)$$

$$i = \frac{V_s}{Lz} \quad \dots(23)$$

Substituting Eq. (23) into Eq. (19) gives :

$$\frac{V_s}{Lz} = \frac{V_s x^2 y}{2L} - V_s y x + C \quad \dots(24)$$

$$\frac{1}{zy} = \frac{x^2}{2} - xL + \frac{CL}{yV_s} \quad \dots(25)$$

But  $y = j\omega C_s$  and  $z = -j/\omega C_s$  and substituting these values into Eq. (25) we get

$$\frac{C_s}{C_g} = \frac{x^2}{2} - xL + \frac{CL}{yV_s} \quad \dots(26)$$

From Eq. (20) when  $I_{e0} = 0$

$$C = \frac{V_s y L}{2} \quad \dots(27)$$

Substituting Eq. (27) into Eq. (26) gives

$$\frac{C_s}{C_g} = \frac{x^2}{2} - xL + \frac{V_s y L}{2} \frac{L}{yV_s} \quad \dots(28)$$

$$\frac{C_s}{C_g} = \frac{1}{2} (x^2 - 2xL + L^2) \quad \dots(29)$$

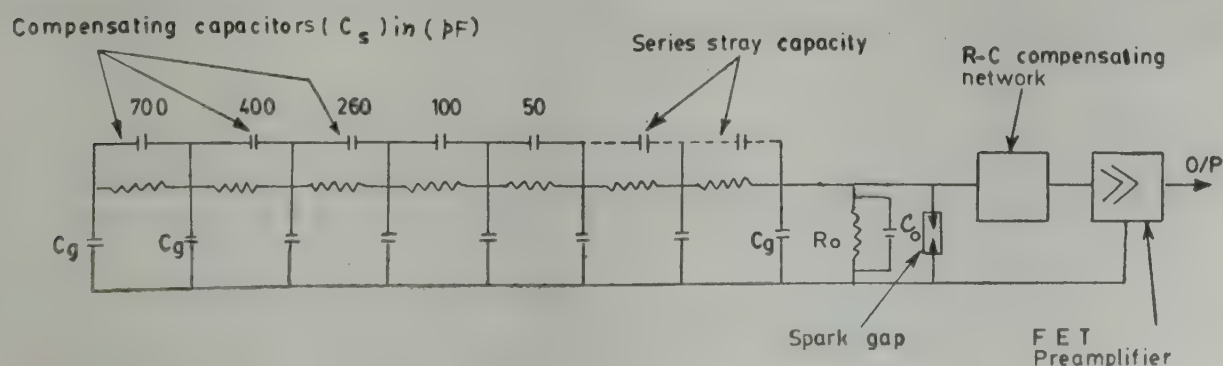


Fig. 8—Complete electrical circuit of R-C divider probe

Eq. (29) shows that for optimum compensation with negligible capacitive current  $C_s$  is a definite function of  $C_g$ .

Calculated values of the parallel capacitance compensation for the top five resistors (Fig. 8) based on Eq. (29), are 700, 400, 260, 100, and 50 pF respectively.

Fig. 8 shows the complete electrical representation of such a probe under the condition with points NN' (as in Fig. 7) grounded and using Eq. (1) for this network the current  $I_0 = (I_R)$  is

$$I_0 = \frac{V_s}{Z_C \sinh \theta L} \quad \dots(30)$$

For applied unit step voltage at the input and using Laplace generalized impedance notation

$$I_0(p) = \frac{1}{Z_C(p) \sinh \theta(p)} \quad \dots(31)$$

where (ignoring inductance  $L_s$  and change in resistance due to frequency) the characteristic impedance

$$Z_C(p) = \sqrt{\frac{R}{C_g' p (1 + RC_g' p)}} \quad \dots(32)$$

and the propagation constant

$$\theta(p) = \sqrt{\frac{RC_g' gp}{1 + RC_g' p}} \quad \dots(33)$$

The voltage  $e_0(p)$  across the low impedance arm of impedance  $Z_0(p)$  is approximately given by :

$$e_0(p) = \frac{Z_0(p)}{Z_C(p) \sinh \theta(p)} \quad \dots(34)$$

where  $Z_0(p) = R_0/(1 + R_0 C_0 p)$  ... (35)

Substituting Eqs. (32), (33) and (35) into Eq. (34) we get

$$e_0(p) = \quad \dots(36)$$

$$\begin{aligned} & \frac{R_0/(1 + R_0 C_0 p)}{\sqrt{R/C_g' p (1 + RC_g' p)} \sinh \sqrt{R C_g' p/(1 + RC_g' p)}} \\ &= \frac{R_0}{R} \frac{1 + RC_g' p}{1 + R_0 C_0 p} \cdot \left\{ 1 + 2 \sum_{K=1}^{\infty} \frac{(-1)^K C_g'}{C_g' + K^2 \pi^2 C_g'} \right. \\ & \quad \left. \cdot \frac{p}{p + [K^2 \pi^2 / R (C_g + K^2 \pi^2)]} \right\} \quad \dots(37) \end{aligned}$$

Using inverse transform

$$\begin{aligned} e_0(t) = & \frac{R_0}{R} \left\{ 1 - \left( 1 - \frac{RC_g'}{R_0 C_0} \right) e^{-t/R_0 C_0} \right. \\ & + 2 \sum_{K=1}^{\infty} (-1)^K \cdot \frac{RC_g'}{RC_g' + K^2 \pi^2 (RC_g' - R_0 C_0)} \\ & \cdot \left[ \frac{C_g}{C_g + K^2 \pi^2 C_s} e^{-K^2 \pi^2 t / R (C_g + K^2 \pi^2 C_s)} \right. \\ & \left. \left. - \left( 1 - \frac{RC_g'}{R_0 C_0} \right) e^{-t/R_0 C_0} \right] \right\} \quad \dots(38) \end{aligned}$$

Normalizing  $e_0(t)$  as

$$\frac{R}{R_0} e_0(t) = A(t) \quad \dots(39)$$

$$A(t) = 1 - \left( 1 - \frac{RC_g'}{R_0 C_0} \right) \quad \dots(40)$$

For  $t=0$

$$A(0) = \frac{RC_g'}{R_0 C_0} \left[ 1 + \dots \right] \quad \dots(41)$$

$$= \frac{RC_g'}{R_0 C_0} \left( \frac{C_g'}{C_s} \right)^{1/2} \cosh \left( \frac{C_g'}{C_s} \right) \quad \dots(42)$$

Response time ( $T$ ) from Eq. (40) is

$$T = \int_0^{\infty} [1 - A(t)] dt \quad \dots(43)$$

$$= R_0 C_0 - RC_g + 1/6 RC_g \quad \dots(44)$$

For the low voltage arm the non-oscillatory condition is

$$R_0 \geq 2 \sqrt{L_0 / C_0} \quad \dots(45)$$

It is evident that the response time of the probe is dependent on the low voltage arm components  $R_0$  and  $C_0$ . By using  $C_0$  (100 pF) to ensure optimum response free from oscillations, the value of  $R_0$  is 47 kΩ. The compensated resistance probe should give a flat response up to 300 kHz with a rise time of 2 μsec.



# BEG : ELECTRICAL CHARACTERISTICS OF 50 kV COMPENSATED RESISTANCE PROBE

## Nomenclature

$V_s$  = applied voltage at the top end of the divider  
 $V_R$  = output voltage at the lower end of the divider  
 $V_R'$  = dc output voltage for an ideal divider  
 $\theta$  = propagation constant =  $zy$  or  $\frac{1}{L} ZY$   
 $Z_C$  = characteristic impedance =  $z/y$  or  $\frac{Z}{Y}$   
 $I_R$  = output current at the lower end  
 $z$  = impedance per unit length  
 $y$  = admittance per unit length  
 $r$  = resistance per unit length  
 $L_S$  = inductance per unit length  
 $C_g$  = stray capacitance to ground per unit length  
 $C_g'$  = total stray capacitance to ground  
 $C_s$  = shunt capacitance per unit length

$C_s'$  = total shunt capacitance  
 $Z$  = total impedance =  $zL = rL + j\omega L_S L$   
 $Y$  = total admittance =  $yL = j\omega C_g L$   
 $R$  = total resistance of the high voltage arm of the divider  
     ( $=rL$ )  
 $R'$  = total dc resistance of the high voltage arm  
 $R_0$  = low-voltage arm resistor  
 $x$  = distance  
 $T$  = response time  
 $\omega$  = frequency in rad/sec  
 $L$  = total length of resistor chain

## References

1. Davis R, *J. scient. Instrum.*, 5 (1928), 305 & 354.
2. Fisher F A, *Trans. Am. IEE*, 77 (1958), 1 & 411.
3. Creed F C *et al.*, *Proc. IEEE PAS*, 86 (1967), 1408.

## Formant Structure of Bengali Vowels & Some Possible Uses of a Tracking Loop Formant Extraction System

S K CHAKRABARTI

Department of Physics, University of Burdwan, Burdwan 713 104

Received 9 May 1979

A three-channel formant extraction system (FES) using automatic phase control circuits for tracking and estimation of frequencies of the formants is described. With a little modification, the system may be used as a frequency dividing vocoder or as a formant tracking vocoder with significant economy in bandwidth and channel capacity required for the transmission of speech. Other possible uses of the system include supplementary hearing aids and as analyzer for speech and speaker recognition systems. Results of the extensive studies on the formant structure of Bengali vowel sounds are also presented. Formant frequency and amplitude data obtained using FES agree well with the results of spectrographic measurements.

### 1. Introduction

Speech sounds are produced by motions of the articulatory mechanism of the vocal tract and are broadly classified as voiced and unvoiced sounds according to the type of excitation utilized in their production. Voiced sounds are produced by quasi-periodic vibration of the vocal cords. The sound generated by the air stream chopped by the vibrating vocal cords is known as "voice-source" which is a complex tone composed of a fundamental frequency, called the pitch, and a large number of higher harmonic partials or overtones. The amplitudes of these partials decrease uniformly with frequency at a rate of about 10 dB per octave [Fig. 1 (a)].

These air pulses produced by the vibrating vocal cords excite the vocal tract whose resonance characteristics are determined by the positions and shapes of the articulators like lips, jaw angle, tongue, etc. These resonances of vocal tract are known as formants. Frequency components near the resonant frequencies of the vocal tract are radiated into air very much magnified, the amount depending upon the damping constants of the resonant cavities. The presence of the formants, therefore, disrupts the uniformly falling-off voice-source spectrum envelope imposing peaks at the formant frequencies, and depending upon the quality factor ( $Q$ ), tends to suppress other portions of the spectrum. It is this perturbation of the voice-source spectrum envelope that produces distinguishable speech sounds and determines vowel quality.<sup>1</sup> More specifically, the formant frequencies enhance voice-source partials of certain frequencies and manifest themselves in the

spectrum vowel sounds as concentrations of acoustic energy in narrow bands of frequencies characterizing the spectrum envelope of vowel sounds [Fig. 1 (b)].

The waveforms of voiced sounds are, therefore, characterized by periodic repetition of the waveform at pitch frequency interval while between these

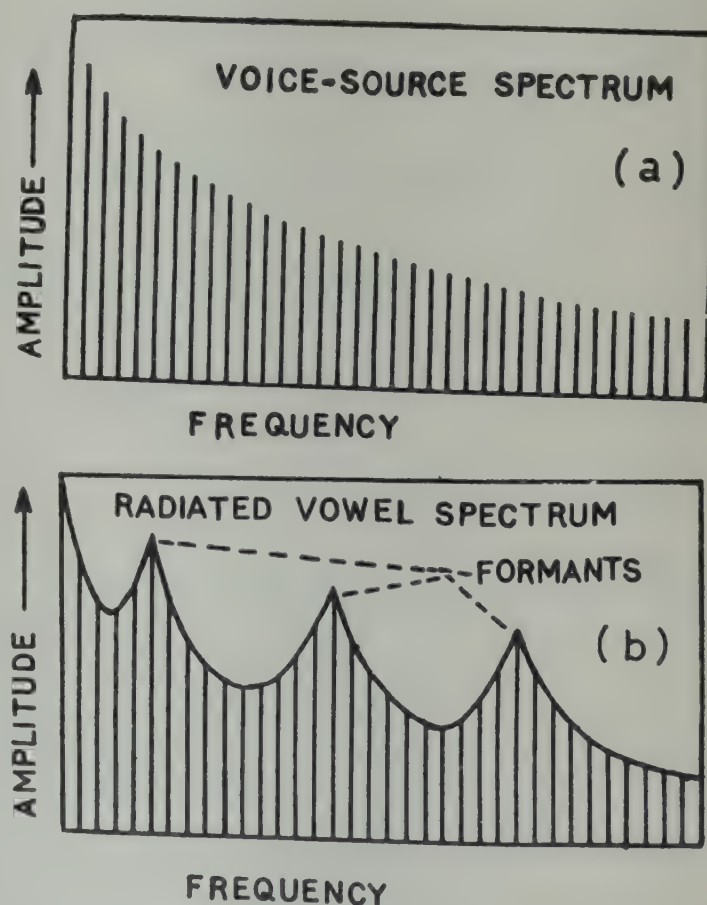


Fig. 1—(a) Voice-spectrum generated by vibrating vocal cords and, (b) spectrum of the radiated vowel sounds



intervals the structure of the waveforms represents dominant formants. In short-time power-frequency spectrum of voiced sounds, the periodic excitation gives discrete line-spectrum consisting of harmonics of the fundamental larynx frequency and, the vocal tract excitation determines spectral envelope.

In the case of unvoiced sounds, vocal cords do not vibrate and the vocal tract is excited by noise generated at a constriction in the vocal tract. The spectrum is noise-like, continuous in frequency although the acoustic energy might be concentrated in formant-like bands due to the presence of the vocal resonances. Analytical and experimental studies have shown that the speech spectrum contains all the information necessary for speech perception.<sup>2,3</sup> Vowel sounds, in particular, are well defined by the fundamental  $F_0$  and the three formant frequencies  $F_1$ ,  $F_2$ ,  $F_3$  and their relative amplitudes.

This shows that speech signal can be described in terms of the properties of the speech-producing mechanism, viz. the vocal tract and its excitation. This also suggests important possibilities for transmission of speech in forms other than the conventional waveform principle which demands nearly 3-3.5 kHz bandwidth for speech of commercial quality. This conventional voice channel is capable of transmitting information at rates much higher than the rate at which information is impressed on the 'voice-source' spectrum, originating in the speaker's vocal cords, by relatively slow movements of the articulators during the action of speaking. This realization led to many efforts towards investigating more efficient means for speech transmission that convey the perceptually significant information and discard the redundant parts of speech. Fundamental to the concept is the derivation of certain perceptually significant elements of speech through real-time analysis of speech waveforms, transmission of these parameters and finally reconstruction of speech signal at the receiver from these low information-rate parameters. In the usual schemes, the main parameters are the moving resonances of the vocal tract, that is, the formants. Speech-band compression systems of this kind are known as formant-tracking vocoders (FTV).<sup>4,5</sup> In such a system, the analyzer performs the task of separating the spectral and excitation information. The former involves extraction of information on the frequencies and spectral amplitudes of the formants and the latter concerns with the determination of pitch (or lack of it) and intensity.

Another type of vocoder based on formant separation and subsequent frequency division at the sending end to restrict the frequency excursion ranges

of the formants is known as frequency-dividing vocoder (FDV).<sup>6</sup> The idea is to avoid the difficult problem of excitation analysis and to achieve modest band saving and synthetic speech of high quality. Practicability of both types of speech-band compression systems depends upon how well the formant mode data can be derived automatically from speech waveforms.

Spectral analysis of speech sounds, on the other hand, is very useful in determining the important acoustical and perceptual features like formant structure of vowel sounds and, in the design of automatic real-time formant analyzers for speech communication systems and speech synthesizers. Determination of formant structure of vowel sounds involves measurement of frequencies, relative amplitudes and bandwidths of the formants. Quantitative data on the formant structure of vowel sounds are valuable in corroborating vocal tract calculations on the mode pattern and various dissipation characteristics of the vocal system. Results of such measurements also outline the basic principles on which the design of speech synthesizers and hearing-aid devices might be based.

The work reported in this paper was therefore, carried out with two-fold objective: (1) to determine the formant structure of Bengali vowel sounds, and (2) to investigate the possibilities of using an automatic real-time formant analyzer in constructing speech-band compression systems. A further purpose of this paper is to outline the possible ways of utilizing the formant extraction method in practical hearing-aid devices and other systems.

## 2. Formant Structure of Bengali Vowels

The formant structure of the Bengali vowels was determined with the help of a tracking-loop formant extraction system (TLFES),<sup>7</sup> a real-time formant analyzer, and a standard sound spectrograph [KEY. Sonagraph Model No. 7029A].

### 2.1 Tracking Loop Extraction of Speech Formants

Study of formant patterns of vowel sounds and their statistical locations shows that the first three formants usually occur in the overlapping frequency ranges 250-1000 Hz, 800-2400 Hz and 2000-3300 Hz respectively. In the case of vowel sounds, almost the whole amount of energy remains concentrated in the formant bands separated by frequencies of relatively low excitation. In any given formant, the energy is usually present in a narrow frequency band of about 100 Hz wide (Table 1) and, therefore, at any instant the speech signal may be regarded as a 3-component



signal having frequencies corresponding to the formant frequencies. The system also utilizes the fact that the first formant is the strongest compared with the others and the second formant is stronger than the third.

Block diagram of the three channel formant tracking and extraction system is shown in Fig. 2. The system utilizes continuously tuned automatic tracking loop filters for effective separation and extraction of the formants. Speech signal is filtered by means of a 250-3300 Hz audio band-pass filter and then translated in frequency by modulating a suitable high frequency carrier,  $F_c$ . The resulting single side band (SSB) signal is then divided into three channels by means of band-pass filters, the centre frequencies and bandwidths of which are commensurate with the frequencies and ranges of excursions of the formants. Each channel contains two subchannels—one for tracking and estimating the frequency of the formant and the other for extracting the formant in its frequency and amplitude. The frequency estimation subchannel houses a phase locking loop (PLL) and a frequency discriminator connected in cascade. PLL consists of three subsystems, a phase detector ( $\phi$ -Det.), a low-pass filter and a voltage controlled oscillator (VCO) connected in sequence (Fig. 2). When the instantaneous frequency of the formant falls within the synchronization range of PLL, the instantaneous VCO oscillation is pulled into synchronism with the incoming signal and the frequency discrepancy between the VCO oscillation and the incoming signal disappears. Under locked condition, the frequency of the VCO oscillation becomes a reasonable estimate of the input frequency and the VCO output reproduces the frequency of the input locked signal and tracks its variations within the synchronization range. Frequency information regarding the desired formant which is present in the input is thus transferred to the VCO. However, the

VCO output does not contain the input amplitude information. For extraction of the formant both in its amplitude and frequency, the VCO output is fed to a frequency discriminator which gives a null output when the frequency of VCO aligns with its open loop value. Thus the formant frequency information will be contained in the dc output of the discriminator which, in turn, controls the centre frequency of a narrow-band tunable filter (NBTF). The output of the tunable filter thus resembles the formant, retaining both its amplitude and frequency information. In each channel, PLL is preceded by an amplitude limiter as the performance of a PLL is level-sensitive. In the laboratory model of the instrument, the synchronization ranges of the PLLs are adjusted so that they conform to the respective formant frequency excursion ranges; VCO free running frequencies, phase detectors, frequency discriminators and NBTFs are tuned in the middle of the respective channel bandwidths. Due care is taken in selecting linear dynamic ranges of the various building blocks of the system. With careful design, the outputs of the tunable filters resemble the formants containing amplitude and frequency information. The outputs of the tunable filters are

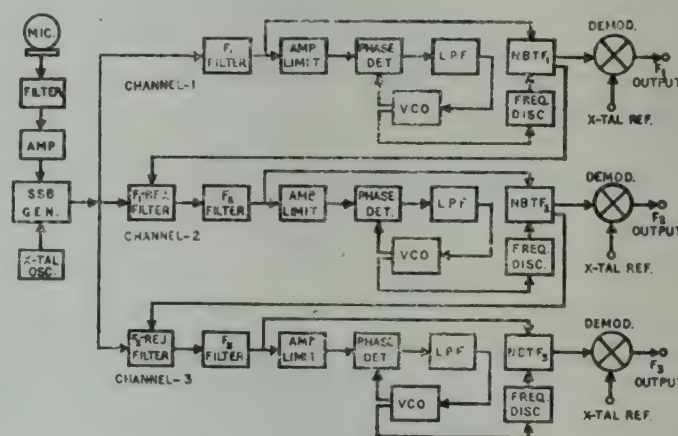


Fig. 2—Schematic block diagram of TLFES

Table 1—Spectrographic Measurement of Formant Structure of Bengali Vowels

Vowel	Sample examined	Formant bandwidth, Hz			Formant frequency, Hz			Formant amplitude, dB		
		$\Delta_1$	$\Delta_2$	$\Delta_3$	$F_1$	$F_2$	$F_3$	$A_1$	$A_2$	$A_3$
/i/	25	34	85	130	325	2270	2946	-4	-21	-28
/e/	16	45	70	92	400	2085	2730	-3	-19	-26
/ae/	14	53	83	127	728	1710	2575	-2	-13	-23
/a/	20	58	64	104	800	1215	2550	-1	-7	-28
/o/	25	46	57	115	650	985	2610	-0	-6	-33
/o/	20	40	71	98	462	925	2680	-3	-15	-35
/u/	20	43	65	92	340	850	2450	-3	-16	-41



demodulated by means of product demodulators to get the formants.

For satisfactory operation of the system, it has been found necessary to ensure that the desired formant in the channel is stronger than the accompanying formants. This is because of the fact that outputs of the channel filters are not essentially single formant signals and the accompanying formants act as interfering signals to deteriorate the performance of the PLL unless they are weaker in strength compared with the desired one. In the first channel, the accompanying formant is the weaker second formant which may fall within the first channel bandwidth. They are several decibels down in strength and become more weak due to the falling response of the channel filter near cut-off and due to the presence of amplitude limiter.

For similar reasons deleterious effects due to weaker third formant components become negligible in the second channel. However, the stronger first formant components create a real problem because they cannot be suppressed by ordinary means. Therefore, an additional  $F_1$ -tracking rejection filter has been incorporated in the second channel. For similar reasons, the third channel also contains  $F_2$ -rejection filter. The stronger  $F_1$ -components occur well outside the third channel bandwidth and they are rejected by the channel filter.

**2.1.1 Measurement of frequencies and amplitudes of formants by FES**—Measurement of frequencies and relative amplitudes of the first three formants of seven Bengali vowel sounds has been carried out with the laboratory model of FES. Demodulated channel outputs of FES were fed to the frequency and amplitude measuring devices. The analysis was based on

pronunciation of 20 informants, all of them having standard colloquial Bengali as their mother tongue. Measurements were taken for utterances of the speakers pronouncing the vowel sounds in isolation and in consonant vowel environment. Throughout the experiment the speakers were asked to use conversational level of effect while making the utterances. The results of the study for 20 men in the age group 20-30 years are plotted in Fig. 3 and also presented in Table 2, which additionally shows the range variations of the formant frequencies of different vowels. Fig. 3 shows that the first formant is lowest for the vowel /i/, increasing up to the position for vowel /a/, and then decreasing up to /u/. The second formant frequency position is highest for vowel /i/ and thereafter decreases gradually to the lowest position for vowel /u/. The vowel /i/ exhibits the most disparate and the vowel /ɔ/ (pronounced as 'a' in 'all') gives rise to most proximate first two formants. It should be pointed out that during analysis no distinction was made for the long and short varieties of the vowels /i/ and /u/ although separate graphemes are used in Bengali script. This is because of the fact that all the seven vowels may be long or short in Bengali dialects.

## 2.2 Spectrographic Measurement of Formant Structure

Sound spectrograph or sonagraph is a very standard audio-frequency spectrum analyzer widely used for speech analysis and phonetic research. The device provides permanent display of short-time amplitude spectrum of a speech signal. Formant frequency, amplitude and bandwidth data are usually obtained manually from these spectrograms. The principle of operation of a sonagraph is as follows.

Table 2—Formant Structure of Bengali Vowels as Measured by FES  
(Sample, 20 male informants)

Vowel	Formant frequency, Hz						Formant amplitude, dB		
	$F_1$		$F_2$		$F_3$		$A_1$	$A_2$	$A_3$
	Average	Range	Average	Range	Average	Range			
/i/	310	270-350	2240	2100-2350	2910	2800-3000	-5	-24	-27
/ɛ/*	385	350-450	2030	1900-2150	2680	2600-2800	-2.5	-21	-24
/æ/	690	650-750	1730	1650-1800	2590	2500-2700	-2	-11	-21
/a/	810	700-850	1245	1150-1350	2600	2500-2700	-1	-5	-26
/ɔ/†	640	600-700	1000	900-1100	2550	2450-2600	0	-8	-30
/o/	430	350-450	920	850-1000	2650	2600-2800	-4	-13	-32
/u/	350	300-400	840	750-900	2430	2350-2500	-3	-18	-38

\* Pronounced as 'e' in 'ten'

† Pronounced as 'a' in 'all'

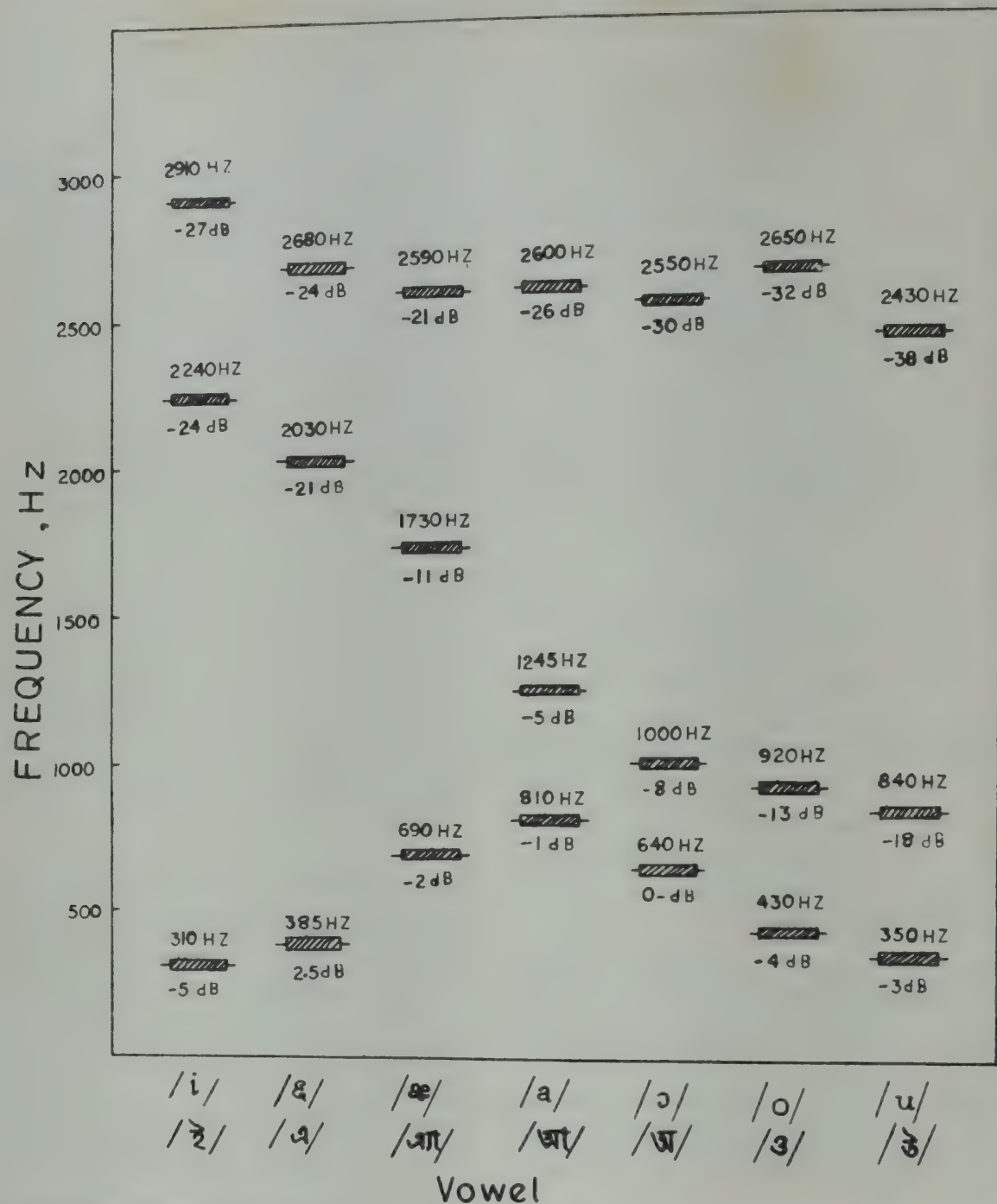


Fig. 3—Mean formant frequencies and their relative amplitudes (relative to  $F_1$  of /o/) of seven Bengali vowels for 20 male speakers

The speech sample to be analyzed is recorded on a magnetic disc. For analysis, the recorded sound is played back repeatedly and the signal is mixed with a carrier of variable frequency to give an output of 200 kHz, which is fed to a fixed bandpass filter. The frequency of the carrier is controlled by the position of a stylus on a recording drum mounted on the same shaft as the magnetic disc. The vertical position of the stylus is geared to the magnetic disc. The output current of the bandpass filter is amplified and passed to the stylus which moves on an electrically sensitive paper fixed to the drum and burns the paper in proportion to the current magnitude. Thus a time-intensity-frequency plot is permanently recorded on the paper.

To obtain 'amplitude section' or frequency versus amplitude portrayal at any given instant along the time scale, the sonagraph is switched to the 'section' position. A cam is placed on the drum periphery at the time of occurrence of the sound whose amplitude section is desired. As the magnetic disc and drum rotate, the cam closes the sectioner switch at the desired instant. Because the stylus scans the frequency scale with the filter, an amplitude (dB) versus frequency portrayal is obtained for the desired instant.

The manner in which the short-time amplitude spectrum at any instant in the utterance is exhibited in such a portrayal is illustrated in the upper portion of Fig. 4 which shows the amplitude section of the



vowel /i/ taken at the instant marked by the arrow. Amplitude-section was taken with 45 Hz filter, using 'high shaping' which introduces 6-dB per octave rise in response of the sonagraph. High shaping was used to make the high formants more nearly comparable with the low formants. The bottom portion of Fig. 4 illustrates the manner in which the broadband spectrogram highlights vocal mode pattern or formants (dark bands) of the vowel /i/.

Formant frequencies and amplitudes were measured using wide-band spectrograms and amplitude sections of different Bengali vowels. The data were obtained manually at the steady state of the vowels. Results of measurements are given in Table 2. The data are the averages for 3 male speakers. Spectrographic measurement corroborates the results obtained using TLFES.

**2.2.1 Measurement of formant bandwidth—**Formant bandwidths are represented by half-power bandwidths (in Hz) of the resonant peaks in the spectra of vowel sounds. The method of measurement of formant bandwidths from amplitude sections of the vowel was first adopted by Bogert.<sup>8</sup> Using amplitude sections of vowel sounds, he drew envelopes over the harmonics of the formants by visual inspection and measured bandwidths 3 dB below the peaks. The measurements are subject to error arising from the wide harmonic spacings. Dunn<sup>9</sup> reported a refinement in the spectrogram method.

In the present study, measurements were carried out in a manner similar to that adopted by Dunn. Wide-band spectrograms of different Bengali vowel sounds were taken and amplitude sections drawn at steady states of the vowels. A number of true suitable resonance curves of different bandwidths ranging from 25 to 250 Hz were inscribed on three sheets of transparent papers (one set of curves in each sheet of paper) in the amplitude and frequency scales of the spectrogram. These sheets were then placed over the peaks of the amplitude sections of the vowels and the curves which fit the individual formant peaks best were selected. The bandwidths of the best fitting curves were taken as the bandwidths of the respective formants. This method of individual formant matching suffers from an error in that a curve with greater bandwidth may be selected for a particular formant if the adjacent formant occurs very close to it. This effect due to adjacent formants is particularly pronounced in the case of first two formants of the vowels /ɔ/ and /a/ for which the first two formants are very close in frequency. In an effort to minimize this error, all the three sheets of transparent papers were simultaneously placed over

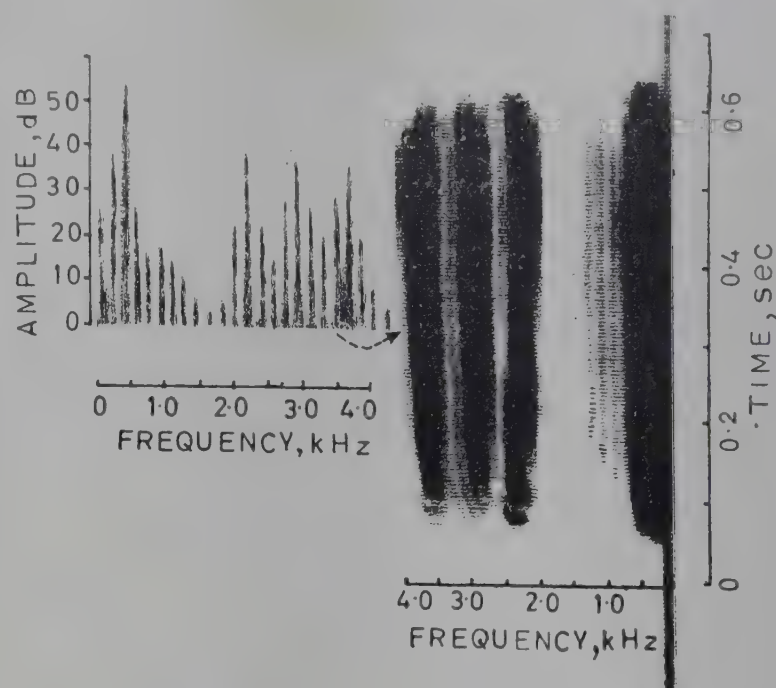


Fig. 4—Wide-band spectrogram of the Bengali vowel /i/ (bottom) and amplitude-section (taken with high-shaping) of the same vowel taken at the instant marked by the arrow

the formant peaks and their overlapping regions computed. The resulting envelope was compared with the actual envelope of the particular vowel spectrum. The set of curves which gave the best fitting envelope after combination and also matched well with the individual peaks, were selected. The bandwidths of the three curves were then taken as the bandwidths of the formants. It was observed that the bandwidths measured by the envelope matching method were 10-15% smaller than those obtained from the individual formant matching method. Considerable variation in the formant bandwidths was observed even for a particular speaker. However, the average values gave a reasonable estimate of formant bandwidths. The average values of the formant bandwidths are shown in Table 2. Altogether 140 samples for seven Bengali vowels uttered by male speakers were measured. While taking spectrograms, signal levels were maintained at a preselected value so as to avoid any overloading of the circuits of the sonagraph to avoid generation of spurious harmonics. The results obtained compared well with those obtained by other investigators.<sup>9,10</sup>

### 3. Vocoder Implementation using TLFES

Speech-band compression systems based on sending-end analysis and receiving-end synthesis are known as vocoders. Vocoders do not try to preserve the original voice waveform. They preserve the perceptually significant characteristics of speech waveforms with the intention of resynthesizing intelligible speech which sounds like original. In this section,



two types of speech-band compression systems mentioned in Section 1 will be described. The requisite formant frequency and amplitude data for either scheme are obtained from tracking loop formant extractor.

### 3.1 Frequency Dividing Vocoder (FDV)

The original interest in speech-band compression by frequency division was aroused from the idea that if every frequency present in the complex speech signal could be divided and multiplied independently, the bandwidth required for transmission of speech could be reduced. Related efforts with a large number of contiguous band-pass filters to operate on each voice harmonic were made.<sup>11</sup> But the requirement of a large number of band-pass filters for separation of the harmonics is a practical problem. The situation may be simplified by giving attention to the formant bands only. Formant bands of speech have similarities to large index frequency modulation<sup>2</sup> and, therefore, the principle of frequency division can be applied to each formant separately to restrict the frequency excursion ranges of the formants. Band-width compression can then be effected by transmitting only the formants and their adjacent components through a channel of narrower bandwidth. At the receiver, the approximate short-time amplitude spectrum will be reconstructed after applying the principle of frequency multiplication on each formant and recombination of the formants.

Fig. 5 shows the schematic block diagram of the FDV. The system has already been implemented in the hardware. The laboratory model has been designed for 2:1 bandwidth reduction. Formant tracking and extraction from input SSB signal was achieved by the TLFES incorporated in the system. In the laboratory model, the outputs of NBTF of TLFES were directly fed to a chain of regenerative-type amplitude preserving frequency dividers. For 2:1 compression of the communication bandwidth the frequency divided outputs from the channels were limited to one-half of the original frequency ranges by static band-pass filters BPF<sub>1</sub>, BPF<sub>2</sub> and BPF<sub>3</sub> (Fig. 5). Outputs of the narrow filters were then added to yield a transmission signal which was confined to about one-half the original bandwidth occupied by the speech signal. Bandwidths of the filters BPF<sub>1</sub>, BPF<sub>2</sub> and BPF<sub>3</sub> were approximately 350, 800 and 700 Hz respectively. Transmitted signal was, therefore, bandlimited to nearly 1850 Hz which is nearly one-half of the original bandwidth.

At the receiver, the received signal was separated once again into three bands by means of bandpass

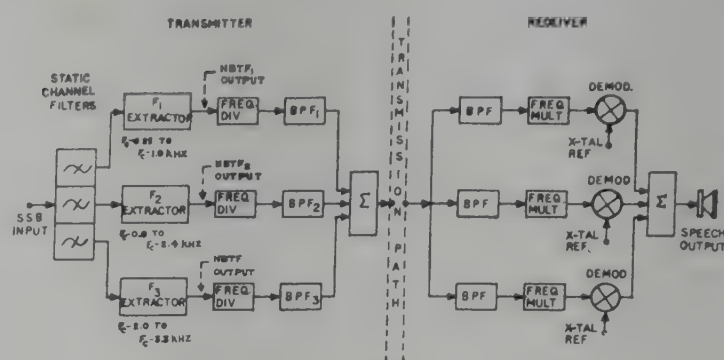


Fig. 5—Block diagram of FDV

filters and the formant bands were restored by frequency multiplication. The resulting signals were demodulated and recombined to reconstruct the output speech signal. The process of frequency division was such that the component of largest amplitude (corresponding to the formant) was divided, and the other adjacent components in the formant band were simply translated down maintaining the original spacings and similarity of amplitudes. Thus the formant bands were well preserved after frequency division. In the case of unvoiced sounds the envelope of the speech spectra exhibits formant-like pattern, although the actual frequency components are noise-like. The operation was similar to those for voiced sounds. The major component in each channel was divided and remainder translated in frequency, thus producing a noise-spectrum with a similar envelope at half the frequency of the major component.

The laboratory model of the system was then tested with natural voiced utterances. It was observed that in the absence of narrowband filters between the frequency dividers and multipliers, the reproduced signals were highly intelligible and almost natural sounding. Listening tests carried out with isolated vowels, words and sentences confirmed that in some cases even the speaker identification was possible.

Inclusion of bandpass filters between the frequency dividers and multipliers introduced slight harshness in the demodulated sound although the output sound quality compared well with that of the input. However, serious distortions like burbling reported earlier in similar system like VOBANC<sup>6</sup> appeared to be absent. In VOBANC, three static bandpass filters were used for separating the formants. This simplification obviously degenerated the speech as the outputs of the channel filters were no longer single formant signals. In the present system, separation of formant bands was accomplished by tracking-loop formant extractor. The purity of the formant bands is probably the reason for improvement in the output speech quality. Such



conclusion, however, requires further investigation on the system performance with higher division ratios. It can be said that the results of the tests carried out with the 2 : 1 bandwidth reduction system are highly encouraging.

Listening tests carried out with the laboratory model of FDV with 10 talkers and same number of listeners showed almost 100% intelligibility for vowels and 85% for consonant articulation.

### 3.2 Formant Tracking Vocoder (FTV)

The circuit arrangement of the proposed FTV is illustrated in Fig. 6. FTV attempts to reconstruct speech signal from spectral and excitation information. In the analyzer, the formant frequency and amplitude data are obtained from the formant extractor. Extraction of pitch is accomplished by a suitable PLL of 200 Hz synchronization range preceded by a 50-250 Hz bandpass filter. Zero-crossing detectors generate slowly varying dc voltages representing the frequencies of the formants  $F_1, F_2, F_3$  and the pitch  $F_0$ . Control voltages  $A_1, A_2, A_3$  representing the formant amplitudes are obtained by rectification and low-pass filtering of the formant extractor outputs. Low-pass filters confine these seven control signals to approximately 25 Hz each. All these control signals and the information regarding voiced/unvoiced switching are then linked to the synthesizer.

Synthesis is achieved by the generation of 'voice' in an excitation generator (pulse generator) and its subsequent spectral shaping in the same way as the spectral shaping performed by the vocal tract on the voice-source spectrum generated in the human larynx. Control signal  $F_0$  controls the frequency of a variable frequency pulse generator. Signals  $F_1$ ,  $F_2$  and  $F_3$  control the centre frequencies of three variable resonant circuits of the synthesizer. In the case of voiced sounds, the voiced/unvoiced switch connects the output of the pulse generator to the inputs of the variable resonant circuits. In the case of unvoiced sounds, a noise generator excites the resonant circuits. Amplitude information is restored by multiplying the control signals  $A_1$ ,  $A_2$  and  $A_3$  with the outputs of the variable resonant circuits. Recombination of the resulting outputs after multiplication gives synthesized speech output. The system generates intelligible speech sounds when the control signals are linked directly to the synthesizer without further processing.

In the case of voiced sounds, PLLs of the formants extractor faithfully track the frequency variations of the formants by locking onto each formant. In the case of unvoiced sounds, the input signal is noise-like in nature. Many inband signals may be present simultaneously in each channel input and

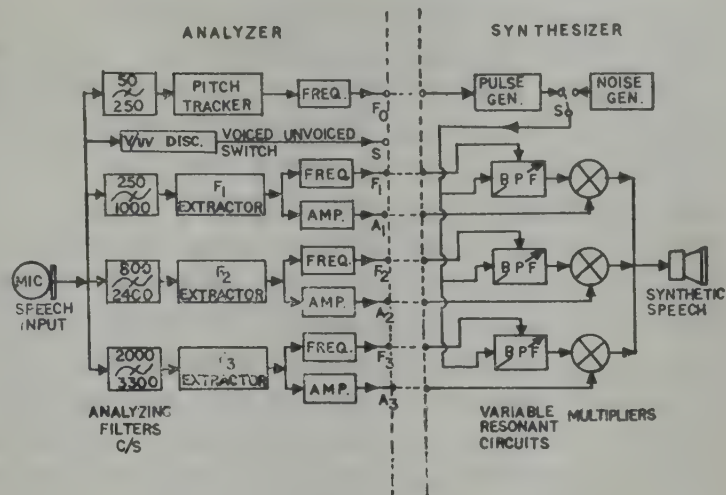


**Fig. 6—Block diagram of FTV**

PLLs may fail to lock onto any one of them. The outputs of the VCO oscillations will be randomly modulated in frequency around their free running frequencies. In any event, the variable resonant circuits of the synthesizer will be tuned around the centres of the respective channels and will select noise bands from the input.

The main difficulty of the system is in the extraction of excitation information. This can be avoided by applying voice-excitation technique in FTV.<sup>12</sup>

#### 4. Some Other Possible Uses of TLFES

#### 4.1 As Supplementary Hearing Aid

Frequency translation of speech spectrum towards lower frequencies is of great importance for providing supplementary aids to persons with partial auditory impairments. In severe cases, the residual hearing is often confined to a small bandwidth, usually in the low frequency end of the audible spectrum and the conventional hearing aids fail to provide required compensation for these losses at high frequency regions of the spectrum. Auditory hearing sensors are oriented towards making maximal use of residual hearing by frequency translation of the speech spectrum to the low frequency range where residual hearing exists. The requirement is to design a system which will transform speech into the lower frequencies and will provide good representation of its informational content.

In one proposal whole speech spectrum is transposed by frequency division to a lower frequency range. Systems based on this idea focus more attention upon frequency division of the individual voice harmonics of speech waveforms.<sup>11-13</sup> A similar system may be designed by using PLLs as frequency selective circuits (as indicated in Section 2) in which each PLL will operate on an individual harmonic. Reconstruction of the short-time amplitude spectrum



will then be achieved by frequency division of the VCO outputs of PLLs and restoration of amplitude information after division. PLLs with harmonic generators inserted into the feedback loops between the VCO outputs and the phase detectors may be used as frequency selective frequency dividers. As many as 30-35 PLLs for separation of harmonics and additional 30-35 PLLs for frequency division will be required. Amplitude information will be restored by the same number of multipliers. Integrated circuit PLLs NE 565, NE 561 and multiplier chip MC 1495 may be used. However, number of channels required and cost of terminal equipment will be a practical problem.

As an alternative, a four-channel system based on PLL pitch and formant extraction may be used. Speech signal will be split into four subbands as indicated in FTV. Four PLLs will track the frequency variations of the pitch and the formants by locking onto them. The outputs of VCOs will contain the frequency information. Four additional PLLs based on the principle of subharmonic synchronization will act as frequency selective frequency dividers. Amplitude information will be restored by multiplying the rectified-smoothed outputs of the channel bandpass filters with the VCO outputs of the frequency dividers. Combined outputs of the multipliers will represent speech spectrum transformed into lower frequencies retaining the informational content of the input speech.

#### 4.2 As Analyzer for Speech and Speaker Recognition Systems

It is well known that vowel sounds are well described by the first three formant frequencies  $F_1$ ,  $F_2$  and  $F_3$ , i.e. maxima of the spectral envelope and their relative amplitudes. Therefore, automatic extraction of these parameters from speech suggests feasibility of automatic recognition of vowel sounds. In fact, formant data have potential application in speech and speaker recognition because of their close relation to the phonetic concept of segmentation. Weibel<sup>14</sup> reported that generally a good separation of the vowels is obtained by plotting the frequencies of the second formant  $F_2$  against that of the first formant  $F_1$ . Doddington<sup>15</sup> made use of the pitch, formant and intensity data to form reference patterns for speaker identification. Frequency data are considered attractive because they are resistant to variations in the amplitude-frequency characteristics of the voice communication link.

Preliminary studies indicate that perfect relationship among the formant frequencies does not exist

for different vowels. It appears that certain interrelation function among the formants might be used for vowel and speaker recognition. Parameters like  $(F_2 - F_1)$ ,  $(F_3/F_1)$  and  $(F_3/F_2)$  have shown satisfactory separation properties and might have prospects for use as recognizing parameters.

Since  $F_1$  and  $F_2$  are more dependent on the vowel sounds and  $F_3$  bears more information about the speaker,  $(F_3/F_1)$  and  $(F_3/F_2)$  and  $F_3$  have more potential for speaker identification. Additional information regarding the speaker may be provided by using information regarding the voice-source fundamental,  $F_0$ .

Usually speech and speaker recognition systems utilize some form of spectrum analysis for collecting these data. The measured parameters are then compared with a set of stored reference patterns. FES described in Section 2 may be used as a useful analyzer for such systems with considerable reduction in the processing time.

#### Acknowledgement

The author is grateful to Dr A K Dutta for pointing out the problem and for his valuable guidance in the preparation of the manuscript. He is also grateful to Prof. D Datta Majumdar of the Indian Statistical Institute, Calcutta, for making available their sonagraph for the present studies. He wishes to thank Prof. S C Chakrabarti, Head of the Department of Physics, University of Burdwan, for his kind interest in the progress of the work. Thanks are also due to the students and research workers of the department who offered their valuable time as informants.

#### References

1. Fletcher H, *Speech and hearing in communication*, (D Van Nostrand, Princeton, N J), 1953.
2. Flanagan J L, *Speech analysis-Synthesis and perception*, (Springer-Verlag, Berlin), 1972.
3. Fant G M, *Acoustic theory of speech production*, (Mouton & Co., Gravenhage, The Hague, Netherlands), 1960.
4. Howard C R, *J. acoust. Soc. Am.*, 28 (1956), 1091.
5. Lawrence W, cited in *Communication theory*, edited by W Jackson (Butterworths, London), 1953, 460.
6. Bogert B P, *J. acoust. Soc. Am.*, 28 (1956), 151.
7. Datta A K & Chakrabarti S K, *Indian J. pure appl. Phys.*, 16 (1978), 463.
8. Bogert B P, *J. acoust. Soc. Am.*, 25 (1953), 791.
9. Dunn H K, *J. acoust. Soc. Am.*, 33 (1961), 1737.
10. House A S & Stevens K N, *J. Speech hear. Res.*, 1 (1958), 309.



11. Schroeder M R, Logan B F & Prestigiacomo A J, *New methods of speech analysis-synthesis and bandwidth compression*, paper presented at the Proceedings of Stockholm Speech Comm. Seminar R I T, Stockholm, Sept. 1962.
12. Flanagan J L, *IRE Trans. Audio.*, AV-8 (1960b), 95.
13. Vilbig F, *J. acoust. Soc. Am.*, 24 (1952), 33.
14. Welbel E S, *J. acoust. Soc. Am.*, 27 (1955), 858.
15. Doddington G R, *J. acoust. Soc. Am.*, 49 (1971), 139.

# Communications

## Preliminary X-ray Study of Pyrene Picrate

S D PURKAYASTHA & A N TALUKDAR

Physics Department, University of Gauhati, Gauhati

Received 17 August 1979; revised received 21 December 1979

Oscillation and Weissenberg photographs by X-rays reveal that the crystal of pyrene picrate, a charge-transfer complex, is monoclinic having eight molecules per unit cell. The systematic absences reveal that the space group is either  $P2/c$  or  $Pc$ . A choice between the two space groups has been made by statistical test of intensity confirming the space group  $Pc$ .

Pyrene picrate (Fig. 1) is a crystalline molecular addition compound, the constituent molecules of which are held together by charge-transfer interaction. Interest in this compound is drawn from the fact that the atoms of this addition compound have nearly the same scattering power and the structural groups are in the form of ring configurations. All these, render the structural investigation of pyrene picrate an attractive problem for application of the techniques of optical transform methods.<sup>1</sup>

Pyrene picrate (m. p. 222 °C) crystallizes from alcohol in the form of red needles, elongated along the  $b$ -axis. Oscillation and Weissenberg photographs show that the crystal is monoclinic and the dimensions of the unit cell are:  $a = 17.89 \pm 0.04$  Å,  $b = 6.82 \pm 0.01$  Å,  $c = 29.23 \pm 0.03$  Å and  $\beta = 82.5^\circ$

The density measured by flotation in a mixture of carbon tetrachloride and acetic acid was found to be  $1.56 \text{ g cm}^{-3}$ . The calculated density corresponding to eight molecules in the unit cell is  $1.62 \text{ g cm}^{-3}$ . Zero-level  $a$ ,  $b$  and  $c$  axis Weissenberg photographs reveal only one type of systematic absence  $h0l$  for  $l = 2n + 1$  indicating that the space group

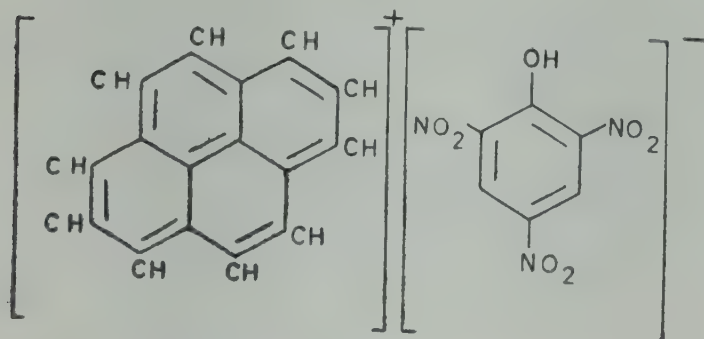


Fig. 1—Structure of pyrene picrate

is either  $P2/c$  or  $Pc$ . Using statistical  $N(z)$  test<sup>2</sup> the space group was deduced as  $Pc$ .

We are indebted to Prof. O N Mathur, of the University of Rewa, for supplying the crystal sample of pyrene picrate and for his interest in the work. One of us (SDP) acknowledges with thanks the financial assistance received from the University Grants Commission, New Delhi.

## References

1. Hanson A W, Lipson H & Taylor C A, *Proc. R. Soc.*, A218 (1953), 371-384.
2. Howells E R, Phillips D C & Rogers D, *Acta Crystallogr.*, 3 (1950), 210.

## Temperature Dependence of $^{35}\text{Cl}$ NQR in Some Chloronitrotoluenes

J UCHIL & D L R SETTY

Department of Physics, University of Mysore  
Mangalagangothri, Konaje 574 152

and

A INDUMATHY & J RAMAKRISHNA

Department of Physics, Indian Institute of Science  
Bangalore 560 012

Received 21 March 1980

The temperature variation of nuclear quadrupole resonance (NQR) frequency is studied in 5-chloro 2-nitro, 4-chloro 3-nitro, 2-chloro 4-nitro and 6-chloro 2-nitrotoluenes. NQR is detected in 5-chloro 2-nitrotoluene for the first time and its temperature variation in the range 77-297 K is reported. No phase transition is observed in this temperature range in any of these compounds except a probable weak transition in 4-chloro 3-nitrotoluene around 90 K.

The first NQR observation in chloronitrotoluene was by Bray and Barnes<sup>1</sup> for the compound 6-chloro 2-nitrotoluene at 77 K. Later Biedenkapp and Weiss<sup>2</sup> reported resonances at 77 K in 4-chloro 3-nitro, and 2-chloro 4-nitrotoluenes. The room temperature work on 6-chloro 2-nitro, and 2-chloro 4-nitrotoluenes was reported by Nagarajan and Murthy.<sup>3</sup> Temperature variation of NQR frequency in the range 90-302 K was carried out on 6-chloro 2-nitrotoluene by Ramakrishna<sup>4</sup> and a possibility of a phase transition at 90 K was surmised in this compound. A complete study of the temperature variation from liquid nitrogen up to the room temperature was carried out by the authors in all these



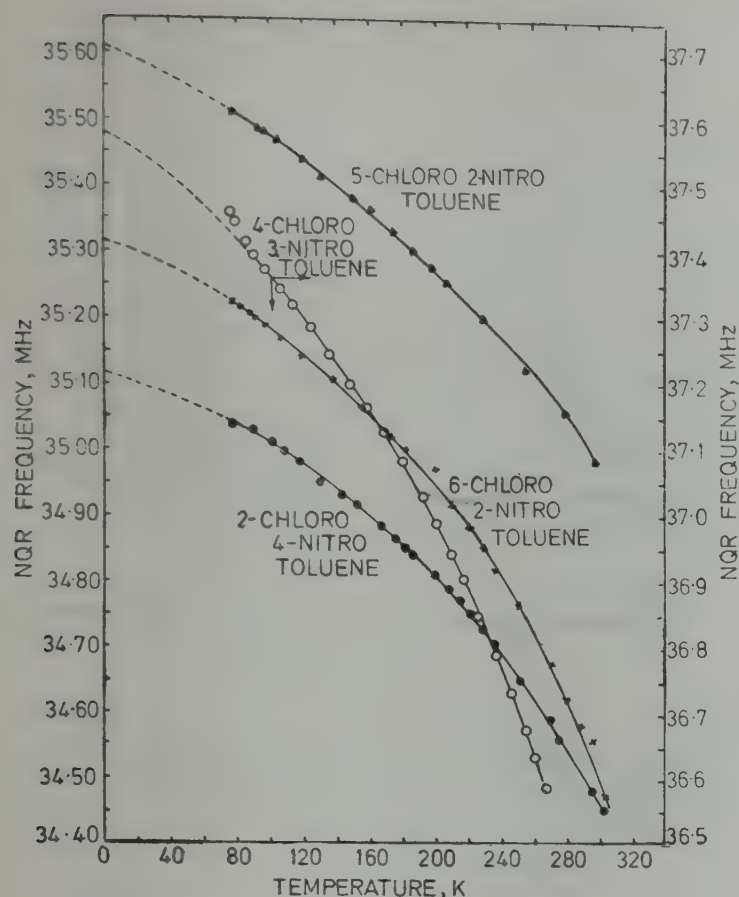


Fig. 1—Temperature variation of the NQR frequency in the four compounds of chloronitrotoluenes

Table 1— $^{35}\text{Cl}$  NQR Frequencies in Some Chloronitrotoluenes

Compound	$\nu$ in MHz		$\nu_0$ in MHz	
	77K	High temp.	Extra-polated	Com-puted
5-chloro 2-nitrotoluene	35.511	34.980 (297K)	35.610	35.505
4-chloro 3-nitrotoluene	37.453	36.584 (260K)	37.585	37.560
2-chloro 4-nitrotoluene	35.043	34.450 (302K)	35.120	35.126
6-chloro 2-nitrotoluene	35.223	34.470 (302K)	35.315	35.307

compounds and the results are presented in this communication which includes a hitherto unreported NQR observation on 5-chloro 2-nitrotoluene and its temperature variation.

The chemicals 6-chloro 2-nitro, and 5-chloro 2-nitrotoluenes were obtained from M/s Koch-Light, England and 4-chloro 3-nitro, and 2-chloro 4-nitrotoluenes from M/s E Merck, W Germany. The compounds 5-chloro 2-nitro, and 4-chloro 3-nitrotoluenes are liquids at room temperature (302 K). Compounds 6-chloro 2-nitro, and 2-chloro 4-nitrotoluenes (which are solids at room temperature) were further purified by recrystallization from

ethanol and were used in the polycrystalline state in these experiments.

A frequency modulated self-quenched super-regenerative NQR spectrometer of Dean's type<sup>5</sup> coupled with a lock-in-amplifier and a strip chart recorder was used to detect the signals. None of the signals was strong enough to be displayed on a cathode ray oscilloscope at low modulation. The low modulation was employed throughout to minimize line broadening due to modulation and to improve the accuracy of frequency measurement. The resonance frequency was fixed using the standard beat-method employing a very stable signal generator. The accuracy of frequency measurement is found to be within  $\pm 1$  kHz and the temperature is measured within an accuracy of  $\pm 0.5$  K. NQR spectrum at 77 K in each compound was recorded by housing the sample coil in a hollow conical-shaped metallic conductor attached to the end of the probe and by immersing it in a liquid nitrogen bath. The temperature variation work was carried out by allowing the assembly to warm up very slowly as the liquid nitrogen evaporates out naturally.

**Results**—The temperature variations of the NQR frequencies studied in four compounds of chloronitrotoluene are given in Fig. 1. The resonance frequencies at the extreme points of the temperature range covered are given in Table 1. A fourth degree polynomial fitted to the observed frequency variation (in kHz) with temperature by the method of least squares using DEC-10 computer for each of the 4 compounds is as follows:

(1) 5-chloro 2-nitrotoluene:

$$\nu_T = 35,605 - 1.0642 T - 0.0024 T^2 - 0.3263 \times 10^{-5} T^3 - 0.1498 \times 10^{-8} T^4$$

(2) 4-chloro 3-nitrotoluene:

$$\nu_T = 37,560 - 1.1510 T - 0.0041 T^2 - 0.9442 \times 10^{-5} T^3 - 0.2049 \times 10^{-7} T^4$$

(3) 2-chloro 4-nitrotoluene:

$$\nu_T = 35,126 - 0.8782 T - 0.0022 T^2 - 0.4721 \times 10^{-5} T^3 - 0.9150 \times 10^{-8} T^4$$

(4) 6-chloro 2-nitrotoluene:

$$\nu_T = 35,307 - 0.9274 T - 0.0024 T^2 - 0.6265 \times 10^{-5} T^3 - 0.1762 \times 10^{-7} T^4$$

NQR frequencies at 0K ( $\nu_0$ ) extrapolated from the experimental curves and from the computed polynomial equations are also given in the last two columns of Table 1. They are very close to each other.

**Discussion**—The NQR line in 5-chloro 2-nitrotoluene is observed for the first time. The measured frequency 35.511 MHz at 77 K is in fair agreement with the value (35.552 MHz) calculated using Bray and Barnes equation.<sup>1</sup> However, the calculated



value ( $35.1 \pm 0.2$  MHz) using Biedenkapp and Weiss equation<sup>2</sup> differs much from the observed value.

The temperature dependence of NQR frequencies (90-302 K) in 6-chloro 2-nitrotoluene has been reported and a first order phase transition was surmised around 90 K by Ramakrishna.<sup>4</sup> To verify this transition the study of this compound has been repeated. However, no phase transition in the temperature range 77 to 302 K is observed as indicated by a smooth variation of the frequency (Fig. 1).

The temperature variation of NQR frequencies of <sup>35</sup>Cl in 4-chloro 3-nitrotoluene has shown a slight discontinuity around 90 K indicating a phase transition which needs further experimental confirmation.

Torsional frequency calculations in all the four compounds referred above are in progress and will be published later.

#### References

1. Bray P J & Barnes R G, *J. chem. Phys.*, 27 (1957), 551.
2. Biedenkapp D & Weiss A, *J. chem. Phys.*, 49 (1968), 3933.
3. Nagarajan V & Murthy C R K, *Curr. Sci.*, 31 (1962), 279.
4. Ramakrishna J, *Indian J. pure appl. Phys.*, 4 (1966), 450.
5. Das T P & Hahn E L, *Nuclear Quadrupole Resonance Spectroscopy, Solid State Physics Supplement-I* (Academic Press, New York), 1958, 90.

#### Centres Associated with 480 K Thermal Glow Peak in KBr:Ti

R V JOSHI & R T CHAUDHARI

Applied Physics Department, Faculty of Technology & Engineering, M S University of Baroda, Baroda 390 001

Received 19 April 1980

Thermal glow curves of pretreated KBr:Ti phosphors exhibit a glow peak at 480 K besides another peak around 400 K. The 480 K peak is observed for specimens with lower Ti concentration after excitation with ultraviolet radiation. It is tentatively proposed that the centres responsible for the peak are single  $Ti^{3+}$  ions in association with cation-anion vacancy pairs.

The present investigation concerns with the study of the behaviour of 480 K glow peak observed in certain pretreated KBr:Ti phosphors. The specimens were prepared by the crystallization from aqueous solution in which the Ti content was of the order of  $10^{-3}$  mf. The powder specimens so obtained have been annealed at 500°C in vacuum and then either cooled slowly or cooled rapidly to room temperature. They were subsequently compressed to tablets in a

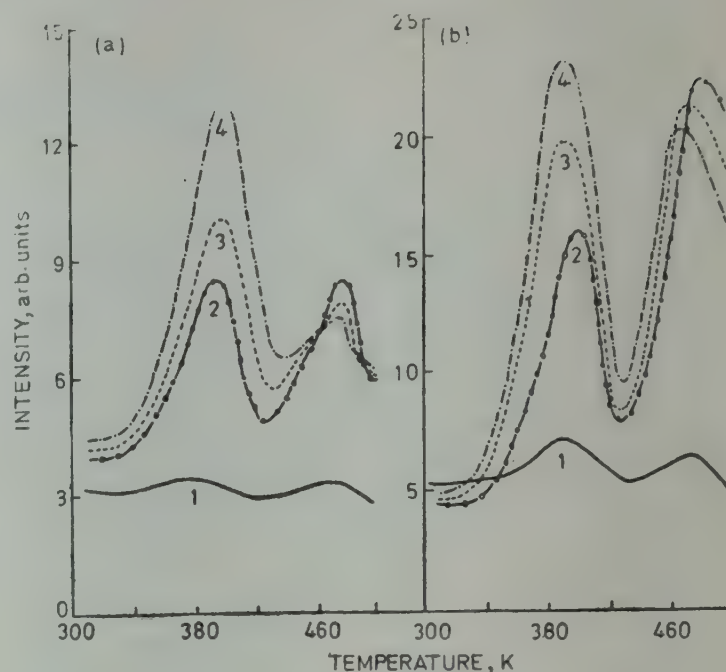


Fig. 1—Thermoluminescence of thermally pretreated KBr:Ti phosphors pressed to tablet form, after excitation with ultraviolet radiation [Curves : 1, 2, 3 and 4 correspond to successive thermal cycles. (a) annealed and slowly cooled sample; (b) annealed and rapidly cooled sample]

stainless steel press. The thermal glow curves were obtained after excitation of the specimens at room temperature by ultraviolet radiation from hydrogen lamp. In each case, the specimen was warmed, at the rate of  $13^{\circ}\text{C min}^{-1}$ , to about 500 K and then returned immediately to room temperature for remeasurement of the glow curve after excitation. The specimen was thus subjected to successive cycles of heating and cooling.

Data presented in Figs. 1 (a) and (b) correspond to the specimens subjected to different thermal pretreatments and then deformed by stressing. In both the cases, the glow curves exhibit two peaks at 400 and 480 K both of which become significant in the second heating run. It is believed that the 480 K peak is a property of single  $Ti^{3+}$  ions since it is observed in phosphors having only low Ti content. The peak appears conspicuously when the slowly cooled or quenched specimen is deformed and then subjected to annealing during first thermal cycle. In the slowly cooled specimen, the dislocation motion induced by deformation would redissolve the precipitated impurity on an atomic scale besides increasing the vacancy concentration and dislocation density in the specimen. In the quenched specimen, the impurity ions could be in the dispersed state along with quenched-in vacancies and the deformation in this case would increase the dislocation content. It is proposed that due to annealing, during the first thermal cycle, thermally stimulated motion of the  $Ti^{3+}$



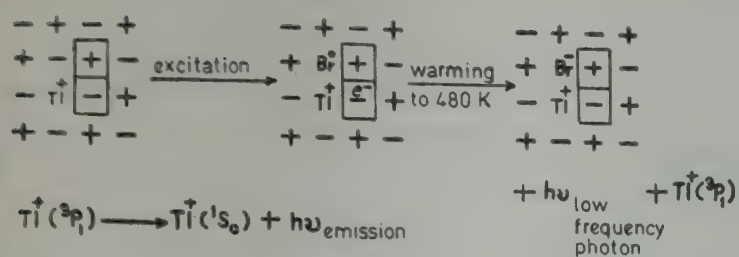


Fig. 2—Steps involved in the thermoluminescence emission process of KBr:Tl phosphors

ions towards dislocations takes place. In this situation, a  $\text{Tl}^+$  ion in the proximity of a cation-anion vacancy pair is presumed to form the luminescence centre for the 480 K glow peak. The excitation of the centre would lead to the transfer of the electron from a neighbouring  $\text{Br}^-$  ion to the negative ion vacancy of the pair. Thus, a hole situated on the bromine atom, gets trapped at the adjacent positive ion vacancy and the electron is trapped at the negative ion vacancy of the pair. On heating the specimen to 480 K, the electron-hole recombination takes place at the hole site with the emission of a photon of low frequency. The excess energy is transferred to the adjacent  $\text{Tl}^+$  ion which then gets excited. The return of the excited  $\text{Tl}^+$  ion to the ground state is accompanied by the characteristic emission of  $\text{Tl}^+$  ion. The steps involved in the above process are illustrated in Fig. 2.

It may be mentioned that the glow peak at 400 K has been discussed earlier.<sup>1</sup> It is attributed to the single  $\text{Tl}^+$  ion in association with a negative ion vacancy in which  $\text{Tl}^+$  ion is in the neighbourhood of dislocation or has been precipitated on it. The increase in the height of 400 K peak and decrease in the height of 480 K peak during subsequent heating runs as observed in Figs. 1 (a) and (b) can be understood on the basis of the migration of  $\text{Tl}^+$  ions towards dislocation due to thermal diffusion. In the results reported earlier<sup>1</sup> it has been mentioned that the 400 K peak in KBr:Tl arises from the generation of negative ion vacancies at the dislocation sites, due to X-ray irradiation of the specimen. In the present experiment, the exciting radiation used is ultraviolet light which is comparatively less energetic. However, it has been reported in the literature that interstitials can also be produced by ultraviolet irradiation.<sup>2-4</sup>

One of the authors (RTC) is grateful to the University Grants Commission, New Delhi, for the award of a research fellowship.

#### References

1. Joshi R V & Chaudhari R T, *Radiat. Eff.*, **41** (1979), 175.
2. Konitzer J & Hersh H N, *J. Phys. Chem. Solids*, **27** (1966), 771.
3. Pooley D & Runciman W A, *Solid St. Commun.*, **4** (1966), 351.
4. Goldstein F T, *Phys. Status Solidi*, **20** (1967), 379.

# Notes

## Resistivity of Thin Bismuth Films

A R VAMDATT

Department of Physics, South Gujarat University  
Surat 395 007

Received 24 September 1979

Resistivity of vacuum-deposited thin bismuth films, having thicknesses below 600 Å, has been measured. The resistivity-thickness variation has been found to deviate considerably from the prediction of the Fuchs theory. This could be explained on the lines suggested by J E Parrott [*Proc. phys. Soc., Lond.*, 85 (1965), 1143]. Magnitudes of the critical angle ( $\theta$ ) and coefficient of specular reflection ( $p$ ) have been obtained for films in certain thickness ranges. Specular reflection in films of thickness  $< 300$  Å and angular dependence of  $p$  are indicated.

Fuchs<sup>1</sup> was the first to analyze rigorously the problem of electrical conduction of thin films. He considered an ideal metal having spherical Fermi surfaces and introduced a parameter  $p$ , the coefficient of specular reflection.

Among metallic films, thin films of bismuth provide interesting results as regards the measurement of Hall effect and electrical resistivity, which naturally underline the necessity of a proper theory to explain them. Thus, for instance, Duggal and Rup<sup>2</sup> observed oscillating Hall coefficient and resistivity in single crystal bismuth films having thicknesses between 250 and 1700 Å at temperatures 90 and 300 K respectively. Similarly, Miller and Moller<sup>3</sup> obtained an oscillating Hall coefficient in the case of bismuth films with thicknesses up to 1800 Å at room temperature. James *et al.*<sup>4</sup> offered an interesting suggestion that the saturation effect of electrical conductivity of bismuth samples, thinned by etching, might be due to diffuse reflection of electrons at etched surfaces.

Neuman and Ko<sup>5</sup> studied the dependence of conductivity of thin (1000-5000 Å) polycrystalline bismuth films on the crystalline grain size. An important conclusion of their study is that the resistivity of the films does not follow any definite variation with film thickness, which is in contrast to the Fuchs theory.

The author studied<sup>6</sup> at room temperature the behaviour of electrical resistivity of bismuth films of

thicknesses below 600 Å prepared by thermal evaporation.

*Experimental details*—The evaporation plant was designed and constructed<sup>7</sup> in the laboratory with provision for annealing and measuring resistances under vacuum to avoid the effects due to absorption and chemisorption of gas molecules on the film surface. The films were deposited at room temperature on 'gold seal' microscope slides by evaporating spectroscopically pure metals from a molybdenum boat at a pressure of nearly  $10^{-5}$  torr. The substrates were first treated with hot chromic acid, rinsed with doubly distilled water and then with isopropyl alcohol. The final cleaning was carried out by ionic bombardment, during the initial stage of evaporation process, and then by a baking process, up to 200°C, under vacuum. The source-to-substrate distance was kept 15 cm throughout. While annealing the films under vacuum, the resistances were measured with a Kohlrausch bridge in conjunction with a sensitive galvanometer ( $10^{-6}$  A/div.) and the temperature was measured with an iron-constantan thermocouple placed in contact with the film.

The thickness of the film was measured by the method of multiple beam interferometry.<sup>8</sup> The gasket was prepared to enable small displacements of the film and hence of the fringe system to be formed. The source of light was a cadmium-mercury tube used in conjunction with a green filter. Interference fringes were observed with a low power microscope of magnification about 15 and the width and displacement of fringes were measured with an estimated error of 5%. The ultimate accuracy in the measurement of film thickness was  $\pm 20$  Å. Only those films for which the measurements of resistances and thicknesses were reproducible to a fair degree of accuracy were taken for the present study.

*Results and discussion*—The films so obtained are found to have an aggregated structure and their resistivities show similar abnormal behaviour with thickness as obtained by Neuman and Ko.<sup>5</sup>

The majority of metals have an electron mean free path of a few hundred angstroms. However, for bismuth it is of the order of one micron. Due to these large mean free paths, electrons in



Table 1—Values of  $\theta$  and  $p$ 

Thickness of film Å	$\theta$ deg.	$p$
Below 300	89	0.05
300-500	84	0.20
Around 600	75	0.45

bismuth may scatter at the grain boundaries as well as at the film surfaces, the latter effect resulting due to the dependence of electron scattering on film thickness. Hence films up to thicknesses of 600 Å have been investigated in the present study.

Investigation of the thickness dependence of resistivity thus requires the study of the parameter  $p$ , denoting the fraction of electrons incident on the boundary surface that are reflected specularly. This parameter was treated as a constant for a long time after it was first introduced.<sup>9</sup> Comparison of electron reflection at the surface with optical reflection has led to the possibility of the dependence of  $p$  on the electron de Broglie wavelength and angle of incidence of electrons at the surface.<sup>9,10</sup> A critical angle  $\theta$  is introduced and it is assumed that  $p = 1$  for incident angles greater than  $\theta$  and  $p = 0$  for incident angles less than  $\theta$ . Brandli and Cotti<sup>9</sup> plotted reduced thin film resistivity as a function of reduced thickness for different values of  $\theta$ . Also, Campbell<sup>11</sup> obtained a similar plot for different values of  $p$  independent of  $\theta$ .

The author has followed the methods of these workers<sup>9,11</sup> to obtain the values of  $\theta$  or  $p$  using the experimental values of film thicknesses and resistivities (Table 1).

**Conclusion**—According to the Fuchs theory, the resistivity of a film must decrease with increasing thickness for all values of  $p < 1$ . However, the variation of resistivity of bismuth films with thickness can be explained in terms of the theory of size effects in electrical conduction proposed by Parrott.<sup>10</sup> He explored the possibility that  $p$  changes abruptly from 1 to 0 when the change of electron wave vector on specular reflection exceeds a certain limit. The theory can be applied to describe the observed resistivity-thickness variation of bismuth films starting with the approximation that constant energy surfaces in bismuth are ellipsoidal.

The values of  $\theta$  or  $p$  (Table 1) lead to the important conclusion that the electron scattering is almost purely specular in bismuth films having thicknesses below 300 Å. It is also noteworthy that  $p$  could also depend on the angle of incidence of the electrons.

## References

1. Fuchs K, *Proc. Camb. phil. Soc. Math. phys. Sci.*, **34** (1938), 100.
2. Duggal V P & Rup R, *J. appl. Phys.*, **40** (1969), 492.
3. Miller D L & Moller G I, *Am. J. Phys.*, **39** (1971), 567.
4. James C, Creasey C J, Aubrey J E & Parrott J E, *Appl. Mater. Res.*, **5** (1966), 55.
5. Neuman M R & Ko W H, *J. appl. Phys.*, **37** (1966), 3327.
6. Vamdatt A R, *Ellipsometric determination of the optical constants of thin metallic films*, Ph D thesis, University of Gujarat, Ahmedabad, 1969.
7. Shah V V & Naik Y G, *Indian J. pure appl. Phys.*, **3** (1965), 20.
8. Tolansky S, *Multiple beam interferometry* (Dover Publications, New York), 1948.
9. Brandli G & Cotti P, *Helv. phys. Acta*, **38** (1965), 801.
10. Parrott J E, *Proc. phys. Soc. Lond.*, **85** (1965), 1143.
11. Campbell D S, *The use of thin films in physical investigations* (Academic Press, New York), 1966, 299.

### Photodielectric Effect in SrS : Mn : Zr Phosphors

KU N RODAY, KU N CHAKRAVORTY, M S SISODIA  
& P C KAMARA

Department of Physics, Government College, Ratlam (M P)

Received 16 July 1979

Photodielectric effect in SrS : Mn : Zr phosphors from 1 kHz to 25 MHz has been measured. A small change has been observed. Results are in agreement with those obtained by Low *et al.* [*J. opt. Soc. Am.*, **44** (1954), 88] for alkaline earth sulphide phosphors. Suitable explanation is given for the results.

It is well known that if a phosphor is considered as a dielectric in a capacitor across which there is an alternating electric field, the real and the imaginary parts of the dielectric constant of the phosphor are affected by illumination using radiations of convenient wavelengths and the phenomenon is known as photodielectric effect (PDE). In alkaline earth sulphide phosphors activated with rare earth activators, the PDE has been measured by Low *et al.*<sup>1</sup> who have reported that there is no change in the dielectric constant upon illumination. This note reports briefly our results on the PDE studies in SrS : Mn : Zr phosphors in the frequency region 1 kHz-25 MHz.

**Experimental details**—Starting from purified SrSO<sub>4</sub>, SrS : Mn : Zr phosphors were prepared by Bhawalkar's method.<sup>2</sup> Carbon was used as the reducing agent, and a mixture of Na<sub>2</sub>SO<sub>4</sub>, NaF and hypo were used as fluxes. Optimum concentration of activators, manganese and zirconium, was determined by trial and error. Two series of samples were prepared : (i) Series in which the quantity of



zirconium was kept constant and the concentration of activator manganese was varied: (ii) Series in which the quantity of manganese added was kept constant and the concentration of activator zirconium was varied.

The samples were fired at 950°C for 3 hr. For dielectric measurements the condenser utilized had one plate made of copper and the other of conducting glass. A thin layer of phosphor along with araldite was spread on the metal plate. The condenser was illuminated by 250-W UV lamp through the conducting glass plate.

Measurements of dielectric constant were made in two steps. The capacity ( $C$ ) and the loss ( $\tan \delta$ ) were determined from 10 kHz to 300 kHz using a dielectric constant and loss measuring testing set, which operated on the principle of Schering's bridge. In the second range,  $C$  and  $\tan \delta$  were determined as a function of frequency using an admittance meter.

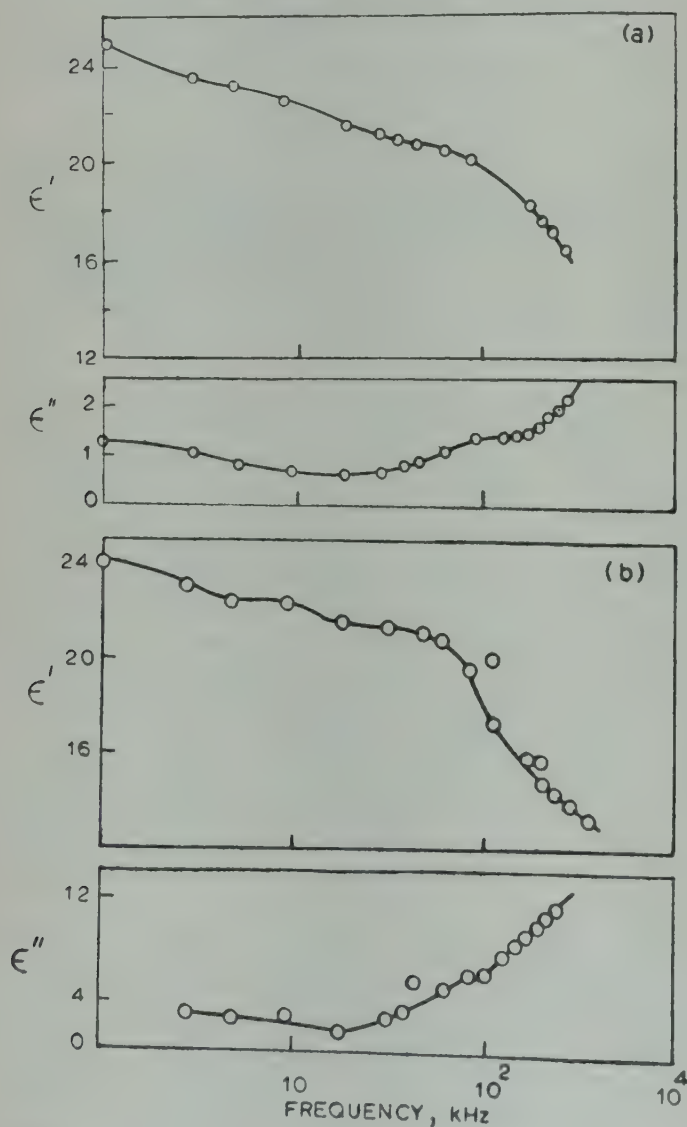


Fig. 1—Variation of  $\epsilon'$  and  $\epsilon''$  with frequency [a, with illumination of the condenser and b, without illumination of the condenser]

In the frequency region from 10 kHz to 300 kHz the capacity  $C$  decreases and then approaches a constant value. In this range the capacity becomes constant at 120 kHz. Upon illumination the capacity increases at first, but then decreases slowly with frequency and approaches the dark value. No significant change in capacity was observed upon changing the intensity of illuminating source. Similar results are obtained in the frequency region 0.45 MHz to 25 MHz. The variation of  $\epsilon'$ ,  $\epsilon''$  and the capacity  $C$  are shown in Figs. 1 and 2, for one of the samples.

It may, however, be pointed out that no Cole-Cole plot is obtainable for the lower frequency region but Cole-Cole plot can be drawn for the higher frequency region and a typical plot is shown in Fig. 3.

*Discussion*—According to Kallmann,<sup>3</sup> the PDE is just another way of measuring the normal photoconductivity of the material. The presence of photoconductivity effectively decreases the distance between the plates of the capacitor and hence

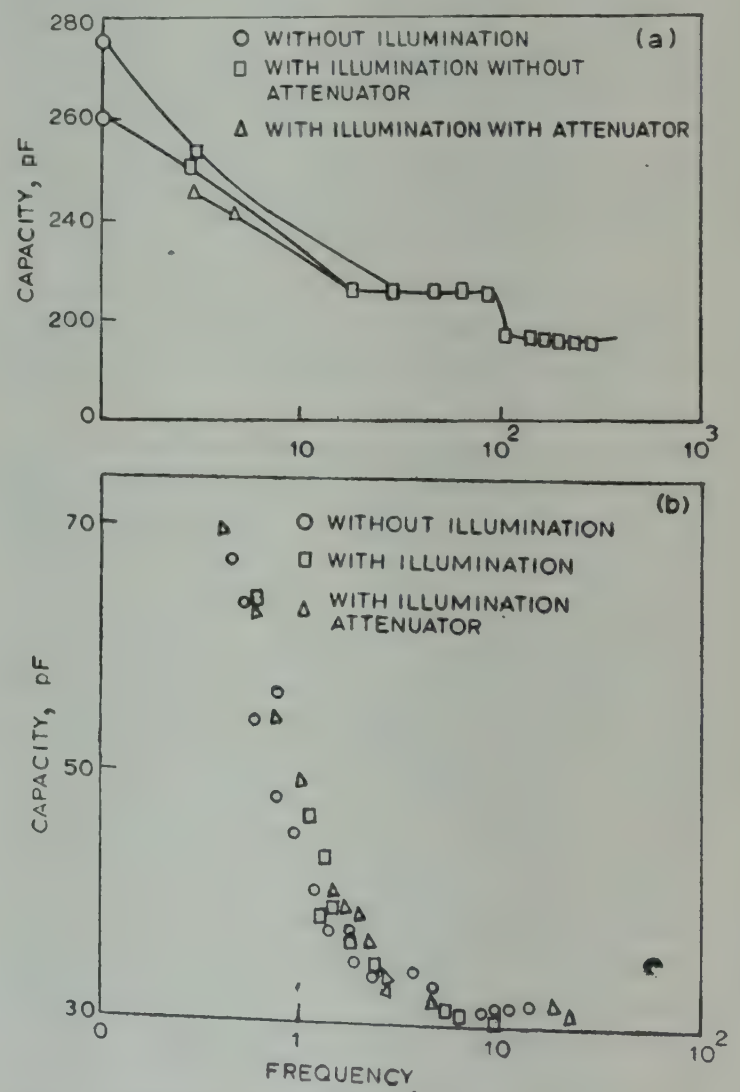


Fig. 2—Capacity  $C$  versus frequency [Freq. scale : a, kHz; b, MHz]



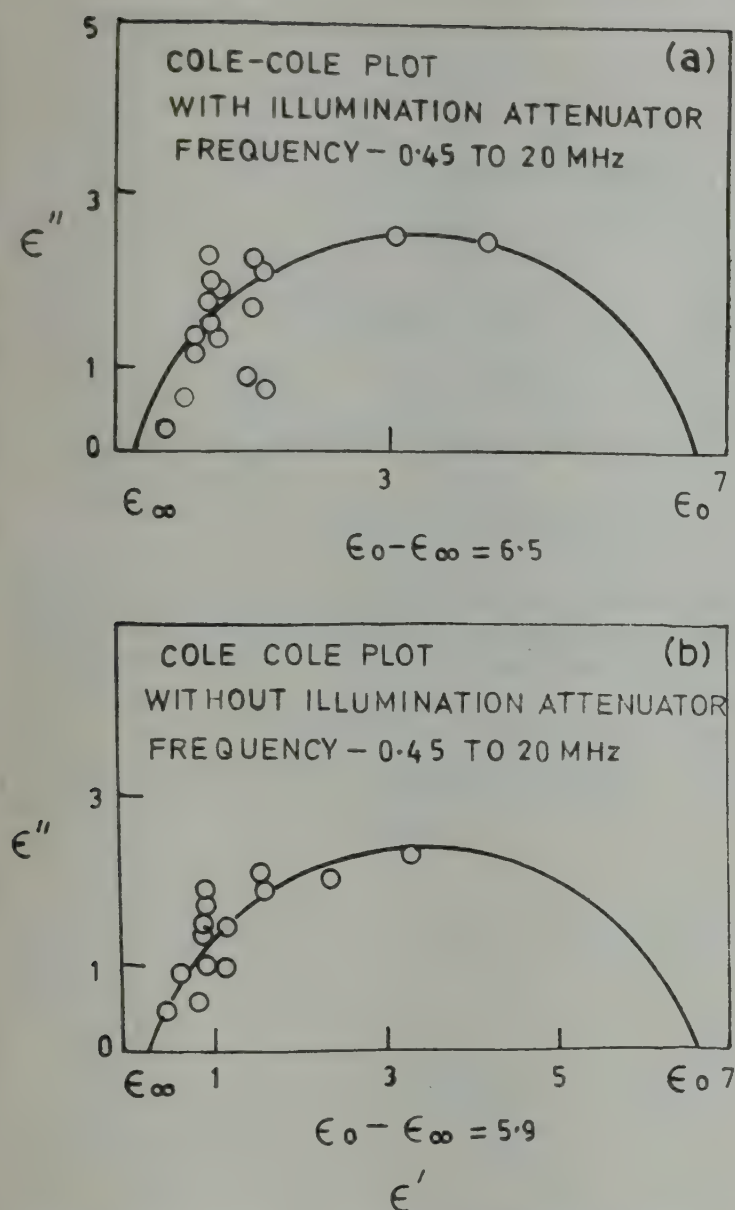


Fig. 3—Cole-Cole plot [Frequency range, 0.45-20 MHz]

increases the capacitance and the apparent dielectric constant.

Changes in capacitance upon illumination are not significant and the small changes obtained get saturated as the intensity of illumination is altered. It points out that the photoconductivity should be very small in SrS : Mn : Zr phosphors. When manganese is used as an activator in ZnS phosphors, Bube<sup>4</sup> has reported that the photoconductivity is very small. A similar behaviour may be expected in SrS. Further, Chakravorty *et al.*<sup>5</sup> have postulated that zirconium forms complex or giant activator centres in SrS and have explained the near non-existence of photoconductivity in SrS phosphors. Thus Kallmann's model seems to explain most of the results obtained by us especially in the lower frequency region.

It has already been stated that Cole-Cole plot can be drawn in the higher frequency region. It can be seen from Fig. 3, that Cole-Cole plot does not pass through zero and  $\epsilon_{\infty} > 0$ .

According to Garlick,<sup>6</sup> the PDE effect is a real change in the dielectric constant of the material which is caused by the presence in the excited material of a large number of highly polarizable centres. Garlick argued against the simple photoconductivity effect because the photocurrent should increase linearly with light intensity but the dielectric changes and trapping states get saturated with light intensity.

Verganas and Malkins<sup>7</sup> have stated that if PDE is due to polarization of one kind, which is characterized by dispersion of frequencies, then  $\epsilon'_{\infty} = 0$  and Cole-Cole plot passes through the origin. If photodielectric effect is due to two kinds of polarization, only one of which exhibits dispersion, then  $\epsilon'_{\infty} > 0$  and the second kind of polarization may be due to localized electrons. In the present investigation, it seems that in the higher frequency region a small but a distinct contribution is also being made due to localized electrons. However, as the photodielectric effect observed is small, it may be said that our results are in agreement with those of Low *et al.*<sup>1</sup>

#### References

1. Low D, Brown B E & Steinberger I T, *J. opt. Soc. Am.*, 44 (1954), 88.
2. Bhawalkar D R, *The Saugar Univ. J. India*, 1 (1952), 209.
3. Kallmann H, Kramer B & Parlmutter A, *Phys. Rev.*, 89 (1953), 700.
4. Bube R H, *Phys. Rev.*, 90 (1953), 70-80.
5. Chakravorty N B, Diwan P S, Kamara P C & Sivarman S, *Indian J. pure appl. Phys.*, 14 (1976), 1015.
6. Garlick G F J & Gibson A F, *Proc. phys. Soc.*, 62A (1949), 731.
7. Verganas I & Malkin G M, *Soviet Phys. Solid St.*, 2 (1961), 2071.

#### Thermoelectric Effect in Fe-Ni Films

M A ANGADI & A M KARGUPPIKAR

Thin Film Laboratory, Department of Physics  
Karnatak University, Dharwad 580 003

Received 29 August 1979; revised received 9 March 1980

The thermal emf of Fe-Ni films grown on a glass substrate is  $\approx 0.013 \text{ mV } ^\circ\text{C}^{-1}$  and this value increases with increase in thickness of films, temperature and series connections of junctions to a maximum of  $6 \text{ mV } ^\circ\text{C}^{-1}$ . Measurements made in vacuum show always lower values than those observed in air.

Thin film thermocouples are extensively used for measuring surface temperature accurately. The preparation and performance of thin film thermocouples have been reported by many authors.<sup>1,2</sup> Thin



film thermocouples of Ni-Fe, Cu-Ni and Cu-constantan are extensively studied by Marshall *et al.*<sup>2</sup> Their measurements show that the thermal emf values increase with the thickness of the film. For *in situ* transport measurements, it is necessary to use such thin film thermocouples to know accurately the surface temperature of the sample. Hence it is desirable to know the thermal emf of such thin film junctions in vacuum which may not be the same as in air. In view of this, we have undertaken the study of thermoelectric effect in vacuum for Fe-Ni and Cu-Ni films. Our preliminary measurements for Cu-Ni films have already been reported.<sup>3</sup>

Fe-Ni films were grown on a glass substrate held at room temperature (20°C) and in vacuum of  $2 \times 10^{-5}$  torr. The substrate was cleaned ultrasonically and by ionic bombardment before depositing the film. The junction was heated locally by means of a heating element of 25 W which enabled us to heat the junction up to 250°C. The heating element was mounted rigidly just below the junction on a glass substrate. The variac was used to monitor the temperature of the heating element and hence the junction. Exactly the same arrangement was also used for our *in situ* measurement. This arrangement was found quite satisfactory for locally heating the junction. The temperature of the thin film thermocouple was measured by a bulk copper-constantan thermocouple which was held rigidly on a heating element. In all our measurements we have kept our cold junction at room temperature (20°C) in air. The details of experimental geometry are shown in Fig. 1.

Our results for Fe-Ni films in air show a thermal emf value of about  $0.013 \text{ mV } ^\circ\text{C}^{-1}$ . This is in agreement with the results of Marshall *et al.*<sup>2</sup> Fig. 2 shows the comparison of observed thermal emf values for two different thicknesses in air and in vacuum. It can be seen from Fig. 2 that thermal emf value increases with increase in thickness in air. However, the thermal emf values in vacuum are much smaller than those observed in air. The typical maximum thermal emf value for our *in situ* measurements on films of thickness of Fe-3200 Å and Ni-2700 Å is  $0.003 \text{ mV } ^\circ\text{C}^{-1}$ .

The reason for such a small value of thermal emf is due to the fact that although the junction is heated locally in vacuum ( $10^{-5}$  torr), the entire glass substrate remains at more or less the same temperature as the junction, i.e.  $dT/dx$  (in the film) is small and hence the thermal emf is smaller in vacuum compared to that in air. However, when we heat the junction locally in air, the ends of the films (i.e.

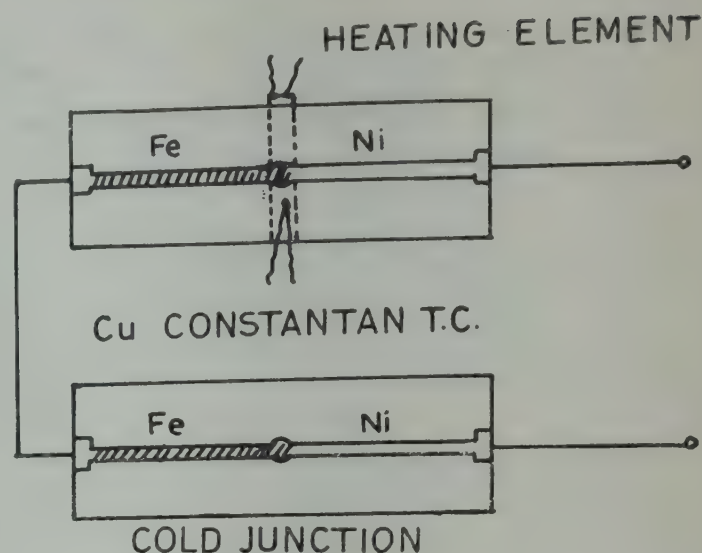


Fig. 1—Experimental arrangement used for thermo-emf measurements in air and in vacuum [The cold junction and hot junction are of same thickness and grown simultaneously.]

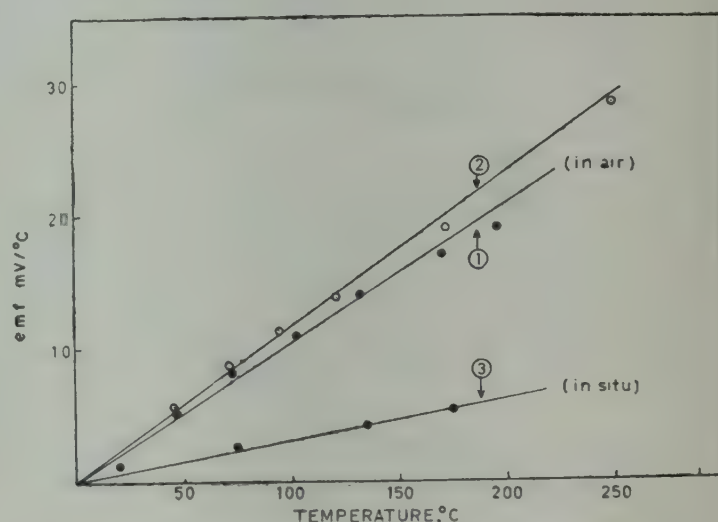


Fig. 2—Temperature dependence of the emf of thin film Fe-Ni thermocouples [The cold end was kept at RT, for both the thermocouples. Curve 1: Fe-1400 Å & Ni-1500 Å, Curve 2: Fe-3200 Å & Ni-2700 Å. Curves 1 & 2 represent measurements done in air. Curve 3: Fe-3200 Å & Ni-2700 Å for *in situ* measurements]

at the contacts) are at very much lower temperature and hence  $dT/dx$  (in the film) is large thereby giving rise to large thermal emf. To confirm this, we heated in air the entire glass substrate ( $2 \text{ cm} \times 6 \text{ cm} \times 0.1 \text{ cm}$ ) on which the Fe-Ni thin film was grown (i.e. no temperature gradient in film). We found that these results were in agreement with our *in situ* measurements. Hence we attribute the small thermal emf observed in our *in situ* measurements to the uniform heating of the entire glass substrate. This would affect the temperature measurements using thin film thermocouples for *in situ* measurements. Hence, care has to be taken in all transport *in situ* measurements, whenever the temperature is measured



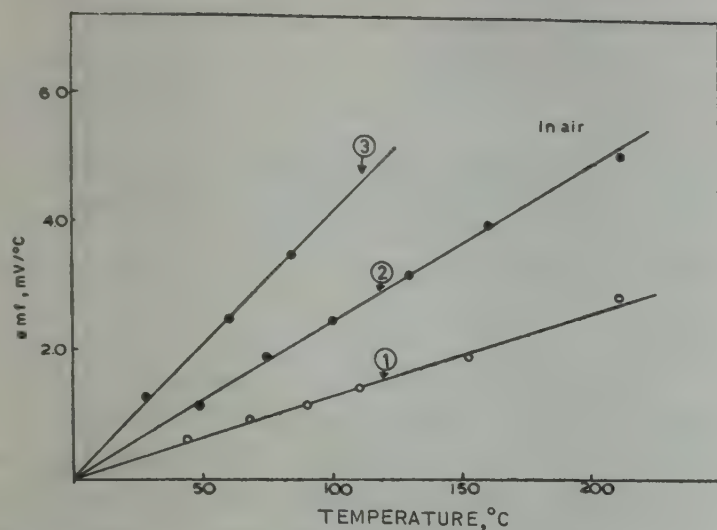


Fig 3—Measured thermal emf-temperature curves for Fe-Ni thin film thermocouples [The cold junction for both the thermocouples was kept at room temperature. Curve 1: One Fe-Ni thermocouple of thickness Fe-2000Å & Ni-1500Å; Curve 2: Two Fe-Ni thermocouples of thickness Fe-1400Å and Ni-1500Å connected in series; and Curve 3: Four Fe-Ni thermocouples of thickness Fe-4000Å and Ni-3600Å connected in series]

using thin film thermocouples to calibrate the thermal emf value in vacuum with respect to that in air.

It is observed that the thermal emf value increases with the thickness of the junction. However, it does not reach the bulk value. So in order to increase the thermal emf values in thin film junctions we have used two or more junctions in series. Fig. 3 shows thermal emf as a function of temperature for two or more junctions in series. The thermal emf increases and reaches a maximum value of  $0.044 \text{ mV } ^\circ\text{C}^{-1}$  for four junctions in series for films of thickness Fe-4000Å and Ni-3600Å.

We propose to further increase thermal emf by connecting several junctions in series and see whether thermal emf increases considerably. Our preliminary measurements on Bi and chromel thin film thermocouple junctions are very promising.

We are grateful to Prof. N Umakantha and Dr B G Mulimani for many helpful suggestions. We thank Prof. E Fawcett, Department of Physics, University of Toronto, Toronto, Canada for sending us pure samples of Fe.

#### References

- 1 Chopra K L, Bahl S K & Randlett M R, *J. appl. Phys.*, **39** (1968), 1525.
- 2 Marshall R, Atlas L & Putner T, *J. scient. Instrum.*, **43** (1966), 144.
- 3 Angadi M A & Karguppikar A M, *Proc. Solid State Physics & Nuclear Physics Symposium* (Department of Atomic Energy, Government of India Bombay-1), **21C** (1978), 252.

#### Lattice Energies of Some Metal Complexes\*

LAMBODAR THAKUR

Post-Graduate Department of Chemistry, Bhagalpur University, Bhagalpur 812 007

Received 5 November 1979

The lattice energies of some metal complexes have been calculated from an empirical equation suggested earlier by L Thakur and A K Sinha [*Indian J. pure appl. Phys.*, **15** (1977), 794]. The significance of the new values has been discussed.

Lattice energies of ionic crystals, particularly of metal complexes, are not accessible by direct experimentation. Theoretical calculation involving quantum mechanical procedures,<sup>1</sup> though accurate, has met with only limited success due to complexity in the spin correlation effects. Consequently, one has to resort to classical, semi-empirical or empirical methods to evaluate lattice energies of ionic crystals and related thermodynamic properties.

The classical treatment assumes ions to be point charges. More recently, Jenkins and Waddington<sup>2</sup> replaced the older point charge calculations by a term by term calculation, assuming ions having extended charge distributions in any crystal. These procedures require a knowledge of the internal structures of the lattice and of the complexions, which become difficult to ascertain.

To circumvent these difficulties, Kapustinskii,<sup>3</sup> on the basis of Born-Landé or Born-Mayer potential, proposed a general method of lattice energy calculation of a crystal of even unknown geometry utilizing only the sum of six coordinated ionic radii ( $r_c + r_a$ ). But a comparison of the values yielded by the equations of Kapustinskii with the more recent cyclic data of Born-Haber-Fajan reveals the limitations of the former method. It has been observed that a single equation is unable to account for the crystal energies of all types of ionic compounds, maintaining the simplicity and accuracy in any procedure. In order to get a better fit with the experimental values, Thakur *et al.* recently proposed the following general equation<sup>4,5</sup> from which lattice energies of a number of ionic crystals including those of complex salts have been computed:

$$U_L (\text{kJ mole}^{-1}) = \frac{1201.6 \sum n Z_1 Z_2}{(r_c + r_a)} \left[ 1 - \log_{10} \left\{ 1 + \frac{p}{(r_c + r_a)^2} \right\} \right] + 10.5 \sum n Z_1 Z_2 \dots (1)$$

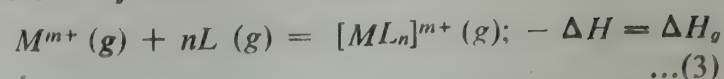
\*Part of the invited talk delivered at the UGC Symposium on 'Metal Complexes', held at the University of Kashmir, Srinagar, during 27-30 Sept. 1979.

where  $p = 2 \text{ \AA}^2$  when  $r_c + r_a \leq 4 \text{ \AA}$ , and  $p = 10 \text{ \AA}^2$  for complex crystals ( $r_c + r_a > 4 \text{ \AA}$ );  $\Sigma n$  is the total number of ions present in the molecular formula of the compound;  $Z_1$  and  $Z_2$  are the ionic charges; and  $(r_c + r_a)$  is expressed in angstrom units.

The present note deals with the cases where the cations or the anions are complex ionic species. For a complex crystal of the type  $[\text{ML}_n] X_m(c)$ , the lattice energy is related to the following thermochemical quantities :

$$U_L + nRT = \Delta H_f^0 M^{m+}(g) + n \Delta H_f^0(g) + m \Delta H_f^0 X^-(g) - \Delta H_f^0 [\text{ML}_n] X_m(c) + \Delta H_g \quad (2)$$

where  $\Delta H_g$  refers to the reaction :



and the other terms have their usual significance. From Eqs. (2) and (3), the metal-ligand bond strengths,  $D(M-L) = -\frac{1}{n} \Delta H_g$ , can be calculated.

Thermodynamic data for complexes formed by ammonia are usually reported for complexes in aqueous solution and relatively little work has been published on the thermodynamics of formation of solid ammines. Lattice enthalpies of some substituted cobalt (III)-ammine complexes and some first-row transition metal (II)-hexammino and -hexaquo

Table 1—Lattice Energies and Complexation Energies (in  $\text{kJ mole}^{-1}$ ) of Some Cobalt (III)-Ammine Complexes at 298 K

Crystal	$r_c + r_a$ $\text{\AA}$	$U_L + nRT + \Delta_0$	$\Delta H_f^0$ complex	$(m-n)$ $\Delta H_f^0 \text{NH}_3(g)$	$\Delta H_f^0$ $M^{3+}(g)$	$(m-n)$ $\Delta H_f^0 \text{Cl}^-(g)$	$\Delta H_g$ complex	Substituted ligand's bond energy
	(Ref. 6)	(Eq. 3)	(Refs. 7, 8)	(Refs. 9-11)	(Ref. 7)	(Ref. 15)		
$[\text{Co}(\text{NH}_3)_6] \text{Cl}_3$	4.21	2995	-1124	-277	6080	-682	-3250	
$[\text{Co}(\text{NH}_3)_5 \text{NO}_2] \text{Cl}_2$	4.11	1570	-988	-367	6080	-455	-4676	-1968
$[\text{Co}(\text{NH}_3)_5 \text{Cl}] \text{Cl}_2$	4.17	1558	-1017	-458	6080	-455	-4626	-1918
$[\text{Co}(\text{NH}_3)_5 \text{Br}] \text{Cl}_2$	4.24	1540	-950	-442	6080	-455	-4593	-1885
$[\text{Co}(\text{NH}_3)_5 \text{I}] \text{Cl}_2$	4.38	1516	-906	-420	6080	-455	-4595	-1887

Substituted ligand's bond-strengths:  $\text{NO}_2^- > \text{Cl}^- > \text{Br}^- \approx \text{I}^-$ .

Table 2—Lattice Energies and Enthalpies of Complexation (in  $\text{kJ mole}^{-1}$ ) of Some Hexammino-Metal (II) and Hexaquo-Metal (II) Chlorides at 298 K

Crystal	$r_c + r_a$ $\text{\AA}$	$U_L + nRT + \Delta_0$	$\Delta H_f^0$ complex	$6\Delta H_f^0 \text{NH}_3(g)$ or $6\Delta H_f^0 \text{H}_2\text{O}(g)$	$2\Delta H_f^0 \text{Cl}^-(g)$	$\Delta H_f^0$ $M^{2+}(g)$	$\Delta H_g$ complex	$D(M^{2+}-X)$
	(Ref. 12)	Eq. (3)	(Refs. 7, 8)	(Ref. 9)	(Ref. 15)	(Ref. 7)		
$[\text{Mn}(\text{NH}_3)_6] \text{Cl}_2$	4.46	1400	-1120	-277	-455	2519	-1507	-251
$[\text{Fe}(\text{NH}_3)_6] \text{Cl}_2$	4.44	1450	-994	-277	-455	2752	-1564	-261
$[\text{Co}(\text{NH}_3)_6] \text{Cl}_2$	4.41	1500	-996	-277	-455	2842	-1606	-268
$[\text{Ni}(\text{NH}_3)_6] \text{Cl}_2$	4.39	1562	-994	-277	-455	2930	-1630	-272
$[\text{Cu}(\text{NH}_3)_6] \text{Cl}_2$	4.38	1525	-873	-277	-455	3054	-1670	-278
$[\text{Co}(\text{H}_2\text{O})_6] \text{Cl}_2$	4.11	1560	-2115	-1451	-455	2842	-1491	-248
$[\text{Ni}(\text{H}_2\text{O})_6] \text{Cl}_2$	4.10	1613	-2103	-1451	-455	2930	-1514	-252

Acid strength :  $\text{Mn}^{2+} < \text{Fe}^{2+} < \text{Co}^{2+} < \text{Ni}^{2+} < \text{Cu}^{2+}$ ; Base strength :  $\text{NH}_3 > \text{H}_2\text{O}$ .



complexes and derivation of certain thermochemical quantities from them, are also reported in this note.

**Results and discussion**—Table 1 presents the lattice energies and complexation energies of only five Cobalt (III)-ammine complexes at 298 K. Unfortunately, there is a dearth of reliable values of thermochemical radii for more complex ions. The enthalpies of formation of the complex crystals, metal ion, substituted anions and gaseous ammonia have been compiled from different sources.<sup>8-9</sup> The ligand field theory predicts the stabilization energy ( $\Delta_0$ ) for  $\text{Co}^{3+}$  complexes. This additional stability of the cobalt (III) complex ion has been approximately estimated to be of the order of 100 kJ mole<sup>-1</sup> based upon spectroscopic observation.<sup>10</sup> Satisfactory agreement between the calculated and the experimental values has been observed by adding  $\Delta_0$  in the computed lattice energy values.<sup>5,11</sup> It can be seen that the substituted ligand's bond-strength decreases in the following order:  $\text{NO}_2^- > \text{Cl}^- > \text{Br}^- \approx \text{I}^-$ .

This is predicted from the spectrochemical series of decreasing ligand-field strengths.<sup>11</sup>

Table 2 presents the lattice energies of some hexammino- and hexaquo-metal (II) chlorides at 298 K. The input data have been compiled from different sources.<sup>7,9,12</sup> The ligand field stabilization energies for  $d^6$ - to  $d^9$ -ions ( $\text{Fe}^{2+}$  through  $\text{Cu}^{2+}$ ) have been compiled from Orgel.<sup>13</sup> It can be seen that the order of acid strength of the metal ion increases in the sequence as predicted by Irving and Williams<sup>14</sup> from  $M = \text{Mn}^{2+} < \text{Fe}^{2+} < \text{Co}^{2+} < \text{Ni}^{2+} < \text{Cu}^{2+}$ .

It has to be emphasized that the thermochemical radii for the complex ions used in the present calculations have been derived by empirical methods<sup>6,15</sup> and there is an element of uncertainty which can be estimated up to  $\pm 5\%$  in the present values. However, this would not alter the arguments presented above.

#### References

1. Hurley A C, *Adv. Quant. Chem.*, 7 (1973), 315.
2. Jenkins H D B & Waddington T C, *Chem. Phys. Lett.*, 31 (1975), 369.
3. Kapustinskii A F, *Quart. Rev.*, 10 (1956), 283.
4. Thakur L & Sinha A K, *Indian J. pure appl. Phys.*, 15 (1977), 794.
5. Thakur L, Sandwar B B & Sinha A K, *Indian J. Chem.*, 17A (1979) 1.
6. Yatsimirskii K B & Pankova L L, *Zh. obshch. Khim.* (Russ. J. Gen. Chem.), 18 (1948), 2051.
7. *Selected values of chemical thermodynamic properties*, NBS Technical Note 270-4, (NBS, Washington D C), 1969.
8. Krestov G A & Yatsimirskii K B, *Russ. J. inorg. Chem.*, 6 (1961), 1170.
9. *Selected values of chemical thermodynamic properties*, NBS Technical Note 270-1 (NBS, Washington, DC), 1965.
10. Ashcroft S J & Mortimer C T, *Thermochemistry of transition-metal complexes* (Academic Press, London), 1970, 10.
11. Thakur L & Sandwar B B, *Indian Natl. Acad. Sci. Lett.*, 1 (1978), 510.
12. Yatsimirskii K B, *J. gen. Chem., USSR*, 17 (1947), 2019.
13. Orgel L E, *An introduction to transition-metal chemistry* (Methuen, London), 1960, 46.
14. Irving H & Williams R J P, *J. chem. Soc.*, (1958), 4144.
15. Thakur L, Sinha A K & Thakur K P, *Indian J. Phys.*, 52A (1978), 510.

#### On the Symmetry Group of Non-rigid Molecule $\text{BF}_2\text{CH}_3$

T S G KRISHNA MURTY, L S R K PRASAD & M KONDALA RAO

Department of Applied Mathematics, Andhra University  
Waltair 530 003

Received 10 September 1979

By introducing a new inversion operator  $E_i^*$ , it has been shown that the symmetry groups obtained by Longuet-Higgins and Altmann schemes, for  $\text{BF}_2\text{CH}_3$  molecule, are isomorphic, even when approximate symmetries of the type considered by Altmann, are used.

The fact that group theoretical methods can be effectively used in the study of nonrigid molecules is well known. The first consistent description of the symmetry of nonrigid molecules was given by Longuet-Higgins<sup>1</sup> (hereafter referred to as LH), which depends to a large extent on the work of Hougen.<sup>2</sup> There are two schemes of establishing the symmetry groups of nonrigid molecules. The first one is due to LH in which one has to start with the formal symmetry operations of the system and then impose the constraints through the so called feasibility conditions, so as to obtain the effective symmetry operations. In the second scheme, proposed by Altmann,<sup>3</sup> the effective symmetry operations are directly written down taking the constraints into consideration right from the beginning. There has been a considerable controversy<sup>4-6</sup> over the equivalence of both the schemes as also about the existence and precise definition of certain operations defined therein. A detailed discussion about both the schemes was attempted by Watson.<sup>4</sup> In this note, we propose to consider in detail Altmann's remark<sup>7</sup> that, if certain approximate symmetries are used, symmetry



operations can be found that are not expressible in LH notation.

LH group of symmetry operations of a nonrigid molecule consists of all feasible permutations and permutation-inversions. For the molecule  $\text{BF}_2\text{CH}_3$ , LH obtained a 12-element group as its symmetry group, by considering the products of all the permutations  $P$  of the identical particles and the inversion  $E^*$  of positions and spins of all the particles of the molecule as a whole and imposing the condition of feasibility. He has shown this group to be isomorphic to the 12-element group corresponding to the case  $s = 3$ , given by Wilson *et al.*<sup>8</sup> Wilson *et al.*<sup>8</sup> also obtained a higher symmetry group of order 24 for the case  $s = 6$  in respect of the same molecule by introducing the additional operation  $C_3^1$ . LH did not make any mention of this 24-element group in his discussion.

Altmann<sup>7</sup> discussed, in detail, the same molecule through the introduction of isodynamic operations. He obtained the 12-element group and established its isomorphism with the LH group. Introducing a new intrinsic operation ( $Z_2^1$ ), called flip, he was able to obtain a 24-element symmetry group isomorphic to the 24-element group of Wilson *et al.*,<sup>8</sup> for the case  $s = 6$ . He further remarked that if approximate symmetries are used, it is possible to find operations that cannot be expressed in the permutation-inversion notation of LH. The flip ( $Z_2^1$ ) is one such operation. Thus symmetry groups can sometimes be used that are not isomorphic to LH group or to a subgroup of it.

In this note, we introduce a new inversion operation  $E_i^*$  in the LH notation, which corresponds to the flip of Altmann. The new operation  $E_i^*$  commutes with all the 12-symmetry operations of LH, thus giving rise to the 24-element symmetry group. Nevertheless, LH stated that the inversion  $E^*$ , as it is, does not exist as a symmetry operation for this entire molecule.

**The new inversion operation  $E_i^*$**  — Using Altmann's scheme, we give in the following the five diagrams representing the isodynamic generating operations of the 24-element group for the  $\text{BF}_2\text{CH}_3$  molecule. For the purpose of comparison, we depict these five operations in Fig. 1, using the unsymmetrical starting configuration of LH.

Following the LH scheme, the generating symmetry operations of the 12-element group for the same molecule are depicted in Figs. 2(a-c).

The group generated by Figs. 2 (b) and (c) is of order 12 and is isomorphic to that of Wilson *et al.*,<sup>8</sup>

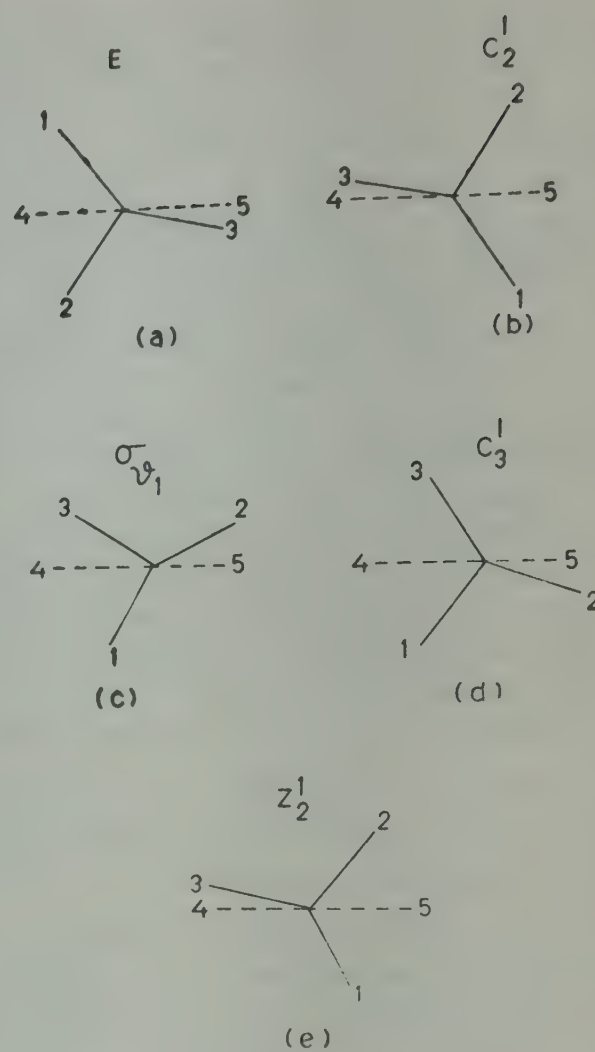


Fig. 1—Isodynamic generating operations of the 24-element group of  $\text{BF}_2\text{CH}_3$  molecule using Altmann's scheme

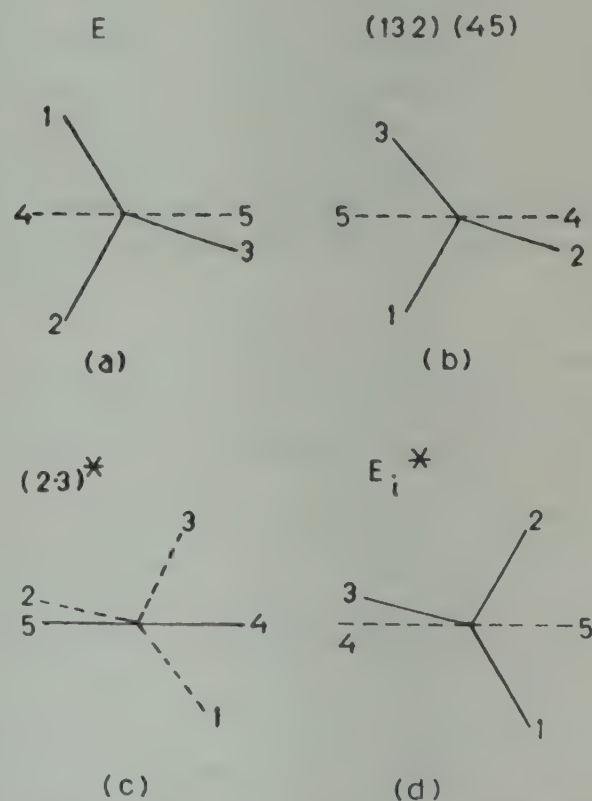


Fig. 2—Symmetry operations of the 12-element group of  $\text{BF}_2\text{CH}_3$  molecule using Longuet-Higgins (LH) scheme



for the case  $s = 3$ . Also, it agrees with that of Altmann, generated by Figs. 1 (b), (c) and (d).

In the light of the introduction of the new intrinsic operation flip ( $Z_2^I$ ) by Altmann while considering approximate symmetries, we are of the opinion that the free rotation property of the methyl group has got to be examined again in the LH scheme. Thus, we propose the following: as far as the free rotation of the methyl group is concerned, it is sufficient if we consider the rotation of the three planar hydrogen atoms about the B-C axis, which passes through the centre of mass of the three hydrogens. Therefore, we apply LH type of feasible symmetry operations, viz. permutations and permutation-inversions to the three hydrogen atoms, regarding them as atoms of a planar molecule. LH has already taken into account the feasible permutations of the three hydrogen atoms. So, we define  $E_3^*$ , represented in Fig. 2d, as the inversion of the three hydrogen atoms through their centre of mass. This is a feasible operation in the LH scheme and it implies that the vibronic interactions between the methyl group and fluorides are ignored as mentioned by Altmann<sup>7</sup> in the case of flip.

It can easily be verified that  $E_3^*$  commutes with all the 12 operations already enumerated by LH, and hence gives rise to the 24-element group in the LH notation, isomorphic to that of Wilson *et al.*,<sup>8</sup> for the case  $s = 6$  and that of Altmann.<sup>7</sup> It can also be seen, by comparison of diagrams in Fig. 1 (e) and Fig. 2d, that the flip introduced by Altmann<sup>7</sup> is expressible in the notation of LH.

Thus, we conclude that the symmetry operation flip introduced by Altmann can be expressed in the LH notation. And, the symmetry groups obtained by both the schemes will be isomorphic, through the introduction of the new inversion operation  $E_3^*$ , even if approximate symmetries are used.

#### References

1. Longuet-Higgins H C, *Molec. Phys.*, 6 (1963), 445.
2. Hougén J T, *J. chem. Phys.*, 37 (1962), 1433.
3. Altmann S L, *Proc. R. Soc. A*, 298 (1967), 184.
4. Watson J K G, *Molec. Phys.*, 21 (1971), 577.
5. Altmann S L, *Molec. Phys.* 21 (1971), 587.
6. Longuet-Higgins H C, *Nature, Lond.*, 274 (1978), 403.
7. Altmann S L, *Induced representations in crystals and molecules* (Academic Press, London), 1977, 337.
8. Wilson (Jr) E B, Lin C C & Lide D R, *J. chem. Phys.*, 23 (1955), 136.

#### Intramolecular Force Fields & Mean Amplitudes of Vibration of Group IV Tetrabromides

R K GOEL, S K GUPTA\* & M L AGARWAL †

Department of Physics, D N College, Meerut 250 002

Received 22 November 1979

The force constants have been calculated for tetrahedral  $XBr_4$  ( $X = C, Si, Ge, Sn$ ) molecules employing OVFF, UBFF and GVFF models. Compliance constants have also been calculated. The trends of force constants, compliance constants and strength of chemical bonds are discussed. The Coriolis coupling constant  $\xi_{33} (f_2 \times f_2)$  has been computed and the trend discussed. Mean amplitudes of vibration for bonded and non-bonded atom pairs at temperatures (0, 298.15 and 500 K) have been computed and characteristic nature discussed. The trends of force constants and mean amplitudes of vibration in isoelectronic series are discussed.

Creighton and Sinclair<sup>1</sup> have recently studied the Raman spectra of crystalline group IV tetrabromides and analyzed the spectra assuming  $T_d$  symmetry. These spectra considerably differ from the spectra obtained by previous workers.<sup>2-5</sup> Thus it was thought worthwhile to compute the various sets of force constants employing general valence force field (GVFF), Urey-Bradley force field (UBFF) and orbital valence force field (OVFF) models, set of compliants and mean amplitudes of vibration using recent vibrational data.<sup>1</sup> It is further aimed to study the trends of force constants and mean amplitudes of vibration in various isoelectronic series.

The  $XY_4$ -type systems possessing  $T_d$  symmetry give rise to four fundamental frequencies which are distributed among various symmetry species as follows:

$$\Gamma_{\text{vib}} = a_1 + e + 2f_2$$

All these vibrations are Raman active except those belonging to  $f_2$  species which are infrared active also. Wilson's FG-matrix method<sup>6</sup> has been used to calculate the force constants in OVFF, UBFF and GVFF models.  $G$  and  $F$  matrices are taken from literature.<sup>7-9</sup> Cyvin's<sup>9</sup> secular equation  $|\Sigma G^{-1} - \Delta E| = 0$  has been followed for the computation of mean amplitudes of vibration. Müller's  $L$ -matrix method,<sup>10-12</sup> L-F method<sup>13</sup> and kinetic constant method<sup>14,15</sup> have been used for solving the  $2 \times 2$  determinant occurring in  $f_2$  species. The expressions for compliance constants

\* Department of Physics, K K Jain Degree College, Khatauli 251 201

† Department of Physics, D S College, Aligarh



and for Coriolis coupling constants are taken from literature.<sup>9</sup> Computations have been carried over a TDC-316 computer.

**Results**—The three sets of GVFF constants obtained using Müller's *L*-matrix method, L-F approximation and kinetic constant method are compared in Table 1. This model includes five force constants, viz.  $f_r$  (bond-stretching),  $f_\alpha$  (angle-bending),  $f_{rr}$  (bond-stretching-interaction),  $f_{\alpha\alpha}$  (bending interaction) and  $f_{r\alpha}$  (stretching-bending interaction). The force constants computed by employing UBFF and OVFF models are collected in Table 2, where  $k_1$  (K),  $k'_\alpha$  (3H),  $A$  and  $B/R$  ( $F$  and  $F'$ ) represent bond-stretching, angle-bending and interaction constants respectively. Table 3 presents the compliance constants where  $c_r$ ,  $c_{rr}$ ,  $c_\alpha$ , etc., similarly correspond to stretching, stretching interaction, bending, etc. Mean amplitudes of vibration for bonded and non-bonded atom pairs at three temperatures are collected in Table 4. The mean amplitudes of vibration calculated for these mole-

Table 1—GVFF Constants (in mdyne/Å) of Group IV Tetrabromide Tetrahedral Systems

Approx. method	$f_r$	$f_{rr}$	$f_\alpha$	$f_{\alpha\alpha}$	$f_{r\alpha}$
CBr <sub>4</sub>					
Müller	3.077 (2.197)*	0.086 (0.394)*	0.287 (0.258)*	0.020	0.364
Kinetic	1.870	0.488	0.456	0.105	0.141
L-F	2.879	0.152	0.289	0.021	0.314
SiBr <sub>4</sub>					
Müller	2.661 (2.03)†	0.076	0.166	0.015	0.186
Kinetic	2.210	0.226	0.184	0.024	0.053
L-F	2.601	0.096	0.166	0.015	0.168
GeBr <sub>4</sub>					
Müller	2.248 (1.95)†	0.114	0.128	0.005	0.107
Kinetic	2.069	0.174	0.133	0.008	0.032
L-F	2.226	0.122	0.128	0.005	0.099
SnBr <sub>4</sub>					
Müller	2.023 (1.85)†	0.072	0.091	0.010	0.061
Kinetic	1.948	0.097	0.092	0.011	0.019
L-F	2.015	0.075	0.091	0.010	0.057

\* Values from Ref. 17, † values from Ref. 19.

Table 2—OVFF and UBFF Constants (in mdyne/Å) of Group IV Tetrabromide Tetrahedral Systems

Force field	$k_1$ (K)	$k'_\alpha$ (3H)	$A$ (F/2)	$B/R$ (−F')
CBr <sub>4</sub>				
OVFF	1.328	0.156	0.251	0.081
LJP	1.412	0.234	0.240	0.037
UBFF	1.401	0.241	0.242	0.043
SiBr <sub>4</sub>				
OVFF	1.8934 (2.0)*	0.129	0.124	0.029
LJP	1.902	0.120	0.123	0.019
UBFF	1.912	0.154	0.122	0.009
GeBr <sub>4</sub>				
OVFF	1.818 (1.9)*	0.151	0.097	0.008
LJP	1.816	0.078	0.097	0.015
UBFF	1.824	0.174	0.096	−0.014
SnBr <sub>4</sub>				
OVFF	1.780 (1.75)*	0.081	0.057	0.015
LJP	1.780	0.075	0.057	0.009
UBFF	1.780	0.093	0.057	0.003

\* Values from Ref. 18

Table 3—Compliance Constants (in Å/mdyne) and Coriolis Constants of Group IV Tetrabromide Tetrahedral Systems

Constant	Systems			
	CBr <sub>4</sub>	SiBr <sub>4</sub>	GeBr <sub>4</sub>	SnBr <sub>4</sub>
$C_r$	0.442	0.433	0.481	0.513
$C_{rr}$	−0.047	−0.029	−0.032	−0.022
$C_\alpha$	4.609	6.953	8.436	11.470
$C_{\alpha\alpha}$	0.282	−0.207	−0.040	−1.363
$C_{r\alpha}$	−0.531	−0.467	−0.396	−0.336
$\xi_{33} (f_2 \times f_2)$	0.899	0.791	0.595	0.473
$(m_X/m_Y)^{1/2}$	0.3877	0.5929	0.9531	1.2189

cules by Sharma<sup>16</sup> obtained on the basis of liquid phase data, except that for CBr<sub>4</sub> are compared in Table 4. Some earlier results obtained by Dixit,<sup>17</sup> Singh<sup>18</sup> and Heath and Linnett<sup>19</sup> are also compared in Tables 1 and 2. Force constants obtained by using Lennard-Jones potential are collected in Table 2 and the Coriolis coupling constants in Table 3.

From Table 1, it is observed that the GVFF results obtained from the three approximation methods



Table 4—Mean Amplitudes of Vibration (in Å) of Group IV Tetrabromide Tetrahedral Systems

System	$U_{X-Y}$ at		
	0 K	298.15 K	500 K
CBr <sub>4</sub>	0.0507 (0.0502)	0.0541 (0.0535)	0.0613 (0.0604)
SiBr <sub>4</sub>	0.0427 (0.0421)	0.0488 (0.0477)	0.0580 (0.0565)
GeBr <sub>4</sub>	0.0380 (0.0377)	0.0482 (0.0474)	0.0594 (0.0584)
SnBr <sub>4</sub>	0.0365 (0.0363)	0.0489 (0.0482)	0.0609 (0.0600)
	$U_{X---Y}$ at		
	0 K	298.15 K	500 K
CBr <sub>4</sub>	0.0467 (0.0468)	0.0736 (0.0743)	0.0934 (0.0944)
SiBr <sub>4</sub>	0.0523 (0.0523)	0.0940 (0.0945)	0.1202 (0.1209)
GeBr <sub>4</sub>	0.0548 (0.0551)	0.1044 (0.1066)	0.1338 (0.1368)
SnBr <sub>4</sub>	0.0596 (0.0596)	0.1267 (0.1279)	0.1612 (0.1646)

Values in parentheses are from Ref. 16, where all values correspond to liquid phase except that for CBr<sub>4</sub>

compare well except for results due to kinetic method in case of CBr<sub>4</sub>. The three sets show a similar trend of variation of the stretching force constant  $f_r$  (which is a measure of the strength of the chemical bond), i.e.  $f_r$  decreases in the order CBr<sub>4</sub> > SiBr<sub>4</sub> > GeBr<sub>4</sub> > SnBr<sub>4</sub>. The trend is also shown by the OVFF and UBFF stretching force constant  $k_1(K)$  given in Table 2 and the compliance constant  $c_r$  (Table 3) except in case of CBr<sub>4</sub>. This is in accordance with the atomic radius of the central atom. A similar trend has been observed by Sanyal *et al.*<sup>20</sup> in II B group tetrahalides. From Table 2, it is observed that the results obtained from Lennard-Jones potential approximation ( $A = 6.5 B/R$ ) are very well comparable to OVFF results. Their trend is also similar to those mentioned above.

It is interesting to compare the stretching force constant values in various isoelectronic series, as done below.

- (i) AlBr<sub>4</sub><sup>-</sup> (1.38) [Ref. 21], SiBr<sub>4</sub> (1.89), PBr<sub>4</sub> (2.269) [Ref. 22],
- (ii) ZnBr<sub>4</sub><sup>2-</sup> (0.677) [Ref. 20], GaBr<sub>4</sub><sup>-</sup> (1.344) [Ref. 18], GeBr<sub>4</sub> (1.818),
- (iii) CdBr<sub>4</sub><sup>2-</sup> (0.775) [Ref. 20], InBr<sub>4</sub><sup>-</sup> (1.358) [Ref. 18], SnBr<sub>4</sub> (1.78).

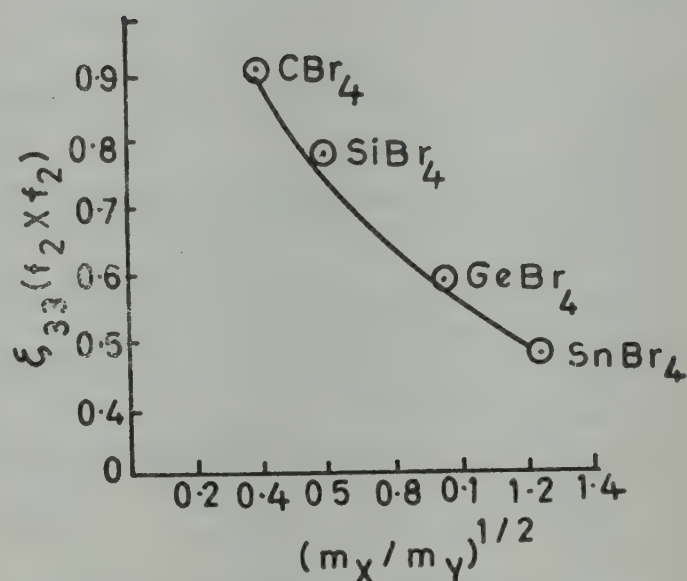


Fig. 1—Mass ratio influence on Coriolis constants in tetrabromide tetrahedral system

It is inferred from the above data that the higher oxidation state is more stable than the lower one. A similar trend is reported in the work of Sanyal *et al.*<sup>23,24</sup>

The Coriolis coupling constant  $\zeta_{33}(f_2 \times f_2)$  variation with mass ratio  $\sqrt{m_X/m_Y}$  is shown in Fig. 1, which is according to the expected trend of variation.

From Table 4, it is found that the mean amplitude values for bonded atom-pairs  $U_{X-Y}$  at room temperature are characteristic. Because of this, the difference of these values from the previous reported values<sup>16</sup> is negligible while the previous force constants compared in Tables 1 and 2 differ considerably from the present values. However the  $U_{X-Y}$  and  $U_{Y---Y}$  vary with temperature as expected. The variations of  $U_{X-Y}$  at room temperature in various isoelectronic series are as follows:

- (i) BBr<sub>4</sub><sup>-</sup> (0.062) [Ref. 16], CBr<sub>4</sub> (0.0541),
- (ii) AlBr<sub>4</sub><sup>-</sup> (0.0556) [Ref. 25], SiBr<sub>4</sub> (0.0488), PBr<sub>4</sub><sup>+</sup> (0.0455) [Ref. 22],
- (iii) ZnBr<sub>4</sub><sup>2-</sup> (0.072) [Ref. 16], GaBr<sub>4</sub><sup>-</sup> (0.056) [Ref. 16], GeBr<sub>4</sub> (0.0488),
- (iv) CdBr<sub>4</sub><sup>2-</sup> (0.07) [Ref. 16], InBr<sub>4</sub><sup>-</sup> (0.056) [Ref. 16], SnBr<sub>4</sub> (0.0489).

These values also favour the above trend, i.e. the higher oxidation state is more stable than the lower oxidation state.

The authors are thankful to Dr S P Gupta, Principal, D N College, Meerut, for providing facilities and encouragement.



## References

1. Creighton J A & Sinclair T J, *Spectrochim. Acta*, **35A** (1979), 137.
2. Clark R J H & Willis C J, *Inorg. Chem.*, **10** (1971), 1118.
3. Shimanouchi T, *National standard reference data series*, (U S Nat. Bur. Stand., Washington 17, NSRDS-NBS 17, March, 1968.
4. Long D A, Spencer T V, Waters D N & Woodward L A, *Proc. R. Soc.*, **240A** (1957), 499.
5. Thomas T E & Orville Thomas W J, *J. inorg. Nucl. Chem.*, **34** (1972), 839.
6. Wilson (Jr) E B, Decius J C & Cross P C *Molecular vibrations* (McGraw-Hill, New York), 1955.
7. Krebs B & Müller A, *J. molec. Spectrosc.*, **22** (1967), 290.
8. Müller A & Krebs B, *J. molec. Spectrosc.*, **24** (1967), 180.
9. Cyvin S J, *Molecular vibrations and mean-square amplitudes* (Universitets forlaget, Oslo, Elsevier, Amsterdam), 1968.
10. Müller A, *Z. Phys. Chem.*, **238** (1968), 116.
11. Peacock C J & Müller A, *J. molec. Spectrosc.*, **26** (1968), 454.
12. Müller A & Peacock C J, *Molec. Phys.*, **14** (1968), 393.
13. Pandey A N, Sharma D K, Verma U P, Arora L D, Gupta S L & Singh B P, *Indian J. pure appl. Phys.*, **14** (1976), 457.
14. Thirugnanasambandam P & Srinivasan G, *J. chem. Phys.*, **50** (1969), 2467.
15. Thirugnanasambandam P, *Proc. seminar Raman & IR spectrosc.* (University of Kerala, Trivandrum), 1964, 174.
16. Sharma D K, *Studies in molecular constants from spectral data*, Ph D thesis, Meerut University, Meerut, 1976.
17. Dixit L, *Studies in molecular vibrations and related bond properties of simple systems*, Ph D thesis, Gorakhpur University, Gorakhpur, 1975.
18. Singh B P, *Studies in molecular force fields and mean amplitudes of vibration of simple molecules*, Ph D thesis, Gorakhpur University, Gorakhpur, 1970.
19. Heath D F & Linnett J W, *Trans. Faraday Soc.*, **44** (1948), 873, 878, 884.
20. Sanyal N K, Goel R K & Pandey A N, *Indian J. pure appl. Phys.*, **13** (1975), 373.
21. Srivastava B B, Dubish A K, Pandey A N & Mittal A K, *Z. Naturf.*, **27A** (1972), 1213.
22. Sanyal N K, Goel R K & Pandey A N, *Indian J. pure appl. Phys.*, **14** (1976), 244.
23. Sanyal N K, Goel R K & Pandey A N, *Indian J. Phys.*, **50** (1976), 659.
24. Sanyal Nitish K, Goel R K & Gupta S K, *Indian J. Phys.*, (In Press).
25. Sharma D K, Pandey A N, Dubish A K & Rai S N, *Z. Naturf.*, **29A** (1974), 1504.

## Molecular Constants of Some Octahedral Hexahalo & Hexaoxy Ions

R K GOEL & S K GUPTA\*

Department of Physics, D N College, Meerut 250 002

Received 8 May 1979; revised received 18 July 1979

The different model force fields, viz. GVFF, MUBFF, MOVFF have been employed to compute the force constants of octahedral ions, viz.  $\text{SnCl}_6^{2-}$ ,  $\text{SnBr}_6^{2-}$  (in the piperdenium and morpholinium salts),  $\text{SbBr}_6^-$ ,  $\text{ReO}_6^{2-}$ ,  $\text{ReF}_6^+$  and  $\text{BrF}_6^+$  using recent vibrational data. The compliance constants have also been calculated. The results are discussed in brief in respect of cation effect, oxidation state and stability of chemical bonds in isoelectronic series. Coriolis coupling constants  $\zeta_1(f_{1u} \times f_{1u})$  have also been computed and their trend discussed. The present computations have been done on a TDC-316 computer.

Recently, Cariati *et al.*<sup>1</sup> have studied the vibrational spectra of hexahalostannate anions (IV), Clark and Duarte<sup>2</sup> that of hexabromoantimonate (V), and Baran<sup>3</sup> that of crystalline  $\text{Ba}_5(\text{ReO}_6)_2$ . Christe and Wilson<sup>4</sup> studied the vibrational spectra of  $\text{BrF}_6^+$  and they analyzed the spectra assuming octahedral symmetry. La Bonville *et al.*<sup>5</sup> have studied the force field of octahedral hexahaloxy molecules and in modified orbital valence force field (MOVFF) reported five force constants with which there is a discrepancy between the observed and the calculated frequencies. Ramaswamy and Muthusubramaniam<sup>6</sup> have reported six force constants in MOVFF with which a good agreement was observed in calculated and observed frequencies. Many workers<sup>7-9</sup> have also used the six constants and found a good agreement between the observed and the calculated frequencies. In case of  $\text{ReO}_6^{2-}$ ,  $\text{ReF}_6^+$  and  $\text{BrF}_6^+$  the GVFF constants have also been calculated by Baran,<sup>3</sup> Baran<sup>10</sup> and Christe and Wilson<sup>4</sup>. In order to apply other model force fields (viz. MOVFF and MUBFF) and to check the validity of approximation methods for solving the determinant occurring in  $2 \times 2$  species, these ions have also been selected with  $\text{SnX}_6^{2-}$  ( $\text{X} = \text{Cl}, \text{Br}$ ) and  $\text{SbBr}_6^-$  for the present study. Further, in the present study it is aimed to investigate; (i) complete set of force constants for these systems employing MOVFF (with six force constants), general valence force field (GVFF) with seven force constants, and modified Urey-Bradley force field (MUBFF) (with seven force constants) models, (ii) the compliance constants, (iii) the

\*Department of Physics, K K Jain College, Khatauli 251201



# NOTES

Coriolis coupling constants, and (iv) to discuss the strength of the various chemical bonds and influence of the oxidation state and cation effect and to study the relative stability in isoelectronic series using recent vibrational data.<sup>1-4,10</sup>  $\text{SbBr}_6^-$  has already been studied,<sup>7</sup> yet because of the availability of new vibrational data the recalculated results are compared with the previous results.

The molecules or ions of the type  $\text{MX}_6$  possessing octahedral symmetry gives rise to six funda-

mental frequencies which are distributed in various symmetry species as:

$$\Gamma_{\text{vib}} = a_{1g} + e_g + 2f_{1u} + f_{2g} + f_{2u}$$

out of these  $\nu_1(a_{1g})$ ,  $\nu_2(e_g)$  and  $\nu_5(f_{2g})$  only are Raman active,  $\nu_3(f_{1u})$  and  $\nu_4(f_{1u})$  are infrared active and  $\nu_6(f_{2u})$  is inactive in both. The inactive fundamental is permitted as binary combination bands or computed with the relation  $\nu_5 = \sqrt{2} \nu_6$ .

Wilson's *F-G* matrix method<sup>11</sup> was employed to calculate the force constant in GVFF, MUBFF and

Table 1—Fundamental Vibrational Wavenumbers (in  $\text{cm}^{-1}$ ) of Some Octahedral Ions

Ion	$\nu_1(a_{1g})$	$\nu_2(e_g)$	$\nu_3(f_{1u})$	$\nu_4(f_{1u})$	$\nu_5(f_{2g})$	$\nu_6(f_{2u})$	Ref.
(pipdH) <sub>2</sub> SnCl <sub>6</sub>	306	230	302	116	162	114.55*	1
(morpH) <sub>2</sub> SnCl <sub>6</sub>	310	235	306	167	170	120.21*	1
(pipdH) <sub>2</sub> SnBr <sub>6</sub>	182	138	210	115	112	79.20*	1
(morpH) <sub>2</sub> SnBr <sub>6</sub>	185	140	220	120	118	83.44*	1
$\text{SbBr}_6^-$	191.5	169	238.5	118.5	103.3	73.04*	2
$\text{ReO}_6^{5-}$	803	548	622	360	455	318.00	3
$\text{ReF}_6^+$	797	734	783	353	359	252.85*	10
$\text{BrF}_6^+$	660	670	775	430	405	286.38*	4

\*Computed by  $\nu_5 = \sqrt{2} \nu_6$

Table 2—GVFF Constants (in  $\text{mdyne}/\text{\AA}$ ) of Some Octahedral Ions

System	$f_r$	$f_{rr}$	$f'_{rr}$	$f_{r\alpha} - f'_{r\alpha}$	$f_{\alpha} - f'_{\alpha\alpha}$	$f_{\alpha\alpha} - f'_{\alpha\alpha}$	$f'_{\alpha\alpha} - f''_{\alpha\alpha}$
(pipdH) <sub>2</sub> SnCl <sub>6</sub> Müller	1.313	0.142	0.076	0.030	0.109	-0.014	-0.014
L-F	1.310	0.142	0.079	0.027	0.109	-0.014	-0.014
(morpH) <sub>2</sub> SnCl <sub>6</sub> Müller	1.377	0.142	0.060	0.062	0.159	0.004	0.004
L-F	1.366	0.142	0.072	0.050	0.159	0.004	0.004
(pipdH) <sub>2</sub> SnBr <sub>6</sub> Müller	1.097	0.110	0.021	0.083	0.146	-0.001	-0.001
L-F	1.067	0.114	0.050	0.063	0.146	-0.001	-0.001
(morpH) <sub>2</sub> SnBr <sub>6</sub> Müller	1.165	0.115	-0.013	0.091	0.161	-0.002	-0.002
L-F	1.134	0.115	0.019	0.068	0.161	-0.002	-0.002
$\text{SbBr}_6^-$ Müller	1.415	0.064	0.057	0.088	0.140	0.007	0.007
L-F	(1.435) <sup>++</sup>	(0.077) <sup>++</sup>	(0.048) <sup>++</sup>	(0.090) <sup>++</sup>	(0.164) <sup>++</sup>	(-0.003) <sup>++</sup>	(-0.003) <sup>++</sup>
$\text{ReO}_6^{5-}$ Müller	3.533	0.541	0.380	0.069	0.474	-0.001	-0.007
L-F	(3.48)*	(0.54)*	(0.42)*		(0.48)*	(0.00)*	(0.00)*
$\text{ReF}_6^+$ Müller	6.075	0.180	0.316	0.088	0.440	0.040	0.040
L-F	(5.92) <sup>+</sup>	(0.22) <sup>+</sup>			(0.44) <sup>+</sup>	(0.04) <sup>+</sup>	
$\text{BrF}_6^+$ Müller	4.896	-0.025	0.079	0.203	0.544	0.043	0.043
L-F	(4.90) <sup>**</sup>	(-0.03) <sup>**</sup>	(0.08) <sup>**</sup>				
	4.862	-0.025	0.112	0.164	0.544	0.043	0.043

<sup>++</sup> Ref. 7; \* Ref. 3; + Ref. 10; \*\* Ref. 4

Table 3—MUBFF and MOVFF Constants (in mdyne/Å) of Some Octahedral Ions

System	Force-field	$K$	$H(D)$	$F$	$F'$	$k$	$h$	$g$
(pipdH) <sub>2</sub> SnCl <sub>6</sub>	MUBFF	1.193	-0.033	0.172	-0.112	0.076	-0.070	-0.014
	MOVFF	1.059	0.178	0.092	-0.192	0.531	-0.098	—
(morpH) <sub>2</sub> SnCl <sub>6</sub>	MUBFF	1.129	0.016	0.205	-0.080	0.060	-0.036	0.004
	MOVFF	1.123	0.190	0.121	-0.163	0.400	-0.078	—
(pipdH) <sub>2</sub> SnBr <sub>6</sub>	MUBFF	0.764	0.036	0.194	-0.027	0.021	-0.014	-0.001
	MOVFF	0.664	0.182	0.150	-0.071	0.300	-0.017	—
(morpH) <sub>2</sub> SnBr <sub>6</sub>	MUBFF	0.803	0.046	0.205	-0.024	-0.014	-0.014	-0.002
	MOVFF	0.685	0.218	0.158	-0.071	0.293	-0.011	—
SbBr <sub>6</sub> <sup>-</sup>	MUBFF	1.063	0.077	0.151	0.024	0.057	0.019	0.007
	MOVFF	1.062	0.237	0.076	-0.051	0.359	0.006	—
		(0.921) <sup>++</sup>	(0.192) <sup>++</sup>	(0.239) <sup>++</sup>	(0.085) <sup>++</sup>	(-0.088) <sup>++</sup>		
ReO <sub>6</sub> <sup>5-</sup>	MUBFF	4.085	0.569	0.178	0.228	0.079	0.156	0.043
	MOVFF	4.453	1.570	-0.169	-0.120	1.099	0.182	—
ReF <sub>6</sub> <sup>+</sup>	MUBFF	5.721	0.261	0.268	-0.092	0.316	-0.006	0.040
	MOVFF	6.893	1.239	0.337	-0.697	1.567	-0.258	—
BrF <sub>6</sub> <sup>+</sup>	MUBFF	4.085	0.569	0.178	0.228	0.079	0.156	0.043
	MOVFF	4.454	1.571	-0.169	-0.120	1.099	0.182	—

<sup>++</sup>Ref. 7.

Table 4—Compliance Constants (in Å/mdyne) of Some Octahedral Ions

System	$c_r$	$c_{rr}$	$c'_{rr}$	$c_{r\alpha} - c''_{r\alpha}$	$c_{\alpha} - c''_{\alpha\alpha}$	$c_{\alpha\alpha} - c''_{\alpha\alpha}$	$c'_{\alpha\alpha} - c''_{\alpha\alpha}$
(pipdH) <sub>2</sub> SnCl <sub>6</sub>	0.805	-0.066	-0.032	-0.285	10.061	1.382	1.382
(morpH) <sub>2</sub> SnCl <sub>6</sub>	0.778	-0.061	-0.034	-0.246	6.463	-0.082	-0.082
(pipdH) <sub>2</sub> SnBr <sub>6</sub>	1.029	-0.079	-0.072	-0.476	7.248	0.237	0.237
(morpH) <sub>2</sub> SnBr <sub>6</sub>	0.967	-0.077	-0.037	-0.435	6.596	0.247	0.247
SbBr <sub>6</sub> <sup>-</sup>	0.770	-0.027	-0.081	-0.386	7.562	-0.201	-0.201
ReO <sub>6</sub> <sup>5-</sup>	0.306	-0.031	-0.015	-0.038	2.117	0.009	0.034
ReF <sub>6</sub> <sup>+</sup>	0.166	-0.004	-0.009	-0.026	2.354	-0.210	-0.210
BrF <sub>6</sub> <sup>+</sup>	0.210	0.001	-0.009	-0.057	1.914	-0.132	-0.132

MOVFF models.  $G$ - and  $F$ -matrices are taken from literature.<sup>6,12</sup> The two-dimensional equation occurring in  $f_{1u}$  species were solved by Müller's  $L$ -matrix method<sup>13-15</sup> and by  $L$ - $F$  approximation.<sup>16</sup> Compliance constants and Coriolis constants ( $f_{1u} \times f_{1u}$ ) have been computed using Cyvin's expression.<sup>12</sup> The present calculations have been carried out on a TDC-316 computer.

The fundamental vibrational wavenumbers used in the present study are listed in Table 1. The computed GVFF constants obtained by Müller's method<sup>13-15</sup> and  $L$ - $F$  method<sup>16</sup> are given and compared in Table 2. The MUBFF and MOVFF cons-

stants are collected in Table 3. A good agreement has been obtained between the observed and the calculated frequencies in the force field models under present discussion. The compliance constants are shown in Table 4. Coriolis coupling constants are presented in Table 5.

The GVFF model includes  $f_r$ , the bond stretching constant,  $f_{\alpha}$ -angle bending constant,  $f_{rr}$ ,  $f'_{rr}$  cis- and trans-bond stretching interactions respectively,  $f_{\alpha\alpha}$ ,  $f'_{\alpha\alpha}$ ,  $f''_{\alpha\alpha}$  — the angle bending interactions and  $f_{r\alpha}$ ,  $f'_{r\alpha}$  — the stretching-bending interaction constants. The MOVFF and MUBFF employ bond stretching force constant  $K$ , angle bending force



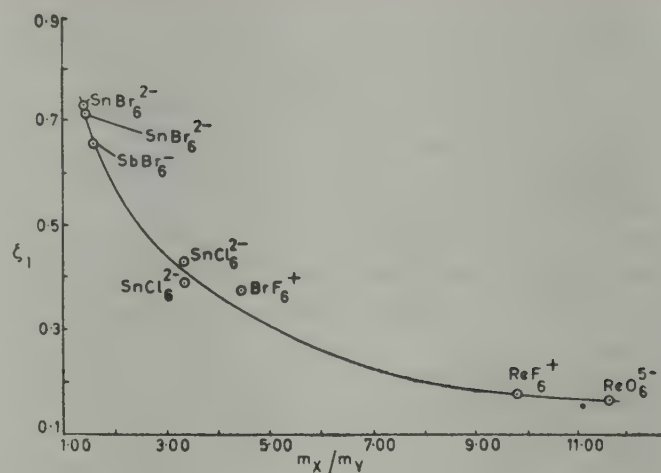
Table 5—Coriolis Coupling Constants of Some Octahedral Ions

System	Coriolis coupling constants		$m_X/m_Y$
	$\zeta_1(f_{1u} \times f_{1u})$	$\zeta_2(f_{1u} \times f_{1u})$	
(pipdH) <sub>2</sub> SnCl <sub>6</sub>	0.386	0.114	3.348
(morpH) <sub>2</sub> SnCl <sub>6</sub>	0.439	0.061	3.348
(pipdH) <sub>2</sub> SnBr <sub>6</sub>	0.727	-0.227	1.485
(morpH) <sub>2</sub> SnBr <sub>6</sub>	0.724	-0.224	1.485
SbBr <sub>6</sub> <sup>-</sup>	0.659	-0.159	1.524
ReO <sub>6</sub> <sup>5-</sup>	0.174	0.326	11.638
ReF <sub>6</sub> <sup>+</sup>	0.179	0.321	9.801
BrF <sub>6</sub> <sup>+</sup>	0.380	0.120	4.206

constant  $D(H)$  and the interaction constants  $F, F', k, h$  and  $g$ .

In order to study the influence of cations on the relative stability of the chemical bonds, it is useful to see the trend in the bond-stretching force constant. From Table 2, the stretching force constant  $f_r$  (in case of SnCl<sub>6</sub><sup>2-</sup> and SnBr<sub>6</sub><sup>2-</sup>) increases from piperdenium salt to morpholinium salt, i.e. the cation in piperdenium salts perturbs the Sn—X (X=Cl, Br) bond more as compared to that in morpholinium salt. The same result is reflected from stretching force constant  $K$  in MOVFF model (Table 3) for these molecules.

It is interesting to study the relative stability of the chemical bonds in isoelectronic series, viz. SnBr<sub>6</sub><sup>2-</sup> and SbBr<sub>6</sub><sup>-</sup>. From Table 2, the stretching force constant  $f_r$  are 1.097 and 1.415 mdyne/Å for SnBr<sub>6</sub><sup>2-</sup> and SbBr<sub>6</sub><sup>-</sup> which corresponds to IV and V oxidation states respectively. It indicates that the higher oxidation state is more stable as compared to lower oxidation state. The same trend is reflected from stretching force constant  $K$  in Table 3. A similar behaviour has been reported by Sanyal *et al.*<sup>17</sup> in case of hexahaloanions. When the  $f_r$  values for other isoelectronic series, viz. (i) TaF<sub>6</sub><sup>-</sup> (3.62)<sup>7</sup>, WF<sub>6</sub> (5.20)<sup>17</sup> and ReF<sub>6</sub><sup>+</sup> (6.07) and (ii) SeF<sub>6</sub> (4.99)<sup>4</sup> and BrF<sub>6</sub><sup>+</sup> (4.89) are compared, it is observed that they also follow the above trend. Comparing the stretching force constant  $f_r$  for ReO<sub>6</sub><sup>5-</sup> (3.533) with TeO<sub>6</sub><sup>6-</sup> (4.12)<sup>9</sup>, it is observed that in octahedral oxyanions the VIth oxidation state is more stable than the VIIth oxidation state. A similar trend has been followed<sup>17</sup> for IO<sub>6</sub><sup>5-</sup> and TeO<sub>6</sub><sup>6-</sup>. Comparing  $f_r$  (Table 2) for

Fig. 1—Variation of Coriolis coupling constant  $\zeta_1 (f_{1u} \times f_{1u})$  with mass ratio  $m_X/m_Y$  of central and ligand atoms

(i) SnCl<sub>6</sub><sup>2-</sup> (1.3) with that for PbCl<sub>6</sub><sup>-</sup> (0.378)<sup>8</sup> and

(ii) ClF<sub>6</sub><sup>+</sup> (5.06)<sup>4</sup>, BrF<sub>6</sub><sup>+</sup> (4.89), it is observed that stretching force constant decreases with increase in mass of central atom. It is in agreement with the trend given in literature.<sup>18</sup>

It is also noted that  $f_{rr} > f'_{rr}$  (Table 2). A similar trend has been observed by other workers.<sup>7,8,17</sup> Force constants calculated by the  $L-F$  method are well comparable to Miller's method (Table 2), i.e. both approximations are applicable to the systems under present study. Further, these values are in good agreement with their previous values in GVFF model (Table 2).

The compliance constant  $c_r$  from Table 4 shows, in general, the reverse trend than that discussed above in case of stretching force constant, which also favours the validity of the computed force constants. The variation of Coriolis constant  $\zeta_1 (f_{1u} \times f_{1u})$  with  $m_X/m_Y$  is shown in Fig. 1, which indicates the expected trend.

One of the authors (RKG) is thankful to the University Grants Commission, New Delhi for financial assistance.

#### References

1. Cariati F, Marotrigiano G *et al.*, *Spectrochim. Acta*, **34A** (1978), 801.
2. Clark R J H & Duarte M L, *J. chem Soc. Dalton*, 1977, 790.
3. Baran E J, *Mon Chem.*, **107** (1976), 1327.
4. Christie K O & Wilson R D, *Inorg. Chem.*, **14** (1975), 694.
5. La Bonville P, Ferraro J R, Wall M C & Basile L J, *Coord. Chem. Rev.*, **7** (1972), 257.
6. Ramaswamy K & Muthusubramaniam P, *Indian J. Phys.*, **45** (1971), 477.
7. Sharma D K, Pandey A N & Goel R K, *Indian J. pure appl. Phys.*, **12** (1974), 455.
8. Goel R K, (Smt) Sharma S & Pandey A N, *Indian J. pure appl. Phys.*, **16** (1978), 102.



9. Pandey A N, Sharma D K & Dubish A K, *Spectrosc. Lett.*, 6 (1973), 491.
10. Baran E J, *Z. Naturf.*, 31A (1976), 1733.
11. Wilson (Jr) E B, Decius J C & Cross P C, *Molecular vibrations* (Mc Graw-Hill, New-York), 1955.
12. Cyvin S J, *Molecular vibrations and mean square amplitudes* (Elsevier, Amsterdam), 1968.
13. Müller A & Peacock C J, *Molec. Phys.*, 14 (1968), 393.
14. Müller A, *Z. Phys. Chem.*, 238 (1968), 116.
15. Peacock C J & Müller A, *J. molec. Spectrosc.*, 26 (1968), 454.
16. Pandey A N, Sharma D K, Verma U P, Arora L D, Gupta S L & Singh B P, *Indian J. pure appl. Phys.*, 14 (1976), 815.
17. Sanyal Nitish K, Goel R K & Pandey A N, *Indian J. Phys.*, 50 (1976), 659.
18. Goel R K, *Theoretical and experimental studies of molecular parameters of some polyatomic molecules and ions using spectroscopic methods*, Ph D thesis, Gorakhpur University, Gorakhpur, 1977.

### Molecular Constants & Vibrational Amplitudes of Some Tetrahedral Systems

NITISH K SANYAL

Department of Physics, University of Gorakhpur  
Gorakhpur 273 001

&

R K GOEL\* & S D SHARMA

Department of Physics, D N College, Meerut 250 002

Received 28 April 1979; revised received 5 November 1979

The complete set of force constants of tetrahedral systems, viz.  $\text{CF}_4$ ,  $\text{NH}_4^+$  ion,  $\text{CrCl}_4$  and  $\text{CrBr}_4$  has been calculated using recent vibrational data employing GVFF, OVFF and UBFF models. The reliability of force constants is tested in case of  $\text{CF}_4$  isotopes. Compliance constants, kinetic constants, shrinkage effects and Coriolis coupling constants are also calculated. The trend of force constants and relative strengths of chemical bonds are discussed. The effect of oxidation state is also discussed in isoelectronic series. The mean vibrational amplitudes for bonded and non-bonded atom-pairs at room temperatures (298.15 K) are calculated and their trend discussed. The computations have been carried out on a TDC-316 computer.

Recently, Jones *et al.*<sup>1</sup> have studied the infrared spectra of isotopes of  $\text{CF}_4$  (namely  $^{12}\text{CF}_4$ ,  $^{13}\text{CF}_4$  and  $^{14}\text{CF}_4$ ), Gallagher and Klein<sup>2</sup> studied the Raman spectra of  $\text{NH}_4^+$  ions at various temperatures in  $\text{NH}_4\text{Ag}_5\text{I}_6$  and Cuoni *et al.*<sup>3</sup> have studied the Raman spectra of chromium tetrachloride ( $\text{CrCl}_4$ ) and chromium tetrabromide ( $\text{CrBr}_4$ ) and analyzed the spectra on the basis of  $T_d$  symmetry. Jones *et al.*<sup>1</sup> established the unique set of force constants for  $\text{CF}_4$ . Cuoni *et al.*<sup>3</sup> studied the force constants of  $\text{CrCl}_4$  and  $\text{CrBr}_4$  on the basis of Fadini's method.<sup>4</sup>

In the present note, the studies of a set of force constants obtained by employing, the general valence force field (GVFF), orbital valence force field (OVFF) and Urey-Bradley force field (UBFF) are reported. Force constants have also been studied using Lennard-Jones potential (LJP) approximation. The compliance constants, kinetic constants, Coriolis coupling constants and shrinkage effects have also been calculated and the trend discussed. Isotopic substitution has been tested in case of  $\text{CF}_4$  isotopes. The mean amplitudes of vibration at room temperature (298.15 K) for these molecules are also calculated.

Wilson's FG-matrix method<sup>5</sup> has been followed to calculate the force constants. The  $G$  and  $F$  matrices are taken from literature.<sup>6-8</sup> The mean amplitudes of vibration have been calculated using Cyvin's secular equation<sup>8</sup>  $|\Sigma G^{-1} - \Delta E| = 0$ . Müller's  $L$ -matrix method<sup>9-11</sup> and  $L$ - $F$  method<sup>12</sup> have been followed for the solution of  $2 \times 2$  determinant occurring in  $f_2$  species. The Cyvin's<sup>8</sup> expressions have been used for compliance constants, shrinkage effects and Coriolis coupling constants and those of Thirugnanasambandam<sup>13,14</sup> are used for kinetic constants.

Table 1—OVFF and UBFF Constants (mdyne/Å) of Some  $\text{XY}_4$  Systems

Molecule		$K_1$ (K)	$K_2$ (3 H)	$A$ (F/2)	$B/R(-F')$
$^{14}\text{CF}_4$	UBFF	4.245	0.674	0.624	0.196
	LJP	4.364	0.978	0.609	0.094
	UBFF	4.091	0.522	0.643	0.309
$\text{NH}_4^+$ (300 K)	OVFF	4.667	1.555	0.137	-0.222
	LJP	5.066	0.809	0.087	0.013
	UBFF	4.986	1.450	0.097	-0.037
$\text{NH}_4^+$ (103 K)	OVFF	4.682	1.593	0.121	-0.228
	LJP	5.081	0.838	0.071	0.011
	UBFF	5.006	1.483	0.081	-0.038
$\text{NH}_4^+$ (All Temp.)	OVFF	4.779	1.627	0.107	0.234
	LJP	5.178	0.864	0.057	0.009
	UBFF	5.106	1.513	0.066	-0.038
$\text{CrCl}_4$	OVFF	2.498	0.212	0.051	-0.033
	LJP	2.501	0.077	0.051	0.008
	UBFF	2.500	0.186	0.051	-0.007
$\text{CrBr}_4$	OVFF	2.044	0.108	0.040	-0.018
	LJP	2.034	0.026	0.041	0.006
	UBFF	2.038	0.093	0.040	-0.004

\* To whom all correspondence should be made



# NOTES

The OVFF and UBFF force constants are reported in Tables 1. The two sets of GVFF force constants obtained by Müller's and L-F approximations are compared in Table 2. The compliance constants and the kinetic constants are given in Table 3 and 4. The vibrational amplitudes for bonded and non-bonded distances and shrinkage effects at room temperatures (298·15 K) are shown in Table 5. The Coriolis coupling constants  $\zeta_{33}$  ( $f_2 \times f_2$ ) and  $\zeta_{24}$  ( $e \times f_2$ ) are presented in Table 1 and their variation is shown in Fig. 1.

From Table 1 it is observed that there is a fair degree of agreement between the OVFF and UBFF set of force constants. Negative values of  $B/R$  have been obtained in all cases except for  $\text{CF}_4$ , which in itself does not have any physical significance. In order to understand the nature of non-bonded interaction, a new set of force constants was calculated using Lennard-Jones potential ( $A = 6\cdot5 B/R$ ). Frequencies reproduced by this method are not in good agreement with the observed frequencies except that in case of  $\text{CF}_4$  ions where the deviation for  $\nu_2$  and  $\nu_4$  is 1·6%. Thus it indicates that the Lennard-Jones potential is inadequate to take into account the interaction between non-bonded atoms as shown by Müller<sup>6</sup> and Sanyal *et al.*<sup>15</sup> From Table 1, the two sets of force constants obtained using L-F and

Müller's approximations are well comparable, i.e. both the approximations are equally applicable to these systems.

The reliability of a set of force constants for  $^{14}\text{CF}_4$  has been tested by calculating the fundamental frequencies of isotopes  $^{13}\text{CF}_4$  and  $^{13}\text{CF}_4$  using the force constant of  $^{14}\text{CF}_4$ . A good agreement is observed in calculated frequencies by the GVFF, UBFF and OVFF set of force constants.

Table 3—Compliance Constants ( $\text{\AA}/\text{mdyne}$ ) of Some  $\text{XY}_4$  Systems

Molecule/ Ion	$c_r$	$c_{rr}$	$c_\alpha$	$c_{\alpha\alpha}$	$c_\alpha$
$^{14}\text{CF}_4$	0·157 (0·161)*	−0·016	1·234	−0·091	0·133
$\text{NH}_4^+$ (300 K)	0·186	−0·004	2·068	0·101	−0·022
$\text{NH}_4^+$ (103 K)	0·187	−0·004	2·068	0·101	−0·022
$\text{NH}_4^+$ (All Temp.)	0·186	−0·003	2·068	0·101	−0·021
$\text{CrCl}_4$	0·376	−0·011	12·096	0·711	0·249
$\text{CrBr}_4$	0·465	−0·014	20·556	1·428	−0·438

\* Ref. 1

Table 2—GVFF Constants (in  $\text{mdyne}/\text{\AA}$ ) and Coriolis Coupling Constants of Some  $\text{XY}_4$  Systems

Molecule		$f_r$	$f_{rr}$	$f_\alpha$	$f_{\alpha\alpha}$	$f_{r\alpha}$	$\zeta_{33} (f_2 \times f_2)$	$\zeta_{24} (e \times f_2)$	$m_X/m_Y$
$^{14}\text{CF}_4$	Müller	7·873	0·455	0·963	0·128	0·877	0·716	−0·306	0·736
	L-F	7·497	0·580	0·972	0·133	0·747			
		(6·96+0·02)*							
$\text{NH}_4^+$ (300 K)	Müller	5·395	0·122	0·485	−0·026	0·060	0·091	−1·311	13·898
	L-F	5·393	0·123	0·485	−0·026	0·055			
$\text{NH}_4^+$ (103 K)	Müller	5·355	0·099	0·485	−0·026	0·060	0·091	−1·313	13·898
	L-F	5·353	0·100	0·485	−0·026	0·055			
$\text{NH}_4^+$ (All Temp.)	Müller	5·401	0·078	0·485	−0·026	0·060	0·091	−1·305	13·898
	L-F	5·399	0·078	0·485	−0·026	0·055			
$\text{CrCl}_4$	Müller	2·722	0·061	0·085	−0·004	0·057	0·479	−0·186	1·466
	L-F	2·717	0·063	0·085	−0·004	0·055			
$\text{CrBr}_4$	Müller	2·227	0·045	0·051	−0·003	0·048	0·674	−0·271	0·651
	L-F	2·222	0·047	0·051	−0·003	0·046			

\* Ref. 1, † Ref. 3.

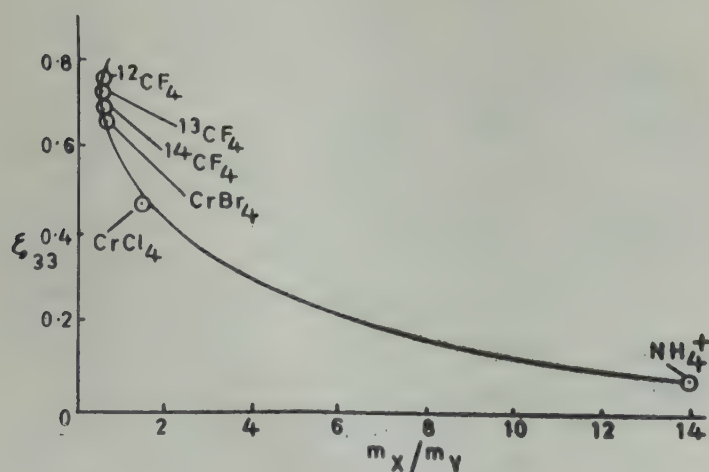
Table 4—Kinetic Constants (in  $10^{-23}$  g) of Some  $XY_4$  Systems

Molecule/ Ions	$K_d$	$K_{dd}$	$K_\alpha$	$K_{\alpha\alpha}$	$K'_{\alpha\alpha}$	$K_{d\alpha}$	$\sum K_\alpha + \sum K_{dd} = 4/\mu_Y$
$^{12}\text{CF}_4$	2.474	0.227	0.685	-0.175	0.016	0.321	12.619
$^{13}\text{CF}_4$	2.481	0.225	0.690	-0.175	0.011	0.318	12.619
$^{14}\text{CF}_4$	2.489	0.222	0.695	-0.175	0.006	0.314	12.619
$\text{NH}_4^+$	0.158	0.003	0.054	-0.009	-0.017	0.044	0.069
$\text{CrCl}_4$	4.810	0.359	1.408	-0.327	-0.100	0.508	23.548
$\text{CrBr}_4$	10.416	0.951	2.889	-0.737	0.059	1.345	53.077

 Table 5—Mean Amplitude of Vibration and Shrinkage Effect of Some  $XY_4$  Systems (in Å)

Molecule/Ions	$U_{X-Y}$ 298.15 K	$U_{X-Y}$ 298.15 K
$^{12}\text{CF}_4$	0.0432 (0.0016)*	0.0539
$^{13}\text{CF}_4$	0.0429 (0.0015)*	0.0539
$^{14}\text{CF}_4$	0.0425 (0.0015)*	0.0539
$\text{NH}_4^+$ (300 K)	0.0759	0.1224
$\text{NH}_4^+$ (103 K)	0.0760	0.1226
$\text{NH}_4^+$ (All Temp.)	0.0758	0.1225
$\text{CrCl}_4$	0.0463	0.1222
$\text{CrBr}_4$	0.0482	0.1526

\* Values in parantheses are the shrinkage effects  $\delta_{Y-X}$


 Fig. 1—Variation of Coriolis coupling constant  $\epsilon_{33}$  with mass ratio  $m_X/m_Y$  of central and legand atoms

Comparing  $f_r$  for  $\text{CF}_4$  (7.497) with that for  $\text{CCl}_4$  (2.691) and  $\text{CBr}_4$  (2.197)<sup>15</sup>, and  $\text{CrCl}_4$  (2.72) with  $\text{CrBr}_4$  (2.227), it is observed that the stability of chemical bonds is in the order  $\text{M}-\text{F} > \text{M}-\text{Cl} > \text{M}-\text{Br}$  ( $\text{M} = \text{C}, \text{Cr}$ ), i.e. decreases with the mass of the peripheral atom. A similar behaviour has been observed by other workers<sup>16,17</sup> also. Comparing  $f_r$  for  $\text{CF}_4$  (7.497) with  $\text{PbF}_4$  (3.31)<sup>16</sup> it is observed that strength of  $\text{M}-\text{F}$  ( $\text{M} = \text{C}, \text{Pb}$ ) bond decreases with the increase of mass of central atom. It is in agreement with the literature values.<sup>17</sup> The same is supported from  $K_1$  (K) from Table 2.

The force constant  $f_r$  or  $K_1$  (K) from Tables 1 and 2 of  $\text{NH}_4^+$  ion in  $\text{NH}_4\text{AG}_4\text{I}_5$  decreases slightly when the temperature is lowered. A similar conclusion was drawn by Gallagher and Klein<sup>2</sup> from vibrational data.

It is interesting to study the relative stability of the chemical bonds in isoelectronic series, viz. (i)  $\text{BeF}_4^{2-}$  II (1.68)<sup>16</sup>,  $\text{BF}_4^-$  III (3.9)<sup>16</sup>,  $^{14}\text{CF}_4$  IV (7.497) from Table 1, (ii)  $\text{TiCl}_4$  IV (2.75)<sup>3</sup>,  $\text{CrCl}_4$  III (2.722) and (iii)  $\text{TiBr}_4$  IV (2.31)<sup>3</sup>,  $\text{CrBr}_4$  III (2.227), for  $K_1$  from Table 2,  $\text{CrCl}_4$  III (2.498),  $\text{MnCl}_4^2-$  II (0.832)<sup>18</sup> and  $\text{CrBr}_4$  III (2.044),  $\text{MnBr}_4^{2-}$  II (0.785)<sup>19</sup>, taking most stable oxidation states of Ti and Cr. From a comparison of these values, it is found that the higher oxidation state is more stable than the lower oxidation state. It is in agreement with the literature values<sup>18</sup> in case of many tetrahalogeno complexes.

Values of compliance constant (Table 3) and mean amplitudes of vibration (Table 5) show a trend opposite to that of the stretching force constant. The shrinkage effects for the three isotopes of  $\text{CF}_4$  is the same, which may be due to their high order and same magnitude of their stretching force constant.

One of the authors (RKG) is thankful to the University Grants Commission, New Delhi, for the financial assistance.

#### References

1. Jones L H, Kennedy C & Ekberg S, *J. chem. Phys.*, 69 (1978), 833.
2. Gallagher D A & Klein M V, *J. chem. Phys.*, 68 (1978), 4804.
3. Cuoni B, Emmenegger F P, Rohrbasser C, Schlapeer C W & Studer P, *Spectrochim. Acta*, 34A (1978), 247.
4. Fadini A, *Z. Naturf.*, 21A (1966), 426.
5. Wilson (Jr) E B, Decius J C & Crose P C, *Molecular vibrations* (McGraw-Hill, New York), 1955.
6. Krebs B & Müller A, *J. molec. Spectrosc.*, 22 (1967), 290.



7. Müller A & Krebs B, *J. Molec. Spectrosc.*, 24 (1967), 180.
8. Cyvin S J, *Molecular vibrations and mean square amplitudes* (Universitets Forlaget Oslo & Elsevier, Amsterdam), 1968.
9. Müller A, *Z. phys. Chem.*, 238 (1968), 116.
10. Peacock C J & Müller A, *J. molec. Spectrosc.*, 26 (1968), 454.
11. Müller A & Peacock C J, *molec. Phys.*, 14 (1968), 393.
12. Pandey A N, Sharma D K, Verma U P, Arora L D, Gupta S L & Singh B P, *Indian J. pure appl. Phys.*, 14 (1976), 457.
13. Thirugnanasambandam P, *Proc. Seminar Raman & IR Spectrosc.*, (University of Kerala, Kariavattom), 1964, 174.
14. Thirugnanasambandam P & Srinivasan S, *J. chem. Phys.*, 50 (1969), 2467.
15. Sanyal Nitish K, Pandey A N & Singh H S, *J. molec. Spectrosc.*, 30 (1969), 144.
16. Dixit L, *Studies in molecular vibrations and related bond properties of simple systems*, Ph D thesis, Gorakhpur University, Gorakhpur, 1975.
17. Sanyal Nitish K, Goel R K & Pandey A N, *Indian J. pure appl. Phys.*, 13 (1975), 373.
18. Sharma D K, *Studies in molecular constants from spectral data*, Ph D thesis, Meerut University, Meerut, 1976.
19. Goel R K, *Theoretical and experimental studies of molecular parameters of some polyatomic molecules and ions using spectroscopic methods*, Ph D thesis, Gorakhpur University, Gorakhpur, 1977.

### Sparking Potentials in Longitudinal Magnetic Fields

A NATARAJAN

Department of Physics, Autonomous P G Centre  
Tiruchirapalli 620 020

&

V SELVARAJAN

Department of Physics, A V V M Sri Pushpam College  
Poondi 613 503

Received 6 April 1979; revised received 4 February 1980

The sparking potentials in dry air in longitudinal magnetic fields have been investigated, for pressures 0.50, 0.44, 0.40 and 0.36 torr. The range of  $H/P$  (Tesla torr<sup>-1</sup>) values studied were 0 to  $56.25 \times 10^{-2}$ . The present investigation shows that at these pressures the presence of the magnetic field decreases the sparking potentials. This lowering of sparking potentials is in agreement with the equivalent pressure concept.

In recent years, considerable work has been carried out to investigate the influence of crossed electric and magnetic fields on the sparking potentials, in gases. But to the best of the knowledge of the authors, no previous measurements of sparking potentials in longitudinal magnetic fields have been reported. Hence the present investigation is of special interest.

According to Gurumurthy and Govindraju,<sup>1</sup> the equation for the breakdown potentials in the presence of magnetic fields is given by:

$$V_{SB} = \frac{1}{(\sigma/E_{SB})_{B/P, E_{SB}/P}} (\alpha/E_s)_{0, E/P} (V_s) \quad \dots(1)$$

where,  $V_s$  is the sparking potential in the absence of a magnetic field;  $V_{SB}$  is the sparking potential in the presence of a magnetic field;  $B$ , the strength of the magnetic field;  $E_s$ , the strength of the electric field at sparking;  $P$ , the pressure in torr, and  $\alpha$  the Townsend's first ionisation coefficient.

Results of the present investigation can be explained using Eq. (1).

The experimental arrangement is shown schematically in Fig. 1. A specially fabricated discharge tube was used for the study of sparking potentials. The electrodes were aluminium discs of diameter 2 cm separated by a distance of 0.48 cm. They were rounded off at the edges to eliminate the effect of sharp edges. Low pressures were produced by a high vacuum pump and measured accurately by a Mcleod gauge. Air was dried by a drying tower containing calcium chloride and allowed into the discharge tube through a needle valve.

Potentials were applied to the discharge tube from a stabilized power supply. Maximum variation in the supply was  $\pm 0.33\%$ . A potential divider arrangement, similar to the one used by Rajapandian,<sup>2</sup> was used to vary the potential across the discharge tube. The potential could be varied in steps of 1.8 V.

The longitudinal magnetic field was produced by an electromagnet. Flat pole pieces (diam. 8 cm) used were separated by a distance of 9.5 cm. The field was uniform at the middle region for a length of 0.75 cm. The field was also uniform throughout the cross-section of the electrodes. Magnetic fields were measured by a calibrated fluxmeter.

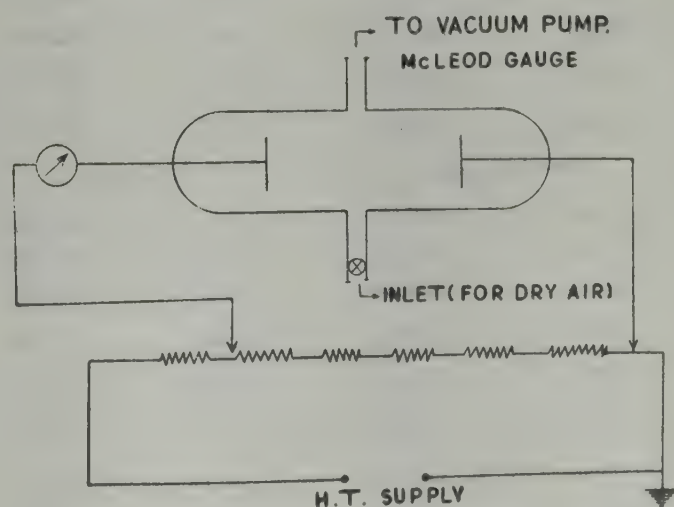


Fig.1 —Schematic diagram of the experimental set-up



In the present investigation, an abrupt change in current was taken as an indication of breakdown, which was observed by a ballistic galvanometer. Break occurred at a current of  $3.57 \times 10^{-7}$  A. A very faint glow was also observed in the middle regions of the electrode, when breakdown occurred.

Before the actual work, the tube was cleaned by chemicals and by a continuous discharge for a few hours. When the pressure was steady, indicated by the Pirani gauge, potential was applied across the discharge tube and sparking potentials determined. The breakdown was very clear and definite. Sparking voltage in the absence of the magnetic field was determined several times to condition the electrodes.<sup>3</sup> When consistent results were obtained a number of times, the magnetic field ( $H$ ) was applied and the sparking potentials determined for selected values of  $H$ . The whole procedure was repeated to ensure consistent results and was performed at various pressures.

The results are reported in Table 1 for different pressures and  $H/P$  values. The nature of variation of the sparking potential with longitudinal magnetic fields is shown in Fig. 2. In Table 1, it is seen that the sparking potential increases with decrease of pressure, in the absence, as well as in the presence of the magnetic field. This indicates that the sparking potentials lie on the left side of the Paschen minimum. This is in agreement with the accepted theory that at

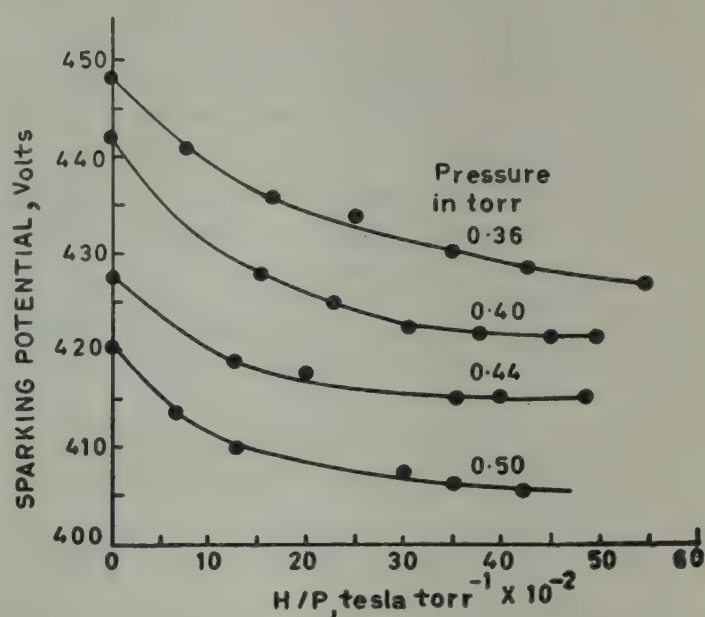


Fig. 2—Sparking potential versus  $H/P$  for 4 different pressures

the left of the Paschen minimum, the sparking voltage should increase with decrease in pressure.

It is also seen from Table 1 that at all the pressures studied, the sparking potential decreases with the magnetic field. In Fig. 2, we observe that the decrease is sharp in the beginning and attains saturation with large  $H/P$  values. The saturation is prominent for higher pressures, rather than for lower ones. This variation is the same as that observed by Gurumurthy and Govinda Raju<sup>1</sup> with crossed electric and magnetic fields. The results of the present investigation when compared with the results of Gurumurthy and Govinda Raju<sup>1</sup> and that of Sengupta *et al.*<sup>4</sup> show that the longitudinal magnetic field is less influential on the sparking potential than the transverse magnetic field. For example, in the present investigation, at a pressure of 0.5 torr (electrode gap 0.48 cm,  $P \times d = 0.24$  torr-cm) the difference in breakdown potentials for a longitudinal magnetic field of 300 gauss (i.e.  $H/P = 600$ ) is 5.4 V, whereas at  $P \times d = 0.24$  torr-cm ( $0.048 \times 5$ ) and for a transverse magnetic field<sup>4</sup> of 310 gauss, the difference in breakdown potentials is approximately 1300 V.

The present investigation shows that the sparking potential decreases with longitudinal magnetic fields. Hence  $(\alpha/E_{SB})_{B/P}$ ,  $E_{SB/P}$  (Eq. 1) should increase with magnetic field. That means, the number of ionizing collisions increases with longitudinal magnetic field in the range of the pressures studied. Blevin and Haydon<sup>5</sup> introduced the concept of an 'equivalent pressure' for the crossed magnetic field. For longitudinal magnetic field also, the field may be assumed to be equivalent to a pressure. So by the application of the longitudinal magnetic field, the total pressure

Table 1—Values of the Sparking Potentials (in V) for Different Values of  $H/P$  (Tesla torr<sup>-1</sup>)

$H/P \times 10^{-2}$	Sparking potential, V	$H/P \times 10^{-2}$	Sparking Potential, V
$P=0.50$ torr		$P=0.44$ torr	
0	419.40	0	426.60
6.0	414.00	6.86	421.20
12.00	410.40	13.72	419.40
18.40	410.40	21.04	419.40
23.50	410.40	26.88	417.60
30.00	408.60	34.31	415.80
35.50	406.80	40.60	415.80
41.00	406.80	46.89	415.80
$P=0.40$ torr		$P=0.36$ torr	
0	422.80	0	448.20
7.50	438.80	8.23	441.00
15.00	428.40	16.46	435.60
23.00	424.80	25.24	433.80
29.38	423.00	32.24	430.20
37.50	423.00	41.16	430.20
44.38	423.00	48.70	428.40
51.25	421.20	56.25	426.60



apparently increases. On the left hand side of the Paschen minimum, an increase in pressure should lead to a decrease in sparking potential, as observed in this investigation. Hence the present results are in agreement with the equivalent pressure concept.

One of the authors (VS) is thankful to the University Grants Commission, New Delhi, for the financial assistance given.

#### References

1. Gurumurthy G R & Govinda Raju G R, *IEEE Trans.*, PS-3 (1975), 131.
2. Rajapandian S, *Prebreakdown currents and sparking potentials in gases in crossed electric and magnetic fields*, Ph D thesis, Indian Institute of Science, Bangalore, 1973.
3. Govinda Raju G R & Rajapandian S, *IEEE Trans.*, EI 11 (1976), 1.
4. Sengupta D, Guharay S K, Ghoshroy D N & Sen gupta S N, *Pramana*, 11 (1978), 661.
5. Bievin H A & Haydon S C, *Aust. J. Phys.*, 11 (1958), 18.

### Plasmon Excitation in Solids during X-ray Scattering

K S SRIVASTAVA

Physics Department, Lucknow University, Lucknow 226 007

Received 4 July 1979; revised received 24 January 1980

The existence of plasmon scattering during the X-ray scattering process has been established. Minimum angle of X-ray plasmon scattering has been calculated for Cu  $K\alpha_1$  radiation as  $9^\circ$  which is fairly close to the observed value of  $10^\circ$ .

The effects of plasmon oscillation on X-ray emission and absorption spectroscopy, photo-electron spectroscopy, soft X-ray appearance potential spectroscopy and Auger electron spectroscopy, etc., have been studied very extensively both theoretically and experimentally during the last 15 years by several workers.<sup>1,2</sup> But the influence of plasmon oscillation on X-ray scattering process has not received much attention. Recently, the author<sup>3</sup> has calculated the maximum angle of X-ray plasmon scattering and in the present note the calculation of the minimum angle is being reported. The existence of plasmon scattering during the X-ray scattering process from the energy conservation point of view has also been established.

The X-ray inelastic scattering by electrons in solids is classified as Compton, Raman and plasmon scattering. The existence of X-ray Raman lines was predicted theoretically by Du Mond<sup>4</sup> and Sommerfeld<sup>5</sup> but it was observed for the first time by Das Gupta<sup>6</sup> and later by Faessler and Muhle<sup>7</sup> and several other workers.<sup>8,9</sup> According to Das Gupta

the energy equation for the X-ray scattering process can be written, to a first approximation, as

$$h\nu_0 = h\nu_m + h\nu_q \quad \dots(1)$$

where,  $\nu_i$  and  $\nu_m$  are the frequencies of the incident and scattered (or modified) X-rays respectively and  $h\nu_q$  is the energy of the photon just sufficient to raise the  $q$ th electron of the scattering atom from the  $q$ th level (or ground state) to the first unoccupied level ( $E_F$ ) above the Fermi surface in the solid material.

It has been found from Das Gupta's results<sup>6</sup> that for certain angles of scattering the calculated values of the scattered radiation energy ( $h\nu_m$ ) from Eq. (1) are consistently higher than the experimentally observed values. This gives us an indication that, for these angles, part of the incident X-ray photon energy is being used in some other process also. If we assume that plasmons are excited during the X-ray scattering process, then part of the incident energy of X-ray photons will be used up in exciting the plasmon and Eq. (1) takes up the form

$$h\nu_0 = h\nu_m + h\nu_q + h\nu_p \quad \dots(2)$$

$$\text{or } h\nu_m = h\nu_0 - (h\nu_q + h\nu_p)$$

where  $h\nu_p$  is the energy required to excite a plasmon. The value of  $h\nu_m$  calculated from Eq. (2) agrees better with the experimental values of Das Gupta<sup>6</sup> than with that from Eq. (1). That is, if X-ray plasmon scattering is also taking place during the Compton and Raman scattering processes then the modified line should be observed at an energy distance of  $(h\nu_q + h\nu_p)$  from the Rayleigh line ( $h\nu_0$ ) rather than at an energy distance of  $h\nu_q$  which is evident from Table 1.

Eq. (2) will hold good for conservation of energy only in the scattering angle range  $10-50^\circ$ . In this range, the only experimental data available are of Das Gupta<sup>6</sup> for Li, LiF and  $\text{Li}_2\text{O}$ . The value of  $h\nu_m$  has been calculated from Eq. (2) and they agree fairly well with the experimental value of Das Gupta<sup>6</sup> as shown in the Table 1.

The possibility of exciting plasmon oscillations in solids by X-rays was predicted by Nozieres and Pines<sup>11</sup> and later, Ohmura and Matsudaira<sup>12</sup> pointed out that plasmons can be excited during the X-ray scattering process if the momentum transferred ( $K$ ) is small or comparable to the critical plasma cut-off wave vector  $K_c$ , i.e.

$$K \leq K_c$$

$$\text{or } (4\pi/\lambda) \sin \theta/2 = 0.47 (r_s)^{1/2} K_0 \quad \dots(3)$$

where,  $K_0$  is the Fermi wave vector;  $r_s$  a dimensionless parameter;  $\lambda$  the wavelength of the incident radiation and  $\theta$  the scattering angle. Pines<sup>13</sup> has



Table 1—Calculated and Experimental Values of X-ray Raman Lines using Li as Scatterer [Modified line scheme (according to author)  $\text{CuK}\alpha_1 - (\text{LiK} + h\nu_p)$ ]

Scattering specimen	Energy calc., eV		Energy Observed by Das Gupta $(h\nu_m)\text{Obs.}$	$(h\nu_m)\text{Obs.} - (h\nu_m)\text{Calc.}$
	by author $(h\nu_m)\text{Calc.}$	by Das Gupta $(h\nu_m)\text{Calc.}$		
Li Metal	7965.9	7973.0	7966.6	0.7
Li in LiF	7985.7	7992.4	7986.2	0.5
Li in $\text{Li}_2\text{O}$	7985.7	7992.4	7985.1	0.6
For Li and $\text{CuK}\alpha_1$ radiation (Ref. 10):				
Energy of incident radiation $h\nu_1$	= 8047.4		eV	
Energy of K absorption edge	= 54.7		eV	
and Plasmon energy	= 7.0		eV	

shown that the value of the coupling constant  $\beta = K_c/K_0$  varies between the limits

$$\beta_{\max} = \frac{K_c}{K_0} = 0.47 (r_s)^{1/2} \quad \dots (4)$$

$$\text{and } \beta_{\min} = \frac{K_c}{K_0} = 0.353 (r_s)^{1/2} \quad \dots (5)$$

Ohmura and Matsudaira<sup>12</sup>, in deriving the condition given by Eq. (3), have used only the maximum value of  $\beta$ . In order to deduce the minimum angle for plasmon scattering, we must use the minimum value of  $\beta$  given by Eq. (5). This value of  $\beta$  can be further modified<sup>14</sup>, by taking into account the cancellation when slow charge is conserved. The effect of this<sup>14</sup> interference term is to reduce  $\beta$  by an amount  $(e^2/\hbar v) F(v)$ , i.e.

$$\beta' = \beta - \left( \frac{e^2}{\hbar v} \right) F(v) \quad \dots (6)$$

where  $F(v)$  is a slowly varying function of velocity of magnitude unity. The value of  $(e^2/\hbar v)$  has been calculated<sup>14</sup> and is of the order of 0.1 for the incident energy of the order of kilo electron volts and so  $\beta'$  is given by

$$\beta' = \beta - 0.1 = 0.353 r_s^{1/2} - 0.1 \quad \dots (7)$$

Thus in case of beryllium

$$\beta' = 0.38 = \frac{K_c}{K_0} \quad \dots (8)$$

$$\text{Hence } K_c = 0.38 K_0 = 0.73 \text{ \AA}^{-1} \quad \dots (9)$$

Using this value of  $K_c$ , the minimum angle of plasmon scattering has been calculated from Eq. (3), using Cr  $K\beta_1$  and Cu  $K\beta_1$  as reference lines obtaining the values  $13^\circ$  and  $9^\circ$  respectively which are in close

agreement with the observed value  $10^\circ$ . Thus the author has removed the discrepancy between the observed and calculated values for the minimum angle of plasmon scattering.

Thanks are due to Dr B G Gokhale, Professor & Head, Physics Department, Lucknow University, Lucknow, for helpful discussion, and also to the University Grants Commission, and CSIR, New Delhi for financial assistance.

#### References

1. Brouers F, *Phys. Status Solidi*, 22 (1967), 213.
2. Arakava E T & William M W, *Phys. Rev.*, 8B (1973), 4075.
3. Srivastava K S, *Solid St. Commun.*, 30 (1979), 19.
4. Du Mond J W M, *Rev. mod. Phys.*, 5 (1933), 11.
5. Smmerfeld A, *Phys. Rev.*, 50 (1936), 38.
6. Das Gupta K, *Phys. Rev.*, 128 (1962), 2181.
7. Faessler A & Muhle P, *Phys. Rev. Lett.*, 17 (1966), 4.
8. Priftis G, Theodossiou A & Alexopoulos K, *Physics Lett.*, 27A (1968), 577.
9. Suzuki T & Tanokura A, *J. phys. Soc. Japan*, 29 (1970), 972.
10. Kunz C, *Z. Phys.*, 196 (1966), 311.
11. Nozieres D & Pines D, *Nuovo Cim.*, 9 (1958), 470.
12. Ohmura Y & Matsudaira N, *J. phys. Soc. Japan*, 19 (1964), 1355.
13. Pines D, *Elementary excitation in solids*, (Benjamin, New York), 1964.
14. Langreth D C, *Noble Symodia*, 24 (1973), 210; *Collective properties of physical system* (Academic Press, New York), 1974.

#### Lifetimes of Single-Particle States Near $^{48}\text{Ca}$

C M BHAT & N G PUTTASWAMY

Department of Physics, Bangalore University  
Bangalore 560 001

Received 17 April 1979; revised received 12 July 1979

The wavefunctions and the lifetimes of the single-particle states in  $^{49}\text{Ca}$  and  $^{49}\text{Sc}$ , and single-hole states in  $^{47}\text{Ca}$  and  $^{47}\text{K}$  have been calculated using the Woods-Saxon central potential. Experimental values available for  $^{49}\text{Sc}$  are in agreement with the calculated values. The matrix elements evaluated using the harmonic oscillator potential are also satisfactory. The quadrupole moments for these states have also been computed.

A study of nuclei near the doubly-magic region  $^{16}\text{O}$ ,  $^{40}\text{Ca}$ ,  $^{48}\text{Ca}$ , and  $^{208}\text{Pb}$  is very important from the shell-model point of view. Single-nucleon-transfer reactions and lifetime measurements for nuclei near  $^{16}\text{O}$ ,  $^{40}\text{Ca}$ , and  $^{208}\text{Pb}$  have helped to provide a better understanding of the structure of the energy levels of nuclei in this region.<sup>1-5</sup> Single-nucleon-transfer reactions on  $^{48}\text{Ca}$  leading to states in  $^{49}\text{Sc}$ ,  $^{49}\text{Ca}$ ,  $^{47}\text{Ca}$ , and  $^{47}\text{K}$  have revealed that the low-lying excited states carry most of the spectroscopic strength.<sup>6-9</sup>



# NOTES

In this note we present the results of our calculation on the lifetimes of the single-particle and the single-hole states for nuclei near  $^{48}\text{Ca}$ .

The single-particle (or single-hole) is assumed to move in a Woods-Saxon central potential of the form

$$V(r) = V_0 (1 + e^x)^{-1} + V_{so}(r) + V_c(r, r_c), \dots (1)$$

where,

$$x = (r - r_0 A^{1/3})/a.$$

$V_{so}(r)$ , the spin-orbit term is defined by

$$V_{so}(r) = -\lambda \frac{\hbar^2}{2mc^2} \frac{1}{r} \frac{d}{dr} [V_0 (1 + e^x)^{-1}]$$

$V_c$  is the Coulomb potential of a uniform charge distribution within  $r_c$  and  $r_c = r_{oc} A^{1/3}$ . The values used for the calculation are:  $r_0 = r_{oc} = 1.25$  fm,  $a = 0.65$  fm, and  $\lambda = 25$ . Further, starting from a real well depth of  $V_0 = -60$  MeV, the depth is searched using a computer programme until the experimental binding energy of the level is matched; the search routine is available as a part of the overall distorted-wave-Born-approximation code 'DWUCK' for the analysis of transfer reactions.<sup>10</sup> The wavefunctions thus obtained<sup>11</sup> are used to evaluate the radial matrix elements which are then used to cal-

culate the quadrupole moment ( $Q$ ) and the lifetime ( $\tau$ ) for nuclei near  $A = 48$ .

The quadrupole moment is calculated using the expression<sup>12</sup>

$$Q = \pm (\delta + Z/A + Z/A^2) \frac{2j-1}{2j+2} \langle r^2 \rangle \dots (2)$$

The positive sign is used for hole states and the negative sign is used for particle states.  $j$  is the angular momentum of the single-particle (single-hole) states.  $Z$  and  $A$  are the charge and mass number of the  $^{48}\text{Ca}$  core. Further,  $\delta = 1$  for proton states and  $\delta = 0$  for neutron states. The calculated values of  $Q$  are given in Table. 1

The lifetime  $\tau$  is calculated from the transition probability  $T_{i \rightarrow f}(\sigma l)$  given by<sup>11,14</sup>

$$T_{i \rightarrow f}(\sigma l) = \frac{8\pi(l+1)}{l[(2l+1)!!]^2} \frac{q^{2l+1}}{\hbar} B(\sigma l) \dots (3)$$

where  $\sigma = E$  (electric) or  $M$  (magnetic), and  $q$  is the wave-vector of the multipole radiation. The partial lifetime is the reciprocal of  $T_{i \rightarrow f}$  and, the lifetime  $\tau$  of any state  $i$  is the sum of the partial lifetimes for decay into all lower states. The reduced transition probability  $B(\sigma l)$  for multipole transition

Table 1—Calculated Values of the Lifetime ( $\tau$ ) and Quadrupole Moment ( $Q$ ) for Nuclear Levels near  $^{48}\text{Ca}$  using the Woods-Saxon Potential

Nucleus	$E_x$ (MeV)	Assumed single-particle configuration	Single-particle spectroscopic strength $G^*$	$Q^{\dagger}_{\text{calc.}}$ (barn)	$\tau_{\text{calc.}}$	$\tau_{\text{exptl}}$ (Ref. 3)
$^{49}\text{Sc}$	0.0	$1f_{7/2}$	7.83 (Ref. 6)	-0.151		
	3.093	$2p_{3/2}$	2.51 (Ref. 6)	-0.095	84.9 fs	$69^{+42}_{-48}$ fs
	4.082	$1f_{5/2}$	0.77 (Ref. 6)	-0.122	0.302 fs	$40^{+20}_{-18}$ fs
	5.686	$2p_{1/2}$	0.46 (Ref. 6)	0	0.987 fs	
$^{48}\text{Ca}$	0.0	$2p_{3/2}$	4.12 (Ref. 7)	-0.038		
	2.028	$2p_{1/2}$	2.20 (Ref. 7)	0	5.99 fs	
	4.007	$1f_{5/2}$	5.94 (Ref. 7)	-0.0505	1.53 fs	
	4.026	$1g_{9/2}$	3.70 (Ref. 7)	-0.068	56.8 $\mu$ s	
$^{47}\text{Ca}$	0.0	$1f_{7/2}^{-1}$	6.7 (Ref. 8)	0.05		
	2.580	$1d_{3/2}^{-1}$	3.6 (Ref. 8)	0.024	4.06 ps	
	2.600	$2s_{1/2}^{-1}$	1.8 (Ref. 8)	0	1.04 ns	
$^{47}\text{K}$	0.0	$2s_{1/2}^{-1}$	1.49 (Ref. 9)	0		
	0.359	$1d_{3/2}^{-1}$	3.88 (Ref. 9)	0.069	27.3 ps	
	3.420	$1d_{5/2}^{-1}$	0.95 (Ref. 9)	0.106	0.695 fs	

\*  $G = (2J+1) C^2 S$  should have the value  $(2J+1)$  for a pure single-particle configuration.

† No experimental values of  $Q$  are available.

of order  $l$  is defined by

$$B(E l) = (e^2/4\pi) S(j_i, l, j_f) \left\langle j_f \mid r^l \mid j_i \right\rangle^2 \quad \dots(4)$$

and

$$B(M l) = \left( \frac{e\hbar}{2mc} \right)^2 l_f [g_s - 2/(l+1) g_l]^2 S(j_i, l, j_f)$$

$$\times \left\langle j_f \mid r^{l-1} \mid j_i \right\rangle^2 \quad \dots(5)$$

In Eq. (5)  $g_l$  and  $g_s$  are the orbital- and the spin-gyromagnetic ratios of the nucleons and,  $S(j_i, l, j_f)$  is a statistical factor.<sup>16</sup> The calculated values of the lifetimes ( $\tau$ ) are given in Table 1. Table 2 lists

Table 2—Calculated Values of the Reduced Transition Probability  $B(\sigma l)$  and the Partial Lifetime for Nuclei near  $^{48}\text{Ca}$  using the Woods-Saxon and the Harmonic-Oscillator Potentials

Nucleus	Initial state	Final state	$E_\gamma$ (MeV)	$\sigma l$	$B(\sigma l)$		Partial lifetime* (Wood-Saxon potential)
					Harmonic oscillator potential	Woods-Saxon potential	
$^{49}\text{Sc}$	$2p_{3/2}$	$1f_{7/2}$	3.093	E2	39.3	34.2	84.9 fs
	$1f_{5/2}$	$1f_{7/2}$	4.082	M1	2.86	2.84	0.302 fs
				E2	37.9	32.3	22.5 fs
	$1f_{5/2}$	$2p_{3/2}$	0.989	M1	0.0	0.36	0.169 ps
				E2	18.4	13.6	63.2 ps
	$2p_{1/2}$	$1f_{7/2}$	5.686	M3	$9.94 \times 10^2$	$1.33 \times 10^4$	63.1 ps
				E4	$1.03 \times 10^4$	$3.85 \times 10^4$	24.5 ns
	$2p_{1/2}$	$2p_{3/2}$	2.593	M1	3.27	3.34	0.987 fs
				E2	44.3	47.5	0.143 ps
	$2p_{1/2}$	$1f_{5/2}$	1.604	E2	45.9	37.0	2.00 ps
				M3	$7.46 \times 10^2$	$0.86 \times 10^4$	656 ns
$^{49}\text{Ca}$	$2p_{1/2}$	$2p_{3/2}$	2.027	M1	2.32	1.16	5.99 fs
				E2	$3.3 \times 10^{-3}$	$4.1 \times 10^{-3}$	3.91 ns
	$1f_{5/2}$	$2p_{3/2}$	4.007	M1	0.0	0.59	1.53 fs
				E2	$1.2 \times 10^{-3}$	$3.24 \times 10^{-3}$	0.242 ns
	$1f_{5/2}$	$2p_{1/2}$	1.979	E2	$1.2 \times 10^{-3}$	$2.07 \times 10^{-3}$	12.9 ns
				M3	$2.0 \times 10^3$	2.23	330 ns
	$1g_{9/2}$	$2p_{3/2}$	4.026	E3	$6.99 \times 10^{-3}$	$1.78 \times 10^{-3}$	56.8 $\mu\text{s}$
	$1g_{9/2}$	$2p_{1/2}$	1.998	M4	$7.8 \times 10^5$	$3.7 \times 10^{-3}$	0.463 s
				E5	$4.3 \times 10^{-3}$	0.06	$0.5 \times 10^{10}$ s
	$1g_{9/2}$	$1f_{5/2}$	0.019	M2	5.45	$1.24 \times 10^2$	0.24 s
				M3	0.338	$1.90 \times 10^{-3}$	$1.02 \times 10^{13}$ s
$^{47}\text{Ca}$	$1d_{3/2}^{-1}$	$1f_{7/2}^{-1}$	2.578	M2	38.7	$1.62 \times 10^2$	4.06 ps
				E3	$2.40 \times 10^{-5}$	$2.70 \times 10^{-5}$	0.089 s
	$2s_{1/2}^{-1}$	$1f_{7/2}^{-1}$	2.599	E3	$4.75 \times 10^{-5}$	$4.79 \times 10^{-5}$	0.045 s
	$2s_{1/2}^{-1}$	$1d_{3/2}^{-1}$	0.021	M1	0.0	0.679	1.04 ns
				E2	$1.64 \times 10^{-3}$	$1.78 \times 10^{-3}$	$1.38 \times 10^3$ s
$^{47}\text{K}$	$1d_{3/2}^{-1}$	$2s_{1/2}^{-1}$	0.359	M1	0.0	0.458	27.3 ps
				E2	10.9	8.48	16.1 ns
	$1d_{5/2}^{-1}$	$2s_{1/2}^{-1}$	3.420	E2	10.9	9.60	0.181 ps
	$1d_{5/2}^{-1}$	$1d_{3/2}^{-1}$	3.061	M1	2.00	2.99	0.695 fs
				E2	16.1	15.0	0.201 ps

\*Partial lifetime expressed in : s, seconds;  $\mu\text{s}$ , microseconds; ns, nanoseconds; ps, picoseconds; fs, femtoseconds



the complete values of the reduced transition probability  $B(\sigma I)$  and the partial lifetimes for each of the transitions; the values of  $B(\sigma I)$  obtained from the harmonic-oscillator potential are also given in Table 2 and they are very close to those obtained from the Woods-Saxon potential.

A survey of Table 1 indicates that the lifetimes calculated using the Woods-Saxon potential are in agreement with the experimental values<sup>13</sup> for the states in  $^{49}\text{Sc}$ . However, the calculated lifetime of the 4.072 MeV state in  $^{49}\text{Sc}$  is too small compared to the experimental value, indicating that this state is perhaps not a good single-particle state. This is borne out from the fact that the single-particle spectroscopic strength is 0.77 instead of the expected value of 6. In fact, such a fragmentation of spectroscopic strength is predicted by the core-polarization model.<sup>15</sup> Regarding the lifetime of the excited states in  $^{49}\text{Ca}$ ,  $^{47}\text{Ca}$ , and  $^{47}\text{K}$ , experimental values would be needed to make a comparison with the predicted values.

It is a pleasure to thank Drs R K Bansal and M Raja Rao for the many useful discussions. One of the authors (CMB) is grateful to CSIR, New Delhi, for providing him with a junior research fellowship.

#### References

1. Ajzenberg Selove F, *Nucl. Phys.*, A281 (1977), 1.
2. Endt P M & Van der Leun C, *Nucl. Phys.*, A214 (1973), 1.
3. Hausser O, Khanna F C & Ward D, *Nucl. Phys.*, A194 (1972), 113.
4. Schmorak M R, *Nuclear Data Sheets*, 22 (1977), 487.
5. Martin M J, *Nuclear Data Sheets*, 22 (1977), 545.
6. Britton R M & Watson D L, *Nucl. Phys.*, A272 (1976), 91.
7. Metz W D, Callender W D & Bockelman C K, *Phys. Rev.*, C12 (1975), 827.
8. Martin P, Buenerd M, Dupond Y & Chabre M, *Nucl. Phys.*, A185 (1972), 465.
9. Doll P, Wagner G J, Knopfle K T & Mairle G, *Nucl. Phys.*, A263 (1976), 210.
10. Kunz P D, DWUCK, University of Colorado (unpublished) 1969.
11. Bohr A & Mottleson B R, *Nuclear structure*, Vol. 1, (W A Benjamin, New York), 1969, Ch. 3.
12. Hornyak W F, *Nuclear structure* (Academic Press, New York), 1975, 134.
13. Struve H, Thomas H C, Bennett M J & Armstrong D D, *Phys. Rev.*, C7 (1973), 1418.
14. Moszkowski S A, cited in *Alpha, beta and gamma ray spectroscopy*, Vol. 2, edited K. Siegbahn (North Holland Amsterdam), 1968, 874.
15. Bansal R K, *Phys. Rev.*, 153 (1967), 1084.

## Second Moment of Solid Hippuric Acid by Wide-line NMR\*

N R JAGANNATHAN, S GANAPATHY & R SRINIVASAN

Department of Physics (Crystallography & Biophysics)  
University of Madras, Guindy Campus, Madras 600 025

Received 13 August 1979

Using the earlier results from this laboratory on the empirical correlation between second moment and molecular weight, reasonably valid within a class of organic compounds, it is shown that the earlier experimental value of second moment and also the theoretical estimation for hippuric acid are grossly in error. The experimental redetermination gives a value of 6.9 gauss<sup>2</sup> at room temperature which is in agreement with the theoretical estimate of 7.6 gauss<sup>2</sup> for rigid lattice.

Hippuric acid  $\text{C}_6\text{H}_5\text{—CO—NH—CH}_2\text{—COOH}$  is N-benzoyl derivative of the amino acid glycine and has been reported<sup>1</sup> to have a second moment, at room temperature, of 12.9 gauss<sup>2</sup> and 32.37 gauss<sup>2</sup> at 77 K. These experimental values at room temperature and at 77 K are claimed to be in agreement with the corresponding theoretical values calculated for  $\text{CH}_2$  and  $\text{NH}$  rotation at room temperature and for the rigid lattice value. The authors also claim that they are close to the values of glycine. The values of glycine itself are reported to be close, namely 12.7 gauss<sup>2</sup> at room temperature and 30.3 gauss<sup>2</sup> at low temperature respectively.<sup>2</sup> The purpose of this note is to point out that both experimental and theoretical values for hippuric acid reported by these authors seem to be erroneous as may become clear from what follows.

We have recently shown that within a class of compounds there is a good correlation between second moment and the molecular weight.<sup>3</sup> For example, all amino acids follow the linear plot

$$Y = -0.165x + 47.45 \quad \dots(1)$$

where  $Y$  is the second moment in gauss<sup>2</sup> and  $x$  is the molecular weight.

Other classes of compounds also have a somewhat similar relation. Broadly, the second moments are systematically higher for compounds containing triplet groups such as  $\text{CH}_3$  and  $\text{NH}_3$ . The values are markedly low when the compounds are mostly made up of singlet-protons such as benzene and derivatives. In fact, this class of compounds has the relation

$$Y = -0.023x + 13.63 \quad \dots(2)$$

\* Contribution No. 617 from the Department of Physics (Crystallography & Biophysics), University of Madras



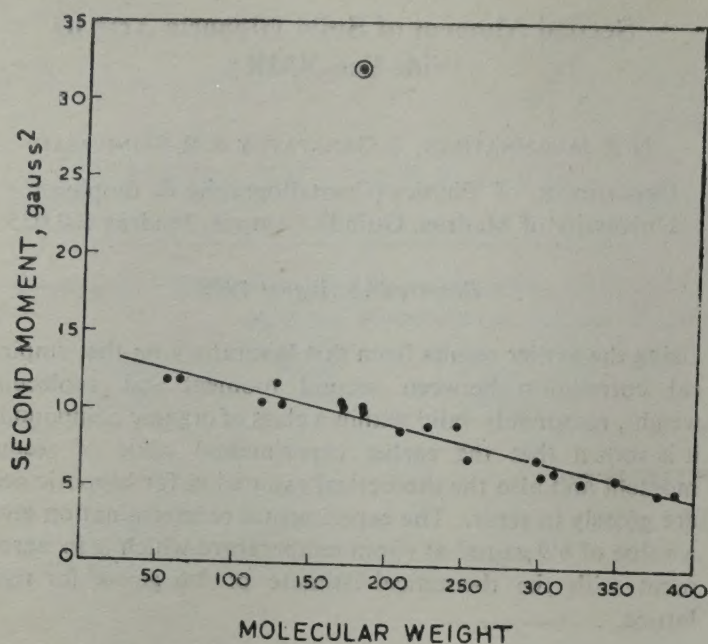


Fig. 1—Plot of rigid lattice second moment for aromatic ring compounds (singlet) against molecular weight [The straight line graph is obtained by least squares fit excluding the entry corresponding to hippuric acid (marked by encircled dot)]

During the course of these analyses it was found that hippuric acid, being benzoyl derivative of glycine has mostly singlet protons on the phenyl ring as well as on the nitrogen and the carboxyl group. There is only one doublet namely in  $\text{CH}_2$  of the alpha-carbon atom. Accordingly this compound should be classed under aromatic ring compounds and derivatives. Fig. 1 shows the plot of experimental values for a number of such aromatic compounds plotted against the molecular weight (taken from the paper by Srinivasan and Ganapathy<sup>3</sup>). Hippuric acid alone stands out as a clear misfit, if we take the value of the experimental second moment of  $32.37 \text{ gauss}^2$  as quoted by the authors cited above. Their theoretical value of second moment of  $31.5 \text{ gauss}^2$  is also obviously very much off the mark.

This is not unexpected since there are no triplets in hippuric acid unlike in glycine although the former is the derivative of glycine.

This prompted us to both calculate the theoretical rigid lattice value and to determine experimentally the second moment for this compound. The theoretical second moment for rigid lattice comes out to be  $7.6 \text{ gauss}^2$  calculated using the TSM programme due to Sjöblom and Tegenfeldt.<sup>4</sup> In these calculations the precise proton locations from neutron diffraction data<sup>5</sup> have been used. Although we could not determine the experimental second moment at low temperature, our experiment at room temperature gives a value of  $6.9 \text{ gauss}^2$ . The difference between room temperature and rigid lattice values of second moment is hardly  $0.7 \text{ gauss}^2$  and is obviously due to the fact that there seems to be no major group rotations possible in the structure.

It may thus be observed that our earlier empirical correlation will be a very simple and useful tool for a quick diagnosis on the correctness of experimental second moment or theoretical estimate based on a model of any compound of a given class, with known molecular structure.

One of the authors (NRJ) thanks the University Grants Commission, New Delhi, for financial assistance.

#### References

1. Purnima Tandon, Banerjee A K & Gupta R C, *Indian J. pure appl. Phys.*, 12 (1974), 533.
2. Kromhaut R A & Moulton W G, *J. chem. Phys.*, 23 (1955), 1673.
3. Srinivasan R & Ganapathy S, *J. Madras Univ., Sec. B*, (1979), in press.
4. Sjöblom R O I & Tegenfeldt J, *J. UUIC-B 13-2* (Institute of Chemistry, University of Uppsala, Sweden), 1971.
5. Murdoch Currie, *J. chem. Soc., Perkin II (Part I)* (1974), 784.







